Aerosol Pollution from Gas Flaring Emissions in the Niger Delta Region of West Africa

Olusegun Gabriel Fawole

School of Geography, Earth and Environmental Sciences,
University of Birmingham, United Kingdom.

This dissertation is submitted for the degree of
Doctor of Philosophy
November 2016

Abstract

Gas flaring, the disposal of gas through stacks in an open-air flame, is a common feature in the processing of crude oil, especially in oil-rich regions of the world. The rates of emission of pollutants from gas flaring depend on a number of factors including, but not limited to, fuel composition and quantity, stack geometry, flame/combustion characteristics, and prevailing meteorological conditions. In this work, new estimated emission factors (EFs) for carbon-containing pollutants (excluding PAH) are derived for a specified subset of flame condition. The air pollution dispersion model, ADMS5, is used to simulate the dispersion of pollutants from gas-flaring stacks in the Niger delta. Fuel composition and flare size play significant role in the dispersion pattern and ground-level concentrations of pollutants.

To assess the significance of gas-flaring to atmospheric aerosol loading, AERONET aerosol signals are clustered using trajectory analysis to identify dominant aerosol sources at the Ilorin site (4.34^o E, 8.32^o N) in West Africa. From 7-day back-trajectory calculations over a 10-year period calculated using the UK Universities Global Atmospheric Modelling Programme (UGAMP) trajectory model, which is driven by analyses from the European Centre for Medium-Range Weather Forecasts (ECMWF), dominant sources are identified, using literature classifications: desert dust, biomass burning, and urban-industrial. Using a combination of synoptic trajectories and aerosol optical properties, a fourth source is distinguished: that due to gas flaring. An estimation of the relative impact of these different aerosol sources on the overall radiative forcing at the Ilorin AERONET site was the carried out.

Dedication

This thesis is dedicated first and foremost to my very present help in times of need, the Author and Finisher of my faith. And, then to my lovely wife, Adebimpe, and our children – Fiyinfoluwa, Oluwadarasimi and Oluwademilade – all of who stood by me through thick and thin.

Lastly, I also want to dedicate this thesis to the blessed memory of my late father: Rev. Samuel Bamidele Olayinka Fawole (1910-1993). Sleep on Daddy!

Acknowledgements

I am greatly indebted to my supervisors: Prof. Angus Rob MacKenzie and Dr. Xiaoming Cai for their support, guidance and tutelage during the entire period of my PhD studies. For their encouraging words, especially during the frustrating months of data acquisition. I also want to thank them for putting up with me, occasionally, 'forcing' my way into their busy daily schedules.

I am equally indebted to post-doctoral colleagues: Marcus Köehler, Irina Nikolova, Rick Thomas and James Levine, for their support in getting me acquitted with the needed bits of specific programming skills during the preliminary days of my PhD studies.

A special appreciation goes to every of my colleagues in Room 412 of the Geography building for creating and sustaining a friendly atmosphere in the room to help douse the tensions of having to meet deadlines and the stress of work. It was very nice having you guys around.

Special thanks goes to my lovely wife and children for their understanding with my staying late in the University, especially during the last year of my research work. We'll definitely make up for the lost family times!

Finally, I should like to thank the Commonwealth Scholarship Commission, UK (CSCUK) for funding my PhD studies without which this achievement would have remain a dream.

Declaration

I hereby declare that except where specific reference is made to the work of others, the contents of this thesis are original and have not been submitted in whole or in part for consideration for any other degree or qualification in this, or any other university. This thesis is my own work and contains nothing which is the outcome of work done in collaboration with others, except as specified in the text and Acknowledgements. This thesis contains fewer than 60,000 words including appendices, bibliography, footnotes, tables and equations and has fewer than 100 figures.

Most of the materials in Chapters 1 and 2 (Introduction and Literature review) have been published in:
Olusegun G. Fawole, X,-M. Cai , A.R. MacKenzie (2016). Gas flaring and resultant air pollution: A review focusing on black carbon. ***Environmental Pollution***, 216: 182-197 10.1016/j.envpol.2016.05.075.

The study discussed in Chapter 6 is in the revision stage of publication in:
Olusegun G. Fawole, Xiaoming Cai, James G. Levine, Rachel T. Pinker, A.R. MacKenzie (2016). Detection of a gas flaring signature in the AERONET optical properties of aerosol at a tropical station in West Africa. ***Journal of Geophysical Research: Atmospheres***.

Olusegun Gabriel Fawole
November 2016

Symbols and abbreviation used

Symbols

u_e	exit velocity of the flue gas ($\mathrm{m\,s^{-1}}$)
s	the air-fuel mass ratio
ρ_e, ρ_∞	fuel gas and ambient air densities, respectively ($\mathrm{kg\,m^{-3}}$)
g	acceleration due to gravity ($\mathrm{m\,s^{-2}}$)
ΔT_f	mean peak flame temperature rise, (K) (taken as the difference between the adiabatic flame temperature and ambient temperature)
d_e	burner diameter (m)
ν_o	kinematic viscosity of the gas-air mixture ($\mathrm{m^2\,s^{-1}}$)
L	characteristic flame length (m)
$\dot{m}_o$	mass flux of the flue gas at the burner exit ($\mathrm{kg\,m^{-2}\,s^{-1}}$)
f_s	stoichiometric mixture fraction
ϕ	equivalent ratio
T_∞	adiabatic temperature (K)
T_{amb}	ambient temperature (K)
Fr_f	Fire Froude number
Fr_g	Fuel Froude number
Ri_L	Richardson ratio
Re_s	Reynolds number
P	atmospheric pressure (Pa)
R	universal gas constant ($\mathrm{m^3\,Pa\,K^{-1}\,mol^{-1}}$)

M_{co}	molar masses of CO ($\mathrm{g\,mol^{-1}}$)
T	ambient temperature (K)
q_i	CO yield of species *i* in the fuel gas.
c_i	percentage molar concentration of species *i* in the fuel gas
A	cross-sectional area of stack ($\mathrm{m^2}$).
$\dot{m}$	total molar flow rate to the flare ($\mathrm{m^3\,s^{-1}}$)
f_i	volume fraction of each hydrocarbon species in the fuel
H_i	net heating value of each hydrocarbon species in the fuel ($\mathrm{J\,s^{-1}}$)
H_r	net heat release rate from fuel ($\mathrm{J\,s^{-1}}$)
H	actual stack height (m)
F_r	fraction of radiative heat loss
C_p	specific heat of dry air ($\mathrm{J\,kg^{-1}\,K^{-1}}$)
R_s	stack inner diameter (m)

Abbreviations

BC	Black carbon
POM	Particulate organic matter
MCS	MCS Mesoscale convective system
ECMWF	European Centre for Medium-Range Weather Forecasts
UGAMP	UK Universities Global Atmospheric Modelling Programme
BB	Biomass burning
CC	Urban (City-City)
DD	Desert dust
GF	Gas flaring
WAM	West African Monsoon
AAE	Absorption Angström Exponent
EAE	Extinction Angström Exponent
FMF	Fine mode fraction
SSA	Single scattering albedo
bcm	Billion cubic meter
OCOM	Mole of oxygen required by a hydrocarbon specie for stoichiometric mixture
NCAR	Number of carbon

Table of contents

Symbols and abbreviation used **vi**

List of figures **xv**

List of tables **xx**

1 Introduction **1**

1.1 Chapter summary 1

1.2 Background 2

1.3 Global oil and gas reserves 4

1.4 Temporal and geographical trends in gas flaring 5

1.5 Oil and gas exploration 11

1.5.1 Composition of natural gas 12

1.5.2 Thermodynamic oroperties of natural gas 12

1.6 Air Pollution 16

1.6.1 Aerosol in the atmosphere 17

1.6.2 Climatic Impact of atmospheric aerosol 17

1.6.3 Black carbon: Sources, distribution and climatic impact 19

1.7 Objectives and structure of the thesis 19

1.7.1 Objectives 20

1.7.2 Structure of the thesis 20

2 Literature Review **22**

2.1 Introduction 22
2.2 Overview of gas flaring process 23
2.3 Gas flaring emissions and environmental impacts 23
2.4 Emissions measurements around real-world gas flaring sites 27
2.5 Types of flares 30
  2.5.1 Steam-assisted flare 31
  2.5.2 Air-assisted flare 32
  2.5.3 Pressure-assisted flare 32
  2.5.4 Non-assisted flare 33
2.6 Estimating emissions from gas flaring 33
  2.6.1 Determining flame regime 35
  2.6.2 Emission factors (EF) for gas flaring emissions 36
  2.6.3 Soot emission from gas flaring 39
  2.6.4 Scaling soot emissions from lab-based studies 42
  2.6.5 Soot modelling 44
  2.6.6 Gas flaring in global models and inventories 46
2.7 West African monsoon 48
2.8 AERONET Dataset 49
2.9 Aerosol radiative forcing 51
  2.9.1 Direct radiative forcing 52
  2.9.2 Indirect radiative forcing 52
2.10 Atmospheric dispersion modelling 54
  2.10.1 Dispersion Models 57
2.11 Conclusion 58

3 Self-consistent estimation of emission factors for gas flaring emissions 60
3.1 Abstract 60
3.2 Introduction 61
3.3 Methodology 64
  3.3.1 Equivalence ratio 64

3.3.2 Mole balancing method 65
3.3.3 Soot scaling parameter 71
3.4 Results and Discussions 72
3.4.1 Soot yield 72
3.4.2 Carbon monoxide yield 73
3.4.3 Carbon dioxide yield 75
3.5 Limitation of the model 83
3.6 Conclusion 83

4 Atmospheric dispersion of gas flaring emissions in the Niger Delta: Impact of prevailing meteorological conditions and flare characteristics 85
4.1 Abstract 85
4.2 Introduction 86
4.3 Study Area 88
4.4 Experimental design and methodology 89
4.4.1 Meteorological parameter 89
4.4.2 Combustion parameters estimates 90
4.4.3 ADMS set-up 91
4.4.4 Emission factors 92
4.4.5 Experimental variables 92
4.4.5.1 Prevailing meteorology during WAM and non-WAM months 92
4.4.5.2 Flare capacity (flow rate) 93
4.4.5.3 Fuel composition 93
4.4.5.4 Plotting of spatial distribution of emission 94
4.5 Results and discussion 94
4.5.1 Stack and natural gas parameters used in these simulations 94
4.5.2 Impact of meteorological variables 98
4.5.3 Impact of flare capacity 103
4.5.4 Impact of fuel composition 104
4.6 Conclusion 105

5 Evidence for a gas-flaring source of alkanes leading to elevated ozone in air above West Africa 109

5.1 Abstract . . . 109
5.2 Introduction . . . 110
5.3 Methodology . . . 112
  5.3.1 Meteorological condition over the West Africa region . . . 112
  5.3.2 Flight details and measurements . . . 114
  5.3.3 Back trajectory calculation . . . 115
5.4 Results and Discussions . . . 116
  5.4.1 Case study I: Flight B228 . . . 117
  5.4.2 Case study II: Flight B231 . . . 122
  5.4.3 Case study III: Flight B222 . . . 127
5.5 Conclusion . . . 127

6 Detection of a gas-flaring signature in the optical and microphysical properties of aerosols at a tropical station over West Africa using AERONET data 131

6.1 Abstract . . . 131
6.2 Introduction . . . 133
6.3 Methodology . . . 135
  6.3.1 Description of the AERONET site and major sources of aerosol . . . 135
  6.3.2 Trajectory calculation and classification . . . 136
  6.3.3 AERONET Data . . . 139
  6.3.4 Climatic condition at the study site . . . 142
6.4 Statistical Analysis . . . 142
  6.4.1 Independent sample t-test . . . 143
  6.4.2 Normality Test . . . 143
  6.4.3 Kolmogorov-Smirnov (K-S) test . . . 144
6.5 Non-Parametric t-test . . . 144
  6.5.1 Mann-Whitney U-test . . . 145
6.6 Results and Discussions . . . 145

6.6.1 Dynamics of seasonal variation of AOD and AE 145
6.6.2 Seasonal dynamics of aerosol absorption: single scattering albedo (SSA) 148
6.6.3 Optical and Microphysical properties of aerosol clusters 148
6.6.3.1 Desert Dust (DD) aerosol cluster 151
6.6.3.2 Biomass burning (BB) aerosol cluster 151
6.6.3.3 Urban aerosol (CC) aerosol cluster 154
6.6.3.4 Gas flaring (GF) aerosol cluster 154
6.7 Statistical analysis of clusters properties 157
6.8 Conclusion 160

7 Analysis of radiative properties and direct radiative forcing estimates of dominant aerosol clusters over an urban-desert region in West Africa 162
7.1 Abstract 162
7.2 Introduction 164
7.3 Methodology 166
7.3.1 Description of the AERONET site and prevailing climatic condition 166
7.3.2 Trajectory calculation and classification 167
7.3.3 AERONET data and analysis 168
7.3.3.1 Relationship between the asymmetry parameter and the backscatter fraction 168
7.3.4 Aerosol Radiative Forcing 169
7.3.4.1 Estimating direct radiative forcing 169
7.3.4.2 Radiative forcing efficiency 171
7.4 Results and Discussions 171
7.4.1 Climatology of aerosol properties 171
7.4.1.1 Temporal variability of aerosol optical depth and Angström exponent at the study site 172
7.4.1.2 Temporal variability of single scattering albedo and backscatter fraction (b) 172

7.4.2 Variability of Angström exponent and aerosol optical depth for the different aerosol classes 174
7.4.2.1 Desert dust 176
7.4.2.2 Urban aerosol 176
7.4.2.3 Gas flaring aerosol 176
7.4.2.4 Biomass burning 177
7.4.3 Aerosol radiative forcing 179
7.4.4 Radiative forcing efficiency (RFE) 180
7.5 Conclusion 182

8 Summary and future works 185
8.1 Summary 185
8.1.1 Development of a model to estimate emission factors and combustion parameters 185
8.1.2 Atmospheric dispersion of gas flaring emissions 186
8.1.3 Evidence of contribution of a gas flaring sources to alkane and enhancement of ozone levels in West Africa 187
8.1.4 Classification and properties of aerosol parameters from AERONET retrievals 187
8.2 Recommendations 188
8.3 Future works 189

References 191

Appendix A Emission factors estimation code 232

Appendix B Trajectory classification algorithm 251

Appendix C Plots of spatial distribution of pollutants 260

List of figures

1.1 (a) The distribution of world natural gas reserves (BP, 2013); (b) The distribution of world oil reserves (BP, 2013) 4

1.2 Trend of natural gas (a) production and (b) flaring in major oil producing nations between 2000 and 2011 (adapted from IEA (2012) and GGFR (2012), respectively). Note the logarithmic y-axis scale. 6

1.3 Trend of quantity flared compared to total production (data from Figure 1.2) 7

1.4 Flaring hot spot sites (1991-2009) as monitored from space are indicated as red spots while grey spots represent position of active volcanoes during the same period 10

1.5 Higher heating value (HHV) as a function of molar mass of fuel gas for the flow station data reported in Table 1.2 14

2.1 Photograph of typical gas flare in the Niger Delta during gas flaring 27

2.2 (a) Spatial variation of SO_2 concentration downwind of six gas flare sites (adapted from Obanijesu et al. (2009)); (b) Spatial variation of CO concentration downwind of six gas flare sites (adapted from Sonibare et al. (2010)); (c) Spatial variation of NO_2 concentration downwind of six gas flare sites (adapted from Sonibare et al. (2010)) 29

2.3 TEM micrograph of soot (a) microstructure (b) agglomerates (Tumolva et al., 2010). 40

2.4 Radiative forcing potential of anthropogenic and natural aerosol and greenhouse gases (IPCC, 2013) 53

2.5 A photograph of emission from an industrial stack (point source) (Stockie, 2011) 55

3.1 Soot yield as a function of Fire Froude number (adapted from McEwen and Johnson (2012) 69
3.2 Relationship between (a) EF_{soot} and HHV, and (b) EF_{soot} and molar mass for various fuel compositions 76
3.3 (a) Relationship between equivalence ratio (ϕ), EF_{CO_2}, EF_{CO} and EF_{soot}, and (b) variation of CO:CO_2 with ϕ 77
3.4 (a) Dialogue screens for inputs into the model, and (b) snapshot of a section of the output screen of the model 80
3.5 Variation of CCE, CO, CO_2, and soot yields with ϕ and flue gas exit velocity for fuel composition I 81
3.6 Variation of CCE, CO, CO_2, and soot yields with ϕ and flue gas exit velocity for fuel composition II 82

4.1 Google Earth imagery showing the Niger Delta. Red place-marks shows active flares (KML data for the flare locations are obtained from (Elvidge et al., 2015)) 89
4.2 Wind roses of wind data during typical (a) December, and (b) January in the region. 95
4.3 Wind roses of wind data during typical (a) February, and (b) June in the region. 96
4.4 Wind roses of wind data during typical (a) July, and (b) August in the region. 97
4.5 Modelled dispersion and monthly mean ground-level concentrations of (a) CO and (b) BC using fuel with lower heat content (fuel I) during a non-WAM months (Jan 2014). 99
4.6 Modelled dispersion and monthly mean ground-level concentrations of (a) CO and (b) BC using fuel with lower heat content (fuel I) during a WAM months (Jul. 2014). 100

4.7 Modelled dispersion pattern and monthly mean ground-level concentration for (a) CO, and (b) BC from two flares of different sizes for Aug. 2014. "L" and "S" represent the large and small flare, respectively. 102

4.8 Dispersion pattern and monthly mean ground-level concentration of (a) CO and (b) BC for the dense fuel composition. 107

4.9 Dispersion pattern and monthly mean ground-level concentration of (a) CO and (b) BC for the less dense fuel composition. 108

5.1 Flight track for (a) B228 (b) B231 (c) B222 and (d) active flare sites in the Niger Delta 113

5.2 Trajectory-density plot for AMMA flights (a) B228b (b) B231b and (c) B222b. The black and green boxes show the region of intense gas flaring and the city of Lagos (Nigeria), respectively. The colour code shows the range of number of trajectories in each of the $1^{o} \times 1^{o}$ gridded boxes. 118

5.3 Complete trajectory plot for flights (a) B222b (b) B228b (c) B231b and, (d) back-trajectory plot for time of flight between 38200 and 39000 seconds on B231 119

5.4 For flight B228b: (a) concentration of CO, NO_X and O_3 against flight time (b) back trajectory plot of time with elevated CO and O_3 in time step of 10 seconds (c) concentration of alkane species against flight time 120

5.5 Variation of flight height with flight time for (a) B228b, and (b) B231b . . . 121

5.6 For flight B231b: (a) plot of concentration of CO, NO_X and O_3 against flight time, and (b) concentration of alkane species against measurement time . . 125

5.7 For flight B231b: (a) back trajectory plot of flight time 31000 – 32000 in time step of 10 seconds, and (b) back trajectory plot of flight time 34500 – 36000 in time step of 10 seconds 126

5.8 (a) For flight B222: (a) plot of concentration of CO, NO_X and O_3 against flight time (b) concentration of alkane species against measurement time . . 129

6.1 Google Earth image showing location of Ilorin AERONET site and the cluster of active gas flaring sites in the Niger Delta, Nigeria (gas flare locations are from the KML file from Elvidge et al. (2015) 138

6.2 An example of trajectory plot together with the areas of major aerosol sources and the AERONET site (BB, DD, CC and, GF represent biomass emissions, desert dust, urban, gas flaring sources while IL indicate the AERONET site at Ilorin, Nigeria) 140

6.3 Temporal variation of monthly averages of (a) AOD at various wavelengths and AE (440-870 nm) (b) FMF (500 nm) 146

6.4 Distribution of daily variation of AOD for non-WAM months at (a) 440 nm, and (b) 675 nm; WAM months at (c) 440 nm, and (d) 675 nm over a five-year period (2005-2009). Bin widths are ∼0.1 units of AOD 149

6.5 Multiyear (2005-2009) seasonal variation of SSA at 440 and 675 nm. Green eclipses denote times, during the WAM months, when SSA decreases with wavelength 150

6.6 Scatter plot of (a) AAE (440-870 nm) versus EAE (440-870 nm) (b) AAE (440-870 nm) versus FMF (500 nm) for the four identified aerosol clusters . 152

6.7 Parts of a typical boxplot 155

6.8 Boxplots for the four identified aerosol classes showing the statistical summaries of (a) AAE (440-870 nm); (b) EAE (440-870 nm); (c) SSA (675 nm); and (d) AE (440-870 nm) 156

6.9 Scatterplot with X and Y error bars for the AAE versus EAE mean values for the four aerosol clusters. The error bars represents the standard deviations 157

7.1 Multiyear daily variation of (a) AOD, (b) Angstrom exponent (AE), and (c) multiyear mean monthly variation of AE 173

7.2 (a) diurnal variation of SSA (675 nm), (b) mean monthly variation of SSA (675 nm), (c) diurnal variation of backscatter fraction, and (d) mean monthly variation of backscatter fraction for 2005-2009 175

7.3 Time series for monthly mean surface albedo at Ilorin for the period (01/2005 – 01/2009) 178
7.4 Direct radiative forcing (DRF) at the TOA for the different aerosol classes . 180
7.5 Radiative forcing efficiency (RFE) for the different classes 181
7.6 The relationship between DRF and AOD (675 nm) for (a) Biomass burning (n=184) (b) Urban (n=215) (c) Desert dust (n=238) (d) Gas flaring (n=180) aerosol classes 183

C.1 Modelled dispersion and monthly mean ground-level concentrations of (a) CO and (b) BC using fuel with lower heat content (fuel I) during a non-WAM months (Jan. 2015). 261
C.2 Modelled dispersion and monthly mean ground-level concentrations of (a) CO and (b) BC using fuel with lower heat content (fuel I) during a non-WAM months (Dec. 2015). 262
C.3 Modelled dispersion and monthly mean ground-level concentrations of (a) CO and (b) BC using fuel with lower heat content (fuel I) during a WAM months (Aug. 2014). 263
C.4 Modelled dispersion and monthly mean ground-level concentrations of (a) CO and (b) BC using fuel with lower heat content (fuel I) during a WAM months (Aug. 2015). 264
C.5 Modelled dispersion pattern and monthly mean ground-level concentration for (a) CO, and (b) BC for flare modelled as non-buoyant source (Aug 2015). 265
C.6 Modelled dispersion pattern and monthly mean ground-level concentration for (a) CO, and (b) BC for flare modelled as non-buoyant source (Jan 2015). 266

List of tables

1.1 Year 2008 estimated volume of gas flared by top 20 gas flaring nations with an estimated error of ±2.11 bcm 9

1.2 Composition (in mole %) and some properties of fuel gas from field stations and literature 15

2.1 Pollutant measurements around several oil and gas facilities 30

2.2 Summary of the features of the different types of flares discussed in Section 2.5 34

2.3 Summary of emission factors and emission rate for soot from industrial flares 41

2.4 Pasquill stability classification 56

3.1 Fuel compositions used in this study (given in molar percentage) 74

3.2 Emission Factor (EF) for soot from gas flaring 78

3.3 Emission factors for CO and CO_2 from gas flaring 78

4.1 Stack and fuel parameters used 94

5.1 Flight details of selected AMMA flights 114

5.2 Statistics of alkane species measured on flight B228. 122

5.3 Statistics of alkane species measured on flight B231. 124

5.4 Statistics of alkane species measured on flight B222. 128

6.1 Mean optical and microphysical properties of the aerosol clusters. The values in brackets are standard deviations showing the spread of the values 153

6.2 Median values of optical and microphysical properties of the clusters. The values in brackets are the 25 % and 75 % percentiles 153
6.3 Statistical comparison (T-test) for clusters' optical and microphysical properties 158

7.1 Summary of parameter for aerosol classes used to estimate their DRF . . . 178
7.2 Mean monthly surface reflectance and cloud amount used 178

Chapter 1

Introduction

1.1 Chapter summary

This opening chapter gives a broad overview of global oil and gas reserves, its exploration, trends of gas flaring as well as highlights the composition and thermodynamic properties of natural gas. An in-depth description of the temporal and geographical trend of gas flaring is undertaken to provide an adequate understanding of gas flaring sites from a global perspective. Overall, it does provide an adequate introduction to the basis for and scope of gas flaring, which is the whole essence of this study. A brief insight to the basics of air pollution and classification of atmospheric aerosol is presented. Finally, the chapter closes with the objectives of the study and overall structure of the thesis.

I have published most of the materials in this chapter of the thesis in: **Olusegun G. Fawole, X,-M. Cai , A.R. MacKenzie** (2016). Gas flaring and resultant air pollution: A review focusing on black carbon. ***Environmental Pollution***, 216: 182-197 10.1016/j.envpol.2016.05.075.

I carried out the review and compiled the manuscript while my supervisors; Prof. A.R. MacKenzie and Dr. Xiaoming Cai, read, edited and made several useful contributions in the analysis and compilation to bring it up to publishable standard.

1.2 Background

Humans need energy to drive their technology: and hence, make life pleasurable and worth living. Different forms of energy are in use and new ones are developed in order to meet the increasing need of this all-important commodity (MacKay, 2008). This quest for dependable, affordable and environmentally benign energy sources has occurred throughout human history; for the last century or so, crude oil has been the focus of world energy. In 2011, crude oil was estimated to provide 52.8 % of the world's energy (13113 Million Tonnes of Oil Equivalent (Mtoe)); with oil and natural gas accounting for 31.5 % and 21.3 %, respectively (IEA, 2013).

Human reliance on oil and gas as an energy source is not without its attendant impact on the environment. During production, detrimental impacts on the environment (air, water and soil) include: oil spills and leakages, venting, sludge disposal, and flaring, to mention but a few (Almanza et al., 2012; Osuji and Adesiyan, 2005; Osuji and Onojake, 2004; Sonibare et al., 2010). The post-production impact of oil and gas on the environment is also a major source of concern. A vast majority of automobiles still run on petrol and diesel. Several studies into ambient air quality have classified automobiles as a principal source of compounds hazardous to the environment and/or human health, such as: black carbon (BC), NO, NOx (i.e., $NO+NO_2$), VOCs, PAH (polyaromatic hydrocarbons), and other ozone precursors (Hitchins et al., 2000; Marr et al., 1999; Monaci et al., 2000).

Gas flaring is often a usual daily activity in oil fields around the world, particularly in oil-rich regions of the world where the infrastructure to capture and utilise and/or market for the gas produced is not available. Despite several calls by international bodies such as the World Bank's initiative; Global Gas Flaring Reduction (GGFR), the volume of gas flared globally seems to have plateaued at around 130 billion cubic meters (bcm: 10^9 m^3) since 2008. According to GGFR (2013), there was an increase of 2 bcm in the volume of gas flared in 2011 compared to the previous year. The latest in this series of initiative by the World Bank, Zero Routine Flaring by 2030, was launched by the Secretary-General of the

United Nations, Ban Ki-Moon and World Bank's President, Jim Yong Kim in May, 2015 (see http://www.worldbank.org/en/programs/zero-routine-flaring-by-2030, last accessed on December 7, 2015).

Gas flaring, a prominent source of BC, has been ignored or underestimated in emission inventories and models, as a result of which models are struggling to predict measurements of BC in regions of intense gas flaring. The intensity of gas flaring and specifics of atmospheric transport combine to enhance the role of gas flaring emissions over very large areas (e.g., the Arctic) (Stohl et al., 2013). Presently, treatment of emissions from gas flaring is rather rudimentary in most global emission inventories.

Gas flaring is classified as a miscellaneous BC-rich source, a group which includes aviation and shipping which together contribute about 9 % to global BC emission (Bond et al., 2013). In contrast to other BC sources in this category, gas flaring is a rather elaborate type of combustion characterized by open-fire resulting in flames that could be up to 8-10 metres in length, with temperature as high as 2000 K. The buoyancy of emissions at the exit of the stack and height at which they are emitted is another unique feature of this class of emission. Gas flaring burns a huge quantity of fuel and is a year round activity at most of the intensive flaring regions of the world. The GAINS (Greenhouse gas Air pollution INteractions and Synergies) model estimated that gas flaring contributes about 4 % of total anthropogenic BC emissions, majority of which are from the leading gas-flaring nations; Russia, Nigeria, and countries in the Middle East (Bond et al., 2013; Stohl et al., 2013). Gas flaring is estimated to contribute 260 Gg to global BC estimates annually (Bond et al., 2013), while in Russia, it is estimated to make the largest contribution of 36.2 % to anthropogenic BC emission (Huang et al., 2015). From a 3-year model simulation, more than 50 % of BC near the surface in the Arctic is estimated to be contribution from gas flaring (Stohl et al., 2013).

Considering the small number of nations that still flare gas, a contribution of 4 % to global BC represents a significant skew in the global apportionment of BC emissions. On a regional scale, the contribution of this ’overlooked’ source of ambient aerosol loading is likely to be significant and its overlook could be a gross scientific oversight.

1.3 Global oil and gas reserves

World-proven natural gas and oil reserves at the end of 2012 stood at 187.3 and 1668.9 trillion cubic metres (tcm: 10^{12} m^3), respectively, sufficient to meet 55.7 years of global production (BP, 2013). The distribution of these reserves among regions of the world is shown in Figures 1.1(a) and (b). The natural gas collected during the exploration of crude oil from the Earth’s crust can be a very good source of fuel; transported in pipes for industrial or domestic use and also recycled back into the processing operation (Davoudi et al., 2013; Elvidge et al., 2009).

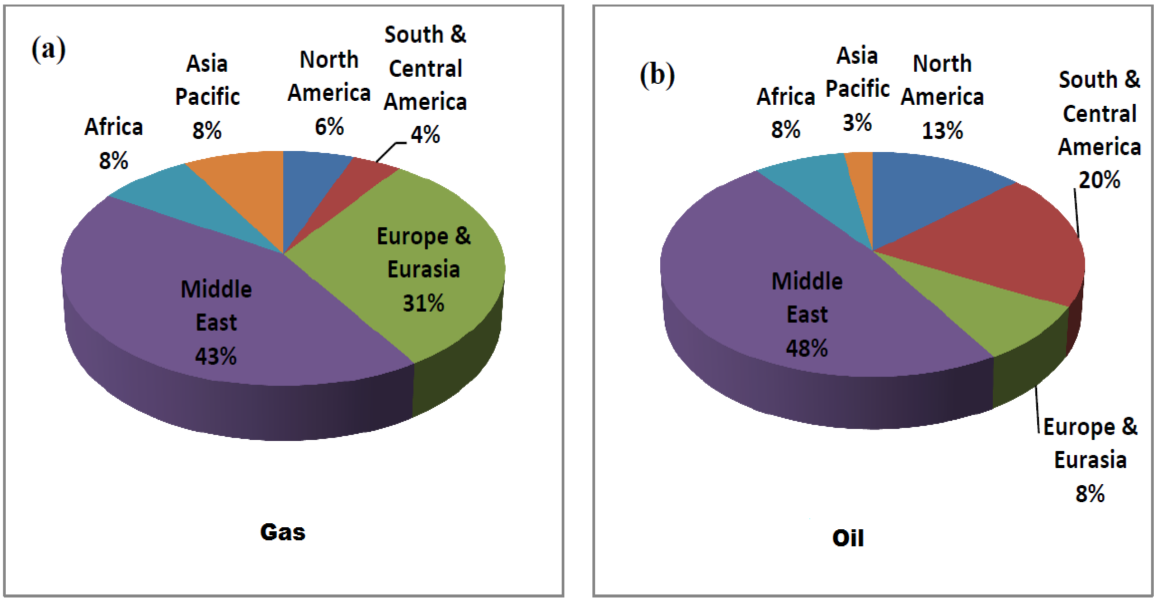

Figure 1.1: (a) The distribution of world natural gas reserves (BP, 2013); (b) The distribution of world oil reserves (BP, 2013)

In developing countries and oil-rich regions where the technology, infrastructure and market to put all of the natural gas to meaningful use are not available or inadequate, the excess natural gas then becomes a waste and is flared or vented. Gas flaring has been termed 'gross waste' by the World Bank's initiative against gas flaring: Global Gas Flaring Reduction (GGFR) because flaring represents direct injection of fossil carbon into the atmosphere without capture and utilization of the heat produced by combustion.

1.4 Temporal and geographical trends in gas flaring

Globally, the all-time peak of the volume of gas flared; 172 bcm, was in 2005 (Elvidge et al., 2009). Figure 1.2(a) shows the quantity of natural gas produced by the top 10 oil producing nations of the world between 2000 and 2011, and for comparison, Figure 1.2(b) shows the estimated quantity of gas flared by these major oil producing nations during the same period of time. The estimated volume of gas flared globally in 2012 is also shown in Figure 1.2(b): the 2012 data is obtained from Elvidge et al. (2015). Data for the plots in Figure 1.2(a) and (b) are from IEA (2012) and GGFR (2012), respectively. Between 2008 and 2011, there was no significant decrease in the amount of natural gas flared. In fact, there was a slight increase between 2010 and 2011. According to BP (2015), the production excludes the quantity flared or recycled. Therefore, total fossil fuel extracted and ultimately released to the environment is the sum of the production and quantity flared.

Figure 1.3 gives the temporal variation of the fraction of total gas extracted that is flared between 2000 and 2011. Nigeria, Libya and Kazakhstan still flare a sizeable amount of their total production. As at 2011, Nigeria and Libya flared about 30 % of their total gas extraction while Kazakhstan flares about 15 %. The 30 % (15.2 bcm) flared by Nigeria is more than twice Libya's total gas extracted (6.3 bcm) for the same period. Russia and Nigeria together account for about 35 % of the gas flared globally (Elvidge et al., 2009). Although, the fraction of gas flared is decreasing for most countries and for the largest emitters, several countries show flat or increasing fractions of gas flared. The estimated quantity of natural gas flared in the US and Canada, as shown in Figure 1.2(b), are just for the off-shore flaring

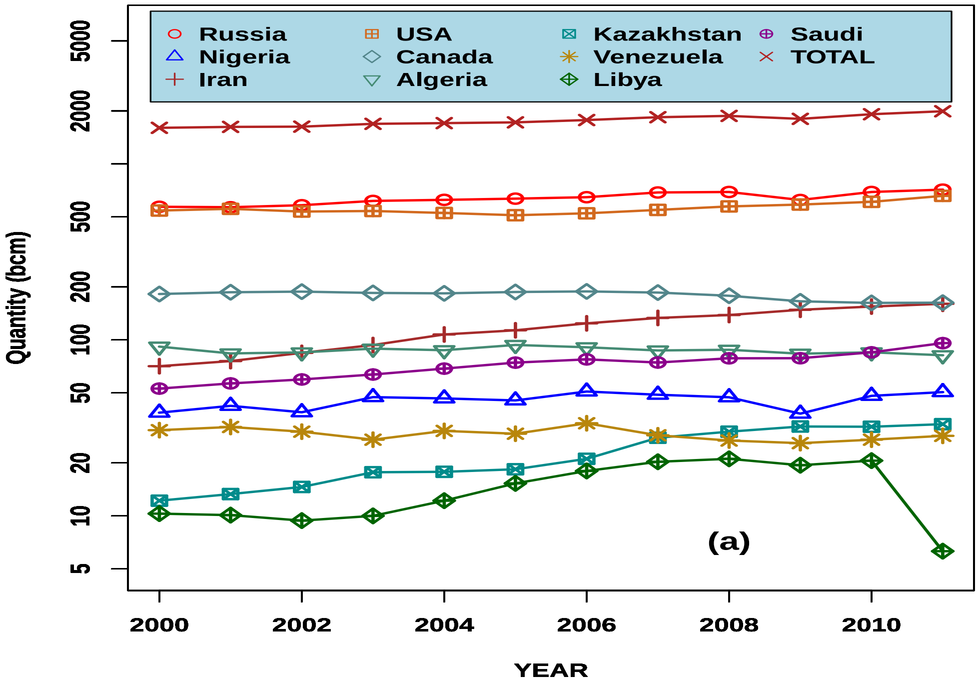

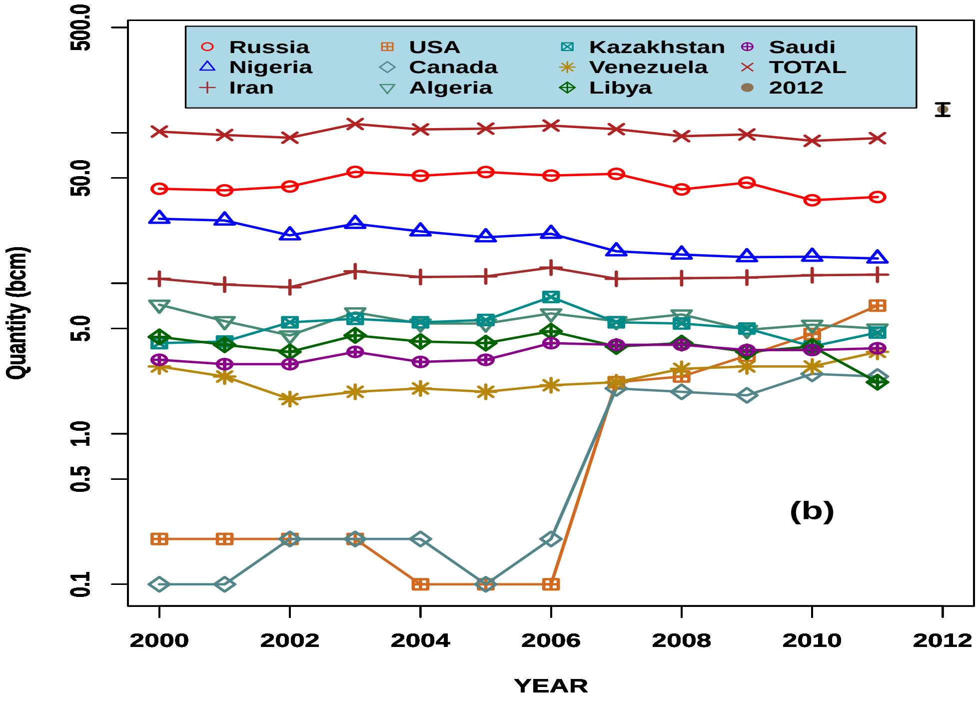

Figure 1.2: Trend of natural gas (a) production and (b) flaring in major oil producing nations between 2000 and 2011 (adapted from IEA (2012) and GGFR (2012), respectively). Note the logarithmic y-axis scale.

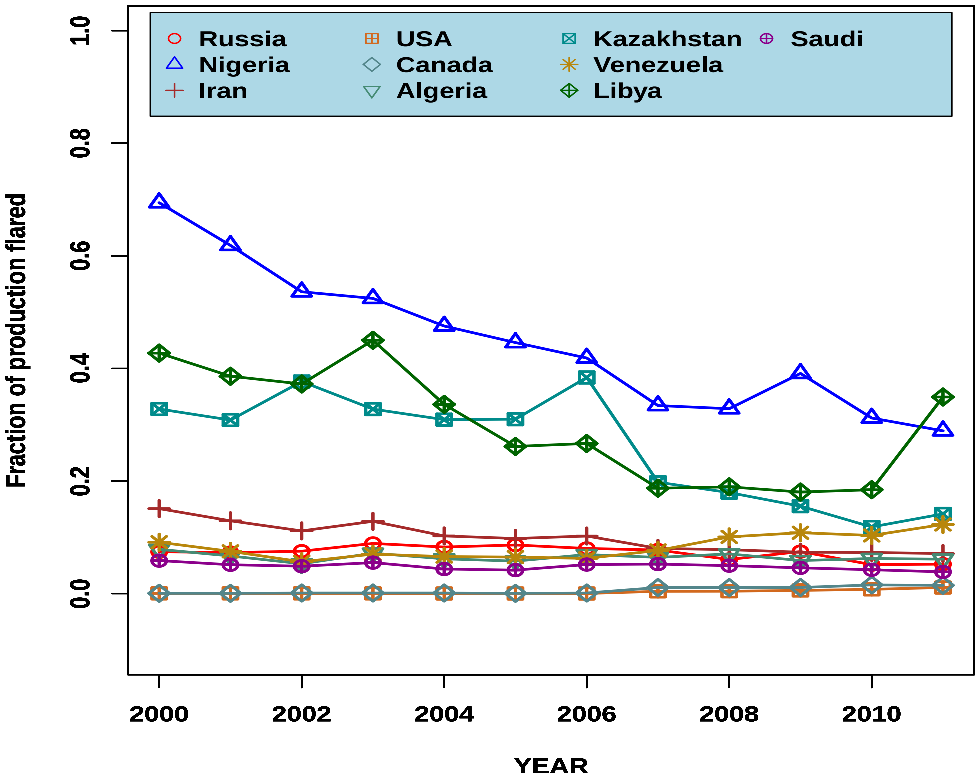

Figure 1.3: Trend of quantity flared compared to total production (data from Figure 1.2)

which is presumably responsible for the very low quantities recorded. After 2006, there is a factor of 22 and 10 increase in flaring from USA and Canada, respectively, resulting, presumably, from increased exploitation of hydrocarbon reservoirs using the unconventional method ('fracking').

Table 1.1 gives the estimates, from satellite data, of the quantity of gas flaring by the top 20 gas-flaring nations of the world in 2008 and a brief summary of the climatic conditions of the region based on the Köppen climate classification (see, e.g., Holden, 2005).

Figure 1.4, reproduced with permission from Casadio et al. (2012), shows the global geographic distribution of gas flaring sites obtained by remote sensing techniques. In Africa, the flaring spots are clustered around the North - Algeria, Libya and Egypt - as well as around the Atlantic Ocean, especially the Niger Delta area of Nigeria. In Europe, they are around Russia and Kazakhstan, and Iran, Iraq, Kuwait, and Saudi Arabia in the Middle East. Satellite remote sensing not only gives a general picture of the spatial distribution of flares, but also a gross estimation globally at national levels.

Elvidge et al. (2015), in 2012, using data collected by National Aeronautics and Space Administration/National Oceanic and Atmospheric Administration (NASA/NOAA) Visible Infrared Imaging Radiometer Suite (VIIRS), identified more than 7000 active flares globally: the bulk of which were found in the upstream sector of the oil and gas industries. During the period, the estimated volume of gas flared globally was 143±13.6 bcm (Elvidge et al., 2015). Compared to 119.3±2.11 bcm estimated for 2008 (Elvidge et al., 2009), this is an increment of about 20 % in the central tendencies of the estimates for both years and is well outside the combined uncertainty bounds of both estimates. An increment of about 20 % over four years, stands in stark contrast to the decrease anticipated as a result of the World Bank's GGFR initiative. A new dimension to the problem is the inclusion of three new countries – India, Egypt and Turkmenistan - in the list of top 20 gas-flaring countries.

The geographical location of the sources of gas flaring emissions (as monitored from space, see Figure 1.4), the atmospheric behaviour of emitted pollutants, and the pollutant "matrix" from other sources into which emission are made, determine to a large extent the effect gas flaring emissions will have on regional pollution loadings and on climate. BC emissions in the peri-Arctic and West African Monsoon (WAM) regions have the potential to interact with regional radiative energy budgets and atmospheric circulations, leading to impacts on their respective regional climates. Gas flaring emissions in the tropics, especially the WAM and South Asian Monsoon (SAM), could have significant regional impact as a result of the intense convective activities and cloud formation in these regions.

Table 1.1: Year 2008 estimated volume of gas flared by top 20 gas flaring nations with an estimated error of ±2.11 bcm

Rank	Country	Gas Flared (bcm) [a]	Regional Climate	Comments [b]
1.	Russia	40.5	(Dfa, Dfb, Dwa, Dwb), (Dfc,Dfd, Dwc, Dwd) and ET	peri-Arctic emissions; pole-ward atmospheric flow around Tibetan anticyclone in northern hemisphere winter
2.	Nigeria	15.1	Am and Aw	Tropical monsoon and trade-wind littoral and tropical wet and dry climate resulting from West African monsoon winds that changes direction with season; climatic condition is controlled by trade wind and movement of the ITCZ
3.	Iran	10.4	Bwh	Tropical and subtropical desert climate characterised by large diurnal temperature range. Deep turbulent boundary layer during the day; shallow stable boundary layer at night. Large-scale subsidence (descending branch of the Hadley circulation) above the boundary layer.
4.	Iraq	7.0	Bsh	Mid-latitude steppe and desert climate characterised by semiarid annual rainfall distribution
5.	Algeria	5.5	Bwh	As for Iran
6.	Kazakhstan	5.2	Bwk	Mid-latitude arid wet and dry climate
7.	Libya	3.8	Bwh	As for Iran
8.	Saudi Arabia	3.5	Bwh	As for Iran
9.	Angola	3.1	Cwa	Humid subtropical climate; equatorward and poleward circulation during winter and summer, respectively, cause changes in the movement of air masses from the cold polar and warm tropics within this climate
10.	Qatar	3.0	Bwh	As for Iran
11.	Uzbekistan	2.7	Csa	Mediterranean climate; it is controlled by the variation between subtropical high in summer and polar westerlies in winter
12.	Mexico	2.6	Af, Aw, Bsh, Bsk, Bwh, Cwa, Cwb, Cfa, Cfb	Complex climatic condition; two tropical, two dry and three temperature climates
13.	Venezuela	2.6	Aw	Tropical wet-dry climate
14.	Indonesia	2.3	Aw, Am	As for Nigeria (see comment above)

15.	USA	2.3	Bsk, Bsh, Bwk, CSa, Csb, Af	Mediterranean/dry summer subtropical climate characterised by moist winter and hot dry summer; subtropical anticyclones are key factor that control this climate
16.	China	2.3	Cfa, Cwa	Humid subtropical climate; during winter the climate is influenced by the Siberian cold and during summer there is an inflow warm of air from the west
17.	Oman	1.9	Bwh	As for Iran
18.	Malaysia	1.9	Af	Tropical rainforest characterised by constant high temperatures and evenly distributed high precipitation; controlled by movement of the ITCZ and rising air along trade wind coast. Strongly affected by el Nino Southern Oscillation
19.	Canada	1.8	Dfb, Dfd, Dsc Af	As for Russia (see above)
20.	Kuwait	1.8	Bwh	As for Iran
	Total	119.3		

[a] Quantity of gas flared is obtained from Elvidge et al. (2009). [b] See Holden (2005)

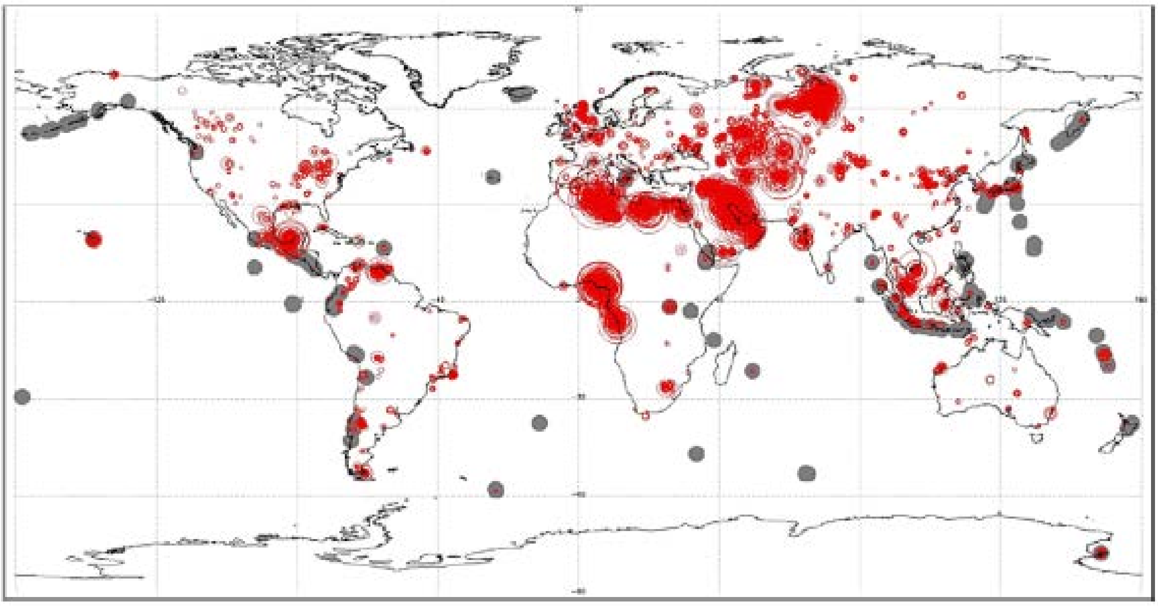

Figure 1.4: Flaring hot spot sites (1991-2009) as monitored from space are indicated as red spots while grey spots represent position of active volcanoes during the same period

Monsoon circulations are characterised by large-scale seasonal reversals of wind regimes. Regions often referred to as ‘monsoonal’ include tropical and near-tropical regions which experience a summer rainfall maximum and most of these regions have a double rainfall maximum (Barry and Chorley, 2009). The annual climatic regime over West Africa has many similarities to that of South Asia. Both are characterised by surface air-flow which is determined by the position of the leading edge of a monsoon trough. Winds are south-westerly to the south of the trough and north-easterly to the North. The lack of a large mountain range in the north of West Africa strongly enhances the northward advance of the WAM in contrast with its South Asian counterpart. The position of the leading edge of the WAM trough may oscillate greatly from day-to-day through several degrees of latitude (Barry and Chorley, 2009). In the WAM, deep convection occurs in organised systems known as Mesoscale Convective Systems (MCS) (Mari et al., 2011; Mathon and Laurent, 2001). Deep convection in the tropics coupled with the movement of the ITCZ is responsible for intense mixing, venting of the atmospheric boundary layer, and long-range transport of aerosols (Law et al., 2010; Reeves et al., 2010; Sultan and Janicot, 2003).

1.5 Oil and gas exploration

Oil exploration can be a very complex and capital intensive process as oil deposits are often located in reservoirs buried far into the Earth. These locations can be in very remote and inhospitable parts of the Earth and can be either on- or off-shore. The multi-staged process of exploration, exploitation and processing of crude oil in its raw form from the Earth’s crust can be broadly divided into upstream, midstream and downstream. Environmental contaminants are expelled into the ambient environment - soil, air and water - at different stages of the process. Crude oil is found in reservoirs which also contain gas. This gas is known as “associated natural gas”, and it is separated from the crude oil at flow stations. Natural gas includes both “non-associated” gas originating from fields producing only gaseous hydrocarbons, and “associated” gas produced in association with crude oil (IEA, 2012). Natural gas comprises mainly hydrocarbons, predominantly short-chained alkanes. At the separation stage, some of the natural gas is captured for domestic and industrial use while the rest is disposed of, usually by flaring in open flames. Below, the term ‘fuel gas’ is used to refer to the natural gas that is flared. The quantity of contaminants expelled at this stage of processing depends on the technology employed, quantity of crude oil processed, flare geometry and design, prevailing meteorological conditions and the composition of the flared gas (E & F Forum, 1994; Ismail and Umukoro, 2014; Johnson and Coderre, 2011; Obanijesu et al., 2009; Ouf et al., 2008; Sonibare and Akeredolu, 2004; Talebi et al., 2014).

Oil and gas are produced in many wells in different parts of the world at rates varying from 50 m^3 to 700 m^3 per day. As a result of the diverse nature of the geological features of the area where these explorations take place, the composition of oil and gas varies from one station to another.

1.5.1 Composition of natural gas

The composition of natural gas from 10 stations from around the world is given in Table 1.2. Fuel gas is a combination of C_1 to C_7+ hydrocarbons which are predominantly alkanes. A typical fuel gas sample contains CH_4, C_2H_6, C_3H_8, nC_4H_{10}, iC_4H_{10}, nC_5H_{12}, iC_5H_{12}, C_6H_{14}, C_7H_{16}, H_2S, CO_2 and N_2, where ‘n’ and ‘i’ stand for ‘normal’ i.e., straight chained, ‘iso’ or branched-chained alkanes, respectively. The separation of gas and liquid is not perfect at the Flow Stations and as such trace amounts of liquid can occur in the gas stream, enhancing the abundance of higher molecular weight alkanes in the fuel gas.

1.5.2 Thermodynamic oroperties of natural gas

The higher heating value (HHV) is the total enthalpy of the complete combustion reaction for the gas mixture, plus the heat of condensation of the water produced during combustion;

lower heating value (LHV) is the total enthalpy of the complete combustion when water remains present in its gaseous form only (Flagan and Seinfeld, 2013). The Volumetric heating value (VHV), measured in kJ mol^{-1}, usually refers to the HHV unless otherwise stated. In gas flaring, HHV, calculable using data from standard thermodynamic tables, defines the total amount of energy available to provide buoyancy to the plume from a flare. Buoyancy is an important parameter in determining the dispersion of gas flaring emissions (Beychok, 2005; Leahey and Davies, 1984). The heat content of a fuel gas depends on its molar mass and by extension the density of the fuel. Figure 1.5 presents the best fit line relating HHV to the molar mass of the fuel gases from the flow stations given in Table 1.2. This plot shows the extent of dependence of HHV on the molar mass, and hence, density of the fuel gas. These properties of the fuel gas, varies with the fuel composition. Note that the HHV values for the laboratory flares in Table 1.2 are lower that the HHV for fuel gases from real-world flow stations.

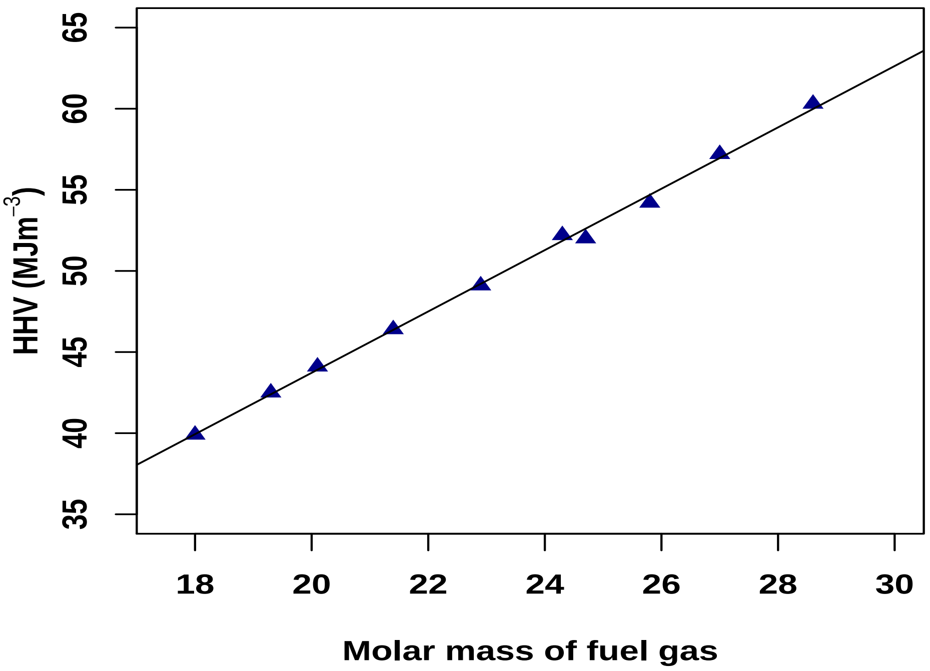

Figure 1.5: Higher heating value (HHV) as a function of molar mass of fuel gas for the flow station data reported in Table 1.2

Table 1.2: Composition (in mole %) and some properties of fuel gas from field stations and literature

Composition	**Flow Stations**										**Lab-based**	
	1	2	3	4	5	6	7	8	9	10	A	B
CH_4	74.3	79.85	56.9	55.5	82.23	78.41	68.14	68.42	72.32	69.58	85.24	74.54
C_2H_6	14.0	11.54	21.2	18.0	2.38	5.68	14.22	7.65	2.41	0.25	7.06	12.17
C_3H_8	5.8	2.25	6.0	9.8	4.24	0.23	10.27	11.27	6.24	12.54	3.11	5.37
nC_4H_{10}	2.0	2.58	3.7	4.5	0.94	0.7	3.23	4.39	8.12	2.35	1.44	2.49
iC_4H_{10}	-	0.14	-	-	5.12	4.12	2.38	4.42	5.12	5.12	-	-
nC_5H_{12}	0.9	3.24	1.6	1.6	2.25	9.12	0.75	0.94	3.14	5.20	-	-
iC_5H_{12}	-	-	-	-	2.14	0.25	1.01	1.55	2.48	2.54	-	-
C_6H_{14}	-	0.14	-	-	0.25	0.23	-	0.18	0.15	1.97	-	-
N_2	2.9	0.1	-	0.2	-	0.05	-	0.16	-	0.24	1.24	2.15
CO_2	-	0.16	7.1	8.9	0.45	1.21	-	1.02	-	0.21	1.91	3.28
H_2S	0.1	-	3.5	1.5	-	-	-	-	0.02	-	-	-
C:H	0.2659	0.2715	0.2569	0.2602	0.2730	0.2751	0.2860	0.2852	0.2893	0.2924	0.2541	0.2570
Molar mass ($gmol^{-1}$)	21.4	21.4	25.8	26.9	22.9	24.7	24.3	25.8	27.0	28.6	19.2	21.5
Molar mass ($gmol^{-1}$) without CO_2 and N_2	20.5	21.3	22.7	22.9	22.7	24.1	24.3	25.3	27.0	28.4	18.0	19.4
HHV(MJm^{-3})	44.8	46.4	47.8	48.7	49.1	52.0	52.2	54.2	57.2	60.3	39.8	42.5

Fuel compositions 2 and 5 – 10 are adapted from (Sonibare and Akeredolu, 2004), 1, 3 and 4 from (Ismail and Umukoro, 2014) and lab-based (A & B) from (McEwen and Johnson, 2012). Compositions 1, 3 and 4 are from Saudi Arabia, Kuwait and Iraq, respectively, while 2 and 5 - 10 are from different flow stations in Nigeria. C:H (mass-weighted carbon to hydrogen ratio), molar masses and higher heating value (HHV) were estimated in this work.

1.6 Air Pollution

Air pollution, the introduction of air pollutants in the form of gases and particulate matter (PM) into the Earth's atmosphere, has received global attention in recent times. Globally, severe air quality problem due to increasing levels of atmospheric air pollutant have been associated with severe respiratory related health problems, increased mortality and morbidity rate, low plant yield, poor visibility and global warming. Industrialization and urbanization has been identified as major cause of air pollution problem. Air pollution can be studied on local, regional or global scales. Long-range transport of atmospheric aerosol has made the process of abating the trend and impact of air pollution more of an international collaboration rather than a local or national issue. Several air quality legislations and emissions standards, such as the USEPA's NAAQS (National Ambient Air Quality Standard) and EU air quality directives, are in place in various nations and regions of the world to improve air quality on both local and regional basis.

An adequate understanding of emissions, interactions, nature and transport of these air pollutants is a major way to reducing their atmospheric concentration, and hence, mitigate their effects on human, plants and the environment. In-situ measurement (Akinlade et al., 2015; Owoade et al., 2016, 2013), remote sensing measurement (Bergstrom et al., 2007; Russell et al., 2010) and modeling (Anejionu et al., 2015b; Hansen et al., 2005) are ways by which these aerosols have been characterized and their impacts studied. Globally, it has been established that air pollution is more intense in urban area and major cities in contrast to sub-urban and rural area owing to human population, volume of traffic and industrialization.

1.6.1 Aerosol in the atmosphere

Atmospheric aerosols based on their source are classified as either primary or secondary pollutants. Primary aerosols (e.g. carbon monoxide) are emitted directly into the atmosphere from their sources while secondary aerosols (e.g. ozone) are formed in the atmosphere from precursor gases. These aerosols also undergo complex chemical reactions, mixing with each other externally or internally (Fassi-Fihri et al., 1997). Sources of these pollutants can be classified as:

- Natural, for example, wind erosion, forest fire, lightning, volcanic eruption, biogenic emissions, sea spray and pollens
- Anthropogenic/man-made, for example, traffic, industrial, domestic heating and cooking

Atmospheric aerosols are also classified in terms of their aerodynamic diameter (D_{ae}) as:

- Coarse mode particulate matter (PM) – these are atmospheric aerosols with aerodynamic diameter, $2.5 \leqslant D_{ae} < 10$ μm often termed $PM_{2.5-10}$;
- Fine mode PM – atmospheric aerosol with aerodynamic diameter, $1 \leqslant D_{ae} < 2.5$ μm often termed $PM_{2.5}$;
- Ultrafine mode PM – atmospheric aerosol with aerodynamic diameter, $D_{ae} < 0.1$ μm often termed ultrafine particles (UFP).

1.6.2 Climatic Impact of atmospheric aerosol

Atmospheric aerosols plays prominent role in the several atmospheric processes. These aerosols may be categorised as tropospheric or stratospheric depending on their position and origin. Atmospheric aerosol interact with the Earth- atmosphere radiative budget both directly by scattering and absorbing incoming solar radiation, and indirectly by altering the radiative properties of cloud (Andreae, 1995). The net effect of atmospheric aerosols is the sum total of the scattering and absorption of incoming solar (shortwave) radiation and outgoing (longwave) radiation. As aerosol become increasingly absorbing versus scattering, a point is reached, depending on the aerosol size and surface reflectance (albedo), where the overall effect of the aerosol layer changes from one of cooling to warming. In addition, if the particles consist of a mixture of purely scattering materials, such as , ammonium sulphate, and partially absorbing material, such as soot, the cooling-warming effect depends on the nature of mixing of the two substances throughout the aerosol layer (Charlson et al., 1992). Particles exist both above and below clouds. The amount of light scattered back to space depends on the properties of both the aerosol layer and the cloud. Direct effect can be observed visually as the sunlight reflected upwards from haze when viewed form mountain top or from aircraft. Indirect effect of aerosols are more complex to assess than direct effects because they depend on a chain of phenomena that connects aerosol levels to concentration of cloud condensation nuclei (CCN), cloud albedo and cloud lifetime. In contrast to Greenhouse Gases (GHGs), which act only on outgoing infrared radiation, aerosol particles can influence both sides of the energy balance (Seinfeld and Pandis, 2016).

GHGs such as CO_2, CH_4, N_2O and the chlorofluorocarbons (CFCs) are virtually uniform globally; aerosol concentrations, on the other hand, are highly variable in space and time (Seinfeld and Pandis, 2016). GHG have a well understood effect on the global radiative budget and their long-term thread are well-known. Therefore, there is much confidence in the GHG component of the estimated climate warming during the next few decades (Twomey et al., 1984). Aerosol residence time in the troposphere are roughly 1-2 weeks. By contrast, not only are GHGs residence time measured in decades to centuries, but because of the great inertia of the Earth's climatic system, the effect of GHGs forcing takes decades to be fully transformed into equilibrium climate warming (Seinfeld and Pandis, 2016).

1.6.3 Black carbon: Sources, distribution and climatic impact

Black carbon (BC) is a product of incomplete combustion of carbonaceous matter (fossil fuel, biomass and biofuels) that has an impact on both air quality and climate. BC is the principal light absorbing component of the atmospheric particle that heats the atmosphere depending on the surface albedo. Locally the sign of the radiative effect may be positive or neagtive depending on the local surface albedo (Vignati et al., 2010). Globally, BC is estimated to cause a radiative forcing of of $0.20 \pm 0.15\ \mathrm{W\,m^{-2}}$ (IPCC, 2007). Globally, estimated annual emission of BC from the identified sources (fossil fuel, biomass and biofuels) is 8.0 Tg/year with an uncertainty range of 2 - 2.9 Tg/year. The contribution of fossil fuel, biofuel and open burning are setimated as 38 %, 20 %, and 42 %, respectively (Bond et al., 2004).

BC has a unique and important role in the Earth's climate system because it absorbs incoming solar radiation, influences cloud processes, and alters the melting of snow and ice covers. Concentrations of BC respond quickly to to reductions in emissions beacuse BC is rapidly removed from the atmosphere by deposition. Hence, reduction in BC emissions represent a potentially viable mitigating strategy that could reduce global climate forcing in the sghort term and slow down associted warming rate (Bond et al., 2013). GAINS estimated BC emission from gas flaring at about 4 % (320 Gg) of the anthropogenic global total with majority originating from Russia, Nigeria nd the Middle east (Bond et al., 2013). In 2010, total anthropogenic BC emission of Russia is estimated as 224 Gg (approx.). Gas flaring is estimated to contribute about 36.3 % to Russia's total anthropogenic BC emissions (Huang et al., 2015).

1.7 Objectives and structure of the thesis

The main aim of this study is to assess and establish the level of the contributions of gas flaring emissions from the oil and gas platforms in the oil-rich Niger Delta area of Nigeria to atmospheric aerosol loading on local and region scales. Hence, justify the need to explicitly include gas flaring in global models and emission inventories.

1.7.1 Objectives

The objectives of this research work are:

i. To develop a pre-module to estimate emission factors of some pollutants and combustion variables for gas flaring;

ii. To evaluate the impact of prevailing meteorological conditions, fuel composition, and flare size on the mean ground-level concentration and dispersion pattern of gas flaring emissions;

iii. To assess the contributions of gas flaring to regional aerosol loadings;

iv. To identify and study the optical and microphysical properties of gas flaring aerosols, and;

v. To estimate the direct radiative forcing of different aerosol types in the region.

1.7.2 Structure of the thesis

This thesis starts with a general introduction to gas flaring from a global perspective; spatial and temporal trend, and geographical location of gas flaring hotspots, paying close attention to the compositional variation and thermodynamic properties of natural gas. A review of recent literature on gas flaring process and resultant pollutants emission, the West African Monsoon (WAM), aerosol radiative forcing and atmospheric dispersion modeling was undertaken. Most of the materials in the literature review chapter have been published (Fawole et al., 2016b). In the next five chapters, results of estimating gas flaring emission, quantifying its contribution to atmospheric aerosol loadings and radiative transfer potential in the Earth-atmosphere system, and assessing the impact of meteorology and fuel composition on the dispersion of gas flaring emission in a case study site (Nigeria) are presented and discussed.

Each of these chapters starts with a brief abstract, introduction and methodology employed before going ahead to present and discuss the major findings. Finally, a summary of the major findings in the study and recommendations for further works is presented.

Chapter 2

Literature Review

2.1 Introduction

During the exploration and exploitation of crude oil, there is the need to separate the natural gas from crude oil at the flow stations. After separation, the natural gas is either harnessed for use, flared or vented. If vented, methane, a prominent component of natural gas, is highly harmful to the environment. Methane has a high global warming potential: It is estimated that, in terms of global warming, methane is 25 times more potent than CO_2 over a 100-year period. Gas flaring is carried out with the aim of converting its hydrocarbon content, especially methane, to products that are less hazardous to the immediate vicinity of the flare site. Flaring is a gross waste of potentially valuable natural resources.

Most of the materials in this chapter has been published in: **Olusegun G. Fawole, X,-M. Cai , A.R. MacKenzie** (2016). Gas flaring and resultant air pollution: A review focusing on black carbon. ***Environmental Pollution***, 216: 182-197 10.1016/j.envpol.2016.05.075.

2.2 Overview of gas flaring process

Gas flaring is classified as a stationary combustion source for the purpose of air pollution regulation (USEPA, 2008). The combustion process involves the rapid oxidation of the fuel gas with the release of heat, gaseous and particulate pollutants, whose nature and quantity depend on the amount and composition of gas fuel burned, the combustion characteristics as well as the flare geometry and design (Ouf et al., 2008; Torres et al., 2012a).

Gas flaring may be categorized as *emergency, process and production* flaring depending on the basis of the flaring (Johnson and Coderre, 2011). *Emergency flaring* is unplanned: it is carried out at large facilities for safety purposes for a short duration of time. During emergency flaring, a large volume of gas is disposed of quickly and, hence, the flow rate of the fuel gas is very high. *Process flaring* is an intermittent disposal of unwanted gas that may last for a few hours or a couple of days at often low flow rate. It occurs during well-testing as well as start-up and shut-down of process units. *Production flaring* may occur continuously for years as long as the oil is being explored and exploited. The flow rate can be very high at particular times especially during the initial development of a gas well (Johnson and Coderre, 2011). As a result of the length of time involved, which can be years, and the flow rate of the gas flared, production flaring is the major process of concern for regional and global pollution, including interaction with climate.

2.3 Gas flaring emissions and environmental impacts

Gas flaring is the process of disposing of gas (referred to as fuel gas below), by combustion in an open flame in the open atmosphere, using a burner tip designed specifically for that purpose, in the course of routine oil and gas production operations (McEwen and Johnson, 2012; OGP, 2000; Stone et al., 1992). Gas flaring is a source of greenhouse gases, ozone precursor gases, VOCs, polycyclic aromatic hydrocarbon (PAH) and particulate matter (PM) in the form of soot (Ana et al., 2012; Gilman et al., 2013; Johnson et al., 2013; McEwen and Johnson, 2012; USEPA, 2011, 2012). These pollutants have been identified to have serious detrimental impacts on animals, vegetation, Earth's climate and humans (Burney and Ramanathan, 2014; Dung et al., 2008; Pope III et al., 2002; USEPA, 2010). The soot emitted from the combustion of natural gas is predominantly BC (Johnson et al., 2013; Smith and Chughtai, 1995).

BC is a strong climate forcer and plays a prominent role in the nature of the Earth's climate because of its ability to absorb solar radiation, and hence, to result in a changed vertical gradient of warming by incoming solar radiation (Ramana et al., 2010; Ramanathan and Carmichael, 2008). It also affects cloud processes as well as decreasing surface albedo on ice and snow causing them to melt faster (IPCC, 2007). It can be short-lived in the atmosphere, as it is removed from the atmosphere by dry and wet deposition (although insoluble in water, it is wettable, particularly when 'aged' by atmospheric oxidation). Within current estimated uncertainties, BC is the second highest contributor to global warming just after CO_2 (IPCC, 2007), and also the main light-absorbing component of atmospheric aerosols (Bond et al., 2013; Chung and Seinfeld, 2005; Jacobson, 2002; Ramanathan and Carmichael, 2008; Seinfeld, 2008).

The radiative forcing capacity of a cloud of aerosol particles depends on the ratio of absorbing components to other components in the cloud (Ramana et al., 2010). The ubiquitous nature of BC coupled with its several effects on the Earth's climate makes the study of its sources and emission rates important. If adequate measures are put in place to reduce BC emission, short-term reduction of radiative forcing can be achieved in the Arctic and other oil-rich regions of the world (Arctic Council, 2013; Feichter and Stier, 2012; Tripathi et al., 2005).

Studies have shown that the contributions from oil and gas processing, especially gas flares, to air pollution have been severely underestimated (Edwards et al., 2013; Johansson et al., 2014; Schultz, 2014; Stohl et al., 2013). This is arguably due to the fact that emission factors (EF) often used to estimate the emissions of pollutants from the oil and gas sector, especially gas flaring, are too general and independent of site specifics such as fuel composition and combustion characteristics. There is a pressing research need for more measurements and development of EFs estimates that vary with the fuel gas composition and combustion characteristics.

At the local scale, ground-level measurements within one kilometre downwind of the flaring sites have indicated an elevated concentration of particulate and gaseous pollutants (Edwards et al., 2013; Obanijesu et al., 2009; Sonibare et al., 2010). Likewise, on a regional scale, flight campaign during ACCESS (Arctic Climate Change Economy and Society) around oil and gas installations in Heidrun, Norway reported elevated concentrations of NO, SO_2 and CO in the lower troposphere (Roiger et al., 2015).

NO_X ($NO+NO_2$), SO_2, BC, CO_2, CO and unburned hydrocarbon are the major pollutant constituents of gas flaring plumes (USEPA, 1995a). The low amount of the nitrogen and sulphur content of the fuel gas notwithstanding, the NO_X and SO_2 emission from gas flaring remain significant because the ambient background level of both pollutants are usually low. Hence, gas flaring can substantially enhance the local concentrations of these pollutants. Complete combustion is often not achieved in most flaring conditions (Leahey et al., 2001). During incomplete combustion, methane (CH_4) and other unburned components of the fuel gas are given off and some fuel components are partially oxidised to CO and soot rather than completely oxidised to CO_2 (RTI, 2011; Strosher, 2000; Villasenor et al., 2003).

Equations (2.1) and (2.2), respectively, give simplified equations for the 'ideal' complete and partial oxidation of the fuel gas. In Equation (2.2), *'rC'* denotes number of moles of soot yield, 'vO_2, excess oxygen in the case of fuel-lean combustion and 'C_aH_b' are PAH and other semi-volatile organics resulting from the pyrolysis of hydrocarbons in the fuel gas. The value of m in Equation (2.2) determines a fuel-lean (over-fired; $m > x + y/4$) or fuel-rich (under-fired; $m < x + y/4$) combustion process. The level of combustion (oxidation) of the fuel gas is dependent on a number of factors: the nature of the flame during combustion, the level of mixing of the gas and air in the reaction zone, the amount of oxidant (oxygen) available, the VHV of the fuel gas and the prevailing condition of the ambient wind (Stone et al., 1992). Flare design and geometry are also key determinants of the level of combustion of the fuel gas.

$$C_xH_y + \left(x + \frac{y}{4}\right) O_2 \rightarrow xCO_2 + \frac{y}{2}H_2O \tag{2.1}$$

$$C_xH_y + mO_2 \rightarrow pCO_2 + qCO + rC + vO_2 + fH_2O + \sum_{a,\,b} d_{a,\,b}\, C_aH_b \tag{2.2}$$

For 'ideal' complete combustion, the oxidation of the hydrocarbon yields carbon dioxide and water only (Equation 2.1), while the oxidation of the sulphur (as H_2S) and nitrogen content of the fuel gas gives SO_2 and NO_X, respectively. In gas flaring, NO_X is produced by thermal cracking of the nitrogen content of the fuel gas and entrained atmospheric nitrogen. The amount of carbon-containing emission (CO_2, CO, C_aH_b, and BC) given off depends on the molar mass of non-CO_2 carbon per mole of the fuel gas (see Table 1.2). Smoking of a gas flare does not necessarily imply that the combustion process is highly inefficient; because a small amount of soot can absorb and scatter perceptible amounts of visible light, a flare with a combustion efficiency of 99 % could still smoke visibly (Castineira and Edgar, 2006). Flares in real-world situations operate at an average efficiency of 68±7 % (Leahey et al., 2001).

Figure 2.1 shows the photograph of flares during active gas flaring activities in the Niger Delta area of Nigeria.

Figure 2.1: Photograph of typical gas flare in the Niger Delta during gas flaring

2.4 Emissions measurements around real-world gas flaring sites

Few data of pollutant measurements around gas flaring sites are publicly available. Data from the ACCESS aircraft campaign experiment in the Arctic (Norway) (Roiger et al., 2015) and a couple of ground-based in-situ measurements in Nigeria (Ana et al., 2012) and the US (Edwards et al., 2013) show significant contributions from gas flaring to ambient air concentrations of these pollutants.

In-situ ground measurements of air pollutants around typical oil and gas facilities where varying degrees of gas flaring take place have been undertaken in the US (Edwards et al., 2014, 2013; Johansson et al., 2014), Mexico (Villasenor et al., 2003), Norway (Roiger et al., 2015), and Nigeria (Ana et al., 2012; Nwaichi and Uzazobona, 2011; Obanijesu et al., 2009; Sonibare et al., 2010). Continuous noise levels higher than the WHO limit of 70 dB were also observed around some gas flaring sites in Nigeria (Abdulkareem and Odigure, 2006; Avwiri and Nte, 2003).

A 4-month sampling of three air pollutants (SO_2, CO and NO_2) around six (6) flow stations in the Niger Delta area of Nigeria was undertaken and reported by Obanijesu et al. (2009) and Sonibare et al. (2010). The measurements were made at 60, 200 and 500 m downwind of the flaring sites. Although, to a varying degree, depending on the capacity of the station, gas flaring could be a prominent daily activity within the stations. Mean pollutants measurements around the six flow stations are shown in Figures 2.2(a), (b) and (c). The variation bar on the bar-plots shows the standard deviation of the measurements over the four-month period. The nature and extent of dispersion of pollutants from a stationary source depend on the local meteorology and topography of the area. As shown in Figures 2.2(a) - (c), the trend of the measurements from the flaring sites are similar to observations from dispersion model studies where concentrations of pollutants decreases exponentially with distance from the source (Hodgson et al., 2007). Site 4 is the only place where a significant deviation from this trend, especially for CO and NO_2, was observed, suggesting the likelihood of contributions from other source(s).

A summary of the few available in-situ ground measurements downwind of gas flaring sites in other regions of the world are given in Table 2.1.

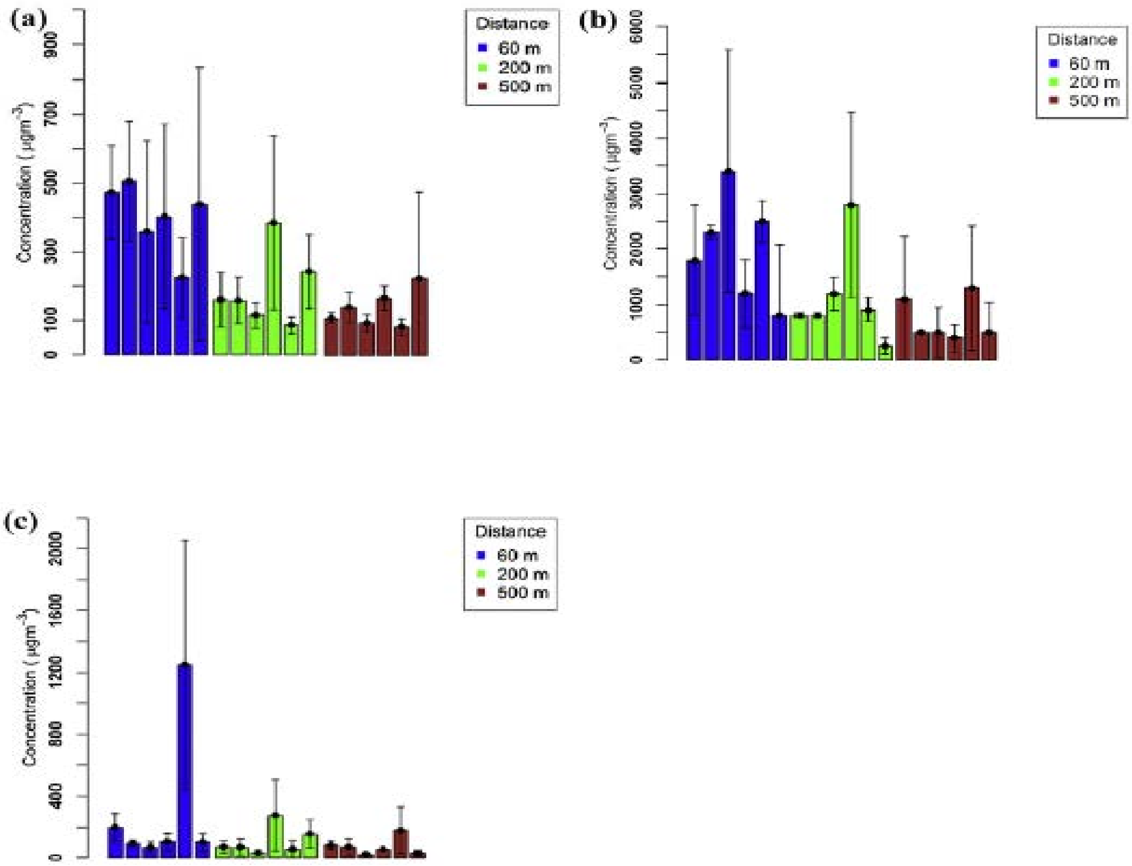

Figure 2.2: (a) Spatial variation of SO_2 concentration downwind of six gas flare sites (adapted from Obanijesu et al. (2009)); (b) Spatial variation of CO concentration downwind of six gas flare sites (adapted from Sonibare et al. (2010)); (c) Spatial variation of NO_2 concentration downwind of six gas flare sites (adapted from Sonibare et al. (2010))

Table 2.1: Pollutant measurements around several oil and gas facilities

BC ($\mathbf{ng\ kg^{-1}}$)	**O_3** **(ppbv)**	**VOC** **(ppbv)**	**PAH** ($\mathbf{ng\ m^{-3}}$)	**NO** **(ppbv)**	**NO_2** **(ppbv)**	**SO_2** **(ppbv)**	**CO** **(ppbv)**	**Ref.**
-	> 120	100 - 350	-	> 3.5	> 7.5	-	> 80	Edwards et al. (2013)
> 40	> 25	-	-	> 1.2	-	> 1.2	> 90	Roiger et al. 2015
-	-	-	0.34 - 3.3 x 10^3	-	-	-	-	Ana et al. (2012)

2.5 Types of flares

Based on the design and operating condition of the system, flares can be categorised as air-assisted, steam-assisted, non-assisted and pressure-assisted. Flares are assisted primarily to enhance the turbulence and mixing of the fuel gas and air in the combustion zone, so as to suppress smoking of the resulting flame (Castineira and Edgar, 2006; Enviroware, 2012; Torres et al., 2012a). The choice of assistance, therefore, affects flame chemistry, as discussed below. Air and pressure-assisted flares are not as efficient as steam-assisted flares in terms of the carbon conversion efficiency (CCE) (Castineira and Edgar, 2006). Complete combustion of the fuel gas requires sufficient air for combustion and adequate mixing of the air and fuel gas. The efficiency of a gas flare at a given moment in time depends on the HHV of fuel gas (see Table 1.2), design of the burner, mixing of air and fuel gas in the combustion zone, composition of the fuel gas, wind speed and direction, and ambient temperature and pressure (Kostiuk et al., 2004; Stone et al., 1992; Torres et al., 2012b).

Equivalence ratio, ϕ, is a measure of the amount of oxygen available for the combustion of the fuel gas (Flagan and Seinfeld, 2013; McAllister et al., 2011). It is defined as:

$$\phi = \frac{\left(\frac{A}{F}\right)_s}{\left(\frac{A}{F}\right)_a} \tag{2.3}$$

where $\left(\frac{A}{F}\right)_s$ is the stoichiometric air-fuel mass ratio and $\left(\frac{A}{F}\right)_a$ is the actual air-fuel mass ratio. $\phi < 1$ implies fuel-lean mixture, that is, more oxygen than is needed for the combustion of the fuel is available; $\phi = 1$, a stoichiometric mixture, where the exact amount of oxygen needed is made available, and $\phi > 1$, a fuel-rich mixture, less oxygen than is needed is available for the combustion of the fuel. Burners used in gas flaring and the entire gas flaring set-up are designed to produce a flame operating at $\phi \sim 1$, taking into account the economic aspects such as cost effectiveness of applying a process like steam assistance.

2.5.1 Steam-assisted flare

A Steam-assisted flare involves the introduction of a steam jet into the combustion zone of the flare to provide added momentum and turbulence to the fuel gas and air, enhancing mixing and as such suppressing the tendency for smoke in the flare (Castineira and Edgar, 2006; Müller-Dethlefs and Schlader, 1976; Stone et al., 1992). Steam assist is the most efficient assist given to flare to suppress smoking during combustion because the steam affects flame chemistry as well as mixing. The steam acts to break up long-chain hydrocarbons to smaller chains that burn with less smoke (Castineira and Edgar, 2006; Fortner et al., 2012; Müller-Dethlefs and Schlader, 1976; Torres et al., 2012a). Steam undergoes thermal dissociation in a flare flame to give H and OH free radicals that react with carbon to give CH_2- and –CHO radical moieties. The steam-induced free radicals enhance the formation of C=O bonds rather than C-C bonds, promoting completeness of combustion. The steam can also react with intermediate products like CO, oxidizing it further to CO_2 (see Equation 2.4) (Castineira and Edgar, 2006; Müller-Dethlefs and Schlader, 1976).

$$CO_{\ (g)} + H_2O_{\ (g)} \rightarrow CO_{2\ (g)}\ + H_{2\ (g)}\ \ (\Delta H = -41\ kJ.mol^{-1}) \tag{2.4}$$

For a steam assisted flare, combustion efficiency starts to decrease when the steam-to-fuel gas ratio goes beyond a threshold which depends on the heat content of the fuel gas and the location at which the steam is injected into the combustion zone in the flare (USEPA, 2014). In the US, a lower heating value (LHV) limit of $11.18\ \mathrm{MJ\,m^{-3}}$ is imposed on fuel gas in order to be suitable for steam-assisted flares (Castineira and Edgar, 2006). Fuel gas with high heat content promotes higher combustion efficiency in steam-assisted flares (McDaniel and Tichenor, 1983; Torres et al., 2012b). Over-steaming results when too much steam is injected into the combustion zone; over-steaming is analogous to over-aeration in air-assisted flares. Over-steaming causes a decrease in the flame temperature by serving as a heat sink. A decrease in combustion efficiency of the flare results, along with increased noise caused by cavitation created within the flame (Castineira and Edgar, 2006; Stone et al., 1992).

The formation of NO_X in steam-assisted flares is reduced, compared to non-assisted flares, and further reduced at large values of equivalence ratio (ϕ) due to a drop in the flame temperature (Miyauchi et al., 1981; Müller-Dethlefs and Schlader, 1976). Steam-assisted flares are rather expensive to maintain, especially for large gas facilities, as a large-scale steam generator is required.

2.5.2 Air-assisted flare

In air-assisted flares, forced air from a low-pressure blower is used as an additional source of momentum and turbulence to the fuel gas in the combustion zone and, hence, enhances the mixing of the fuel gas and air in the zone (Castineira and Edgar, 2006; Stone et al., 1992; Torres et al., 2012a). Air-assisted flaring involves the installation of an air blower that provides the forced air at the bottom of the stack. The major advantages of the air-assisted flare are that it is less expensive to run, extends the life-span of the flare by cooling the tip of the flare and is easier to maintain than other configurations (Castineira and Edgar, 2006). For an air-assisted flare, the combustion efficiency of the flare decreases linearly above a threshold limit of the air assist to fuel-gas ratio, but the rate of decrease is slow for a fuel gas with a higher VHV (Torres et al., 2012b). Incomplete combustion can occur when air-fuel gas ratios go beyond the optimum value, to the extent that the flame may be put out as a result of over-aeration (Castineira and Edgar, 2006).

2.5.3 Pressure-assisted flare

In pressure assisted flares, the fuel gas stream pressure is controlled by varying the volume flow of the fuel gas, and used to enhance the mixing of the fuel gas and air in the combustion zone. A high-pressure burner is used to promote atomization of any liquid hydrocarbon and enhance the mixing of the fuel gas with air to bring about a complete or near-complete combustion. Pressure assistance often requires significant amount of space in a remote area because of the burner arrangement at ground level. Fuel gas exit velocity increases with pressure at the burner. Pressure-assisted flares usually have burners arranged on the ground and as such must be located carefully within the oil and gas production plant (Enviroware, 2012; Stone et al., 1992).

2.5.4 Non-assisted flare

For non-assisted flares, no provision is given to provide momentum and enhanced mixing for the fuel gas and air. The method is often used for gases with low VHV, that is, fuel gas having low C-to-H ratio (in alkanes, C-to-H ratio increases from a minimum value of 0.25 for methane; see Table 1.2). The C-to-H ratio determines the smoking tendency of hydrocarbons, with smokiness increasing with C-to-H (USEPA, 1995a). Note that the experimental fuel gas compositions listed in Table 1.2 are at or below the lowest C-to-H ratio of the flow station gas compositions listed. Non-assisted flaring is used for gases that require smaller amounts of air to undergo complete combustion (Enviroware, 2012; Stone et al., 1992).

2.6 Estimating emissions from gas flaring

Emissions from a typical gas flare can be solids, liquids or gases. As a result of the inaccessible nature of full-scale real-world gas flares, several techniques have been used to quantify the amount of emissions from such flares. Such methods include measurement or source monitoring often by lab-based, pilot-based study or field-based study (Johnson and Coderre, 2011; McEwen and Johnson, 2012), application of emission factors obtained from measurements and scaling calculations (Giwa et al., 2014; Huang et al., 2015; Sonibare and Akeredolu, 2004; Talebi et al., 2014; USEPA, 1995a), and simulations, often by computa-

Table 2.2: Summary of the features of the different types of flares discussed in Section 2.5

	Steam-assisted	**Air-assisted**	**Pressure-assisted**	**Non-assisted**
Method	Steam is introduced into the combustion zone to enhance mixing.	Air is introduced from a blower to enhance the mixing and turbulence of the fuel gas in the combustion zone	The vent pressure of the gas flow is used to enhance mixing at the tip of the flare burner	No assistance is given to the combustion process
Efficiency	Most efficient in terms of suppressing soot formation. Some of the CO formed can be oxidized to CO_2	Less efficient than the steam assisted flare but relatively efficient than the other two types	Not as efficient as steam and air-assisted but can equally suppress sooting.	Only efficient for non-sooting combustion especially in light hydrocarbons
Benefits	Fuel with high heat value, and hence, high sooting propensity can be disposed of with relatively less soot	Prolongs the life span of the flare tip. Less expensive than steam-assisted and easy to maintain, hence, it is the most commonly used.	Enhance combustion efficiency when the gas flux pressure is sufficiently high enough without the additional cost of steam and air generation	Can be used for occasional emergency flaring of near smokeless gas.
Relative size	They are often large flares as they include the steam generator and are usually employed in large gas facilities.	Not as large as the steam assisted.	May be of same size as air-assisted flare depending on the flow capacity of the facility.	Often smaller in size compared to the other types
Shortcoming	Over-steaming can result in reduced efficiency of flare. It is also expensive to maintain on a large-scale.	Over- aeration can also result in less efficiency. A limit of air assist to gas ratio must be maintained for effectiveness of the flare.	The fluctuation of gas flow pressure has a bearing consequence on the efficiency of the combustion. Requires large space in a remote area.	Cannot be used for dense fuels with high sooting propensity which are typical gas in oil and gas processing facilities.

tional fluid dynamics (CFD) (Almanza et al., 2012).

In real-world flares, complete combustion cannot be achieved always and everywhere. Incomplete combustion of the fuel gas can be due to poor efficiency of the flare system, flame temperature (flame dynamical characteristics), insufficient oxygen resulting in poor stoichiometric air/fuel gas mixing ratio, the condition of the fuel gas in the combustion zone and prevailing ambient meteorological condition (Stone et al., 1992). Carbon monoxide (CO) can represent 24 – 80 % (of carbon on molar basis) of emissions for an incomplete combustion process (Torres et al., 2012b).

2.6.1 Determining flame regime

It is important to define clearly the configuration of the fire (flare) as this is essential for an adequate estimation of the yield and transport of pollutant species from the combustion process. Flames can be classified along a spectrum ranging from turbulent diffusion flames (of the kinds discussed above) to pool fires (e.g. tar-pool fire) based on the nature and dynamics of the fuel in the flame as well as the design of the burning process (Delichatsios, 1993a, 1987). The focus of this thesis is gas flares, which are classified as turbulent jet-diffusion flames. They are so classified because of the high pressure associated with the release of the fuel gas into the flame.

Jet-diffusion flames in the environment can be categorized based on the momentum flux ratio, R, of the jet plume versus the horizontal momentum flux of the ambient wind (Huang and Wang, 1999). Flares with high R ($R > 10$) may be further categorized depending on whether the flame characteristics are driven by the buoyancy of the hot plume or momentum of the fuel gas (McEwen and Johnson, 2012). Both buoyancy and momentum are important in determining the character of flares. A combination of several dimensionless parameters – Richardson number, Richardson ratio, fire Froude number, gas Froude number, and Reynolds number - have been used in studies to characterise the regime of the flame in a jet-diffusion flame. The Froude numbers measure the ratio of the inertia force on an element of the fluid (in this case, gas or fire) to the weight of (i.e. gravitational force acting on) the fluid element. The fire Froude number, Fr_f, gas Froude number, Fr_g and Reynolds number, R_e, have proved to be useful dimensionless parameters to define the flame regime (Becker and Liang, 1982; Delichatsios, 1993a,b, 1987; Sivathanu and Faeth, 1990).

$$Fr_g = \frac{u_e f_s^{\frac{2}{3}}}{(gd_e)^{\frac{1}{2}} \left(\frac{\rho_e}{\rho_\infty}\right)^{\frac{1}{4}}} \tag{2.5}$$

$$Fr_f = \frac{u_e f_s^{\frac{2}{3}}}{\left(\frac{\Delta T_f}{T_\infty} gd_e\right)^{\frac{1}{2}} \left(\frac{\rho_e}{\rho_\infty}\right)^{\frac{1}{4}}} \tag{2.6}$$

$$Re_s = \frac{u_e d_e}{\nu_o} \tag{2.7}$$

$$f_s = \frac{1}{s+1} \tag{2.8}$$

In the definition of Fr_f in Equation (2.6), $\left(\frac{\Delta T_f}{T_\infty}\right)$.g is the effective acceleration generated by individual hot eddies burning at the flame temperature (Delichatsios, 1987). Among the three dimensionless numbers defined by Equations (2.5) - (2.7), the Reynolds number is used to determine the status of flow, either turbulent or laminar. The fire Froude number, Fr_f, is used to identify the dominant mechanism between buoyant-generated turbulence and momentum-generated turbulence. In practice, Fr_f can be used to parameterise soot yield from turbulent diffusion flames (Delichatsios, 1993b; McEwen and Johnson, 2012).

2.6.2 Emission factors (EF) for gas flaring emissions

The emission factor (EF) of a pollutant is the amount of the pollutant released into the atmosphere per unit activity or per unit raw material consumed. It can be obtained from experimental measurements carried out on several sources which represent a particular emission source type. For example, road transport emission factor can be compiled by measuring the amount of each pollutant (CO_2, CO, PM, NO_X) given off by cars (petrol and diesel), heavy duty vehicles and motorcycles from fuel burned for every km travelled (Gertler et al., 1998; USEPA, 1995a; Zhang and Morawska, 2002) under given driving conditions. It is often expressed in $\mathrm{g\,m^{-3}}$ (pollutant produced per unit volume of raw material consumed), $\mathrm{g\,kg^{-1}}$ (pollutant produced per unit mass of raw material consumed), $\mathrm{g\,km^{-1}}$ (pollutant produced per unit distance travelled). Emission factors have been compiled by several agencies, which include the US Environmental Protection Agency (USEPA), the European Environmental Agency (EEA), the UK's Department for Environment, Food and Rural Affairs (Defra), and GAINS (Greenhouse gas Air Pollution Interactions and Synergies), for several source categories based on technical sessions of lab-based studies, pilot studies or actual field measurements. Of these agencies, ECLIPSE and USEPA have EFs specifically for emissions from gas flares: the GAINS emission factor for BC from gas flaring is 1.6 $\mathrm{g\,m^{-3}}$: the equivalent USEPA value has four discrete values between 0 and 6.4 $\mathrm{g\,m^{-3}}$ depending on the smokiness of the flame (see Table 2.3). Stohl et al. (2013) in their study used emission factor of 1.6 $\mathrm{g\,m^{-3}}$ obtained from ECLIPSE (Evaluating the Climate and Air Quality Impacts of Short-lived Pollutants) emissions data set to simulation BC emissions in the Arctic.

It is difficult to carry out an accurate estimate of emission from gas flares directly from field measurements. Conventional experimental techniques are not suited due to the severe operating conditions that occur in the flaring process and the almost uninhabitable nature of the gas flaring area to both human and the field equipment during the process of gas flaring (Ismail and Umukoro, 2014; McDaniel and Tichenor, 1983; McEwen and Johnson, 2012; RTI, 2011; Talebi et al., 2014).

In Chapter 13 of USEPA's 5th edition of the compilation of air pollutant emission factors known as "AP-42", published in January 1995, emission factors (EF) for pollutant emitted from industrial flaring of waste gas were given; these were recently updated in 2014 (though still in the draft stage) except those for soot. The EFs published in 1995 were based on a study conducted by McDaniel and Tichenor (1983) aimed at determining combustion efficiency and hydrocarbon destruction efficiency for flares operated under different condition. The recent updates of EFs in AP-42 give emission factors of CO, NO_X, and soot as 0.17 $kg\,GJ^{-1}$, 1.43 $kg\,GJ^{-1}$ and 0 - 6.4 $g\,m^{-3}$, respectively.

The fuel used in the pilot study to estimate EFs for industrial flare pollutants in the AP-42 compilation was predominantly propylene and inert diluents. As such, the EFs, especially for soot, might not be an adequate representation of a typical flare in the oil and gas industry with varying fuel gas composition (Table 1.2). For AP-42, the collection of soot at the experimental stage was not done by a conventionally accurate method. For instance, the particulate matter (soot) given off was not collected isokinetically in accordance with USEPA's method 5 for sampling particulate matter from stationary source (USEPA, 2000). An emission factor of 0.0 $\mu g\,l^{-1}$ (microgram per litre of fuel gas at standard temperature and pressure) given for soot in non-smoking flares of industrial flares in AP-42 is of limited utility and presumably denotes a upper limit of 0.05 $\mu g\,l^{-1}$, because the soot yield from flares is never likely to be precisely zero. Even seemingly modest emission of soot (BC) can be significant, given what is now known of the effects of BC on climate, weather and human health (Bond et al., 2013; IPCC, 2013; Ramanathan and Carmichael, 2008; Tripathi et al., 2005; Wang et al., 2014).

The mass/mole balancing technique for estimating the yield of pollutants from the combustion of hydrocarbon is a widely used technique. Using this technique, Ismail and Umukoro (2014) and Sonibare and Akeredolu (2004) estimated the yield for SO_2, NO_X, CO_2 and CO from the combustion of fuel gas (hydrocarbon with inert diluents) at various levels of combustion. Both studies did not account for unburned carbon (soot) even for their 'severely' incomplete combustion process reactions. Ismail and Umukoro (2014) varied combustion efficiency (CE) and air available for combustion, and with CE as low as 0.5 (50 %) still did not account for unburned carbon.

2.6.3 Soot emission from gas flaring

Soot, which is predominantly BC, is a product of the incomplete combustion of biomass, solid fuel and fossil fuel (Golber, 1985; Koch et al., 2009) . Globally, fossil fuel combustion is estimated to contribute 3 Mt of BC to the atmosphere annually (Bond et al., 2004). Annually, the contribution of gas flaring to global BC concentration is estimated to be 260 Gg (Bond et al., 2013), that is approximately 0.1 % of the total contribution from fossil-fuel use, of which Russia is estimated to contribute 81.0 Gg (Huang et al., 2015).

The formation and quantification of soot from the combustion of hydrocarbon is a rather complex thermo-chemical process that is not well understood, despite decades of research (Castineira and Edgar, 2006; Haynes and Wagner, 1981; Johnson and Coderre, 2011; Maricq, 2009). Soot given off from the combustion of hydrocarbon is predominantly elemental carbon and the amount given off depends on a number of factors, including the efficiency of the combustion process and the fire dynamical characteristics.

The diameter of soot particles emitted ranges between 10 – 200 nm and most commonly lies between 10 and 50 nm. Figure 2.3 shows a TEM micrograph of soot particle and agglomerates from acetylene flames. The very fine particles of soot are from seemingly ’non-sooting’ flames while at the other extreme are those from heavily sooting flames (Flagan and Seinfeld, 2013; Glassman, 1996; Haynes and Wagner, 1981). Combustion of hydrocarbon components of the fuel gas has PAH and BC signatures which can be used as tracers for emissions from the flaring of fuel gas (Fortner et al., 2012; Maricq, 2009).

Soot is formed when the carbon particles are cooled below their ignition temperature and there is a deficiency of oxygen (Stone et al., 1992). Considering the variation of the composition of gas flared from one station to the other, EFs available for estimating emissions from gas flares are overly generalised. The fuel gas used in most of the studies to estimate the EFs is either propylene or propane or a mixture of both with nitrogen added to alter the heat content as well as the use of predominantly methane-based fuels which are known to be

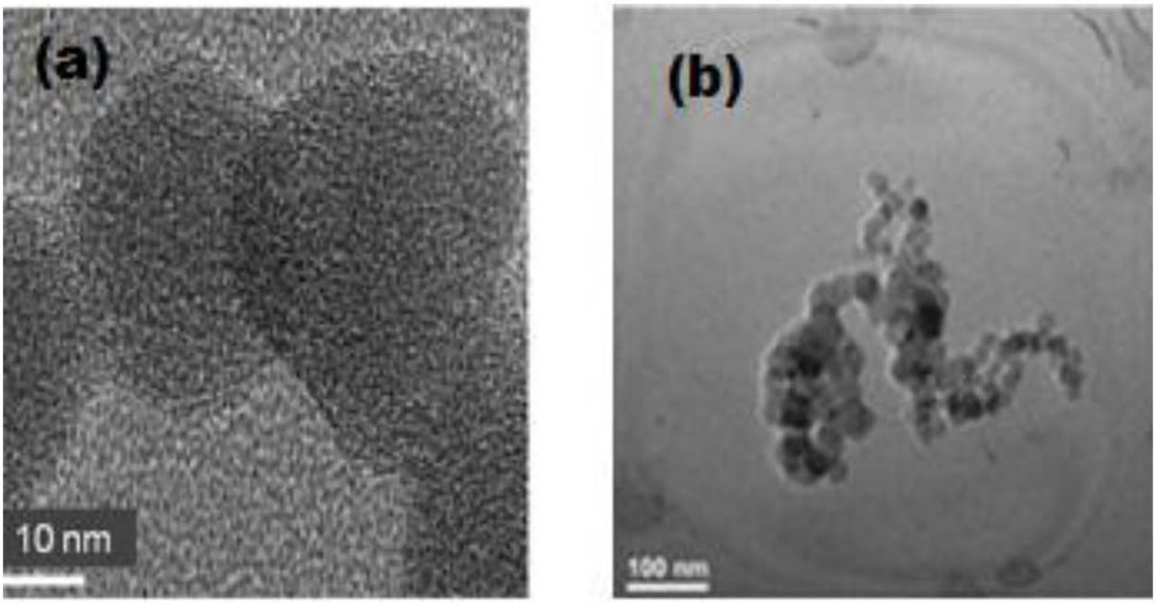

Figure 2.3: TEM micrograph of soot (a) microstructure (b) agglomerates (Tumolva et al., 2010).

low-sooting.

Several attempts have been made to quantify and study the characteristics of soot yield from gas flares using various approaches in lab-based, pilot-based and field-based studies as well as simulation techniques. Emission factors from some of these studies are given in Table 2.3. The disparity in emission factors and emission rates obtained from different studies as highlighted in Table 2.3 could be attributed to the compositions of the various fuel and flaring conditions adopted in the various studies. Other emission factors not highlighted Table 2.3 are based on USEPA AP-42 emission factors.

The studies by Johnson and Coderre (2011) and Johnson et al. (2013) gave emission rates ($\mathrm{g\,s^{-1}}$) and not emission factors ($\mathrm{g\,m^{-3}}$) because both were actually field studies that quantified the soot given off per unit time by estimating the travel speed of the soot in space using a charge couple device (CCD) camera viewing a real field flare.

Table 2.3: Summary of emission factors and emission rate for soot from industrial flares

Study (Year)	**Emission factor ($\mathbf{g\ m^{-3}}$ of fuel burned)**	**Emission rate ($\mathbf{g\ s^{-1}}$)**	**Type of study**	**Fuel**
USEPA (1995)	0.0, 0.9, 4.2 6.4 [a]	-	pilot study	80 % propylene 20 % propane
Johnson et al. (2011)	-	2.0 (± 0.66)	field study	associate natural gas
Almanza et al. (2012)	-	0.025 – 0.22	CFD simulation	associated natural gas
McEwen and Johnson (2012)	0.51	-	lab-scale flare	hydrocarbon (alkanes)
Johnson et al. (2013)	-	0.067	field study	-
GAINS (2011)	1.6	-	modelling	-
IMP (2006) [b]	-	3.37	simulation	associated natural gas
CAPP (2007)	2.563	-	-	associated natural gas

[a] 0.0 is for non-smoking flame, 0.9 for light smoking flares, 4.2 for averagely smoking flare and 6.4 for heavily smoking flares. [b] cited in (Almanza et al., 2012).

Emission of soot from the combustion of hydrocarbon varies with the VHV of the gas and, as such, the emission factor for soot can be estimated from its VHV (McDaniel and Tichenor, 1983; RTI, 2011; Torres et al., 2012b). McEwen and Johnson (2012), using a lab-based experiment, studied the BC emission from the combustion of hydrocarbon. The study varied the VHV of the fuel gas and measured the soot yield for each combustion process. The VHV used here is the higher heating value (HHV), or gross heating value. The relationship between the two variables (soot yield and HHV) obtained from the study by McEwen and Johnson (2012) is given in Equation (2.9):

$$EF_{soot} = 0.0578(VHV) - 2.09 \tag{2.9}$$

When the composition of the fuel gas is known, its VHV can be calculated from standard thermochemical tables (cf. Table 1.2). It should, however, be noted that because the VHV contains no information on flame dynamics, this relationship is only appropriate for the flame dynamics conditions of the experiment. Although, Equation (2.9) is a readily available relationship to estimate soot emission from hydrocarbon combustion, its application is restricted to a complete or near-complete combustion process. Inserting the estimated VHV into the relation developed by McEwen and Johnson (2012) gives an estimate of the soot yield in $\mathrm{g\,m^{-3}}$.

2.6.4 Scaling soot emissions from lab-based studies

Lab-based studies of emissions from flares are the most common and readily available method to estimate emissions from full-scale flares. However, considering the size (diameter) of the flare stack, flow rate of fuel gas, exit velocity, and the resultant buoyancy of full-scale flare, there is a need to scale up the emissions yield from lab-based studies to be representative of a full scale flare. In earlier studies, several dimensionless parameters have been considered for such scaling purpose; these include Richardson ratio, Ri_L (Becker and Liang, 1982), fire Froude number, Fr_f (McEwen and Johnson, 2012), and the first Damköhler ratio, Da_1 (Becker and Liang, 1982). The Richardson ratio, Ri_L , is defined as the ratio of the buoyancy-generated turbulent kinetic energy (TKE) of the flame to the TKE of emitted gas jet at the exit:

$$Ri_L = \frac{gL^3}{(U_e d_e)^2}\left(\frac{\rho_\infty}{\rho_e}\right) \tag{2.10}$$

Richardson ratio is the basis to assess the turbulent regime of the flame: when $Ri_L \ll 1$, buoyancy-induced mixing between emitted gas jet and background air is much weaker than jet-induced mixing, and consequently the flame is dominated by forced convection; when $Ri_L \gg 1$, jet-induced mixing is much weaker than buoyancy-induced mixing and the flame is dominated by natural convection. Fire Froude number, Fr_f, is defined in Equation (2.6) and can be interpreted as the ratio of the jet's inertia to the buoyancy force acting on it. Fire Froude number can be used to assess the dominating force to “stretch” the flame: when $Fr_f \gg 1$, the jet's momentum is the dominating factor and when $Fr_f \ll 1$, the flame's buoyancy force is the dominating factor. Comparing Fr_f against Ri_L, we understand that both are used to assess the dominating factor between jet-related quantity and buoyancy-related quantity, but there are two differences: (1) the quantity is momentum ($\propto$ velocity) for Fr_f, but TKE ($\propto$ velocity x velocity) for Ri_L ; (2) the ratios between jet-related quantity and buoyancy-related quantity are reciprocal: $Ri_L \propto$ (buoyancy-related quantity)/(jet-related quantity) whereas $Fr_f \propto$ (jet-related quantity)/(buoyancy-related quantity). Therefore, these two parameters are closely related and mathematically their relationship should be $Ri_L \propto Fr_f^{-2}$. A precise relationship between them can be derived from Equations (2.6) and (2.10):

$$Ri_L = \left(\frac{\rho_\infty}{\rho_e}\right)^{\frac{3}{2}} \left(\frac{L}{d_e}\right)^3 \left(\frac{T_\infty}{\Delta T_f}\right) f_s{}^3 . Fr_f^{-2} \tag{2.11}$$

It is noted that $\left(\frac{L}{d_e}\right)^3$ can be interpreted as the volume expansion ratio of the flaring gas due to burning and $\left(\frac{T_\infty}{\Delta T_f}\right)^{-1}$ can be approximated as the inverse of the relative temperature increase of the flaring gas due to burning. Based on the gas law, these two are proportional to each other for an isobaric process (from the exit to the flame tip) which is a good assumption for gas flaring, i.e. $\left(\frac{L}{d_e}\right)^3 \propto \left(\frac{T_\infty}{\Delta T_f}\right)^{-1}$, or equivalently, $\left(\frac{L}{d_e}\right)^3 \left(\frac{T_\infty}{\Delta T_f}\right) \approx$ const. Therefore, Equation (2.11) confirms the relationship of $Ri_L \propto Fr_f^{-2}$. This suggests a strong dependence between adopting Ri_L and adopting Fr_f as the scaling parameter.

The first Damköhler ratio, Da_1, however, is defined as the ratio of residence time of fuel in flame (τ_{res}) to the chemical time of the burning process (τ_{chem}):

$$Da_1 = \frac{residence\ time\ in\ flame,\ \tau_{res}}{chemical\ time,\ \tau_{chem}} = \left(\frac{L}{U_e}\right) / \tau chem \tag{2.12}$$

It describes the extent of the oxidation process within the flame in relation to the oxidant's feed rate. For a large Da_1 (i.e. $\tau_{res} \gg \tau_{chem}$), the velocity fluctuating component does not have much influence on the chemistry of the flame. The chemical reaction is able to proceed to completion within the residence time in the combustion zone, resulting in intensive chemical reaction and hot diffusion flame. For a small Da_1 (i.e. $\tau_{chem} \gg \tau_{res}$), turbulence can significantly affect the chemistry and structure of the flame. The rate of chemical reaction and hence, heat release may be affected, causing combustion product to be mixed with reactants within a time interval shorter than the chemical reaction time (Liberman, 2010; Williams, 1964). From the perspective of processes, Da_1 involves an extra dimension (i.e. chemical processes) which is not reflected by either Ri_L or Fr_f. In principle, we should consider Da_1 as one more scaling parameter.

2.6.5 Soot modelling

Mathematical modelling is a technique that has been used by scientists and engineers over the years to understand the relationship between sets of input and output parameters in a process, especially where the 'real world' process is often remote or grossly complicated to assess. The region of validity of such model outputs is often limited as several assumptions and constants are applied in the modelling to further simplify the process being studied.

Soot formation and oxidation in pre-mixed and non-premixed (diffusion) hydrocarbon flames have been studied using several modelling techniques including computational fluid dynamics (CFD). The main problem with mathematical modelling of turbulent combustion of hydrocarbons is the problem of modelling turbulent flow and chemical kinetics and the interaction between flow and chemical reaction (Magnussen and Hjertager, 1977). Kennedy (1997) classified models used for studying soot formation as empirical correlations, semi-empirical correlation models and models with detailed chemistry and physics of soot formation. The flame temperature, C:H ratio and number of carbon atoms in the fuel (hydrocarbon) are important parameters considered to have strong influence on the sooting propensity of the hydrocarbon (Harris et al., 1986). These parameters have been the basis of measurements used in most empirical correlation models.

In the study modelling soot formation and combustion, Magnussen and Hjertager (1977) assumed that soot is formed from gaseous hydrocarbons in two stages; (a) formation of radical nuclei, and (b) soot particle formation from these nuclei. Applying expressions for the rate of formation of radical nuclei and rate of soot particle formation expressions developed by Tesner et al. (1971a), Tesner et al. (1971b) in their model, tested on both pre-mixed and diffusion flame, predicted that soot concentrations are in close agreement with experimental data. They concluded that soot formed are contained in eddies and burned away during turbulence dissipation.

Moss et al. (1989), using a two-equation model for the evolution of soot volume fraction and number density, simulated the formation of soot. They included the influences of nucleation, surface growth and coagulation on the rate of soot formation. As given in Equations (2.13) and (2.14), their model contains simplified expressions to quantify particle nucleation, growth and coagulation; using three empirical constants that are dependent on the fuel to control the rate of these processes. A major finding from their study is that soot volume fraction is proportional to the square of pressure.

$$\left\{ \frac{d\left(\frac{n}{N_O}\right)}{dt} \right\} = \alpha(\zeta) - \beta(\zeta)\left(\frac{n}{N_O}\right)^2 \tag{2.13}$$

$$\rho_s \left\{ \frac{df_v}{dt} \right\} = \gamma(\zeta)n + \delta(\zeta) \tag{2.14}$$

where ρ_s is the assumed density for solid carbon (1.8 x 10^3 $\mathrm{kg\,m^{-3}}$), N_o is Avogadro's number, n is number density, t is time, f_v is volume fraction, and ζ is the mixture fraction.

Rates of the processes are expected to be a function of the mixture fraction. The rates of the processes are defined explicitly in terms of the fuel density, ρ, temperature. T, and fuel mole fraction, X_C as described in Equation 2.15:

$$\left. \begin{array}{r} \alpha \equiv C_\alpha\, \rho^2\, T^{\frac{1}{2}}\, X_C\, exp\left(\frac{-T_\alpha}{T}\right);\ \beta \equiv C_\beta\, T^{\frac{1}{2}} \\ \gamma \equiv C_\gamma\, \rho\, T^{\frac{1}{2}}\, X_C\, exp\left(\frac{-T_\gamma}{T}\right);\ \delta \equiv C_\delta\, \alpha \end{array} \right\} \tag{2.15}$$

coefficients $C_{\alpha,\beta,\gamma,\delta}$ and activation temperatures, T_α and T_γ are obtained from experimental data. In Equations 2.13, the first and second term on the right are nucleation and coagulation processes, respectively. And, in Equation 2.14, the first and second term on the right represent the growth and nucleation, respectively.

Lautenberger et al. (2005) developed a CFD (Computer Fluid Dynamics) model to study the formation and oxidation of soot. Since their aim was to generate sufficiently accurate predictions of soot emission concentrations in order to estimate CFD simulations of fire radiation from turbulent flames, considerations were given only to phenomena which were essential. Soot estimation in their model was based on a further simplified form of the two-equation model of Moss et al. (1989). There are no fuel-specific constants in their estimations, but rather, they used the laminar smoke point height to account for the sooting propensity of different fuels. The smoke point of a flame is its length just before the onset of the release of visible smoke. Length of a flame is dependent on the extent of completeness of the combustion and heat content of the fuel gas (Beychok, 2005).

The use of CFD simulation has made it possible to make predictions about the relationships between the various processes involved in soot formation and oxidation in both pre-mixed and diffusion hydrocarbon flames as well as the sensitivity of the soot formation to some of the complex phenomena. However, the veracity of CFD simulation results in limited by the availability of field measurements for model evaluation.

2.6.6 Gas flaring in global models and inventories

To the best of our knowledge, the only two emission datasets that explicitly includes gas flaring emissions are EDGAR (Emissions Database for Global Atmospheric Research) and ECLIPSE (Evaluating the Climate and Air Quality ImPacts of Short-livEd Pollutants) gridded emissions datasets.

In EDGAR v4.2, emissions for gas venting and flaring were calculated for 1994 onwards using the amount of gas flared estimated from satellite observations of intensities of light from various gas flares. The estimated quantities of gas flared and emission factors obtained from either inventory guidance documents or confidential information were used to generate gridded annual emission datasets for different countries on a resolution of 0.1^o x 0.1^o. In 2005, the inclusion of new primary data sources for gas flaring in EDGAR v4.2 gives rise to a change of +75 % of EDGAR 4.1 value (130 Tg) in global CO_2 emission (European Commission, 2009).

ECLIPSE is provided by the IIASA (International Institute for Applied Systems Analysis). Emission calculations for the historical years (2005 – 2010) were developed in a series of regional and global projects. For gas flaring, emissions were calculated using data available from NOAA, NASA and the World Bank collaborative work to estimate the volume of gas flared globally. The volume of gas flared was estimated using NASA MODIS active fire detection products (Elvidge et al., 2007, 2011). Emission factors and other parameterizations were obtained from peer-reviewed data on emission performance of various technologies. The calculation was performed with the IIASA GAINS model (Klimont et al., 2013). The ECLIPSE v4 global emission dataset is available on a 0.5^o x 0.5^o lon-lat resolution.

Stohl et al. (2013), performing a 3-year BC simulation in the Arctic, using a Lagrangian particle dispersion model FLEXPART driven by the ECLIPSE dataset, estimated that more than 40 % of mean surface BC surface concentration in the Arctic is attributable to gas flaring. Although, more studies on the sensitivity of global models to gas flaring emissions are needed to give a clear and precise quantification of the contribution of gas flaring emission to global aerosol loadings, the change in global $\mathrm{CO_2}$ level in EDGAR4.2 underscores the importance of an explicit inclusion of gas flaring emissions in global models.

2.7 West African monsoon

The West African Monsoon (WAM) is a coupled atmosphere-ocean-land system characterized by winter dry and summer rainfall seasons. The dry and rainfall seasons run typically from November through March, and April through October, respectively. A slight break in rainfall, locally referred to as August break, is often experienced in August. Monsoon circulations are characterized by large-scale seasonal reversals of wind regimes. Regions often referred to as 'monsoonal' include tropical and near-tropical regions which experiences a summer rainfall peak and most of these regions have a double rainfall maximum (Barry and Chorley, 2009). The climatic regime over West Africa has many similarities to that of South Asia. Both are characterized by surface air-flow which is determined by the leading edge of the monsoon trough. Winds are south-westerly to the south of the trough and north-easterly to the North. The lack of a large mountain range in the north of West Africa strongly enhances the northward advance of the WAM compared to its South Asian counterpart. The position of the leading edge of the WAM trough may oscillate greatly from day-to-day through several degrees of latitude (Barry and Chorley, 2009).

The predominant seasonality of the WAM is governed by the movement of the Intertropical Convergence Zone (ITCZ) and Intertropical front (ITF). The ITF is the northern limit of the southwesterly winds of the monsoon. The pre-onset stage of the West African Monsoon (WAM), usually in May-June, is characterized by the movement of the Intertropical Front (ITF) further north to $15^o\ N$ which brings in the first period of rain. A further shift of the ITF to its northernmost position around $20^o\ N$ takes place in July-August, a period which signifies the full development of the WAM (Sultan and Janicot, 2000, 2003). At the onset of the WAM, there is an abrupt shift in the latitudinal position of the ITCZ from a location of $5^o\ N$ in May-June to a location at $10^o\ N$ in July-August.

In the WAM, deep convection occurs in organized systems known as Mesoscale Convective Systems (MCS) (Mari et al., 2011; Mathon and Laurent, 2001). Deep convection in the tropics associated with the ITCZ is responsible for intense mixing, venting of the atmospheric boundary layer, and large-range transport of aerosol (Law et al., 2010; Reeves et al., 2010; Sultan and Janicot, 2003).

2.8 AERONET Dataset

The Aerosol Robotic Network (AERONET) provides globally distributed measurements of aerosol spectral optical depth (AOD) and sun radiance. The AERONET program is a federation of ground-based remote sensing aerosol networks with more than 400 stations globally (http://aeronet.gsfc.nasa.gov/) (Chubarova et al., 2016). The stations are equipped with identical automated sun- and sky-scanning spectral radiometers. Solar-powered CIMEL Electronique 318A spectral radiometers are installed in these stations (Holben et al., 1998). Direct sun measurements (AOD and sun radiance) are made at seven wavelengths (λ = 340, 380, 440, 500, 670, 870 and 1020 nm) while an inversion algorithm is used to obtain aerosol retrieval at four wavelengths (λ = 440, 670, 870 and 1020 nm) (Dubovik and King, 2000). Aerosol retrieval obtained are aerosol size distribution, refractive index (real (n) and imaginary (k) part), single scattering albedo (SSA) and phase function, p(θ).

The radiative energy of incoming solar radiation is characterized by its radiant flux density which for simplicity is termed *intensity, I* (Lenoble et al., 2013). For a light of intensity, I, incident perpendicularly on an aerosol column of infinitesimal thickness dx, the loss of light intensity due to scattering and absorption per unit path length, dx, is given as:

$$dI = -\beta_e I dx \tag{2.16}$$

where β_e is the extinction coefficient expressed in m^{-1}. The overall extinction is due to absorption (radiative energy is transformed into another form of energy), and scattering (a fraction of the incident light changes direction and hence is lost to the incident intensity). The extinction coefficient is the sum of the absorption coefficient, β_a, and scattering coefficient, β_s.

$$\beta_e = \beta_a + \beta_s \tag{2.17}$$

For an ensemble of particles, the extinction, absorption and scattering coefficients in Equation (2.17) are obtained by multiplying the extinction (C_e), absorption (C_a) and scattering cross-sections (C_s), expressed in m^2, by the number of molecules or particles per unit volume of the aerosol column.

For a finitely thick layer, say a column, of aerosol, the integration of Equation (2.16) gives the Bouguer-Beer's exponential extinction law:

$$I_T = I_o \; exp \; (-\tau_e) \tag{2.18}$$

where I_T is the transmitted light intensity, I_o the incident light intensity and τ_e is the optical thickness of the aerosol layer.

Aerosol optical thickness (AOD), τ_e, is a measure of the extinction of incoming solar radiation by atmospheric aerosol. It quantifies the fraction of light prevented from reaching the Earth's surface by atmospheric aerosols. While an AOD value of 0.1 indicates a clean atmospheric, a value > 0.5 indicates a hazy and aerosol laden atmosphere.

The wavelength dependence of scattering is quantified by Angstrom Exponent, AE, (α) as given in Equation (2.19).

$$\alpha = -\frac{ln\left(\frac{\tau_1}{\tau_2}\right)}{ln\left(\frac{\lambda_1}{\lambda_2}\right)} \tag{2.19}$$

where τ_1 and τ_2 are the AOD at wavelengths λ_1 and λ_2, respectively. Fine aerosols such as aerosol from fossil fuel combustion interact more strongly with the shorter wavelength band of incoming solar radiation whereas coarse aerosol such as mineral dust interact almost evenly with all wavelengths of incoming solar radiation (Haywood et al., 2008). Values of

AE for urban-industrial and dust aerosols is in the range 1.2 – 2.5 and - 0.1 - 0.7, respectively (Dubovik et al., 2002).

Single scattering albedo (SSA) is the ratio of the scattering coefficient to the extinction coefficient (Yu et al., 2006). It is the probability that radiation incident on an aerosol column will be scattered in lieu of absorption. SSA, ω, plays a significant role in determining the sign (+/-) of the direct radiative forcing of aerosol loadings. The relationship for SSA is given in Equation (2.20).

$$\omega = \frac{\beta_s}{\beta_s + \beta_a} \tag{2.20}$$

2.9 Aerosol radiative forcing

The Earth's atmosphere absorbs, scatters, and emits electromagnetic radiation. If the Earth's climate system is in equilibrium, then absorbed incoming solar radiation is balanced by the radiation emitted by the earth and atmosphere. The perturbation of this equilibrium by a forcing agent (e.g. aerosol) is termed radiative forcing (RF). RF can be positive (warming) or negative (cooling) depending on the absorbing ability of the aerosol. According to Myhre et al. (2013), RF is defined as the change in net downward radiative flux at the tropopause after allowing for stratospheric temperatures to readjust to radiative equilibrium, while holding surface and tropospheric temperatures and state variables such as water vapour and cloud cover fixed at the unperturbed values. RF is expressed in Watts per square meter ($\mathrm{W\,m^{-2}}$).

Atmospheric aerosols affect the radiative budget of the earth-atmosphere system both directly and indirectly (Kaufman et al., 2001). These effects can be estimated both for top of atmosphere (TOA) and bottom of atmosphere (BOA). A better way to compare the forcing ability of aerosols of different optical depths is by calculating the radiative forcing efficiency which is simply the radiative forcing per unit AOD.

2.9.1 Direct radiative forcing

When perturbation of the radiative budget of the Earth-atmosphere system is as a result scattering and absorption of incoming solar radiation and outgoing long-wave radiation due to increased concentration of atmospheric aerosol, then the resulting radiative forcing is referred to as *Direct Radiative Forcing* (DRF). The anthropogenic AOD could be converted into DRF using several possible calculations and radiative transfer models. The aerosol optical properties and vertical profile, and the surface albedo are required for this estimation.

Several postulations have been put forward and applied to estimate the DRF of aerosol. The mostly applied derivation is the one by Charlson et al. (1991). According to Charlson et al. (1991), for top of atmosphere (TOA), the DRF (ΔF) can be estimated by the expression in Equation (2.21):

$$\Delta F \cong -\frac{1}{2} S_o {T_{at}}^2 (1 - A_c)(1 - R_s)^2 \overline{\beta} \delta \tag{2.21}$$

where S_o is the solar constant, T_{at} is the atmospheric transmission, A_c is the fractional cloud amount, R_s is the surface reflectance, $\overline{\beta}$ is the spectral weighted backscattered fraction, and δ is the spectral-weighted AOD.

2.9.2 Indirect radiative forcing

When atmospheric aerosol absorbs radiation, they eventually dissipate such radiation, thereby altering the microphysical properties and lifetime of clouds which may affect the water cycle. Such a forcing is termed *Indirect Radiative Forcing* (IRF). The alteration of the microphysical properties of the clouds can suppress rainfall in an atmosphere with high concentrations of pollutant due to the fact that the aerosol particles can act as both cloud condensation nuclei (CCN) and ice nuclei (IN), thereby inhibiting the formation of large raindrops (Haywood and Boucher, 2000; Ramanathan et al., 2005; Rosenfeld, 2000). Indirect aerosol radiative forcing is relatively more complicate to estimate due to the current lack of understanding of the cloud-aerosol interaction (Chylek and Wong, 1995).

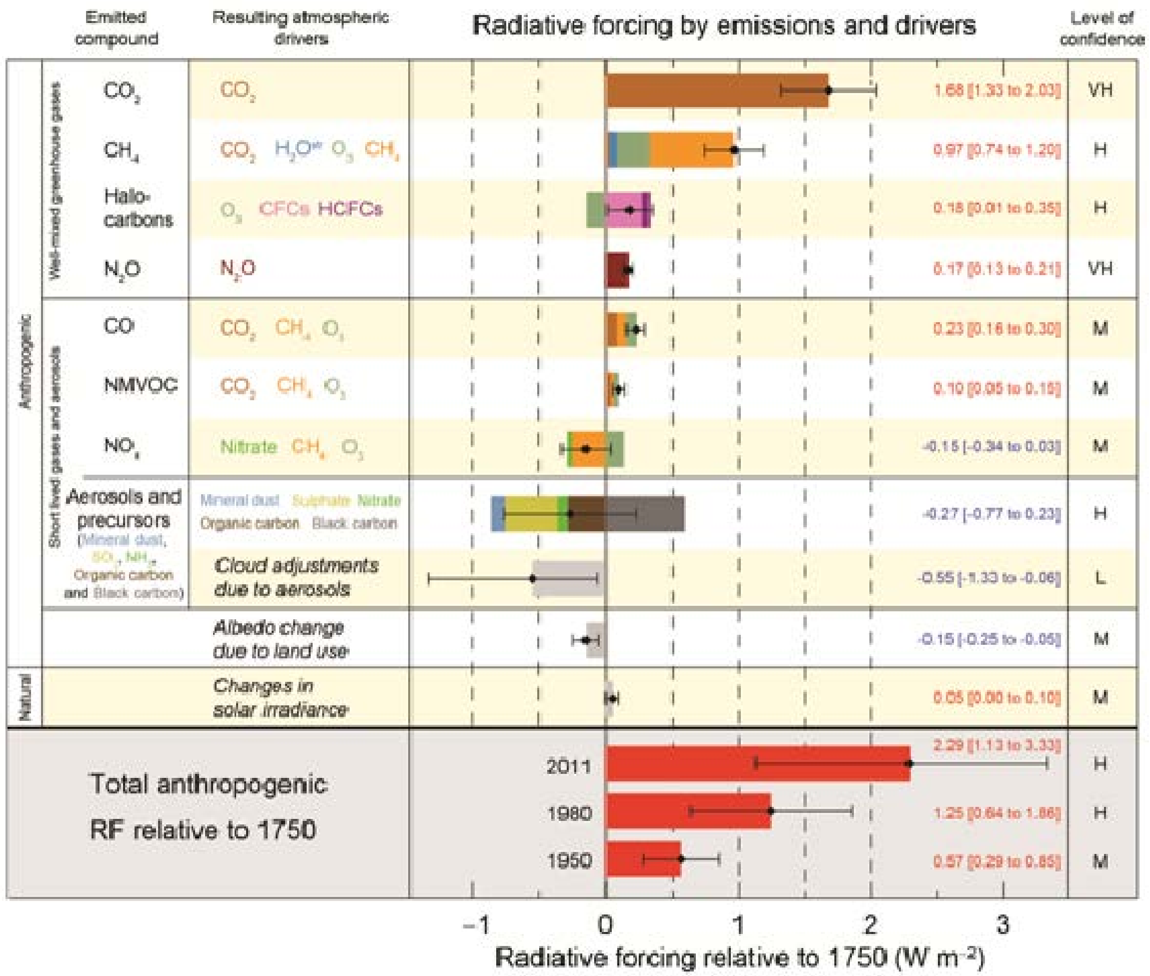

Figure 2.4: Radiative forcing potential of anthropogenic and natural aerosol and greenhouse gases (IPCC, 2013)

Figure 2.4 shows the radiative forcing estimates in year 2011 relative to 1750 and aggregated uncertainties for principal climate change drivers. Radiative forcing values shown in the plots are global average radiative forcing, partitioned according to the emitted compounds or processes that result in a combination of drivers (IPCC, 2013).

Several radiative transfer packages and models have been used to calculate both the direct and indirect radiative forcing of aerosol of different sources at different seasons and regions. Among the most used are the Santa Barbara DISORT Atmospheric Radiative Transfer

(SBDART) code (Ricchiazzi et al., 1998), libRadtran package (Emde et al., 2015) and TUV (Tropospheric Ultraviolet and Visible) model.

2.10 Atmospheric dispersion modelling

Air pollution dispersion modeling is essentially the mathematical simulation of how air pollutants disperse in the ambient air; it describes numerically the relationships which exist between emissions, meteorology, atmospheric concentration, deposition and other factors. It establishes an unambiguous and deterministic source-receptor relationship as well as does an assessment of the fractional contribution of each emission source to the receptor areas (Zannetti, 2013). The air motions in the atmosphere transport air pollutants (gaseous and particulate matter) between the source and receptor sites. This transportation is via two main processes: (i) advection by wind, and (ii) turbulent diffusion (see Figure 2.5).

The transportation of emitted air pollutants away from its source brings about a mixing of the pollutants in a larger volume of air having lower concentrations of these pollutants, thereby lowering the concentration of these pollutants as they move away from the source (Turner, 1994). Sources of emission can be classified as a point, line, area or volume source depending on its geometry and nature of release (Arya, 1999).

Most air pollution problems take place in the planetary boundary layer (PBL): a region in which the atmosphere experiences the presence of the surface through vertical exchanges of momentum, heat and moisture (Zannetti, 2013). The diffusion of pollutants in the PBL depends on the vertical component of mean wind speed and direction, and turbulence state in the PBL; all of which depend on the atmospheric stability. The height of the PBL, known as *mixing height*, determines the extent to which pollutants emitted from a surface or elevated source is mixed in the atmosphere.

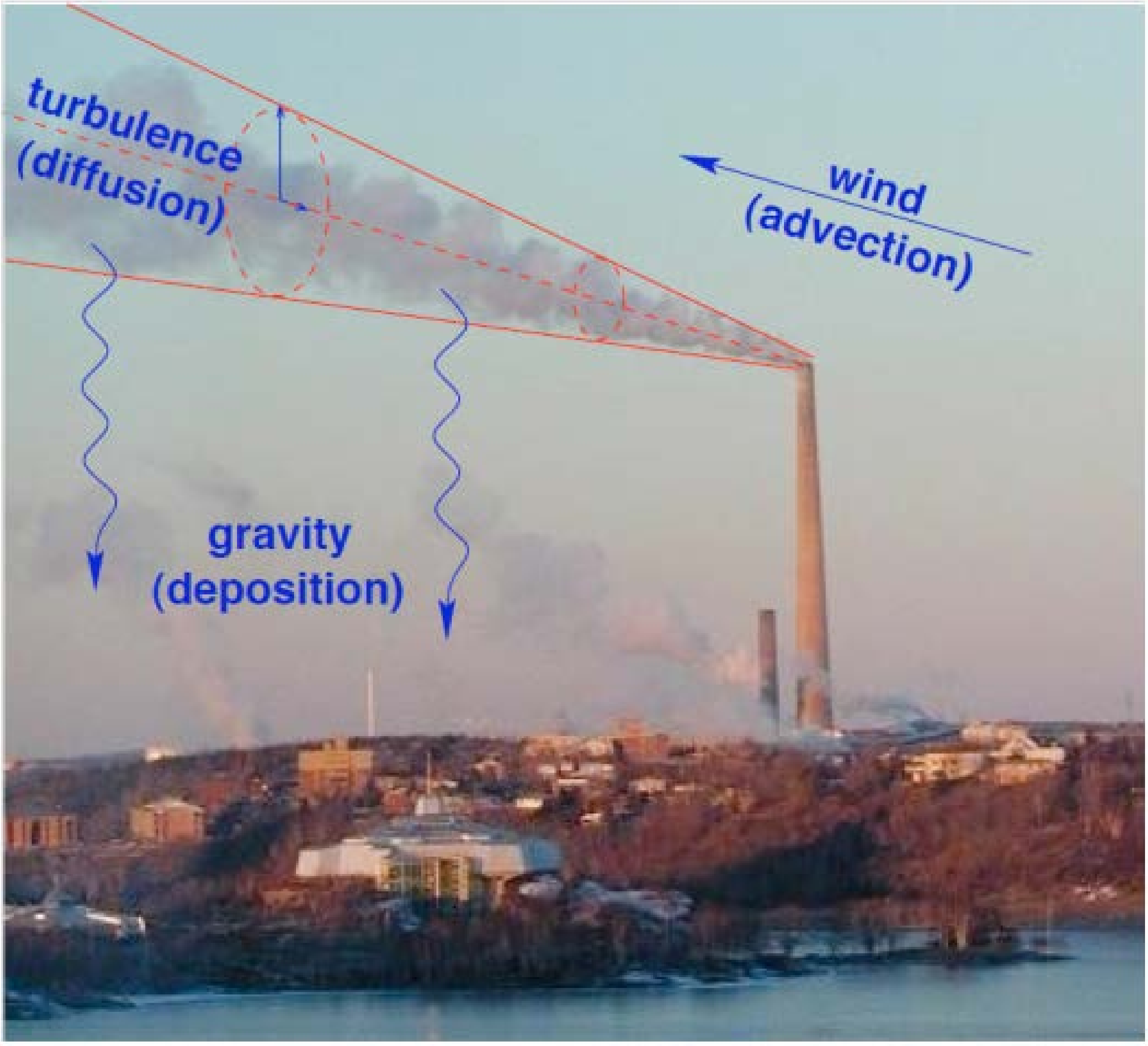

Figure 2.5: A photograph of emission from an industrial stack (point source) (Stockie, 2011)

.

Atmospheric variables that affect the dispersion of air pollutants are wind speed and direction, and atmospheric stability. Surface roughness is equally an important property of the dispersal medium that is considered in modelling the dispersion of a pollutant in the medium. For the dispersion modeling purpose, the stability condition of the dispersal medium is required. The commonest and mostly used classification of atmospheric stability used in dispersion modelling is the Pasquill discrete stability classification shown in Table 2.4.

Table 2.4: Pasquill stability classification

	Insolation			Night	
Surface wind speed (at 10 m) $\mathrm{m\,s^{-1}}$	Strong	Moderate	Slight	Thin overcast (> 4/8 low cloud)	< 3/8 cloud
< 2	A	A - B	B	-	-
2 - 3	A - B	B	C	E	F
3 - 5	B	B - C	D	D	E
5 - 6	C	C - D	D	D	D
> 6	C	D	D	D	D

Source: (Pasquill, 1961).

In the Pasquill stability classification shown in Table 2.4: A, extremely unstable; B, moderately unstable; C, slightly unstable; D, neutral; E, slightly stable; F, moderately stable. The transportation of pollutants in the atmosphere is governed by the atmospheric advection-diffusion equation (AADE) which, following Ermak (1977), can be written as:

$$\frac{\partial C}{\partial t} = \frac{\partial}{\partial x}K_x\frac{\partial C}{\partial x} - U\frac{\partial C}{\partial x} + \frac{\partial}{\partial y}K_y\frac{\partial C}{\partial y} + \frac{\partial}{\partial z}K_z\frac{\partial C}{\partial z} + W_z\frac{\partial C}{\partial z} \tag{2.22}$$

where C is the concentration of the pollutant at a point (x, y, z) at time t, K_x, K_y and K_z are the coefficients of eddy diffusivity in the x, y and z directions, respectively, U is the mean wind speed, and W is the particle settling velocity as a result of gravitational pull.

Applying the basic assumptions of the Gaussian plume approach (temporal steadiness and negligible along-wind diffusion), Equation (2.22) is reduced to:

$$U\frac{\partial C}{\partial x} - W_z\frac{\partial C}{\partial z} = \frac{\partial}{\partial y}K_y\frac{\partial C}{\partial y} + \frac{\partial}{\partial z}K_z\frac{\partial C}{\partial z} \tag{2.23}$$

Solving Equation (2.23) by Laplace transform in the Cartesian coordinate gives the Gaussian plume formula (Eq. 2.24). For an elevated point source at height H, Equation 2.24 becomes Equation (2.25) (Arya, 1999). Equation (2.25) gives the steady state downwind concentration ($\mathrm{g\,m^{-3}}$) of a pollutant from a point source located at (0, 0, H) and emitting at a constant rate Q ($\mathrm{g\,s^{-1}}$).

$$\overline{C}(x,y,z) = \frac{Q}{2\pi\bar{u}\sigma_y\sigma_z} exp\left(-\frac{y^2}{2\sigma_y{}^2} - \frac{z^2}{2\sigma_z{}^2}\right) \tag{2.24}$$

$$\overline{C}(x,y,z) = \frac{Q}{2\pi\bar{u}\sigma_y\sigma_z} exp\left(-\frac{y^2}{2\sigma_y{}^2}\right)\left\{exp\left[-\frac{(z-H)^2}{2\sigma_z{}^2}\right] + exp\left[-\frac{(z+H)^2}{2\sigma_z{}^2}\right]\right\} \tag{2.25}$$

where σ_y and σ_z are the horizontal and vertical Gaussian plume dispersion parameters, respectively.

2.10.1 Dispersion Models

The effective height of a plume (Δh) from a source and an estimate of the concentration downwind of the source can be obtained by solving one of the several relations for effective stack height, such as the one by Briggs (1965) (see Equation 2.26 and 2.27), and the dispersion equation, respectively.

$$\Delta h = 1.6.F^{\frac{1}{3}}.u^{-1}.d^{\frac{2}{3}} \qquad (neutral \quad condition) \tag{2.26}$$

$$\Delta h = 1.6.F^{\frac{1}{3}}.u^{-1}.(10.h_s)^{\frac{2}{3}} \qquad (unstable \quad condition) \tag{2.27}$$

When a computer code is used for the repetitious solution of these equations, then the code is referred to as a dispersion model (Turner, 1994). Eulerian and Lagrangian models are numeric solutions to the advection-diffusion equation under conditions that make the application of the Gaussian (analytic) solution impossible. The basic difference between the Eulerian and Lagrangian model is in the reference systems. While the Eulerian reference is fixed with respect to the Earth, the Lagrangian reference system follows the average atmospheric motion of the particle. Both process models and dispersion models require the input of data which includes meteorological parameters, emission parameters, terrain elevations and some other factors that could influence air flow and chemistry.

2.11 Conclusion

The World Bank has been at the fore-front of the campaign to reduce gas flaring through the public-private partnership project tagged "Global Gas Flaring Reduction (GGFR)" (http://www.worldbank.org/en/programs/gasflaringreduction). The "Zero Routine Flaring by 2030" initiative was launched in April 2015 by the World Bank, United Nations, governments and oil companies. As at April 17 2015, a total of nine countries have agreed to the "Zero Routine Flaring by 2030" initiative. At the time of writing this review, some major flaring nations have yet to sign up to the initiative. Indeed, some major flaring countries still struggle to meet targets for gas flaring set in the late 1980s.

Considering the wide spectrum, quantity and effects of pollutants emitted from gas flaring, coupled with the estimated quantity of gas flared globally, it is surprising that so little effort has been put into adequately understanding the yield of pollutants, especially BC, from the process in real world field situations. The wide variation of fuel gas compositions from flow stations around the world underpins the importance of developing strategies that take these compositions into consideration when estimating emissions.

The steep decrease in fraction of total gas production flared between 2000 and 2006 seems to have stabilised between 2007 and 2010, and the fraction has even increased in 2011. The overall quantity of gas flared since 2000 has been steady at between 93 and 110 bcm. An increase in total production since 2009 has brought about a corresponding increase in the quantity of gas flared. Incentives and stringent policies are not yet in place to encourage more companies and countries to partner with the World Bank in their "Zero Routine Flaring by 2030" initiative.

Elevated concentrations of BC, CO, H_2S, SO_2, NO, NO_2 and PAH measured around flaring sites (from ground based and aircraft measurements) is indicative of the detrimental impact of gas flaring on the environment. Clusters of gas flaring sites around the tropics and near-tropic regions of the world, where there is the likelihood on enhanced atmospheric mixing of the emissions into the lower and even mid-troposphere, coupled with the high temperature of the emitted plume suggests the possibility of long-range transport of these pollutants.

Emission factors used for BC emission from gas flaring are inadequate to estimate emission from a typical real-world gas flare as most of the fuels used in the studies for such emission factors are not representative of fuel gas from most flow stations around the world. In the studies that employed the mass/mole balancing technique to estimate pollutants from the combustion of hydrocarbons, estimated EFs for CO_2 and CO have been given, but there is no consideration of the amount of unburnt carbon given off. It should be noted that these studies did not consider flame dynamics changes in their estimations. When estimating emissions from gas flares, there is the need to ascertain the nature (regime) of the combustion flame as the flame nature and temperature plays pivotal role in determining the pollutants yield, and this has not yet been routinely considered in dispersion modelling and global inventories.

Global models need to update the sources of BC to include gas flaring, especially in regions prone to long-range transfer of gas flaring emission from leading gas flaring nations including Russia, Nigeria and nations of the Middle East.

Chapter 3

Self-consistent estimation of emission factors for gas flaring emissions

3.1 Abstract

At about 6-8 % of global natural gas production, the process of gas flaring continues to be significant, particularly in oil-rich regions of the world. With its broad spectrum of ambient air contaminants, such as CO, CO_2, SO_2, soot (BC), Polycyclic Aromatic Hydrocarbon (PAH) and NO_X, it is of great concern to environmental scientists, air quality monitoring agencies and stakeholders. This study proposes a novel approach to the estimation of emission factors of soot (EF_{soot}), CO (EF_{CO}) and CO_2 (EF_{CO_2}). The emission estimates depend on the quantity and varying composition of fuel gas, flame dynamics characteristics (represented by the fire Froude number, Fr_f) and equivalence ratio, ϕ, of the fuel-air mixture. Soot emission estimates is presented as a function of fire Froude number for lab-based test gases, in order to validate the scheme, and for two real-world fuel-gas compositions (labelled compositions I and II), which are two extreme cases in terms of density, having mass weighted carbon-to-hydrogen (C:H) ratio of 0.25 and 0.29, respectively. The soot yield of the lab-based test case was scaled up to estimate the soot yield of a full scale flare using the Richardson number as scaling parameter. The approximately 16 % difference in fuel composition, indicated by the C:H ratio, results in increases by factors of about 3,

1.4 and 1.7 in $\mathrm{EF_{soot}}$, $\mathrm{EF_{CO}}$ and EF_{CO_2} ($\mathrm{g\,m^{-3}}$), respectively, when all other variables are held constant at values characteristics of real-world flares. For both fuel compositions, the ratio of $\mathrm{EF_{soot}}$ to $\mathrm{EF_{CO}}$ at the fuel-lean region ($\phi < 1$) is higher; it lies in the range 0.031 – 0.13 and 0.0012 – 0.0055 for the fuel-lean ($\phi < 1$) and fuel-rich ($\phi > 1$) regions, respectively.

To explore a range of fire Froude numbers, the volume flow flux of the fuel gas is varied while keeping the stack diameter constant, hence allowing the exit velocity of the flue gas to vary. For given fuel compositions, $\mathrm{EF_{CO}}$ and $\mathrm{EF_{CO_2}}$ are less dependent on Fr_f, depending more on ϕ, whereas $\mathrm{EF_{soot}}$ varies significantly with both Fr_f and ϕ.

At $\phi = 1$, $\mathrm{EF_{CO}}$, $\mathrm{EF_{CO_2}}$ and $\mathrm{EF_{soot}}$ (in $\mathrm{g\,m^{-3}}$) estimated for fuel compositions I and II are 7.78, 1980.0 and 0.58 and, 10.08, 3365.5 and 1.73, respectively. Our approach and results may be adopted to generate an emissions inventory of the species associated with gas flaring on regional and global scales.

The materials in this chapter has been presented at conferences, and hence, are available from online conference abstract database and conference proceedings.

3.2 Introduction

Natural gas comprises mainly of hydrocarbons occurring in geological deposits, and consists mainly of methane. It includes both “non-associated” gas, originating from fields producing hydrocarbons only in gaseous form, and “associated” gas, produced in association with crude oil and separated at a flow station (IEA, 2012). Gas flaring is the widely used method of disposing of some of these gases, which are often termed unwanted or hazardous. Gas flaring is the controlled burning, in open flame, of associated gas that is produced at various stages of crude oil exploration and exploitation (Beychok, 2005; EEA, 2006; Stone et al., 1992). The flared gas will, for the purpose of this study, be referred to as ‘fuel gas’ since it serves as fuel for the flare flame. In recent years, especially 2014 - 2016, there has been renewed efforts at the estimation of emissions from gas flaring activities as well as assessing and quantifying contributions of gas flaring to atmospheric pollution, particularly in the Bakken region of North Dakota, USA and the Arctic (Li et al., 2016; Schwarz et al., 2015; Weyant et al., 2016).

A number of undesired pollutants are emitted during gas flaring. Carbon dioxide (CO_2) is an inevitable consequence of flaring; other pollutants are emitted particularly when the combustion process is inefficient or incomplete as a result of insufficient oxygen to oxidise the hydrocarbon in the fuel gas or the ineffectiveness of the process (Flagan and Seinfeld, 2013; Fortner et al., 2012). For a comprehensive detail on the broad spectrum of emissions from gas flaring see Fawole et al. (2016b).

The nature and quantity of pollutants given off during the combustion process depend on a number of factors which include air-fuel mass (or mole) ratio, fuel gas composition, fuel flow rate, mixing of fuel gas and air, efficiency of the burner and prevailing ambient meteorology (Castineira and Edgar, 2006; Fortner et al., 2012; Ismail and Umukoro, 2014; Sivathanu and Faeth, 1990; Sonibare and Akeredolu, 2004; Stone et al., 1992; Talebi et al., 2014; Torres et al., 2012a,b). Studies have identified gas flaring as a prominent contributor to global air pollution index with the oil-producing regions most affected (Edwards et al., 2014, 2013; Fawole et al., 2016b; Gilman et al., 2013; Li et al., 2016; USEPA, 2012). About 1 – 8 % of global, 15 – 30 % of oil-rich regions and more than 50 % of Arctic BC emission could be attributed to gas flaring (Huang et al., 2015; Stohl et al., 2013).

Considering the volume and spatial distribution of gas flaring globally, it is rather surprising that so few studies have attempted to estimate emissions from full-scale flaring processes. Estimates of emission factors (EF) from the process of gas flaring have been attempted using a pilot-scale study (McDaniel and Tichenor, 1983; Talebi et al., 2014) or a lab-based study (McEwen and Johnson, 2012), simulation (Almanza et al., 2012; Ismail and Umukoro, 2014; Sonibare and Akeredolu, 2004) and field measurement (Johnson et al., 2013; Johnson and

Coderre, 2011).

BC, a principal light-absorbing species in the atmosphere (Koch et al., 2009), has been identified as the second major contributor to global warming after CO_2 (Santos et al., 2014). Fossil fuel-derived BC has equally been identified as a stronger global warming agent than biomass-derived BC (Andreae, 1995; Bond et al., 2013; Hansen et al., 2005; Ramana et al., 2010; Ramanathan and Carmichael, 2008). BC may also contribute significantly to visibility degradation (Bond et al., 2013; Feichter and Stier, 2012; Jacobson, 2002; Seinfeld, 2008; Tegen et al., 1997), as well as contributing a large fraction to the fine particulate mass fraction found in ambient air, especially around highly populated and industrialized regions of the world (Chow et al., 1996; Kirchstetter et al., 1999).

Measuring the soot (BC) yield in an open fire like a gas flare is a difficult task (Haynes and Wagner, 1981; Johnson and Coderre, 2011). Several attempts have been made to quantify soot yield in terms of the fuel and fire characteristics, flow conditions and burner geometry in pilot-scale and lab-based studies (Becker and Liang, 1982; Delichatsios, 1993b; Sivathanu and Faeth, 1990). Carbon conversion efficiency (CCE) is a measure of the extent of conversion of the carbon content of the fuel gas to carbon dioxide, usually expressed as a percentage (Bourguignon et al., 1999). CCE is often used to determine the completeness of combustion and it can be as low as 62 % in associated gas flares (Strosher, 2000). At a CCE of about 99 %, visible smoking can still be observed in a flare (Siegel, 1980). The carbon content of the fuel gas may be emitted as carbon dioxide, carbon monoxide, total hydrocarbon (THC) and BC. The amount of each fraction emitted depends on the degree of completeness of combustion which could be estimated from the CCE. Both completeness of combustion and CCE are overall measures of fuel conversion; either can be further subdivided into component due to fuel-to-air stoichiometry and a component due to imperfect mixing.

The purpose of this work is to develop a simple self-consistent method which requires few inputs from the user and takes into account the flame dynamics to study the variation of

CO, CO_2 and soot emission with varying fuel gas composition, flow characteristics, stack geometry and equivalence ratio in a typical gas flare. Firstly, the characteristic physical and chemical parameters defining the flare is introduced and then used to derive a system of equations to estimate the EFs. The approach is validated by comparing the results with those from similar test flares from literature. Finally, the variation of the EFs with realistic changes in the fuel composition are examined and the implications of the results for global emission inventories are discussed.

3.3 Methodology

3.3.1 Equivalence ratio

For the purpose of this work, the degree of combustion is determined in terms of the amount of oxygen available for the combustion of the fuel gas. This is measured as the air-fuel mass ratio. The stoichiometric air-fuel ratio $\left(\frac{A}{F}\right)_s$ gives the theoretical proportion of air mass needed for the complete combustion of the fuel, where A denotes 'air', F denotes 'fuel' and the subscript 's' denotes 'stoichiometric mixture'. During combustion, the stoichiometric mixture is not always and everywhere attained, hence, it is necessary to calculate the actual air-fuel ratio $\left(\frac{A}{F}\right)_a$, where 'a' denotes 'actual mixture' (Flagan and Seinfeld, 2013). The equivalence ratio (ϕ) is then defined as:

$$\phi = \frac{\left(\frac{A}{F}\right)_s}{\left(\frac{A}{F}\right)_a} \tag{3.1}$$

Thus $\phi = 1$ is a stoichiometric, $\phi < 1$ a fuel-lean (under-fired) and $\phi > 1$ a fuel-rich (over-fired) mixture.

The quantity of combustion products, especially soot, varies significantly with the equivalence ratio, ϕ (Huang et al., 2015). When $\phi < 1$ (excess air, but still with sufficient fuel:air mix to support combustion), combustion could be assumed to be complete with excess oxygen given off unreacted as a combustion by-product (Flagan and Seinfeld, 2013; McAllister et al., 2011). The combustion products for an 'ideal' complete stoichiometric combustion (ϕ =1) are relatively easy to quantify as CO_2, water and the fully oxidized products of any trace components (e.g., N_2 and H_2S converted to NO_2 and SO_2). Complete combustion is often not achieved in most flaring conditions as pyrolysis converts some of the fuel gas to many complex chemical species rather than the 'ideal' CO_2, SO_2, NO_2 and H_2O (Leahey et al., 2001; Strosher, 2000).

The products of combustion for $\phi > 1$ are more difficult to specify and estimate because there is not enough oxygen to completely burn all of the fuel gas (Flagan and Seinfeld, 2013; McAllister et al., 2011). Higher values of ϕ give rise to cooler flames that do not support fast combustion kinetics and, hence, favour the production of sooty flames (Stone et al., 1992). Lower flame temperature reduces the buoyancy and mixing of fuel gas and air in the combustion zone (Stone et al., 1992), with implications on how the emissions are dispersed into the ambient atmosphere.

3.3.2 Mole balancing method

For an 'ideal' stoichiometric mixture (ϕ = 1) of a single hydrocarbon (e.g., an alkane) and air, the generalized equation for complete combustion is:

$$C_xH_y + \left(\frac{y}{4} + x\right) O_2 \rightarrow x\, CO_2 + \left(\frac{y}{2}\right) H_2O \tag{3.2}$$

where *'x'* and *'y'* are integers, the relationship between which defines the hydrocarbon (e.g., y = 2x +2 for an alkane). For a mixture of various hydrocarbons, as in fuel gas, *'x'* and *'y'* are real numbers calculated from the molar composition of the gas. In a first step away from ideality, these calculated values of *'x'* and *'y'* could be scaled to take account of unburnt hydrocarbon, removing the need for the factor C_aH_b in Equation (2.2). Taking into account the effects of the equivalence ratio, ϕ (which is treated henceforth as an empirical input) and incomplete oxidation, as discussed above, a generalized combustion equation (GCE) is proposed which is given as:

$$C_xH_y + \frac{1}{\phi}\left(\frac{y}{4}+x\right)O_2 \rightarrow p\,CO_2 + q\,CO + r\,C + vO_2 + \left(\frac{y}{2}\right)H_2O \qquad (3.3)$$

where *'p', 'q', 'r' and 'v'* are real numbers whose values are determined by the degree of completeness of oxidation achieved in the flame. In forming Equation (3.3), the assumption is that all hydrogen is converted to water and therefore, all black carbon (soot) is made up purely of elemental carbon. The parameter *'v'* in Equation (3.3), number of moles of 'unused' oxygen, is defined to ensure that all molar quantities are positive definite.

From Equation (3.3), the following conservative relations can be obtained:

$$x = p + q + r \qquad (3.4)$$

$$\frac{1}{\phi}\left(x+\frac{y}{4}\right) = p + \frac{q}{2} + v + \frac{y}{4} \qquad (3.5)$$

from Equations (3.4) and (3.5);

$$q = \left(2x+\frac{y}{2}\right)\left(1-\frac{1}{\phi}\right) + 2v - 2r$$

$$= 2\left(x+\frac{y}{4}\right)\left(1-\frac{1}{\phi}\right)+2v-2r$$

$$q = 2(OCOM)\left(1-\frac{1}{\phi}\right)+2v-2r \tag{3.6}$$

p = NCAR - q - r

$$p = NCAR-2(OCOM)\left(1-\frac{1}{\phi}\right)-2v+r \tag{3.7}$$

where NCAR = x is the number of carbon atom in the hydrocarbon species and OCOM the number of moles of oxygen required by the hydrocarbon specie for stoichiometric mixture.

For $\phi > 1$; it is assumed that $v = 0$ (i.e. no unused oxygen)

$$\text{Hence, q} = \left(2x+\frac{y}{2}\right)\left(1-\frac{1}{\phi}\right)-2r,$$

for $\phi \leq 1$; v $\neq 0$

Combustion of natural gas gives off CO and CO_2 in specific ratios which depend on the source as well as efficiency of the process (Djuricin et al., 2010). Formation of CO depends principally on the amount of air available – lesser or in excess - for the combustion process (Bishop and Stedman, 1996). For gas flaring, the ratio of the emission factor of CO to that of CO_2 obtained from literature are 0.0024 (EEMS, 2008), 0.0032 (USEPA, 2014) and 0.0042 (UK Offshore Association). In this work, for the condition $\phi \leq 1$, the USEPA value of 0.0032 will be used as it was obtained from a pilot study carried out on emissions from gas flares. From USEPA (2014);

$$\frac{EF_{co}}{EF_{co_2}} = \frac{M_{co}\,q}{M_{co_2}\,p} = 0.0032$$

where M_{co} and M_{co_2} are the molar masses of CO and CO_2, respectively.

$$\frac{q}{p} = 0.005$$

$$\frac{q}{p} = \frac{2(OCOM)\left(1-\frac{1}{\phi}\right)+2v-2r}{NCAR-2(OCOM)\left(1-\frac{1}{\phi}\right)-2v+r} = 0.005 \tag{3.8}$$

Hence;

$$v = \frac{0.005NCAR-2.01OCOM\left(1-\frac{1}{\phi}\right)+2.005r}{2.01} \tag{3.9}$$

$$\left.\begin{aligned} v = \frac{0.005\ NCAR+2.005\ r}{2.01} \\ q = 2v-2r \end{aligned}\right\} for\ \phi = 1 \tag{3.10}$$

Therefore, there are three equations (3.4, 3.5 and 3.9) relating four unknowns *(p, q, r, v)* and three input parameters *(x, y, ϕ)* which are insufficient to evaluate *p, q, r and v*. One further relationship is required.

In this study, a method using the fire Froude number, Fr_f suggested by Delichatsios (1993b) and improved upon by McEwen and Johnson (2012) has been developed as a basis to constrain the parameter, *r*, for the 'unburned' carbon. In the experimental study of McEwen and Johnson (2012), soot yields were plotted as a function of the fire Froude number (see Fig. 3.1). In this study, the soot yield from the lab-based McEwen and Johnson (2012) experiment have been scaled-up to estimate the soot yield from a full-scale flare using a scaling parameter (Becker and Liang, 1982; Canteenwalla et al., 2007). The scaled-up soot yield data is then used to constraint the term *'rC'* in the GCE (see Equation 3.3) and *'r'*in Eq.

(3.9) and, hence, obtain 'p', and 'q'.

Fire Froude number, Fr_f (Eq. 3.11) is a dimensionless parameter related to the flame dynamics characteristics.

$$Fr_f = \frac{u_e f_s^{\frac{3}{2}}}{\left(\frac{\Delta T_f}{T_{amb}} g d_e\right)^{\frac{1}{2}} \left(\frac{\rho_e}{\rho_a}\right)^{\frac{1}{4}}} \tag{3.11}$$

where $f_s = \dfrac{1}{s+1} = \dfrac{\phi}{\left(\dfrac{a}{f}\right)_s + \phi}$

Figure 3.1: Soot yield as a function of Fire Froude number (adapted from McEwen and Johnson (2012)

For this study, Fr_f of the combustion flame is dependent on the air-fuel mass ratio and hence on one of our input variables, the equivalence ratio, ϕ. The adiabatic temperature, T_θ, for the different combustion type and fuel compositions is calculated as the roots of the quadratic in Equation (3.12):

$$h_i(T_\theta) - h_i(T_{amb}) = a_i(T_\theta - T_{amb}) + \frac{b_i}{2}({T_\theta}^2 - {T_{amb}}^2) \tag{3.12}$$

(Flagan and Seinfeld, 2013).

where h_i is the temperature-dependent molar specific enthalpy for the ith species of hydrocarbon; T_θ and T_{amb} are the adiabatic and ambient temperature, respectively; and a_i and b_i are thermodynamic constants given in $\mathrm{J\,mol^{-1}\,K^{-1}}$ (available from electronic databases and handbook such as JANAF thermochemical tables).

For this model, the typical range of adiabatic temperatures obtained for various fuel compositions is 1900 - 2440 K. Use of Equations (3.11) and (3.12) means that a further input parameter, T_{amb}, must be supplied. The appearance of ambient temperatures in Equations (3.11) and (3.12) is also the first appearance of environmental condition in the problem, indicating that the geographical context of flaring may be significant in determining emission factors.

To relate fully the soot yield in Figure 3.1 to our proposed input parameters (x, y, ϕ, T_{amb}), it is necessary to consider the difference between the test flame in the study of McEwen and Johnson (2012) relative to real-world gas flaring. The chemistry of soot depends sensitively on the composition of the fuel (Kostiuk et al., 2004). The fuel used in McEwen and Johnson (2012) is made up of four alkane species (CH_4, C_2H_6, $\mathrm{C_3H_8}$ and $\mathrm{nC_4H_{10}}$); methane ($\mathrm{CH_4}$) is 85.24 % by volume of the fuel gas. The C:H ratio of the fuel used by McEwen and Johnson (2012) is 0.25 (approx.), a value less than 0.27 - 0.29 for typical fuel composition in real-world gas flares (Fawole et al., 2016b). Fuel gas with high carbon to hydrogen ratio has a greater propensity to smoke (Akeredolu and Sonibare, 2004).

3.3.3 Soot scaling parameter

Lab-based study of emissions from flares is the most common and readily available method to estimate emissions from full-scale flares. Considering the size (diameter) of stack, higher fuel flow flux, and invariably the flue gas exit velocity of full-scale flares, there is the need to apply a scaling parameter to lab-based flare emission yields in order to estimate the yield from a full-scale flare (Fawole et al., 2016b). In previous studies, Richardson ratio (Becker and Liang, 1982), flame length (Schug et al., 1980) and Damköhler ratio (characteristic residence time) (Sivathanu and Faeth, 1990) are parameters that have been considered for such scaling purposes.

In the present work, the Richardson ratio, Ri_L, has been used to scale up the soot yield data from the lab-based study by McEwen and Johnson (2012). Ri_L, as defined by Becker and Liang (1982) (Eq. 3.13) is used for the scaling, as it involves the buoyancy of the flame which is a parameter also considered in fire Froude number, Fr_f. Also, Ri_L has a good correlation with soot emission from propane flame (Becker and Yamazaki, 1978).

$$Ri_L = \frac{buoyancy\ of\ flame}{source\ momentum\ flux} \cong \frac{\pi g \rho_\infty L^3}{\rho_e A {u_e}^2} \tag{3.13}$$

Ri_L varies with fuel composition as a result of the dependence of flame length (L) on the net heat released by the fuel during combustion.

For example, for a value of Fr_f = 0.005, the soot yield from McEwen and Johnson (2012) flame is 0.42 g of soot/kg of fuel burned (see Figure 3.1). For the same Fr_f, scaled-up values of soot yield are 0.79 and 1.11 g of soot/kg of fuel burned for fuel compositions I and II (see Table 3.I), respectively. The model calculates the fire Froude number, Fr_f, from the inputs (x, y, ϕ, T_{amb}, ρ_a, g, d_e) supplied by the user. The calculated Fr_f is used to estimate total soot yield from the scaled-up experimental data. The contribution of CH_4 to this total soot yield is calculated, since the composition of the fuel used by McEwen and Johnson (2012) is known.

If, for the sake of simplicity and in the absence of a more process-based structural relationship, it is assumed that the soot yield per component, χ_i, of a fuel mix of n hydrocarbon components is a simple linear function of the contribution of hydrocarbon i to the overall (non-CO_2) carbon budget, then we have:

$$\chi_i = \frac{C_i\, F_i}{\sum\limits_{j=1}^{n} C_j F_j} . S_i . \chi_{Tot} \tag{3.14}$$

In Equation (3.14), C_i is the number of carbon atoms in the empirical formula of component i, F_i is the volume fraction of component i, and χ_{Tot} is the total soot yield from the flame. The parameter S_i is a dimensionless empirical function (such as the Richardson ratio described above) that accounts for the greater propensity of a full-scale flare to soot as a result of the stack size, flame characteristics and fuel gas flow characteristics.

3.4 Results and Discussions

3.4.1 Soot yield

Two fuel compositions obtained from Sonibare and Akeredolu (2004), as given in Table 3.1, has been used to evaluate the effect of fuel composition of the EFs. Other parameters such as the fuel gas densities and molar masses are also provided in Table 3.1. The ambient temperature (298 K), stack diameter (0.75 m) and atmospheric pressure (1.0133 x 10^5 Pa) are kept constant during the calculation.

For fuel composition I, at ϕ = 1.0, the fire Froude number, Fr_f = 0.0045. Scaling down the soot yields for each hydrocarbon species in the fuel gas by their percentage molar concentration in the fuel gas, gives a total soot yield of 0.0143 $\mathrm{g\,mol^{-1}}$ of the fuel gas under the conditions stated above.

EF_{soot} = total soot yield ($\mathrm{g\,mol^{-1}}$) x molar density of fuel ($\mathrm{mol\,m^{-3}}$)

Hence, estimated EF_{soot} = 0.58 $\mathrm{g\,m^{-3}}$ (equivalent to 0.00076 kg of soot/kg of fuel burned)

For a flow flux = 1.174 $\mathrm{m^3\,s^{-1}}$ (Abdulkareem, 2005), the soot emission rate (ER) is 0.69 $\mathrm{g\,s^{-1}}$. For fuel composition II under the same condition, the estimated EF_{soot} = 1.73 $\mathrm{g\,m^{-3}}$. This is equivalent to 0.0015 kg of soot/ kg of fuel burned and an emission rate of 2.03 $\mathrm{g\,s^{-1}}$ for the same fuel flow flux.

In the estimation proposed in this work, the amount of carbon in the fuel gas that ends up as soot for the conditions ($0.8 \leq \ \phi \ \leq 1.3$) ranges between 0.1 - 0.35 % (by mass). The CCE is between 99.5 and 33.7 % (see Figures 3.5 and 3.6 for the variation of CCE with ϕ).

3.4.2 Carbon monoxide yield

For a fuel gas made up of N alkane species, the emission factor for carbon monoxide (EF_{co}) is estimated as:

$$EF_{co} = \frac{n_{co}}{n_{fuel\ gas}} \frac{PM_{co}}{RT} \tag{3.15}$$

where $\frac{n_{co}}{n_{fuel\ gas}} = \sum_{i}^{n} q_i c_i$ (ratio of mole of CO produced per mole of fuel gas burnt)

Under the combustion conditions given above for soot, for fuel gas composition I

Table 3.1: Fuel compositions used in this study (given in molar percentage)

	I	**II**
CH_4	88.72	69.58
C_2H_6	5.93	0.25
C_3H_8	1.28	12.54
nC_4H_{10}	0.26	2.35
iC_4H_{10}	0.26	5.12
nC_5H_{12}	0.06	5.20
nC_5H_{12}	0.09	2.54
C_6H_{14}	0.06	1.97
C_7H_{16}	0.1	-
N_2	0.66	0.24
CO_2	2.55	0.21
H_2S	0.03	-
C : H	0.25	0.29
HHV* ($\mathrm{kJ\,mol^{-1}}$)	939.8	1480.4
Molar mass ($\mathrm{g\,mol^{-1}}$)	18.5	28.6
Density ($\mathrm{kg\,m^{-3}}$)	0.75	1.2

* Higher (gross) heating value of the fuel gas.

$$\frac{n_{co}}{n_{fuel\ gas}} = 0.0054$$

By Equation (3.15), this gives EF_{co} = 6.16 $\mathrm{g\,m^{-3}}$ (equivalent to 0.0082 $\mathrm{kg\,kg^{-1}}$ of fuel burned). For fuel flow flux = 1.174 $\mathrm{m^3\,s^{-1}}$, ER = 7.2 x 10^{-3} $\mathrm{kg\,s^{-1}}$.

For composition II:

$$\frac{n_{co}}{n_{fuel\ gas}} = 0.0093;$$

Hence, EF_{co} = 10.69 $\mathrm{g\,m^{-3}}$ (equivalent to 0.0092 $\mathrm{kg\,kg^{-1}}$ of fuel burned and 1.3 x 10^{-2} $\mathrm{kg\,s^{-1}}$).

3.4.3 Carbon dioxide yield

$$EF_{co_2} = \frac{n_{co_2}}{n_{fuel\ gas}} \frac{PM_{co_2}}{RT} \tag{3.16}$$

where $\frac{n_{co_2}}{n_{fuel\ gas}} = \sum_i^n q_i c_i$ (ratio of mole of CO_2 produced per mole of fuel gas burnt)

M_{CO_2} – molar masses of CO_2 ($\mathrm{g\,mol^{-1}}$)

p_i and c_i - the CO_2 yield and percentage molar concentration of species i in the fuel gas.

Under the combustion conditions given above, for fuel gas composition I:

$$\frac{n_{co_2}}{n_{fuel\ gas}} = 1.10$$

By Eq. (3.16), this gives EF_{CO_2} = 1.98 $\mathrm{kg\,m^{-3}}$ (equivalent to 2.62 $\mathrm{kg\,kg^{-1}}$ of fuel burned and 2.32 $\mathrm{kg\,s^{-1}}$)

For composition II:

$$\frac{n_{co_2}}{n_{fuel\ gas}} = 1.86$$

Hence, EF_{CO_2} = 3.35 $\mathrm{kg\,m^{-3}}$ (equivalent to 2.87 $\mathrm{kg\,kg^{-1}}$ of fuel burned and 3.93 $\mathrm{kg\,s^{-1}}$).

For 10 different fuel gas compositions obtained from literature (Sonibare and Akeredolu (2004) and Ismail and Umukoro (2014)), the relationships between their soot yield and, molar mass and higher heating value (HHV) are presented in Figure 3.2. The soot yields and HHV of these fuel gas compositions are estimated from this model for ϕ = 1. It should be noted that HHV can only be calculated at ϕ = 1 because HHV is the amount of heat given off by the complete combustion of a fuel. For these fuels, the range of the molar mass and HHV are 18 - 28.6 $\mathrm{g\,mol^{-1}}$ and 39.9 – 60.3 $\mathrm{MJ\,m^{-3}}$, respectively.

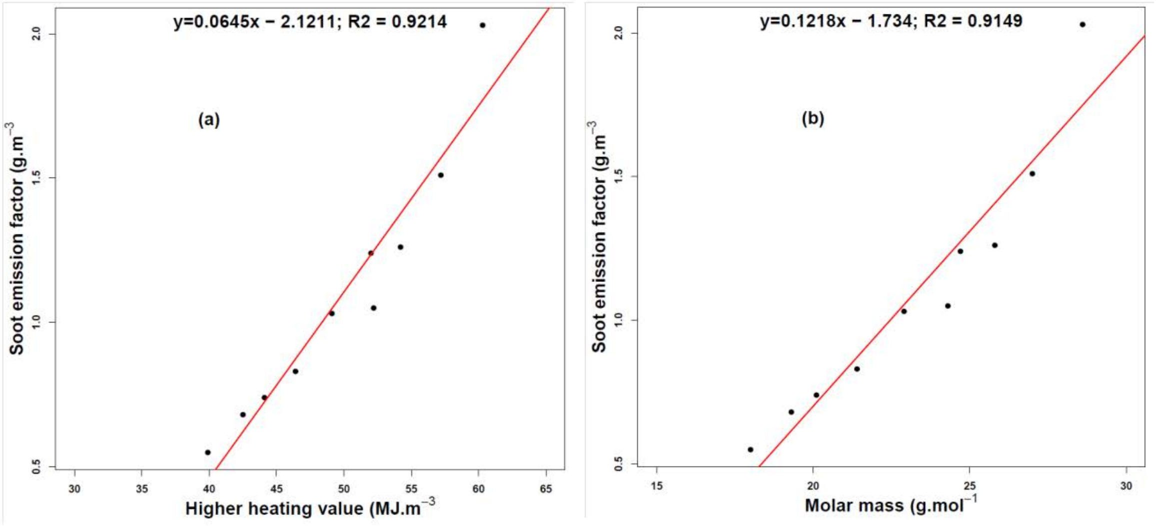

Figure 3.2: Relationship between (a) EF_{soot} and HHV, and (b) EF_{soot} and molar mass for various fuel compositions

For this study, it is assumed that the carbon content of the fuel gas ends up as CO_2, CO and soot. Hence, omitting the presence of PAH and other incompletely oxidised hydrocarbon. For the denser fuel composition (composition II), the variation of CO_2, CO and soot with equivalent ratio, ϕ is shown in Figure 3.3(a) while Figure 3.3(b) shows the variation of CO:CO_2 ratio with ϕ. The gradient of CO:CO_2 gets steeper as equivalence ratio increases but almost plateaued when $\phi < 1$.

A comparison of the EF estimates from this study with those obtained from similar study from literature – lab-based, pilot study, field measurement and calculations – are presented in Tables 3.2 and 3.3. It should, however, be noted that this work considered two very different fuel compositions (light and dense). As such, two different EFs will be quoted for comparison in Tables 3.2 and 3.3 below.

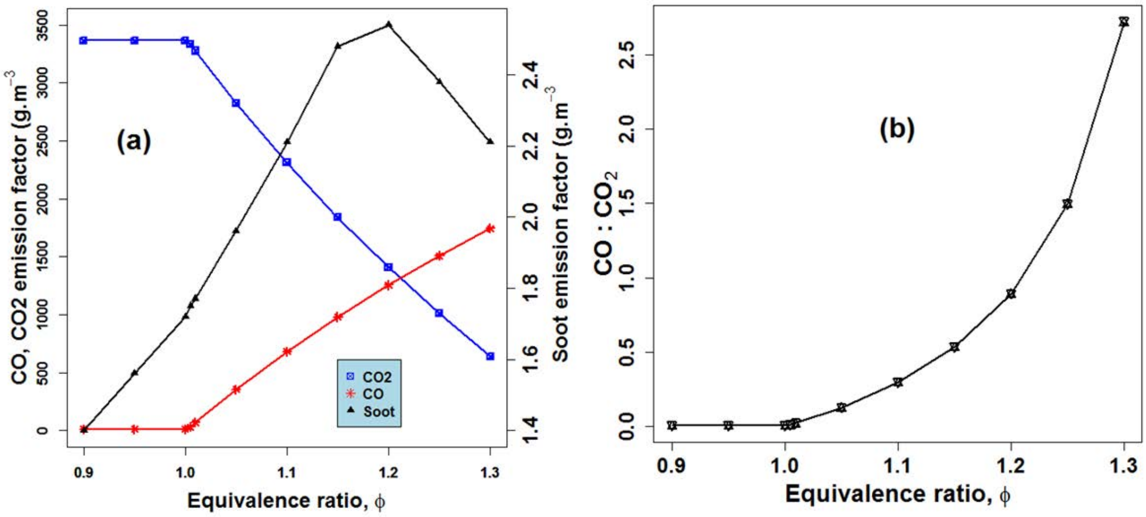

Figure 3.3: (a) Relationship between equivalence ratio (ϕ), EF_{CO_2}, EF_{CO} and EF_{soot}, and (b) variation of CO:CO$_2$ with ϕ

The method developed here produced EFs and emission rates (ERs) that compare favourably well with those obtained from similar studies in literature. ER is the product of EF ($\mathrm{g\,m^{-3}}$) and fuel flow flux ($\mathrm{m^3\,s^{-1}}$). Fuel flow flux varies significantly from one field to another; it can be as high as 32.3 $\mathrm{m^3\,s^{-1}}$, the estimated value for an active flare in Venezuela which is ranked #1 globally (Elvidge et al., 2015). In this model, EF_{soot} values of 0.58 and 1.73 $\mathrm{g\,m^{-3}}$ obtained for fuel I and II, respectively, fall within the light- and averagely-smoking flare category for AP 42 estimates.

Emission rates of 6.9 x 10^{-4} and 2.02 x 10^{-3} $\mathrm{kg\,s^{-1}}$ obtained for fuel I and II, respectively, compare well with those obtained in similar studies by IMP (2006) and Almanza et al. (2012). Fuel flow flux = 1.174 $\mathrm{m^3\,s^{-1}}$ has been used for the estimations in this study. The values obtained for EF_{CO} and EF_{CO_2} compare well with those from UKOA, (Talebi et al., 2014) and (USEPA, 1995a).

The graphs in Figure 3.5 and 3.6 show the 2-dimensional variation of EF_{soot}, EF_{CO} and EF_{CO_2} with equivalence ratio, ϕ, and flue gas exit velocity, V_s, as well as the variation of CCE with ϕ for the two fuel compositions used in this study. The exit velocity of the flue gas was

Table 3.2: Emission Factor (EF) for soot from gas flaring

	EF (kg/10^3m^3 of fuel)	**EF (kg.s^{-1})**	**Type of fuel**
USEPA (1995)	0, 0.9, 4.2, 6.4	-	80 % propylene, 20 % propane
Johnson et al. (2013)	-	6.7 x 10^{-5}	-
McEwen and Johnson (2012)	0.51	-	85.2 % CH_4; 7.1 % C_2H_6; 3.1 % C_3H_8; 1.4 % nC_4H_{10}
IMP (2006) [a]	-	3.37 x 10^{-3}	-
Almanza et al. (2012)	-	2.24 x 10^{-4}	associated gas
Johnson and Coderre (2011)	-	2.0±0.66 x 10^{-3}	-
GAINS (Stohl et al., 2013)	1.6	-	-
This work - Fuel I	0.58	6.9 x 10^{-4}	associated gas
Fuel II	1.73	2.02 x 10^{-3}	associated gas

[a] quoted from Almanza et al. (2012).

Table 3.3: Emission factors for CO and CO_2 from gas flaring

	CO (kg/kg)	CO_2 (kg/kg)	CO (kg/s)	CO_2 (kg/s)	CO (kg/GJ)	CO_2 (kg/GJ)
EEMS (2008)	0.0067	2.8	-	-	-	-
USEPA (1995a)	-	-	-	-	0.16	50.2
The Norwegian Oil Industry Association [a]	-	-	-	-	0.026	63.6
Talebi et al. (2014)	-	-	-	-	0.1 - 0.59	49.0 - 51.6
United Kingdom Offshore Association (UKOA) [a]	-	-	-	-	0.26	61.8
This work - Fuel I	0.0082	2.6	0.007	2.32	0.24	69.23
This work - Fuel II	0.0092	2.87	0.013	3.93	0.26	74.3

[a] quoted from Talebi et al. (2014).

varied by varying the volume flux ($\mathrm{m^3\,s^{-1}}$) of the fuel gas while the stack diameter is kept constant. Soot given off is dependent on both the equivalent ratio and the flame dynamics characteristics as measured by the fire Froude number (see Figures 3.5 and 3.6). Low values of V_s, (for example, 2.0 $\mathrm{m\,s^{-1}}$) can produce very sooty flames at higher values of ϕ. At high flue gas exit velocity (> 6 $\mathrm{m\,s^{-1}}$) and high ϕ (> 1.1), the low value of soot emitted is probably due to the fact that some of the fuel 'escaped' unburned as a result of the high exit velocity and low amount of oxygen available.

The heavier the fuel gas, the more oxygen needed for its combustion. The molar masses of fuel compositions I and II are 18.5 and 28.6, respectively. A difference of 0.04 in the value of C:H for fuel composition I and II results in increase by factor of $\sim$3, $\sim$1.4 and $\sim$1.7 in EF_{soot}, EF_{CO} and EF_{CO_2}, respectively. This underlines the importance of fuel composition in the estimation of pollutant emissions from the combustion of hydrocarbons. The importance of a qualitative idea of the amount of air available for the combustion, the fuel gas flow rate and stack characteristics (diameter) are also demonstrated with the wide variation of emission quantities.

These EF estimations for (CO, $\mathrm{CO_2}$, and soot) have been coded into MATLAB as a pre-processor for dispersion modeling software. The user supplies the fuel composition (preferably, in percentage molar composition), equivalence ratio (ϕ), ambient temperature, atmospheric pressure, stack diameter and fuel gas flow flux ($\mathrm{m^3\,s^{-1}}$). The pre-processor generates estimates for the EFs of soot, $\mathrm{CO_2}$, CO, $\mathrm{SO_2}$ and $\mathrm{NO_X}$ ($\mathrm{NO_X}$ as a function of net heat released (Pohl and Soelberg, 1985)). Other combustion parameters generated by the pre-processor are flame length (m), net heat released ($\mathrm{MJ\,s^{-1}}$), flue gas exit velocity ($\mathrm{m\,s^{-1}}$), buoyancy and momentum flux.

Figure 3.4 shows snapshots of the dialogues for the inputs interface of the model as well as a section of its output screen.

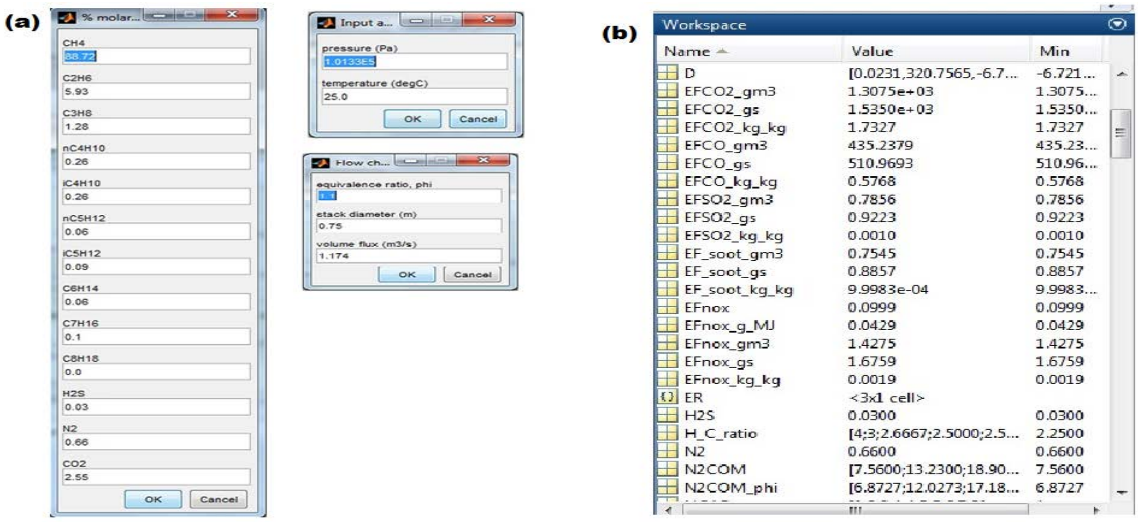

CH4: 88.72
C2H6: 5.93
C3H8: 1.28
nC4H10: 0.26
iC4H10: 0.26
nC5H12: 0.06
iC5H12: 0.09
C6H14: 0.06
C7H16: 0.1
C8H18: 0.0
H2S: 0.03
N2: 0.66
CO2: 2.55

pressure (Pa): 1.0133E5
temperature (degC): 25.0

equivalence ratio, phi: 1.1
stack diameter (m): 0.75
volume flux (m3/s): 1.174

Name	Value	Min
D	[0.0231,320.7565,-6.7...	-6.721...
EFCO2_gm3	1.3075e+03	1.3075...
EFCO2_gs	1.5350e+03	1.5350...
EFCO2_kg_kg	1.7327	1.7327
EFCO_gm3	435.2379	435.23...
EFCO_gs	510.9693	510.96...
EFCO_kg_kg	0.5768	0.5768
EFSO2_gm3	0.7856	0.7856
EFSO2_gs	0.9223	0.9223
EFSO2_kg_kg	0.0010	0.0010
EF_soot_gm3	0.7545	0.7545
EF_soot_gs	0.8857	0.8857
EF_soot_kg_kg	9.9983e-04	9.9983...
EFnox	0.0999	0.0999
EFnox_g_MJ	0.0429	0.0429
EFnox_gm3	1.4275	1.4275
EFnox_gs	1.6759	1.6759
EFnox_kg_kg	0.0019	0.0019
ER	<3x1 cell>	
H2S	0.0300	0.0300
H_C_ratio	[4;3;2.6667;2.5000;2.5...	2.2500
N2	0.6600	0.6600
N2COM	[7.5600;13.2300;18.90...	7.5600
N2COM_phi	[6.8727;12.0273;17.18...	6.8727

Figure 3.4: (a) Dialogue screens for inputs into the model, and (b) snapshot of a section of the output screen of the model

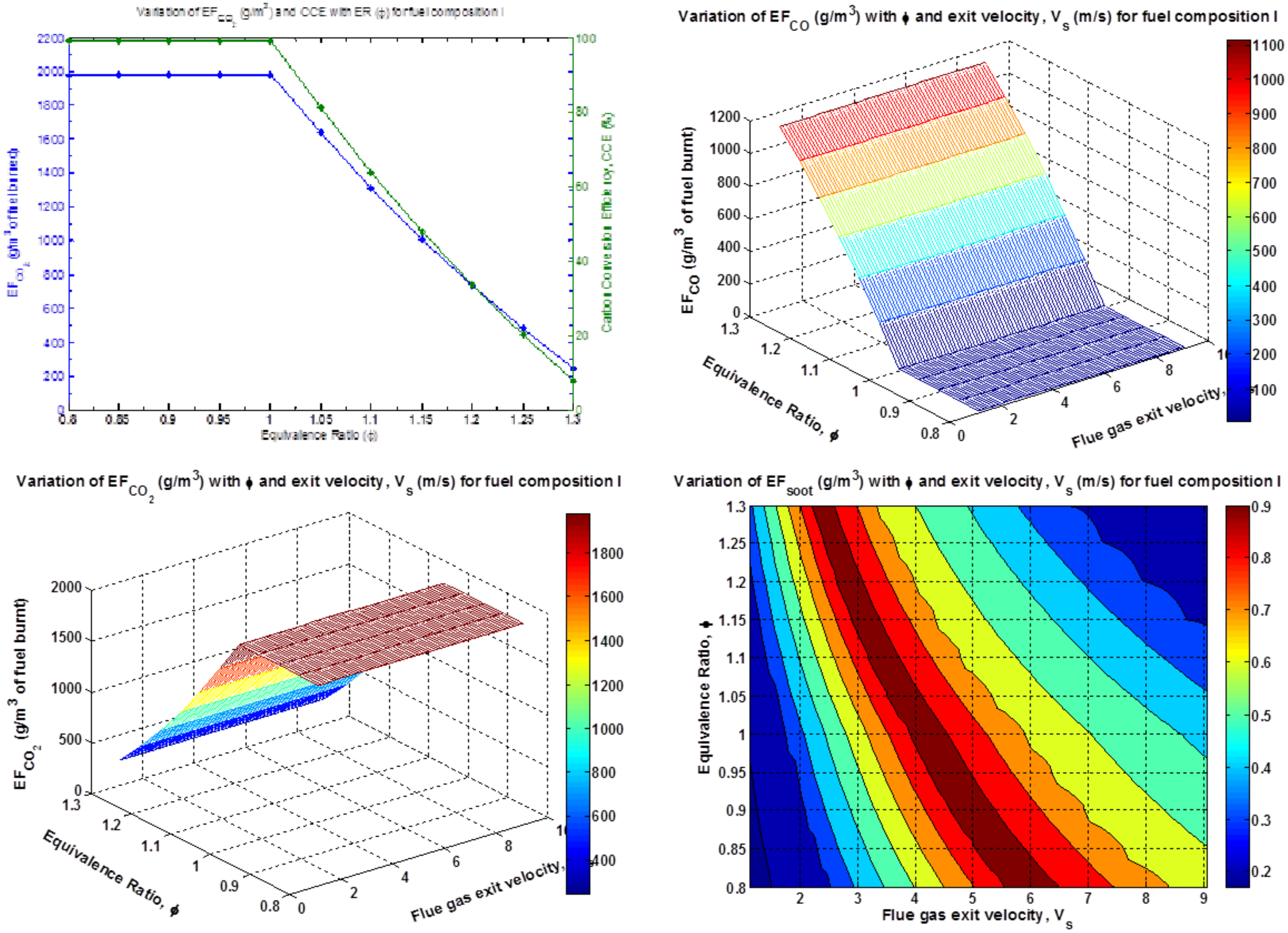

Figure 3.5: Variation of CCE, CO, CO$_2$, and soot yields with ϕ and flue gas exit velocity for fuel composition I

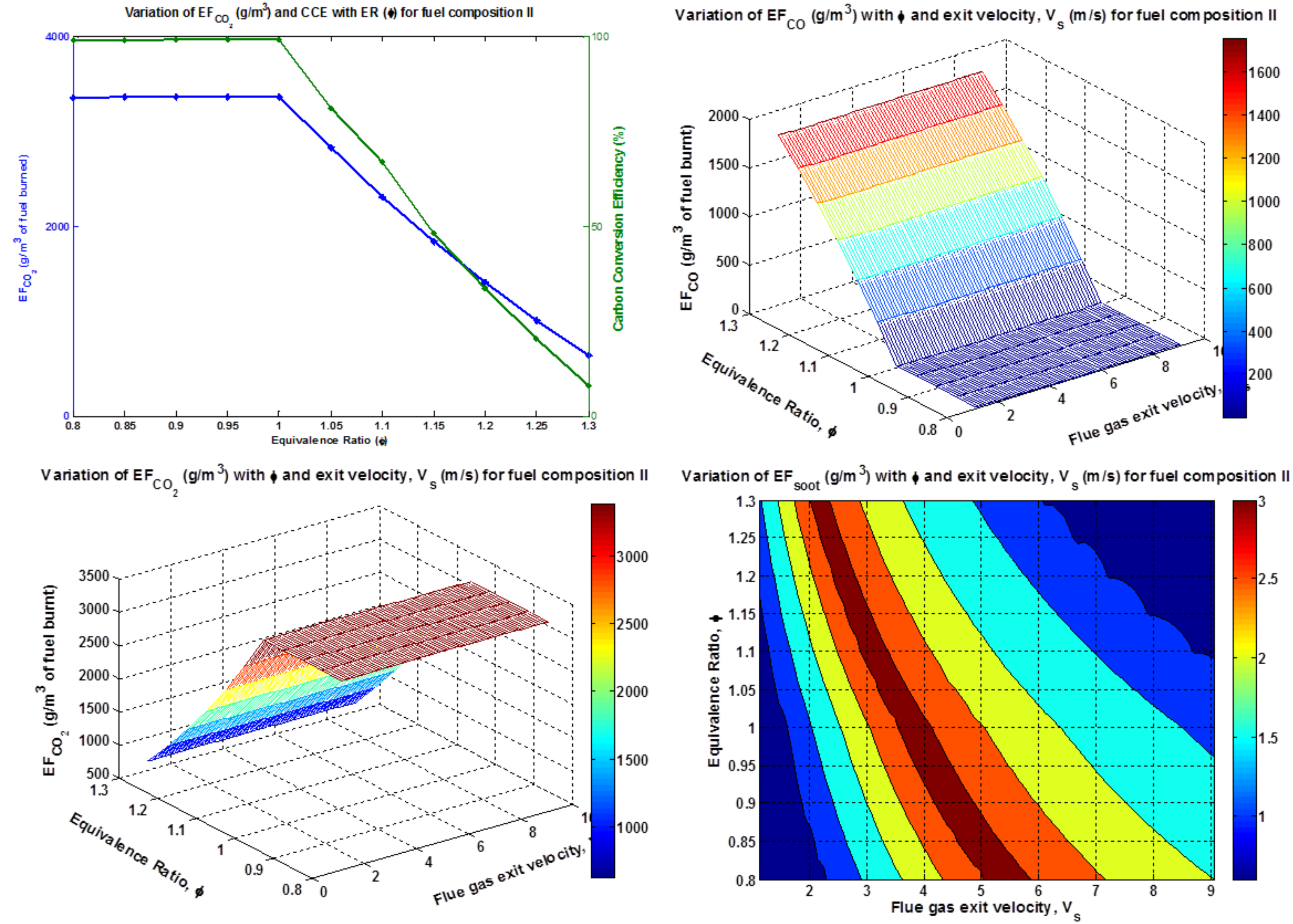

Figure 3.6: Variation of CCE, CO, CO$_2$, and soot yields with ϕ and flue gas exit velocity for fuel composition II

3.5 Limitation of the model

To generate emission factors (EFs) of carbon-containing emissions, the model requires the composition of the fuel gas to be supplied. This input (fuel gas composition), in most cases, is not made available by oil and gas companies, a factor that will hamper the use of the model to obtain reliable estimates of gas flaring contributions to atmospheric aerosol loadings on a global scale. Output of the model is only valid between $0.8 \leq \phi \leq 1.3$. Equation (3.5) - (3.10) will not hold outside this range of values of ϕ.

3.6 Conclusion

This work has developed a simple self-consistent technique that takes into consideration the fuel composition and flame dynamics characteristics in estimating the emission factors of carbon-containing emissions from a typical gas flaring process. The dependence and variation of pollutant emissions on fuel gas composition, fuel flow flux, stack characteristics and equivalence ratio, ϕ, were demonstrated using two fuel gases of varying composition – light and heavy fuel. The composition of the fuel gas plays a very prominent role in the nature and quantity of pollutants emitted from the combustion process. The mass-weighted carbon to hydrogen (C:H) ratio is equally another important factor that significantly affects the yield of pollutants.

The estimates from the pre-processor can be further validated and improved by more elaborate field measurements from gas flaring sites rather than lab-based or pilot-scale studies. It (pre-processor) can also be made more accurate when other experimental works can provide similar data to better constrain '*rC*'. Presently, the study by McEwen and Johnson (2012) is the only known study that can be applied directly in our proposed estimation technique. Experimental work that gives soot yield from hydrocarbon, typically alkane, combustion as a function of a combustion (fuel or flame) dynamics parameter is quite suitable for the method proposed here. The pre-processor developed here can find application in the oil and gas industry. It can support the work of environmental officers in the oil and gas industry to estimate pollutants emission for the combustion of associated gas, especially in typical flares.

Chapter 4

Atmospheric dispersion of gas flaring emissions in the Niger Delta: Impact of prevailing meteorological conditions and flare characteristics

4.1 Abstract

An understanding of the dispersion and level of emissions source of atmospheric pollutants, whether point, area or volume sources, is required to inform policies on air pollution and day-to-day predictions of pollution level. Very few studies have carried out simulations of the dispersion pattern and ground-level concentration of pollutants emitted from real-world gas flares. The limited availability of official data on gas flares from the oil and gas industries makes accurate dispersion calculations difficult. Using ADMS 5, this study assessed the sensitivity of dispersion and ground-level pollutant concentrations due to gas flares to: prevailing meteorological condition; fuel composition; and flare size. Although, the ground-level concentrations of pollutants, inland, are lower, the dispersion of pollutants is towards both the inland and coastal communities during the non-WAM months (December and January). In the WAM months, the ground-level concentrations of the pollutants are

higher and are dispersed predominantly over the inland communities. Less buoyant plumes from smaller flares (lower volume flow rates) and/or flaring of fuel with lower heat content results in higher ground-level concentrations closer to the flare. Considering the number of flares scattered around the region, a mitigation of the acute local pollution would be to combine short stacks flaring at lower volume flow rates to enhance the volume flow rate of a single exhaust, and hence, the buoyancy of the plume exiting the stack.

4.2 Introduction

With an estimated daily production of 2.7 million barrels, Nigeria is currently ranked 12th on the list of crude oil producing nations of the world (OPEC, 2015). In Nigeria, the exploration and exploitation of crude oil has brought serious degradation to the environment of the oil producing communities and air quality of the West Africa sub-region (Ana et al., 2012; Anomohanran, 2012; Dung et al., 2008). The Niger Delta, the oil producing region of Nigeria, contains over 300 active flare sites (Elvidge et al., 2015) scattered around residential communities and farm lands, where over a quarter of the total natural gas production in the oil-rich country is flared annually (Fawole et al., 2016b; Ite and Ibok, 2013). In 2008, about 15.1 billion cubic meter (bcm) of natural gas is estimated to have been flared in the region (Elvidge et al., 2009). Remoteness of exploration sites, non-availability of market, and inadequate piping to transport the gas are some of the reasons responsible for the continuous and persistence of gas flaring in the region. Gas flaring is a prominent source of carbon monoxide (CO), carbon dioxide (CO_2), NO_X (NO+NO_2), Soot (predominantly black carbon (BC)) and poly aromatic hydrocarbon (PAH) (Ana et al., 2012; Johnson et al., 2013; USEPA, 2011, 2012).

The geometry of the flares - height, inclination and diameter - differs from one flow station to another. These geometries play a prominent role in the dispersion of emission from these flares (Turner, 1994; Zannetti, 2013). Emissions from high temperature combustion processes, such as power generation, industrial facilities and gas flaring have much higher release temperatures compared to the ambient air. On their release from their stacks, these high temperatures make them highly buoyant. The combined effect of both the buoyancy and momentum of emissions from the stack causes the plume to rise above the initial height of the stack and enhances near-source dispersion (Arya, 1999). Due to their unique nature and feature, dispersion of emissions from this class of emission source (buoyant) is treated differently from passive non-buoyant sources (MoE Ontario, 2009).

The composition of gas flared varies significantly from one flow station to another. These varying compositions play prominent roles in the combustion parameters of the gas (Fawole et al., 2016b). Combustion parameters such as heat content, net heat released, buoyancy flux and momentum flux are major determinants of the plume rise and, hence, the dispersion pattern and trend of emissions from gas flaring stacks.

Prevailing meteorological conditions are of utmost importance in the dispersion of emission from any emission sources. Wind speed, wind direction and atmospheric stability play greater roles in the advection and dispersion of emission in the plume releases whether buoyant or non-buoyant plumes (Arya, 1999; Zannetti, 2013). The West Africa region, and hence, the Niger Delta, witnesses strong reversal of wind directions as a result of the movement of the intertropical convergence zone (ITCZ) and intertropical front (ITF) (Sultan and Janicot, 2000, 2003). The West African Monsoon (WAM) months (April – September) are characterised by rainfall and prevailing south-westerly winds while the non-WAM months (November – March) are often extremely dry months characterised by the Harmattan and prevailing North-easterly winds (Marais et al., 2014).

Atmospheric Dispersion Modelling System (ADMS) is a robust state-of-the-science Gaussian dispersion model developed by the Cambridge Environmental Research Consultant (CERC) and recommended by the United state Environmental Protection Agency (USEPA). ADMS, in addition to AERMOD, is one of the most widely used dispersion models within the environmental science community. AERMOD (AMS/EPA Regulatory Model) is developed by

AERMIC (American Meteorological Society (AMS)/United States Environmental Protection Agency (EPA) Regulatory Model Improvement Committee). It is a steady-state plume model designed for short-range (up to 50 km) dispersion of air pollutant emissions from stationary sources. ADMS has been used to simulate the dispersion of pollutants and validated across varieties of atmospheric condition, terrains and emission conditions (Carruthers et al., 1997; Connan et al., 2011; Heist et al., 2013). ADMS uses Monin–Obukhov similarity to define the structure of the planetary boundary layer and then computes the steady state Gaussian solutions to describe the diffusion of pollutants (Heist et al., 2013).

In order to monitor levels of air pollutants in ambient air, estimate pollutants concentration downwind of emitting sources and carry out several regulatory processes, atmospheric dispersion models are used to simulate the dispersion of pollutants from their sources. In this study, using ADMS 5, we investigate the impact of prevailing meteorology during the peak periods of the WAM and non-WAM months, flare size and fuel compositions on the dispersion of emissions from gas flares in the Niger Delta area of Nigeria. As well as establishing typical dispersion characteristics for Nigerian gas flaring, the study discusses possible mitigation options for the most acute local pollution.

4.3 Study Area

The Niger Delta, situated in the southern part of Nigeria, is bordered by the Gulf of Guinea on the South and located between 4.3 – 7.7^o N and 4.4 – 9.5^o E. All the oil exploration and exploitation facilities in Nigeria are located in the Niger Delta. More than 900 active oil wells (Osuji and Onojake, 2004) and over 300 active flares are scattered around the region (Elvidge et al., 2015). According to 2009 estimates, the region's 75,000 km^2 landmass is occupied by about 31 million people (Young, 2013). Figure 4.1 shows the Niger Delta region and the location of active flare scattered around the region. Of the 325 active flare sites identified in the Nigeria oil field in 2012 by Elvidge et al. (2015), 97 ($\sim$ 30 %) rank among the top 1000 largest flares of the 7467 individual flares identified globally. In the study area, gas flaring

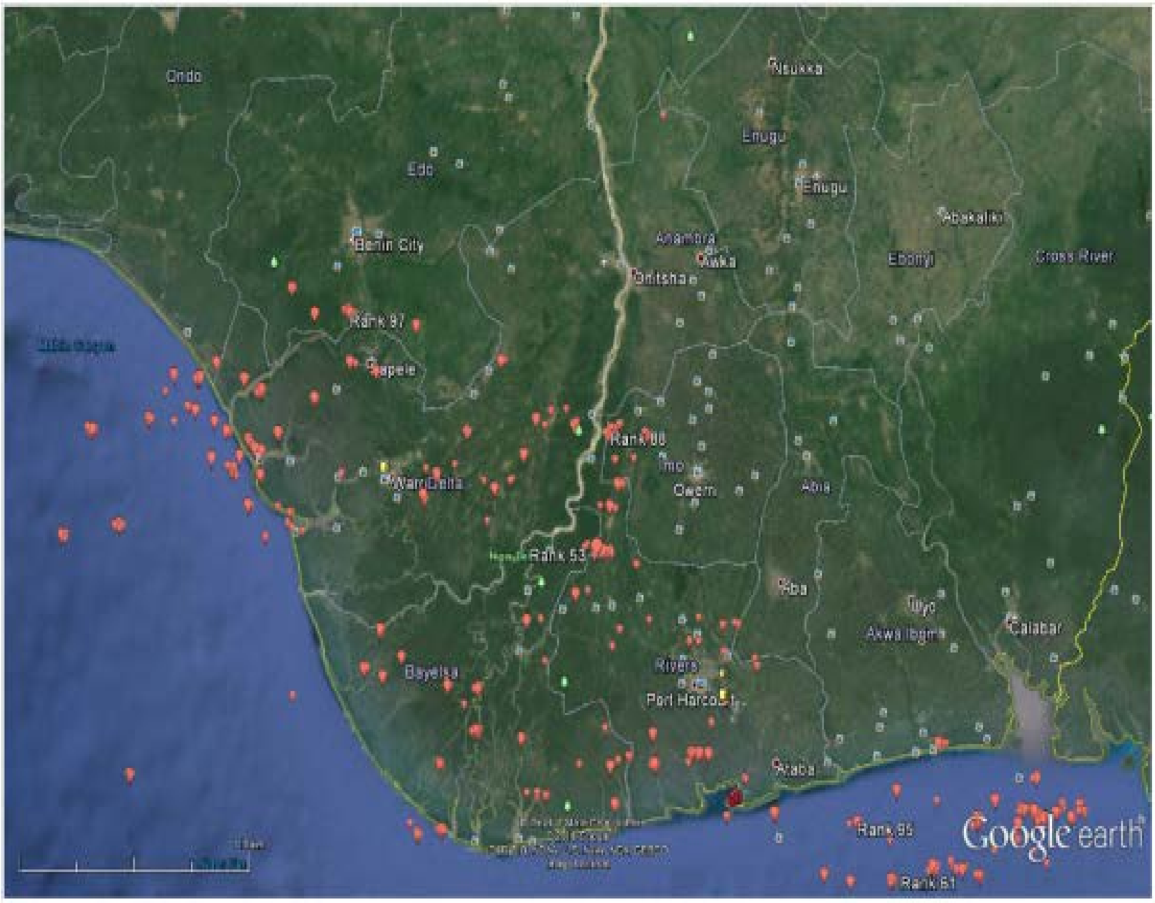

Figure 4.1: Google Earth imagery showing the Niger Delta. Red place-marks shows active flares (KML data for the flare locations are obtained from (Elvidge et al., 2015))

activities has been a persistent daily activity in the several flow stations and rigs from the inception of oil exploration over four decades ago.

4.4 Experimental design and methodology

4.4.1 Meteorological parameter

During the non-WAM months, the prevailing wind in the region is the north-easterly wind while the south-westerly winds prevail during the WAM months. Due to the non-availability of adequate in-situ ground measured hourly meteorological data (wind speed, wind direction, cloud cover and relative humidity) in the Niger Delta, Automated Surface Observing System (ASOS) data (NOAA, 1998; Yang et al., 2016) from a nearby airport in Cotonou, Benin, where sufficient hourly meteorological data needed for studies such as this is readily available, is used for the simulations. For days when data are available at the Lagos airport, there is a significant correlation between data at the two sites (that is, Lagos and Cotonou).

4.4.2 Combustion parameters estimates

Simulating the dispersion of emissions from high temperature sources such as gas flares requires adequate parameterization of the plume rise (Leahey and Davies, 1984; MoE Ontario, 2009; USEPA, 1995b). The following combustion parameters were computed using widely accepted methods available from literature: (a) net heat release rate, H_r; (b) plume rise, Δh; (c) buoyancy flux, F_b; (d) momentum flux, F_m; (e) effective diameter, D_{eff}.

$$H_r = \dot{m} \sum_{i=1}^{n} f_i \, H_i (1 - F_r) \tag{4.1}$$

(Beychok, 2005)

$$\Delta h = 4.56 \times 10^{-3} \left(\frac{H_r}{4.1868} \right)^{0.478} \tag{4.2}$$

(Beychok, 2005)

$$Effective\ stack\ height = H + \Delta h \tag{4.3}$$

$$F_b = \frac{g H_r}{\pi C_p \rho_\infty T_a} \tag{4.4}$$

(MoE Ontario, 2009)

$$F_m = \frac{u_e H_r}{\pi C_p \rho_\infty (T_s - T_a)} \tag{4.5}$$

(USEPA, 1995b)

$$F_b = g u_e {R_s}^2 \left(\frac{T_s - T_a}{T_s} \right) \tag{4.6}$$

Equating the buoyancy flux from the flare (hot source) (Equation 4.4) to general buoyancy flux equation (Equation 4.6), while keeping other stack parameter constant yields the effective stack diameter, D_{eff} (m):

$$D_{eff} = 0.1066\sqrt{\frac{T_s}{T(T_s - T_a)} . \frac{H_r}{u_e}} \tag{4.7}$$

Although the fraction of heat loss depends on the combustion condition of the flare, we have, as recommended by the Alberta Environmental Agency (Alberta Environment, 2003), assumed a heat loss fraction of 25 %. The heat content of the fuel is calculated from the enthalpy of formation of its constituent alkane species and then reduced by 25 %. The net heat released by a typical gas flared in oil and gas fields across the globe varies significantly due to the large variation in the composition of natural gas from one field to another.

4.4.3 ADMS set-up

The flaring scenario is set-up in ADMS as a buoyant plume point source with the supply and enabling of the source efflux parameters - buoyancy flux (F_b) and momentum flux (F_m) - option as alternatives to the velocity, volume flow rate or mass flux option. The stack downwash option is also switched off because of the high upward momentum of the plume (CERC, 2012). The flares were then located on the shapefile map in ArcMAP 10.2 using their co-ordinates. As given in Table 4.1, the diameter and height of flare used are 0.75 ma and 30 m, respectively. No background concentration was given in the input file as these were not available for the sites. An area of 80 x 85 km was used as the output grid size with a resolution of 2 x 2 km (approx.). Hourly meteorological data (wind speed, wind direction, cloud cover, and ambient temperature) were obtained from the Automated Surface Observing System (ASOS) meteorological dataset (NOAA, 1998) for Cotonou airport. The height of the meteorological data and surface roughness was given as 10 m (NOAA, 1998) and 0.2 (agricultural area) (CERC, 2012). Long-term avergaes of carbon monoxide and BC are simulated for the period and conditions on interest.

4.4.4 Emission factors

In this study, the dispersion of particulate (black carbon, BC) and gaseous (carbon monoxide, CO) emissions from typical gas compositions and flare conditions in the Niger Delta area of Nigeria is simulated. Emission factors of 1.6 gm^{-3} (Stohl et al., 2013) and 0.0067 $kg.kg^{-1}$ (EEMS, 2008) is used for black carbon (BC) and carbon monoxide (CO), respectively. The dispersion of other pollutants that are chemically passive on the timescale of plume dispersion (e.g., CO_2, SO_2, PAH) will scale linearly according to the ratio of their emission factors to that of CO.

$$Emission\ rate\ (gs^{-1}) = A \times EF \times \left(1\ -\ \frac{Eff}{100}\right) \tag{4.8}$$

(USEPA, 1995a)

where: A - activity rate (in this case, the fuel volume flux ($m^3 s^{-1}$)

Eff - emissions reduction efficiency (%)

The flare efficiency is assumed to be 75 %, the upper limit of the 68±7 %, suggested by Leahey et al. (2001) in their study to assess the efficiencies of flares.

4.4.5 Experimental variables

The model runs in ADMS were set up to assess the impact of the prevailing meteorology, fuel composition and flare capacity (in terms of volume flow flux) on the dispersion pattern and variation of ground-level concentrations of typical flares in the Niger Delta.

4.4.5.1 Prevailing meteorology during WAM and non-WAM months

The range of the wind speed in the Cotonou airport dataset is 3.0 – 5.7 $\mathrm{m\,s^{-1}}$ and 1.2 – 4.2 $\mathrm{m\,s^{-1}}$ during the WAM and non-WAM months, respectively. The relatively high mean wind speed during the WAM months is attributable to sea-breeze from the Gulf of Guinea. Figures 4.2 - 4.4 shows some of the wind roses of the non-WAM (DJF) and WAM (JJA) months considered in this study. The wind direction during the WAM months is predominantly south-westerly while in the non-WAM months, they are southerly, northerly and north-westerlies.

To assess the impact of meteorological variables on the dispersion of gas flaring emissions, the dispersion pattern and ground-level concentrations of CO and BC, for real-world flares in the Niger Delta during the months of July and August, and December and January, which are the peaks of the WAM and non-WAM seasons, are considered.

4.4.5.2 Flare capacity (flow rate)

Two (one large and one small) flares in the study area were considered in this study. Globally, these flares are ranked 53 ($5.25^oN, 6.60^oE$) and 363 ($5.24^oN, 6.62^oE$) out of the over 7000 active flares identified by Elvidge et al. (2015). For these two flares, the estimated total volumes of gas flared in 2012 are 0.278 and 0.0917 billion cubic meters (bcm) (Elvidge et al., 2015). With the assumption of a constant flow rate, the fuel volume flow rates are 8.815 and 2.908 $\mathrm{m^3\,s^{-1}}$, respectively. The fuel volume flow rate influences the gas exit velocity and rate of heat released, and hence, the buoyancy and momentum flux of the plume.

4.4.5.3 Fuel composition

The composition of natural gas plays significant role in its thermodynamic properties. Although, assumed to be predominantly methane, the composition of natural gas varies significantly across oil fields. Using two very different fuels in terms of composition, and hence, density, the impact of fuel composition on the dispersion of emissions from gas flares is assessed. The emission factor of carbon monoxide (CO) used in this study is given as mass of pollutant per mass of natural gas $\mathrm{kg\,kg^{-1}}$, and as such, the density of the gas affects the CO emission rates. The composition, molar mass and density of the natural gas used are as given in section 3.4.1. Note that the less dense fuel is “sour” – that is, it contains sulphur in the form of H_2S – and so will produce acid gas (SO_2) emissions.

4.4.5.4 Plotting of spatial distribution of emission

The ADMS-ArcGIS link option in ArcMap 10.2 is employed to display ADMS outputs of modelled pollutants as transparent filled contours on map of the region. An area of 80 by 85 km around the flare is used as the output grid in the model set-up.

4.5 Results and discussion

4.5.1 Stack and natural gas parameters used in these simulations

The actual stack height, actual stack diameter, buoyancy flux, momentum flux, effective diameter and effective height used for the two fuel compositions in these simulations are given in Table 4.1.

Table 4.1: Stack and fuel parameters used

	Actual height (m)	**Actual diameter (m)**	**Buoyancy flux $m^4.s^{-3}$**	**Momentum flux $m^4.s^{-2}$**	**Effective height (m)**
Fuel I	30.0	0.75	638.7	137.7	42.8
Fuel II	30.0	0.75	1936.3	1265.5	49.4

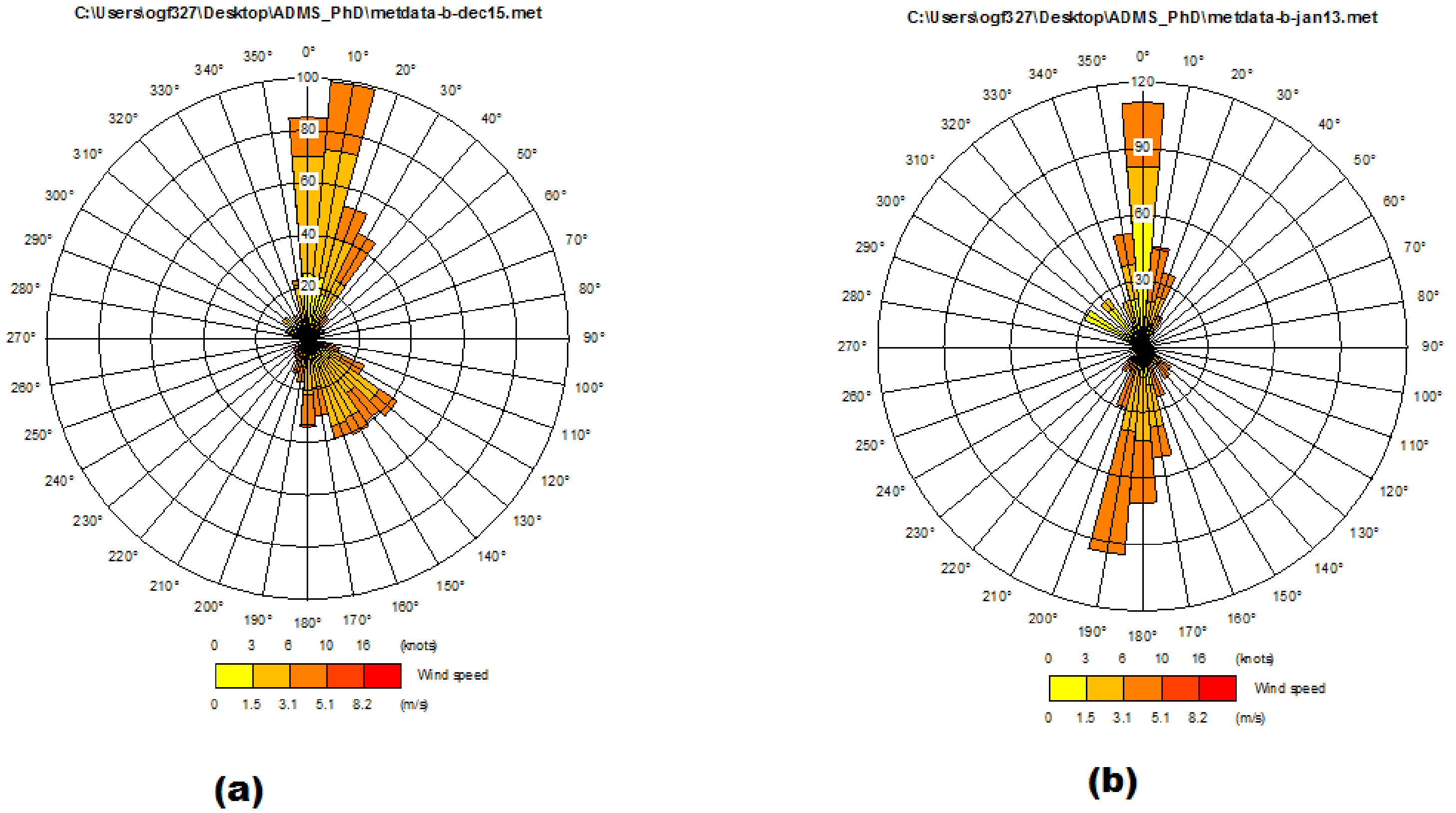

Figure 4.2: Wind roses of wind data during typical (a) December, and (b) January in the region.

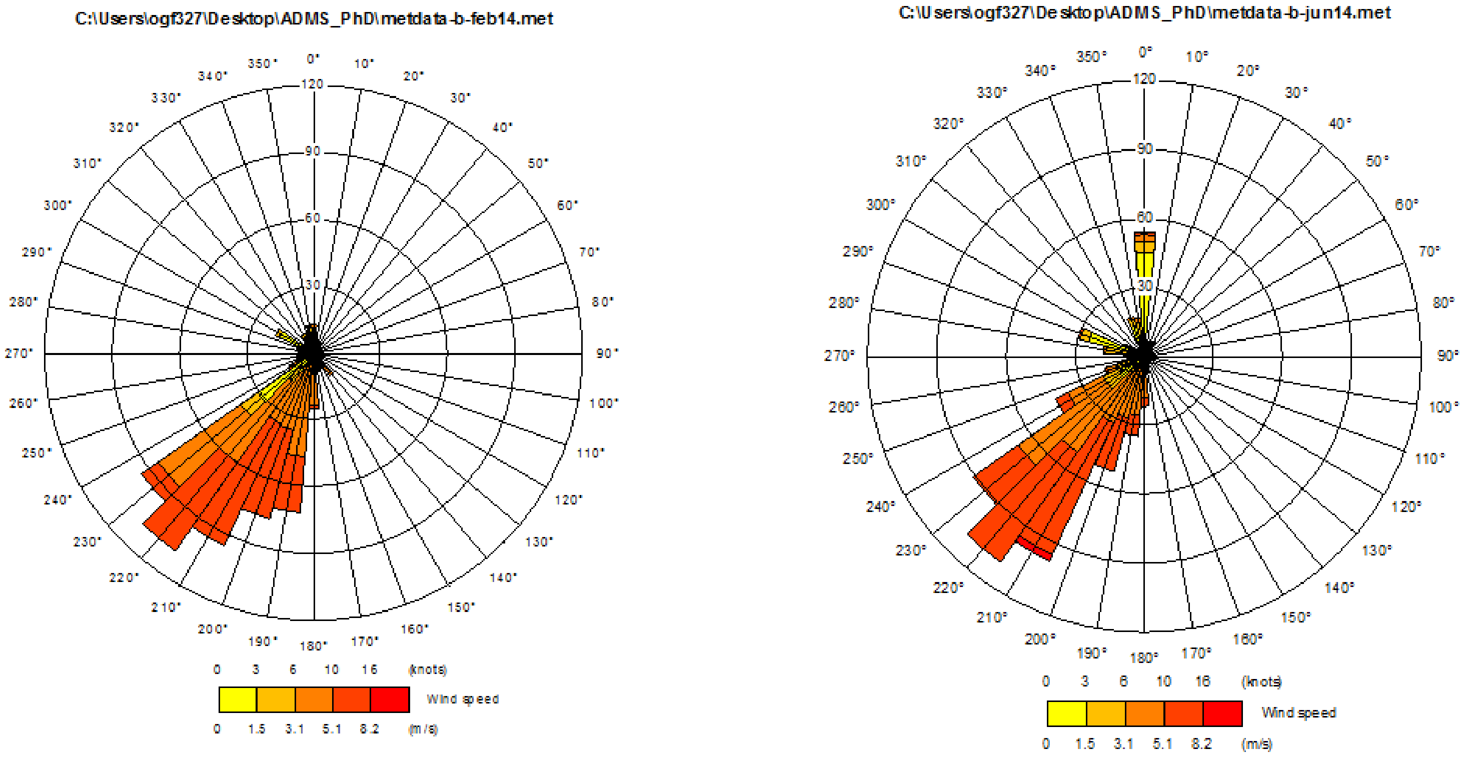

(a) (b)

Figure 4.3: Wind roses of wind data during typical (a) February, and (b) June in the region.

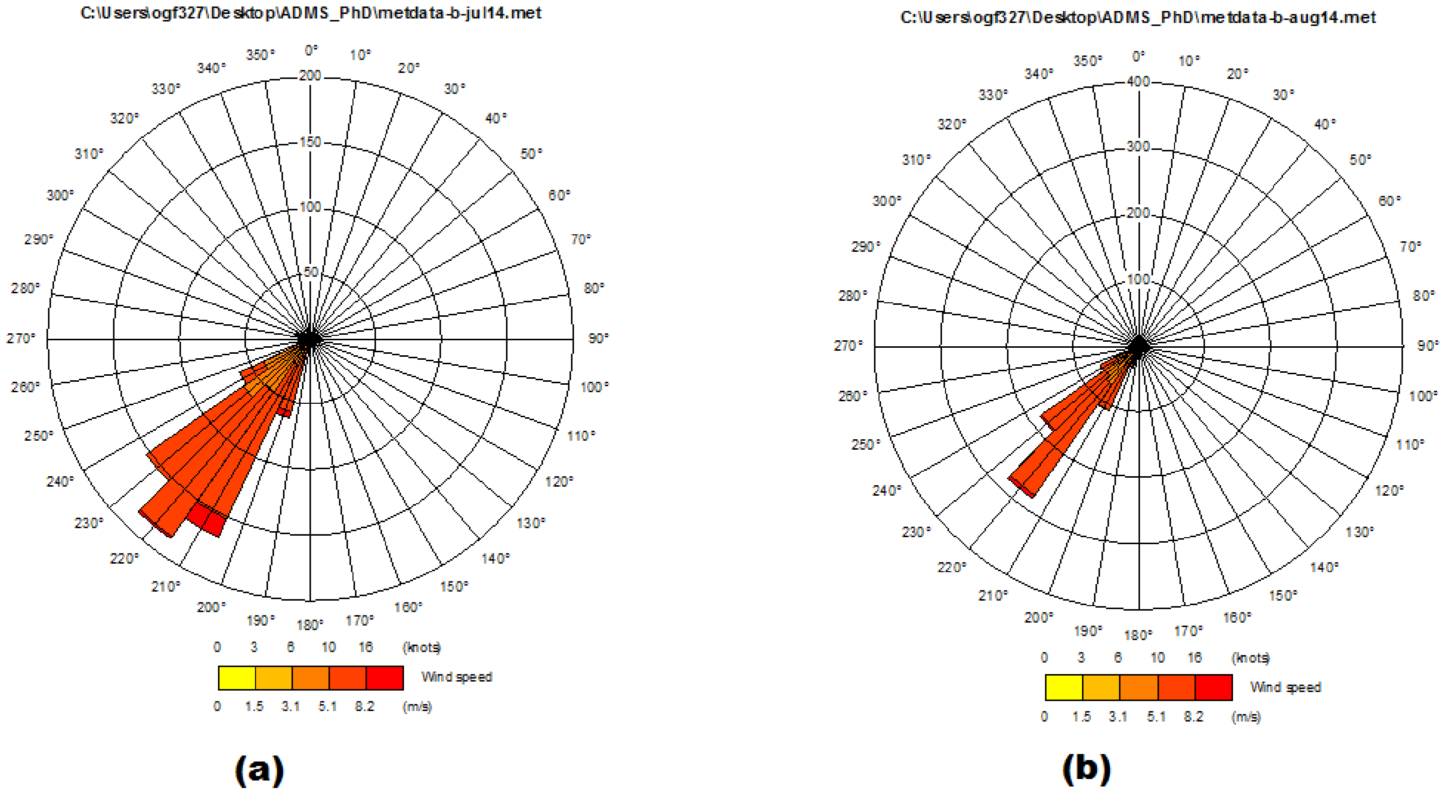

Figure 4.4: Wind roses of wind data during typical (a) July, and (b) August in the region.

4.5.2 Impact of meteorological variables

The impact of the prevailing meteorological variables during the highly distinctive seasons in the region on the dispersion of emissions from gas flaring is modelled for the peak of the WAM and non-WAM months for a two-year period (2014 and 2015). The ground-level concentration and spatial distribution is plotted on a 80 by 85 km grid. The smaller flare with a flow flux of 2.908 $m^3 s^{-1}$ and the less-dense fuel composition was used to study the impact of meteorological variables on pollutants dispersion.

During the non-WAM months, that is, November and December, the dispersion of the emissions is in the direction of both the inland and coastal communities. The ground-level concentration is lesser towards the inland communities but higher over the coastal communities and ocean around the Gulf of Guinea. This pattern of dispersion is very similar for the four non-WAM months modelled. The 90th and 95th percentile of CO and BC monthly mean ground-level concentrations are in the range of 0.09 – 0.15 and 0.16 – 0.20 $\mu g\,m^{-3}$ and; 0.02 – 0.03 and 0.03 – 0.04 $\mu g\,m^{-3}$, respectively. The highest ranges of monthly mean ground-level concentration of CO and BC observed during these months are 0.73 - 1.81 $\mu g\,m^{-3}$ and 0.15 - 0.36 $\mu g\,m^{-3}$, respectively. As presented in the plots of spatial distribution in Figure 4.3, during the non-WAM months, emissions from this stack reaches more communities, albeit at a lower concentrations levels compared to the WAM months (see Figures 4.5 and 4.6). So

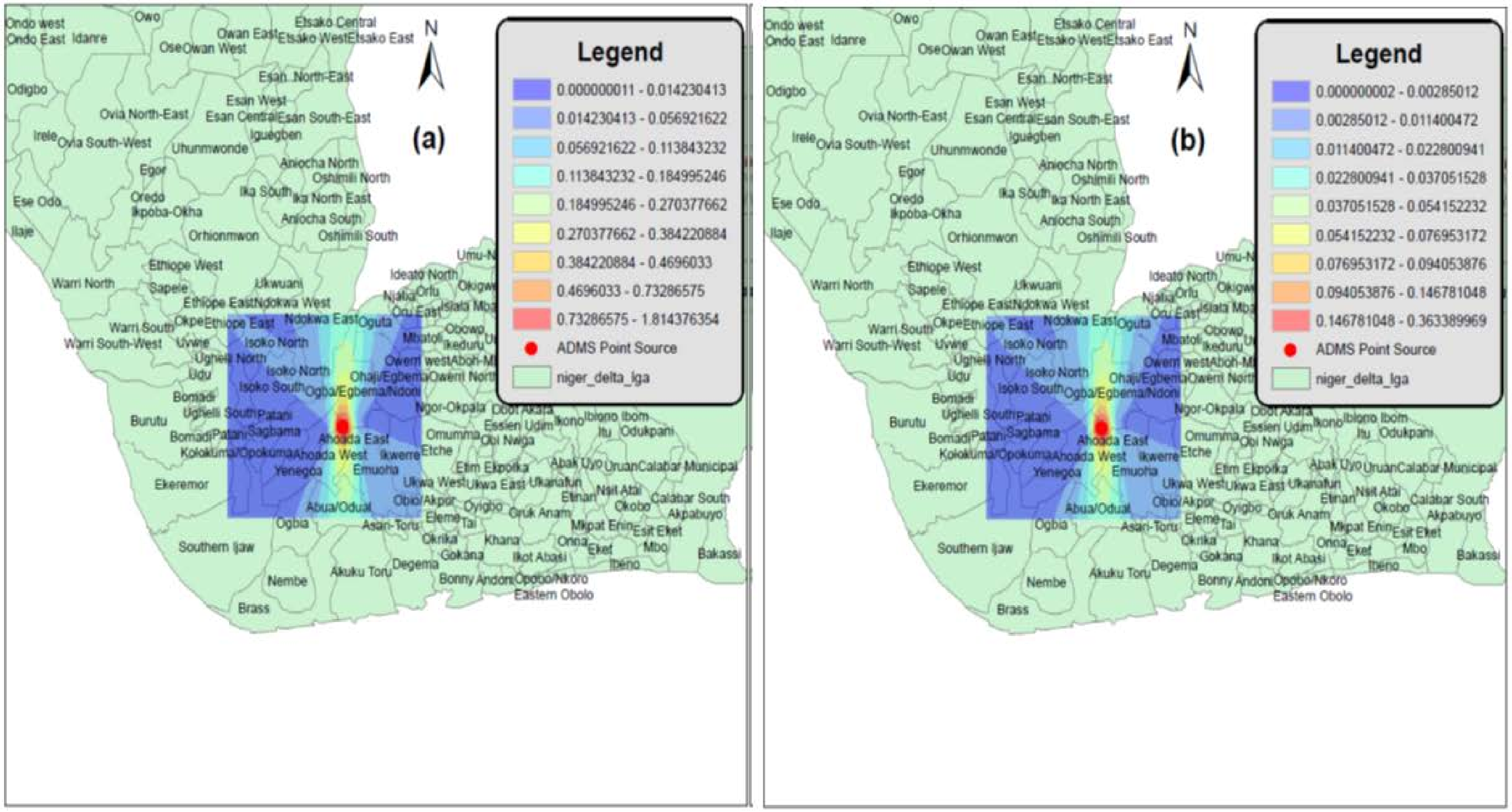

Figure 4.5: Modelled dispersion and monthly mean ground-level concentrations of (a) CO and (b) BC using fuel with lower heat content (fuel I) during a non-WAM months (Jan 2014).

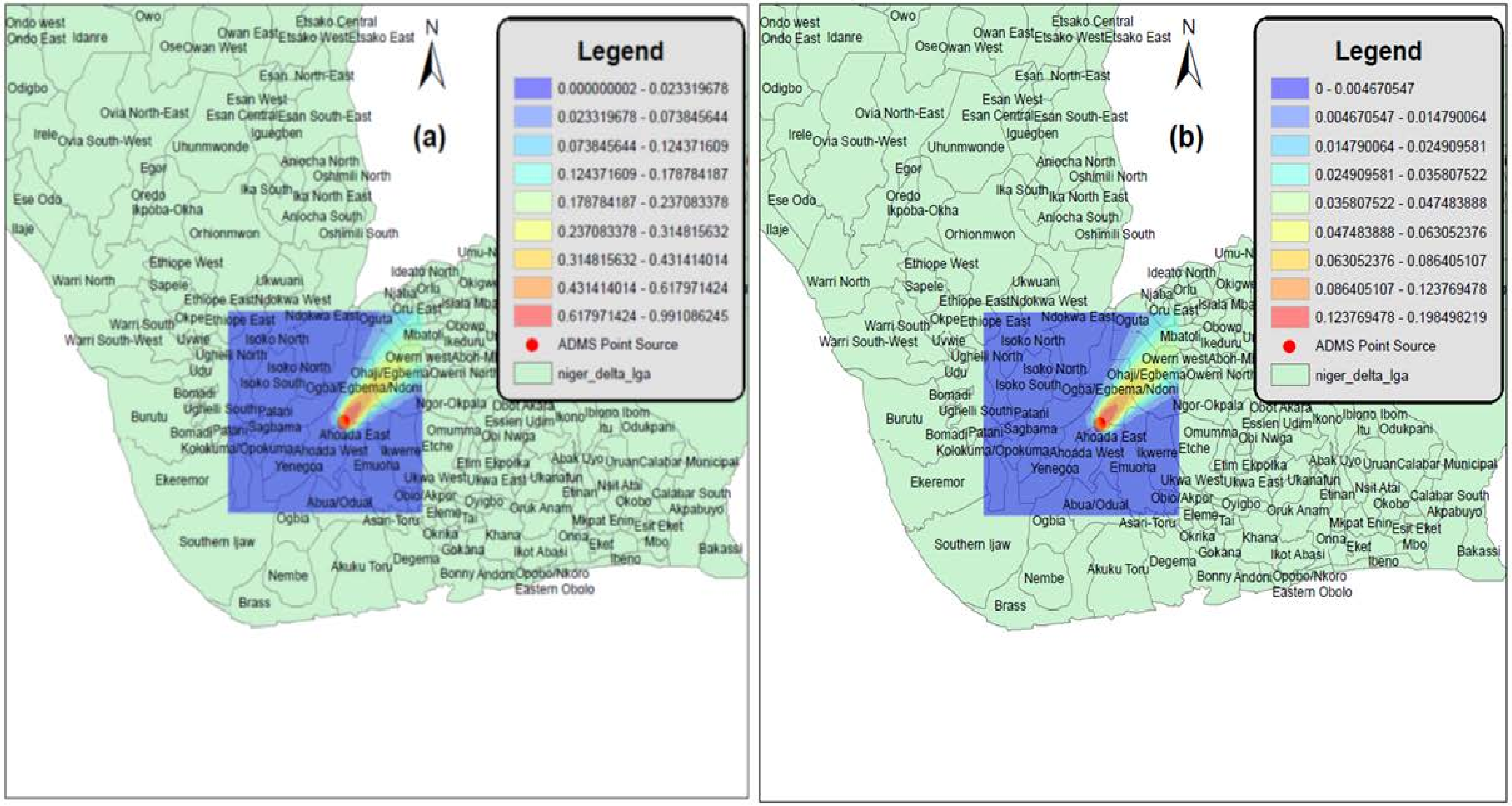

Figure 4.6: Modelled dispersion and monthly mean ground-level concentrations of (a) CO and (b) BC using fuel with lower heat content (fuel I) during a WAM months (Jul. 2014).

there will be higher individual exposures during the WAM months, but greater population dose during the non-WAM months.

During the peak of the WAM months (July and August), emissions are predominantly dispersed over the inland communities where human population is higher. As presented in the plots of the spatial distribution of monthly mean ground-level concentration (Figure 4.6) and the percentiles discussed below, spatial distribution of higher ground-level concentrations is greater during these months owing to the higher wind speeds in the WAM months compared to the non-WAM months (see section 4.4.4.1). The 90th and 95th percentile of CO and BC monthly mean ground-level concentrations are in the range of 0.02 – 0.11 $\mu g\,m^{-3}$ and 0.2 – 0.25 $\mu g\,m^{-3}$ and; 0.02 – 0.04 $\mu g\,m^{-3}$ and 0.04 – 0.05 $\mu g\,m^{-3}$, respectively. The highest range of monthly mean ground-level concentration of CO and BC during these months are in the ranges 0.62 - 0.99 $\mu g\,m^{-3}$, and 0.12 - 0.2 $\mu g\,m^{-3}$, respectively. More plots of spatial distribution of the pollutants, during the WAM and non-WAM months considered are presented in appendix C.

It should be noted that this is just one of the over 300 active flares in the Niger Delta. Where dispersion plumes overlap, the combined ground-level concentration enhancement will be a linear sum of the concentration from each overlapping plume. Results of these simulations show the level and pattern of dispersion during the peaks of the predominant seasons in the region. Considering the number and distribution of flares in the region, the WAM months will be the most severe period of poor air quality around the inland communities in the region. During the non-WAM months, there will be enhanced levels of BC, CO and other greenhouse gases

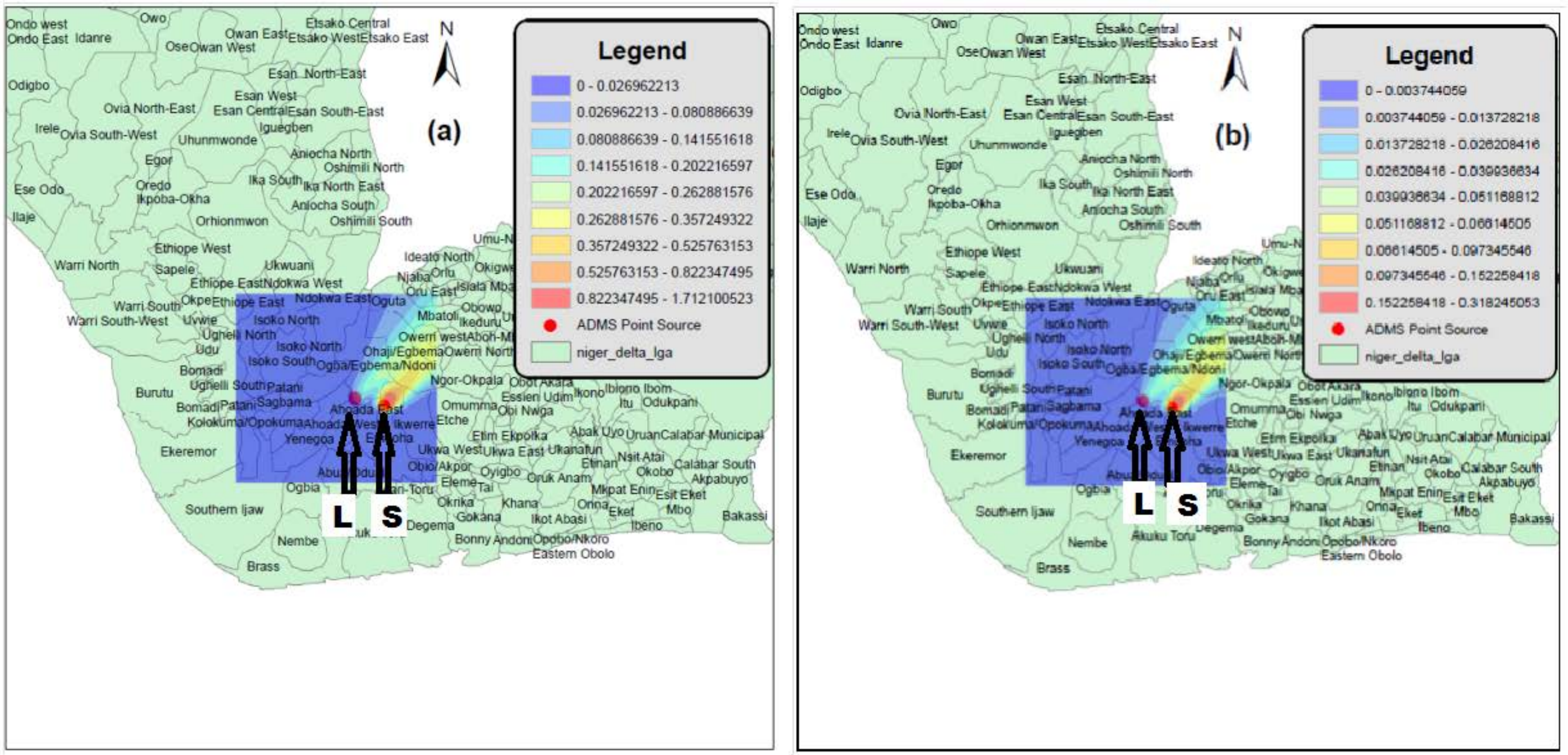

Figure 4.7: Modelled dispersion pattern and monthly mean ground-level concentration for (a) CO, and (b) BC from two flares of different sizes for Aug. 2014. "L" and "S" represent the large and small flare, respectively.

(GHGs) from gas flaring over the Gulf of Guinea, thereby, significantly increasing the aerosol optical depth (AOD) over the ocean around the Gulf of Guinea. The surface reflectance (albedo) over the ocean is highly variant (Jin et al., 2004) and as such, the Earth-atmosphere radiative budget in the region over the ocean might be significantly perturbed during this period due to elevated level of aerosol loading.

Modelling the flares as a non-buoyant source gives significant difference to the monthly mean ground-level concentrations. For example, for a typical non-WAM month (Jan. 2015), the highest range of monthly mean ground-level concentration of CO and BC are 8.65 - 13.92 $\mu g\, m^{-3}$ and 1.73 - 2.79 $\mu g\, m^{-3}$, respectively. Plots of spatial distribution of the pollutants for a flare modelled as non-buoyant sources is given in the appendix C.

4.5.3 Impact of flare capacity

Flare capacity, that is, the volume flow rate of the fuel $m^3\, s^{-1}$ in the stack, is a determinant of the emission rate $g\, s^{-1}$ of pollutants used in modelling the dispersion of pollutants from a source. The volume flow rate contributes to the magnitude of the buoyancy and momentum flux of the plume as it determines the exit velocity of the fuel into the flame as well as the net heat release rates.

Using the two real-world flares discussed in section 4.4.4.2, the dispersion of CO and BC from two real-world flares of different sizes under the same atmospheric condition was modelled. In Figure 4.7, "L" and "S" represent the large and small flare, respectively.The higher concentration in the tail of the dispersion pattern for the “small” flare (see Figure 4.7) is as a result of the lower buoyancy of the plume exiting the stack. This lower buoyancy is occasioned by the lower exit velocity of the fuel into the flame. The region of higher concentration is also further downwind in the large flare (see Figure 4.7). The highest ground-level concentration of the two flares differs by a factor of about 4.

Instead of flaring gas from short stacks at flow stations with low volume flux, two or more of such flares could be linked up to enhance the volume flow rate and also increasing the stack height, so as to reduce the ground-level concentrations of pollutants. For regions like the Niger Delta were there are a great many flaring stack, the benefits of this merger might be very limited. However, if the plume buoyancy is sufficiently large, as suggested by the difference between the output from flares when modelled as a buoyant and a non-buoyant source (see Figures C.5 and C.6 in the appendix), for some of the stack emissions to penetrate through the inversion at the top of the planetary boundary layer, then ground level concentration might be substantially reduced at the expense of more regional contribution.

4.5.4 Impact of fuel composition

The composition of natural gas flared affects the quantity and dispersion pattern of emissions from real-world flares. It affects the quantity of radiant heat given off, effective height and effective diameter, all of which are essential determinants in the dispersion of emission from the flare. The thermodynamic parameter of the two compositions of natural gas considered in this study is presented in chapter 3 (section 3.4.1). The plume exiting the stack for the fuel with less heat content (less dense fuel) is less buoyant, and hence the ground-level concentrations are higher and the distance downwind at which this higher ground-level concentration is observed, is shorter than that for the fuel with the higher heat content (dense fuel).

Meteorological data for August 2015 is used to study and assess the impact of fuel composition on the dispersion pattern and ground-level concentration of pollutants from real-world flare in the Niger Delta. For the less dense fuel, the 90th and 95th percentile of CO and BC ground-level concentrations are 0.11 and 0.21 $\mu g\,m^{-3}$, and 0.02 and 0.04 $\mu g\,m^{-3}$, respectively. The range of the highest ground-level concentration of CO and BC are 0.62 - 0.92 $\mu g\,m^{-3}$ and 0.13 - 0.19 $\mu g\,m^{-3}$, respectively. For the fuel with the higher heat content (dense fuel), the 90th and 95th percentile of CO and BC ground-level concentrations are 0.05 and 0.1$\mu g\,m^{-3}$, and 0.01 and 0.02 $\mu g\,m^{-3}$, respectively, while the range of the highest ground-level concentration of CO and BC are 0.14 - 0.17 and 0.03 - 0.04 $\mu g\, m^{-3}$, respectively.

Although, the range of highest ground-level concentrations of CO and BC for the two fuel compositions during periods considered in this study varies substantially, their 90th and 95th percentiles of CO and BC ground-level concentrations vary by a factor of about 2. A fact, once again, underpinning the importance of understanding the composition of the gas flared in order to be able to adequately quantify its contribution to ambient aerosol loading.

The emission factor for CO used in this study, as stated in section 4.4.3, is dependent on the density of the fuel. Figures 4.8 and 4.9 shows the plots of the spatial distribution of ground-level concentration of pollutants emitted from the flare for the dense and less dense fuel compositions, respectively. From Figure 4.9, the ground-level concentration within the proximity of the flare is higher than that for the denser fuel composition in Figure 4.8.

4.6 Conclusion

This work assesses the impact of fuel composition, flare size and meteorological parameter on the dispersion and ground-level concentrations of carbon monoxide and black carbon. Although the actual height and diameter of the real-world flares used in this study are not known, we have tried to use values obtained for similar flares in the literature. During the non-WAM months, emissions are dispersed both towards the communities inland and on the coast, though with at lesser concentration level towards in the inland communities compared to the WAM months. Hence, higher individual exposures is experienced during the WAM months, but greater population dose during the non-WAM months. The ground-level concentration around the inland communities is higher in the WAM months. Rather than use shorter stacks to flare gas at flow stations with low volume flow flux, and hence, strongly enhancing ground-level concentration of pollutant, it is suggested that two or more of such stations be linked together to increase the volume flow flux. Increasing the volume flow flux, increases the buoyancy and momentum flux of the plume emanating from such stacks and, thereby, reducing ground-level concentrations.

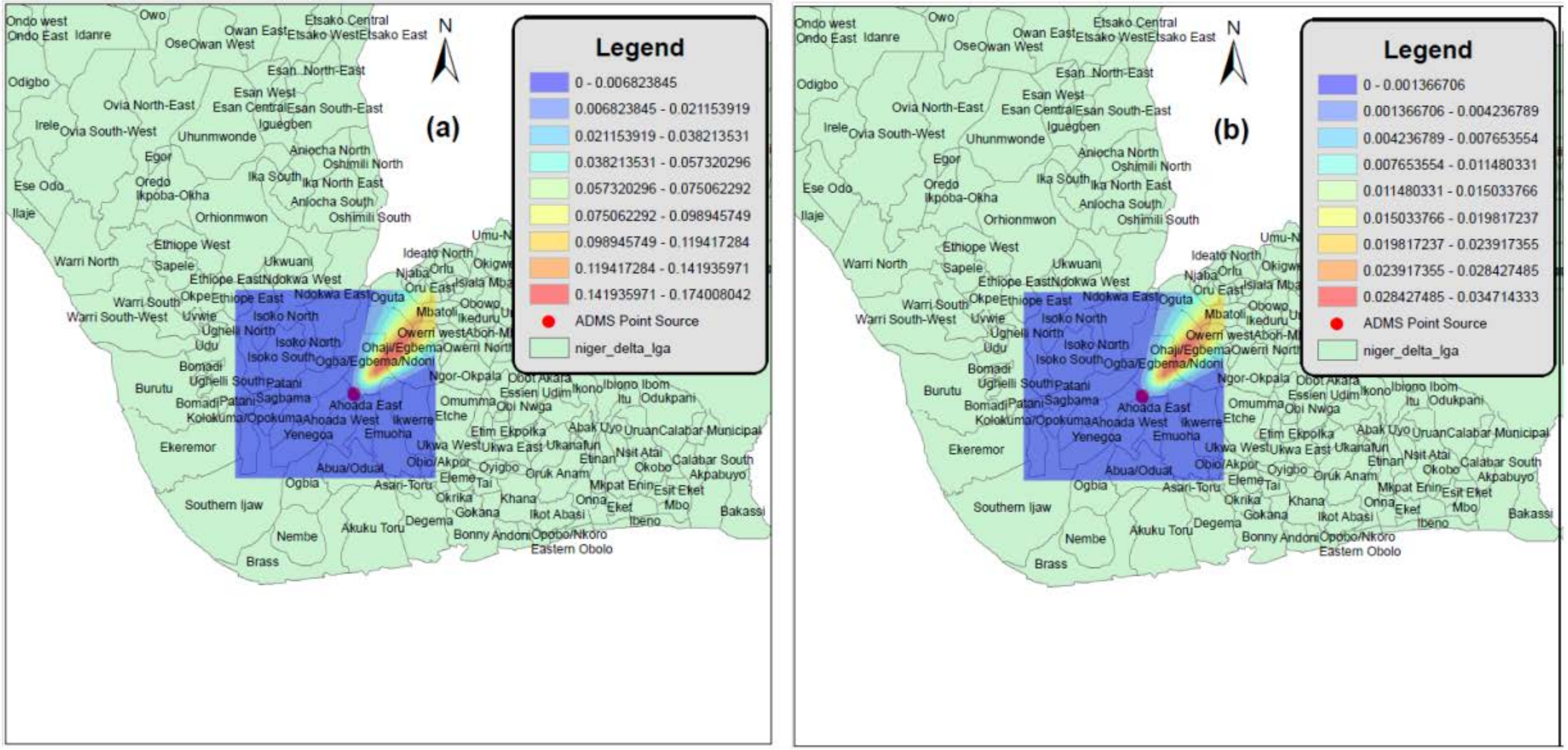

Figure 4.8: Dispersion pattern and monthly mean ground-level concentration of (a) CO and (b) BC for the dense fuel composition.

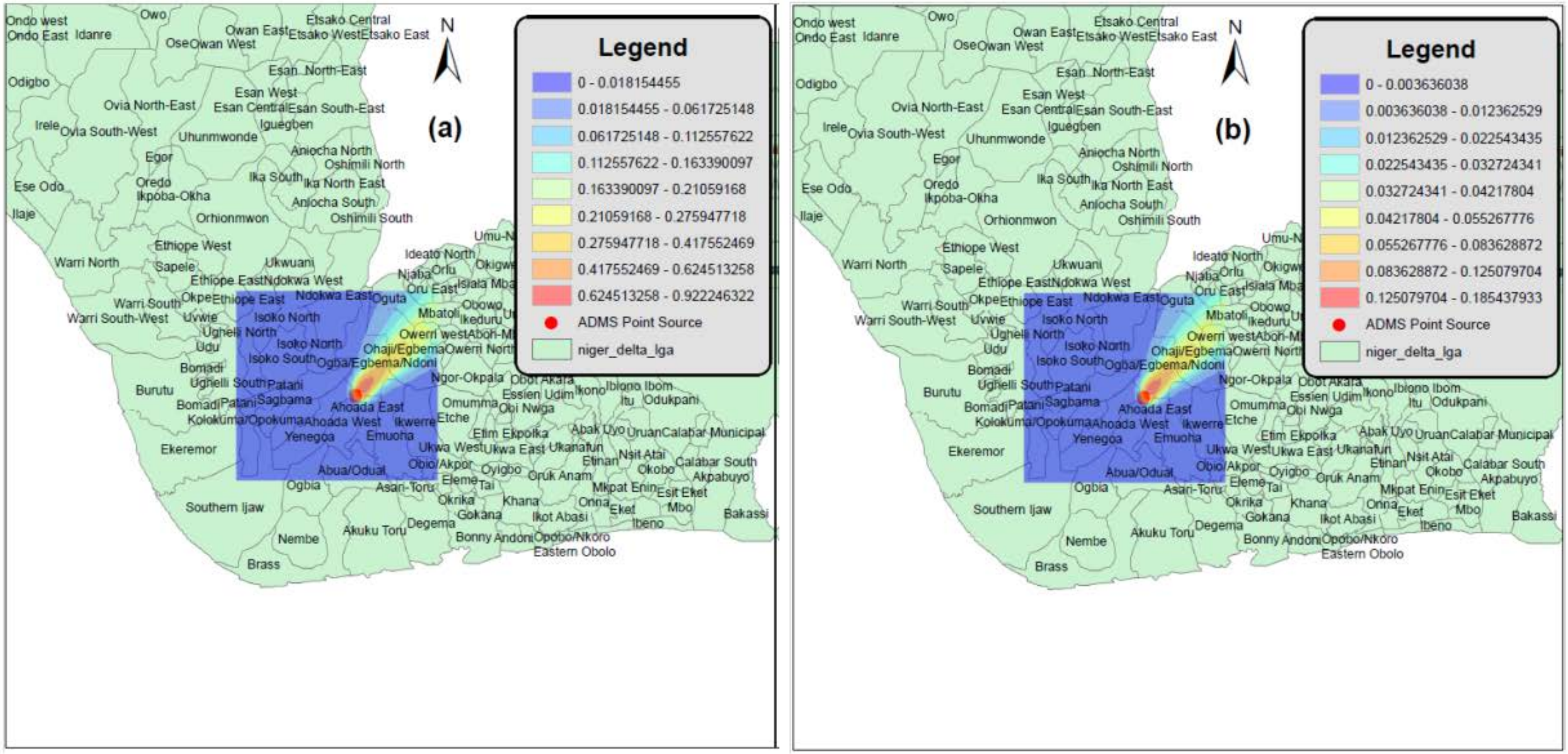

Figure 4.9: Dispersion pattern and monthly mean ground-level concentration of (a) CO and (b) BC for the less dense fuel composition.

Chapter 5

Evidence for a gas-flaring source of alkanes leading to elevated ozone in air above West Africa

5.1 Abstract

As part of the African Monsoon Multidisciplinary Analysis (AMMA) project, the FAAM BAe-146 research aircraft sampled the lower and mid-troposphere around the West Africa sub-region. Back trajectory analysis of the air parcels sampled on-board during the entire duration of the flights showed the history and fate of the air parcels. Data from flights B228 and B231 showed strongly enhanced carbon monoxide and ozone levels attributable to emissions of anthropogenic origin from gas flaring in the Nigeria oil fields and Lagos. The elevated levels of ozone and CO observed at about 6 km above the sea-level on flight B231 were attributed to long-range transport of biomass burning plume from the East, around Sudan. The strongly enhanced mixing ratios of short-chained alkanes and CO (> 400 ppb) observed from measurements on flights B228 and B231 are indicative of natural gas/combustion sources. Flight B222 sampled air parcels strongly impacted by emissions from Lagos but not from the Nigeria oil field and measured relatively lower mixing ratios of ozone, CO and short-chained alkanes species. Results from this study strongly suggests gas flaring emissions

in the Niger Delta area to be a prominent contributor to the enhanced levels of short-chained alkane species observed in Lagos mega-city, especially during the West Africa Monsoon (WAM) months and, hence, a significant source of atmospheric aerosol in the sub-region.

5.2 Introduction

African Monsoon Multidisciplinary Analysis (AMMA), an internationally funded program, was undertaken to enhance our understanding of the West African Monsoon (WAM) and the impact of its variability on the environment, atmospheric chemistry and socio-economy of the sub-region (Redelsperger et al., 2006). The program was designed to run between 2001 and 2009. During the Enhanced Observing Period (EOP) between 2005 and 2007, there were the implementation of specific land-based and sea-based measurements while 2006 was the year of Special Observing Period (SOP) (Lebel et al., 2010). During the SOP, there were intensive surface and air (research aircraft and balloons) measurements.

The FAAM BAe-146 research aircraft made about 19 scientific flights (labelled B215 - B235) during SOP2 between July 17 and August, 17, 2006. Of particular interest in this study are BAe-146 flights that are suggested, by back-trajectories analysis, to have been significantly impacted by gas flaring emissions from the intense flaring activities in the Nigeria oil field, south of the country. Specifically, air parcels sampled on three of the flights (B222, B228 and B231) were suggested to have been impacted by anthropogenic emissions from the south of Nigeria, which compared to the North, is more industrialised and has higher population density. The Niger Delta, the region of intense gas flaring in southern Nigeria, contains over 300 active flare sites (Elvidge et al., 2015) scattered around local communities and farm sites on a land mass of about 70,000 km^2 (Osuji and Onojake, 2004) (see Figure 5.1(d)). The heart of the Niger Delta is less than 300 and 400 km from Lagos (Nigeria) and Cotonou (Benin), respectively. With an average speed of 6 $\mathrm{m\,s^{-1}}$, a common occurrence in the region, emissions from the region of intense gas flaring in the Niger Delta take about 13 and 18 hours to be transported to Lagos and Cotonou, respectively. It should be noted that August marks the peak of the WAM when the Intertropical Convergence Zone (ITCZ) and Intertropical Front (ITF) are northernmost (Sultan and Janicot, 2003). Hence, significant inland transport of emissions is highly favoured.

Pollutants from gas flaring are highly buoyant when exiting the stack due to the exit temperature which could be >1900 K in a typical gas flare in the oil and gas industry. Nigeria, Africa's leading oil exporting country, still flares about a quarter of her annual natural gas production (Ite and Ibok, 2013). In 2006, as a result of an increase in Nigeria's daily oil production quota by the Organization of Oil Producing Countries (OPEC) (OPEC, 2015), there was an increase in the estimated amount of gas flared compared to the preceding years (Anejionu et al., 2015a; Fawole et al., 2016b). The years 2005 and 2006 were years of intensive oil production in Nigeria as a result of the increased quota of production by OPEC, with the achievement of the all-time high daily production in November, 2005. In 2006, the level of air pollution from gas flaring from the Niger Delta was more intense than preceding years due to the level of oil exploration and exploitation (Anejionu et al., 2015b).

In this study, trajectory ensembles associated with different measurement periods on selected AMMA flights were identified and assessed. A 7-day back trajectories along every second of the entire flight periods for flights B222, B228 and B231 was initiated. As a result of the large volume of time for each flight, each flight time was split into two, comprising of about 12000 - 14000 seconds each. An analysis of every second of the flight duration rather than the 10 seconds time steps often used in similar studies in the literature were done because of the highly varying nature of plumes encountered on these flights as indicated by the broad range of the concentration of emissions measured on these flights.

The meteorological condition in the West African region, especially during the WAM is discussed in Section 5.3.1. Section 5.3.2 gives detailed highlights of the selected flight paths and pollutants measurement while Section 5.3.3 discusses the back trajectory calculations for the entire flight duration of the selected flights (B222, B228 and B231) as well as their trajectory density plots. Section 5.4 presents a discussion of results and major findings from the variation of the patterns and mixing ratio levels of the several measurements on-board the flights of interest.

5.3 Methodology

5.3.1 Meteorological condition over the West Africa region

The WAM is characterised by two prominent seasons, the dry (November-February) and the rain (March-October) seasons. Desert dust and biomass burning aerosols are predominant during the dry season while the onset of the WAM brings in the moist south-westerly wind which is associated with rainfall. The meteorological condition over West Africa is significantly influenced by the ITCZ which is the zone of convergence of the trade winds of the two hemispheres. The movement of the ITCZ shifts the belt of planetary winds and pressure systems both northwards and southwards depending on the period of the year. In Coastal area of West Africa, the rainy season is generally observed between April and July, and a second but shorter spell of rainy season in September and October (WMO, 2015). In West Africa, the Sahel and Coastal areas have annual rainfall range of 450 – 1050 mm and 1400 – 2700 mm, respectively.

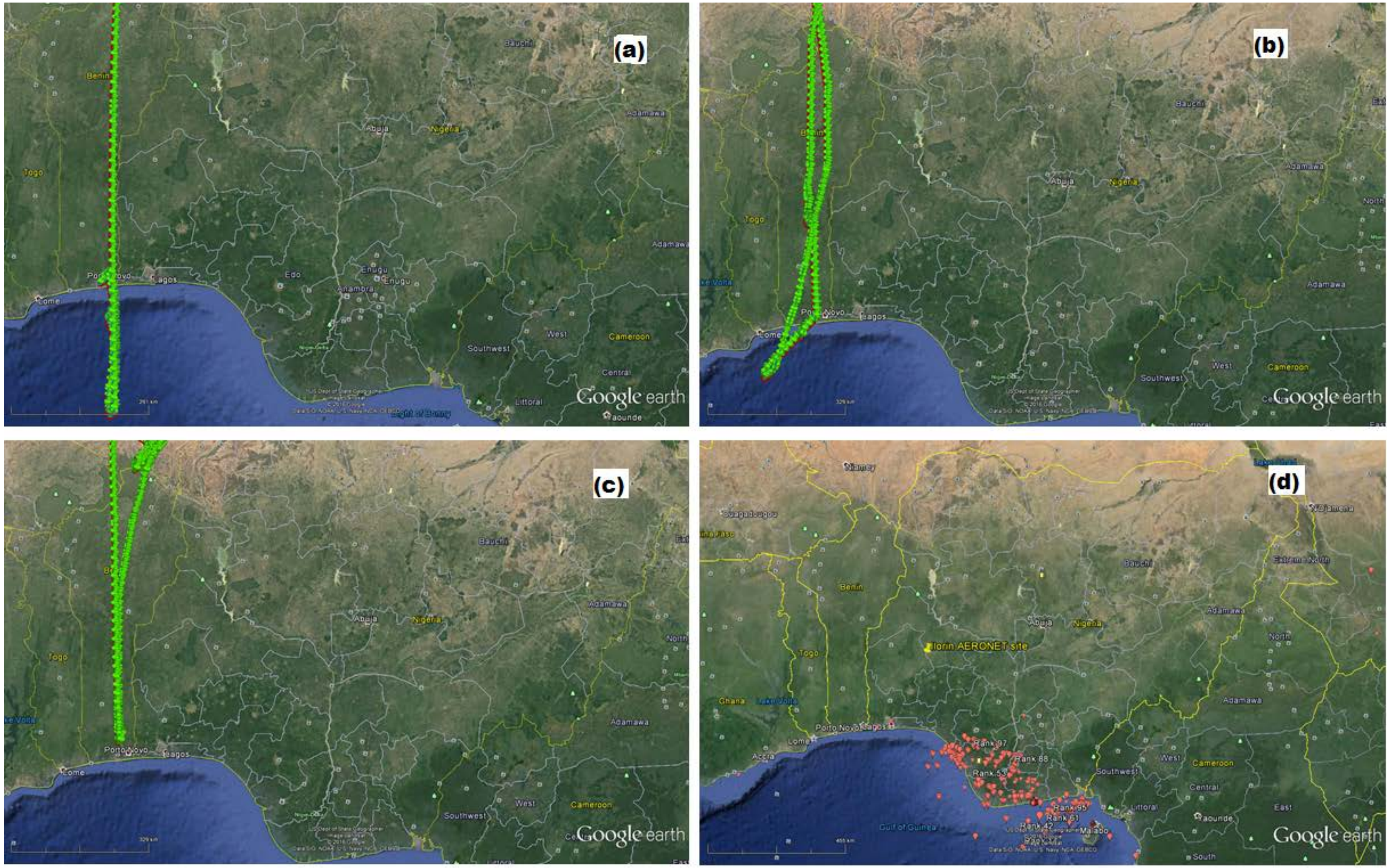

Figure 5.1: Flight track for (a) B228 (b) B231 (c) B222 and (d) active flare sites in the Niger Delta

Table 5.1: Flight details of selected AMMA flights

Flight	Date	Time of flight	Path of flight
B222	July 30, 2006	11:26 - 15:48	13.5 - 6.6^o N 2.4 - 3.4^o E
B228	August 8, 2006	09:41 - 13:34 and 15:09 - 19:10	13.5 - 3.9^o N 2.3 - 2.6^o E
B231	August 13, 2006	07:01 - 11:32	13.5 - 5.1^o N 1.3 - 2.5^o E

In the West Africa sub-region, the shifts of the ITCZ and ITF, to a large extend, control the circulations in the lower troposphere. During the peak of the (WAM) between July and September, the ITCZ and ITF can shift as far as 12^o N and 20^o N, respectively. At this period of the year, there is the formation of mesoscale convective systems (MCS) as a result of the position of the ITCZ and presence of elevated terrains to the east (Mari et al., 2011). Large organised MCS develop on a regular basis during the peak of the WAM enabling the rapid vertical uplift of gases and aerosols to the upper troposphere. During the peak of the WAM in 2006, convective activity resulting from MCS were slightly enhanced (Janicot et al., 2008).

5.3.2 Flight details and measurements

Three AMMA flights came within proximity of getting impacted by emissions from gas flaring emissions from the Niger Delta area. Details of these flights are given in Table 5.1. The flight track is plotted on Google Earth (Figure 5.1(a) - (c)). Flight tracks data are obtained from the British Atmospheric Data Centre dataset (http://browse.ceda.ac.uk/browse/badc/faam/data/2006). Active flare sites data shown in Figure 5.1(d) are obtained from the KML file in the supplementary data of Elvidge et al. (2015).

The FAAM BAe-146 flights involved in this analysis are flights B222, B228 and B231 which took place on July 30, August 8 and 13, 2006, respectively. To have an estimate of the extent of the contributions of the different regions to air parcel sampled, trajectory densities of the air parcels sampled on these flights were generated (see Figure 5.2(a), (b) and (c)). While flights B228 and B231 encountered plumes from the gas flaring region in the Niger Delta and urban plume from Lagos, plumes sampled on B222 were significantly impacted by urban emissions from Lagos but not from the Niger Delta. During AMMA flight campaigns, pollutants measured on several of the scientific flights were attributed to both biomass burning and urban-industrial emissions (Reeves et al., 2010). In the lower and mid-troposphere, at that time of the year (July – August), biomass burning aerosols are mainly due to long-range transport from central and south Africa into the West Africa sub-region; while inland flow and convective uplift of urban-industrial aerosol are enhanced by the positions of the ITCZ and enhanced MCS, respectively.

Observations used in this analysis are mixing ratios of ozone (O_3), carbon monoxide (CO), NO_X ($NO + NO_2$) from the core chemistry payload, and VOCs (alkanes) from the non-core payload (Hopkins et al., 2009; Mari et al., 2011; Reeves et al., 2010). O_3, CO and NO_X were measured using TECO 49 UV photometer, TECO 42 chemiluminescence instrument and Aerolaser AL5002, respectively. The VOCs were collected in canister and then analysed by dual channel PTV-GC-FID, a technique used in the analysis of VOCs in the atmosphere, where their concentrations could be less than 1 pptv (McQuaid et al., 1998). On most of the AMMA flights, single cycles of measurements of the VOCs ranges between 30 - 90 seconds.

5.3.3 Back trajectory calculation

To understand the history of air masses sampled on the selected AMMA flights, 7-day back trajectories were calculated for every second of these flight tracks. The flight durations for flights B222, B228 and B231 are 29390, 29340 and 24012 seconds, respectively. To reduce computing time, the flight data were split into two almost equal parts ((a) and (b)) before the trajectory calculations. For example, the 24012 seconds on flight B321 was split into 12000 and 12012 seconds, and herein referred to as B231a and B231b, respectively. Using the flight data (flight time, longitude, latitude and atmospheric pressure), 7-day back trajectories were calculated using the UK Universities Global Atmosphere Modelling Programme (UGAMP) offline trajectory model (Methven, 1997). This model is driven by six-hourly ERA-Interim (European Centre for Medium-Range Weather Forecasts Interim Re-Analysis) wind analyses data. Three dimensional meteorological data are interpolated to the trajectory locations. For each integration time, values of meteorological fields (temperature, potential temperature and pressure) are assigned as attributes to the particle in the trajectory. A detailed technical description of the UGAMP trajectory model can be found in Methven (1997) and Methven et al. (2001).

The trajectories were plotted using the National Center of Atmospheric Research (NCAR) Graphics/NCL trajectory plotting package, kmapline (Noone and Simmonds, 1999). Plots of the 7-day back trajectory of entire air parcels sampled on the selected AMMA flights are shown in Figure 5.3. The trajectory density plot was done using the trajLevel option in the back trajectory function of the openair package written in the R software (Carslaw and Ropkins, 2012). The trajLevel option in openair considers the number of trajectories (i.e. trajectory frequency) in a particular grid square (Carslaw, 2015).

5.4 Results and Discussions

From the trajectory-density plots of flights B228b and B231b trajectories, more than 25 % of the air parcels sampled on-board both flights had been impacted by anthropogenic emissions from Lagos (green boxes in Figure 5.2) and the oil fields in the Niger Delta area (black boxes in Figure 5.2). The trajectory-density plot of B222 shows that more than 25 % of the air parcel sampled on this flight had been impacted by anthropogenic urban emissions from Lagos while less than 1 % had been impacted by emissions from the oil fields in the Niger Delta. Figure 5.2 shows the trajectory-density plots for the b portions of the three flights considered in this study. The b portions of the flights have been considered because those were the portions of the flights that came within proximity of emissions from either Lagos or the Niger Delta region.

Using the trajectory density plots, the extent of the contributions of different region to aerosol loadings in air parcels sampled can be quantified. The b portions of the selected flights were chosen because at some time during the flight air parcels sampled during these stretches of the flight were suggested to have been impacted by emissions from the oil fields in Niger Delta and urban emissions from Lagos. Elevated concentrations of carbon monoxide, ozone and alkane were observed during these portions of the flights.

5.4.1 Case study I: Flight B228

Flight B228 took place on August 8, 2006 during the SOP 2 phase of the AMMA campaign in West Africa. The flight was from Niamey (Niger) to Cotonou (Benin), and then to Lagos to map emissions around the city. Figure 5.4 presents the plots of the mixing ratio of alkanes, carbon monoxide (CO), ozone, NO_X against flight time, and 7-day back trajectory at flight times with elevated measurements of these pollutants. Significantly enhanced CO and alkanes mixing ratios are indicative of fossil fuel combustion (De Gouw et al., 2004). Short-chain alkanes ($C_3 - C_6$) have been use as indicators of fossil fuel combustion as they are less common from biomass burning sources (Seila et al., 1989). Volatile organic compounds such as cyclopentane and cyclohexane in ambient air have been strongly linked to gas flares, oil refineries, and natural gas sources (Gilman et al., 2013; Liu et al., 2008; Sanchez et al., 2008). The ability of an air mass to form ozone is strongly dependent on the ratio of NO_X to non-methane hydrocarbon (NMHC) it contains (Seinfeld and Pandis, 2016).

Here attempts are made to demonstrate that strongly elevated levels of NO_X, CO and O_3 (> 90 ppb) were observed simultaneously in air parcels that have been impacted by both gas flaring emissions and urban aerosols in Lagos. For multiyear (1997-2003) analysis from the MOZAIC programme, the range of ozone observed within the planetary boundary layer (PBL) during August around Lagos is in the range of 30 - 70 ppb (Sauvage et al., 2005).

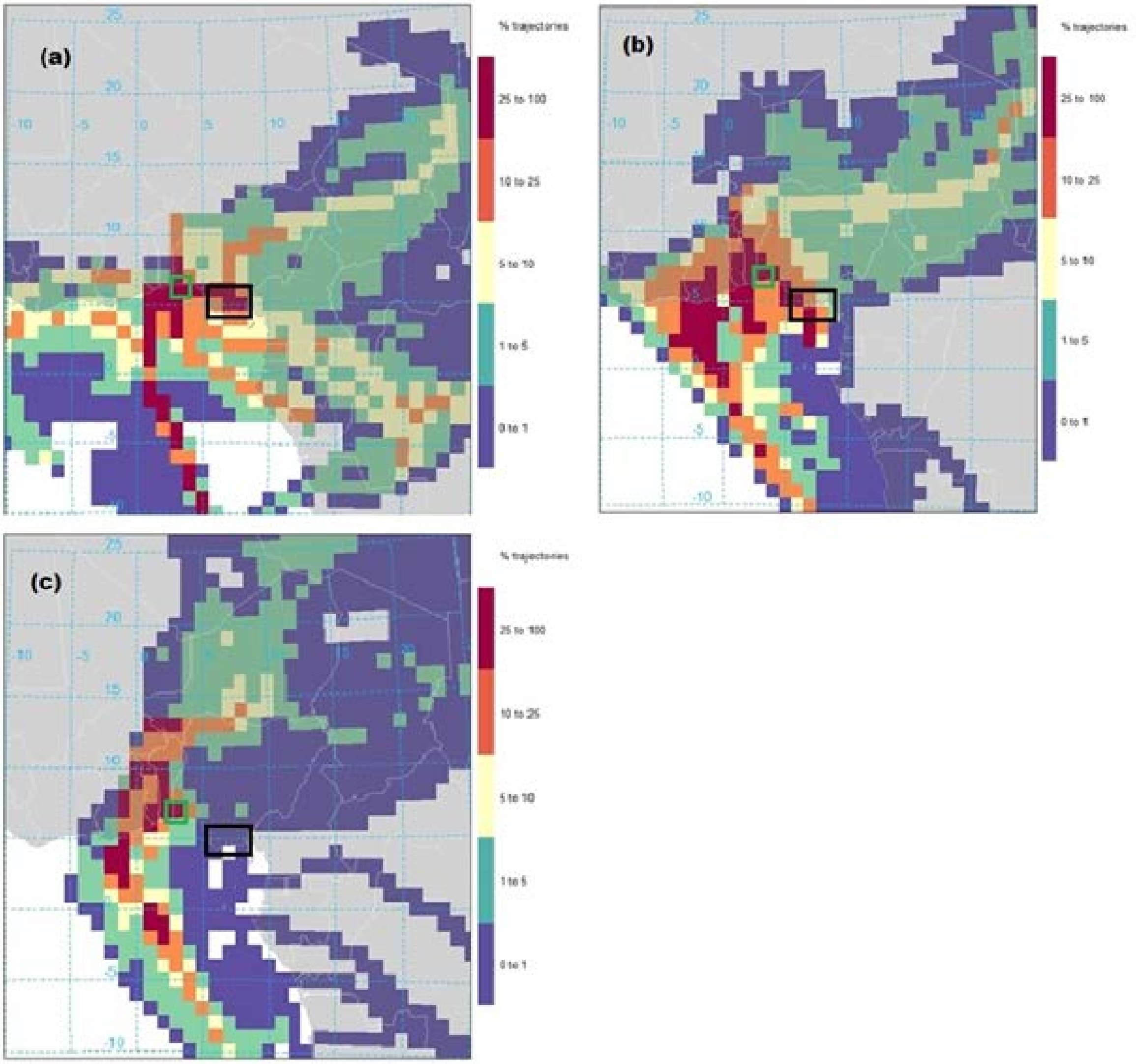

Figure 5.2: Trajectory-density plot for AMMA flights (a) B228b (b) B231b and (c) B222b. The black and green boxes show the region of intense gas flaring and the city of Lagos (Nigeria), respectively. The colour code shows the range of number of trajectories in each of the 1 ^{o} × 1 ^{o} gridded boxes.

Figure 5.4(b) shows the back trajectory plot for flight time between 43600 – 44700 seconds, a period of elevated ozone, NO_X and CO measurements shown in Figure 5.4(a). As shown in Figure 5.4(c), higher concentrations of NMHCs were also measured during this portion of the flight. These elevated measurements of ozone, CO and NO_X were observed around an altitude of 1.5 – 3 km (see Figure 5.5(a)), which corresponds to the 700 – 800 hPa shown in

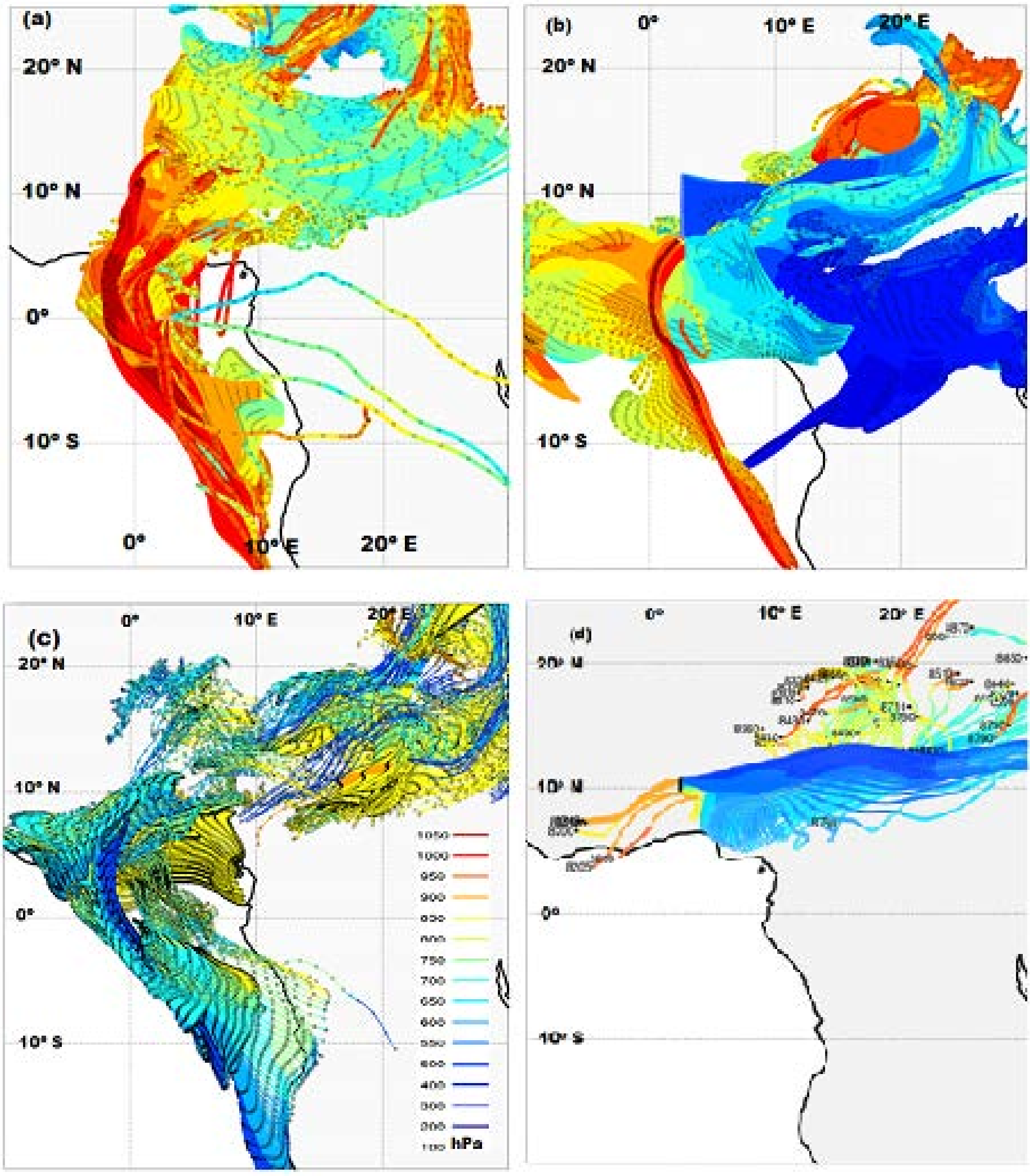

Figure 5.3: Complete trajectory plot for flights (a) B222b (b) B228b (c) B231b and, (d) back-trajectory plot for time of flight between 38200 and 39000 seconds on B231

the colour-coded pressure in the back trajectory plot in Figure 5.4(b).

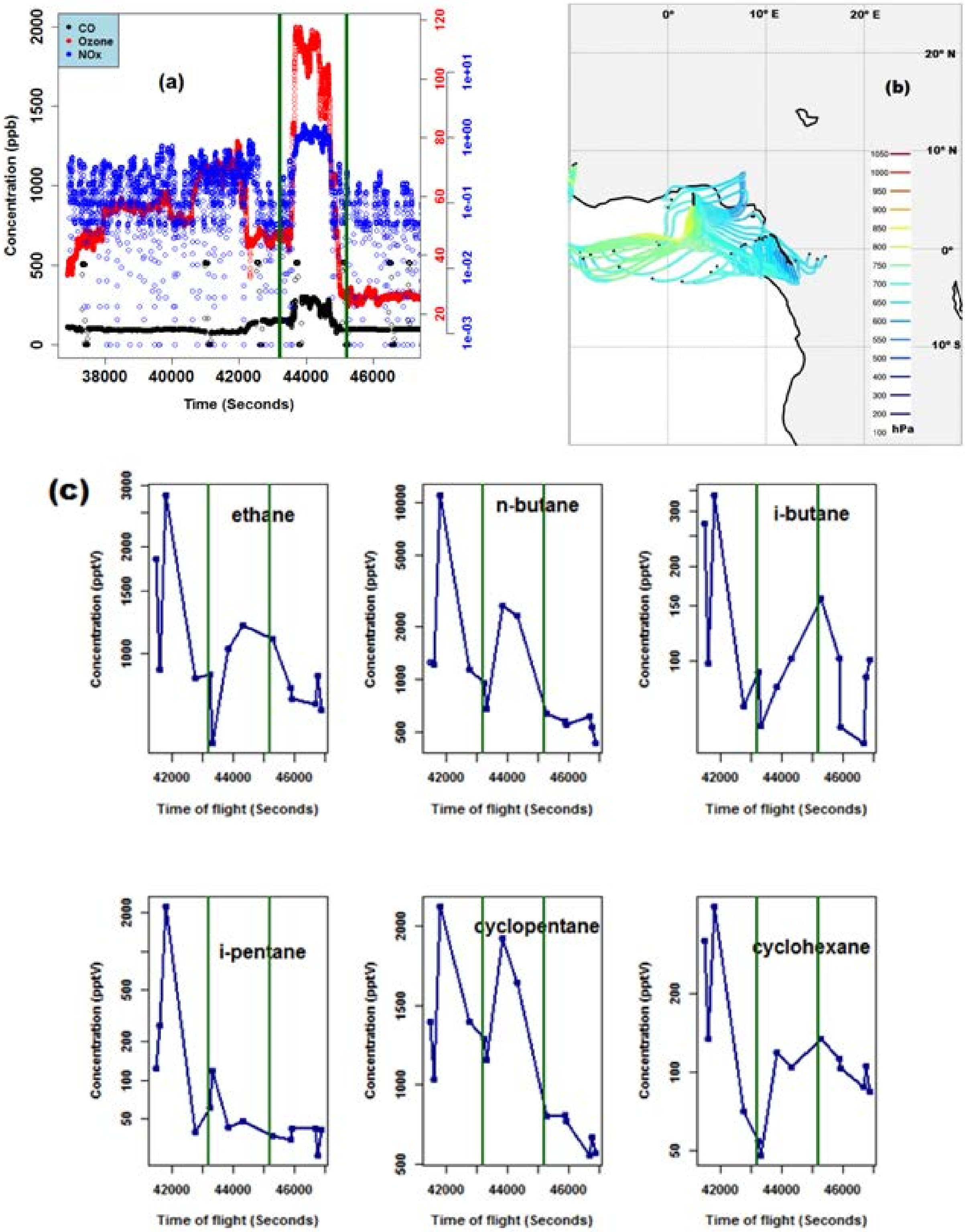

Figure 5.4: For flight B228b: (a) concentration of CO, NO_X and O_3 against flight time (b) back trajectory plot of time with elevated CO and O_3 in time step of 10 seconds (c) concentration of alkane species against flight time

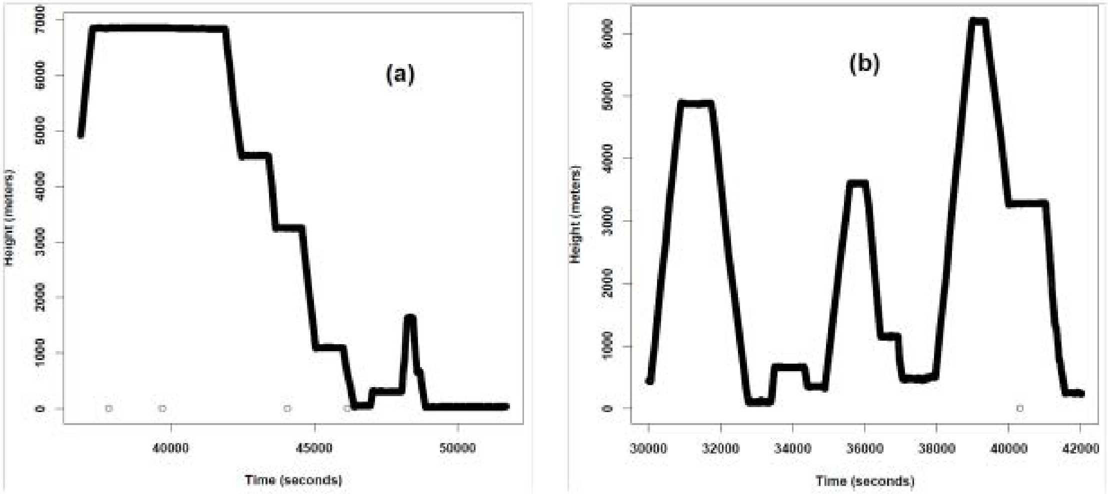

Figure 5.5: Variation of flight height with flight time for (a) B228b, and (b) B231b

Of all BAe-146 flights during the AMMA flight campaign, ozone concentration in excess of 90 ppb was measured on B228 and B231 only. These are the only flights that measured air parcels that were suggested to have been significantly impacted by gas flaring emission from the Nigeria oil field, as shown in the trajectory density plot in Figure 5.2. With combustion temperature often >1900 K and fuel-rich combustion conditions, gas flaring is a significant source of atmospheric NO_X by both thermal NO_X and prompt NO_X processes (Fawole et al., 2016b). Carbon monoxide (CO) and NMHCs are also common emissions from gas flaring, and their emission rates increase steadily with decreasing completeness of combustion process of the fuel gas. It should, however, be noted that while CO, O_3 and NO_X are measured every second, NMHCs measurements are averaged between 30 and 90 seconds.

During flight times between 43600 and 44700 seconds, there was significant enhancement of CO to up to 300 ppb in the layer between 2 and 3km; with accompanying enhanced NMHC measurements. The green vertical lines in Figures 5.4(a) and 5.4(c) shows the range of times within which elevated measurements of ozone, CO and NO_X were observed and the corresponding time-step for alkane species measurements on flight B228. Figure 5.4(c) shows the time profile of ethane, butanes, pentanes, and cycloalkanes with concentration of over 250, 300 - 10000, 2000 and 300 - 2000 pptV, respectively. Such high concentrations

Table 5.2: Statistics of alkane species measured on flight B228.

	mean	**min**	**max**	**median**
CO (ppbv)	127.2	0.043*	1999.9	98.4
Ozone (ppbv)	44.1	9.5	117.8	43.8
ethane (pptv)	1068.3	553.1	2817.5	865.8
i-butane (pptv)	120.3	54.3	338.9	94.8
n-butane (pptv)	1757.0	429.9	11143.6	813.6
i-pentane (pptv)	226.5	26.0	2252.1	42.6
cyclopentane (pptv)	1152.5	556.1	2123.1	1093.9
cyclohexane (pptv)	135	47.8	429.4	104.5

* very low value might be due to equipment failure.

of alkanes are indicative of natural gas sources, particularly from the oil and gas sector (Hopkins et al., 2009; Minga et al., 2010). These enhanced levels of CO and alkane together with elevated NO_X concentration (> 2 ppb) are suggested to be responsible for the elevated ozone level (120 ppb) rather than long-range transport. Long-range transport of pollutants is not evident in the 7-day back trajectory plot shown in Figure 5.4(b). Table 5.2 shows a summary of the statistics of the carbon monoxide (CO), ozone (O_3) and alkane species measured on-board flight B228.

5.4.2 Case study II: Flight B231

Flight B231 flew from Niamey to Cotonou and over the ocean around the Gulf of Guinea on August 13, 2006. The ’b’ portion of the flight (B231b) came within proximity of Nigeria and the air parcel sampled on-board was suggested to have been impacted by emissions from the gas flaring region in the Niger Delta and Lagos, Nigeria (see Figure 5.2(b)). The back trajectory plots in Figs. 5.7(a) and 5.7(b) are for flight times 31000 - 32000 and 34500 – 36000 seconds, respectively. These times correspond to the periods of elevated CO and ozone measurements; there was also a corresponding increase in NO_X measurements at these periods. Although, fewer and 20 – 30 seconds averages, NMHCs measurements shows significantly similar trends at these periods of elevated CO, ozone and NO_X measurements (see Fig. 5.6(b)). Heights at which air plumes from the intense gas flaring region were encountered during flight times 31000 - 32000 and 34500 – 36000 seconds are between 3 - 3.5 km and 2 - 3 km, respectively. These heights correspond to that shown in the colour coded atmospheric pressures, in Figures 5.7(a) and 5.7(b), 650 – 800 hPa and 750 – 850 hPa, respectively. These times, that is, 31000 – 32000 second and 34500 – 36000 seconds, were on the to - and fro - laps of the flight over the ocean around the Gulf of Guinea (see Fig. 5.1(b)).

The periods of strong enhancement of CO and NO_X occurred during time of flights 31000-32000 and 34500 – 36000 second. During these enhancement periods of mixing ratios, CO mixing ratio was up to 480 and 440 ppb, respectively while ozone was up to $\sim$128 ppb and $\sim$118 ppb, respectively. These periods equally exhibited elevated NO_X mixing ratio up to $\sim$2.5 ppb. As shown in Figure 5.6(b), mixing ratio for alkanes – ethane, propane, butanes and pentanes – were also enhanced during these periods. The green vertical lines in Figures 5.6(a) and 5.6(b) shows the range of times within which elevated measurements of ozone, CO and NO_X were observed and the corresponding time-step for alkane species measurements on flight B231. Minga et al. (2010) suggested, from their simulation, that the only way to reach excessively high ozone concentration within few hours in their model was to increase amount of reactive VOCs to levels recorded around petrochemical facility. In their study to estimate emissions from Lagos, Hopkins et al. (2009) concluded that the substantial downwind enhancement of ethane is attributable to fugitive natural gas leakage. The enhanced CO measured simultaneously is indicative of a combustion source rather than a leak, which in this study, has been suggested to be gas flaring sources in the Niger Delta. Owing to the unique and significantly varying nature of gas flaring emissions, ratios of

Table 5.3: Statistics of alkane species measured on flight B231.

	mean	**min**	**max**	**median**
CO (ppbv)	163.6	0.043*	535.1	123.1
Ozone (ppbv)	44.0	0*	128.9	31.7
ethane (pptv)	961.2	467.2	2758.1	859.3
propane (pptv)	94.2	22.0	248.2	81.1
i-butane (pptv)	33.3	0*	92.8	18.3
n-butane (pptv)	45.2	2.6	200.2	27.7
i-pentane (pptv)	40.5	0*	459.3	12.2
n-pentane (pptv)	22.7	0*	264.3	9.6

* value might be due to equipment failure.

emissions often used as tracers for fossil fuel combustion could not be directly applied to emissions analysed in this study. Hence, a case is made for further studies to adequately characterise emissions from gas flares in the oil and gas sector, especially for VOCs.

Slight enhancement of ozone to up to 75 ppb was measured around flight time between 38570 and 38700 at a height of ∼5 – 6 km. This was accompanied by a similar enhancement of CO up to ∼220 ppb, but there was no substantial enhancement in the levels of alkanes measured. This could be attributed to long-range transport of biomass burning plume from the East, around Sudan (see Figure 5.3(d)). Table 5.3 presents the statistics summary of CO, O_3 and alkane measure on flight B231.

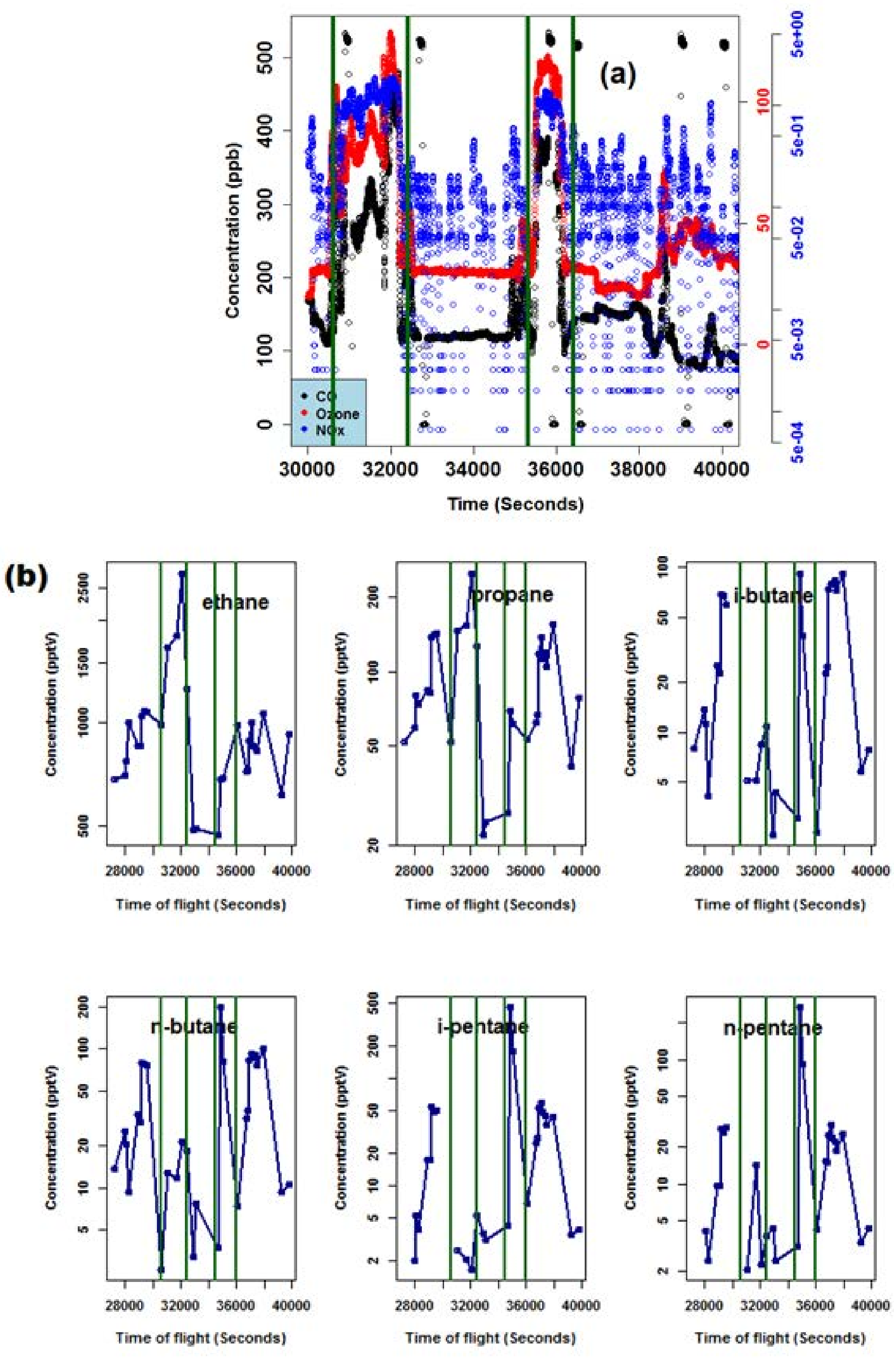

Figure 5.6: For flight B231b: (a) plot of concentration of CO, NO_X and O_3 against flight time, and (b) concentration of alkane species against measurement time

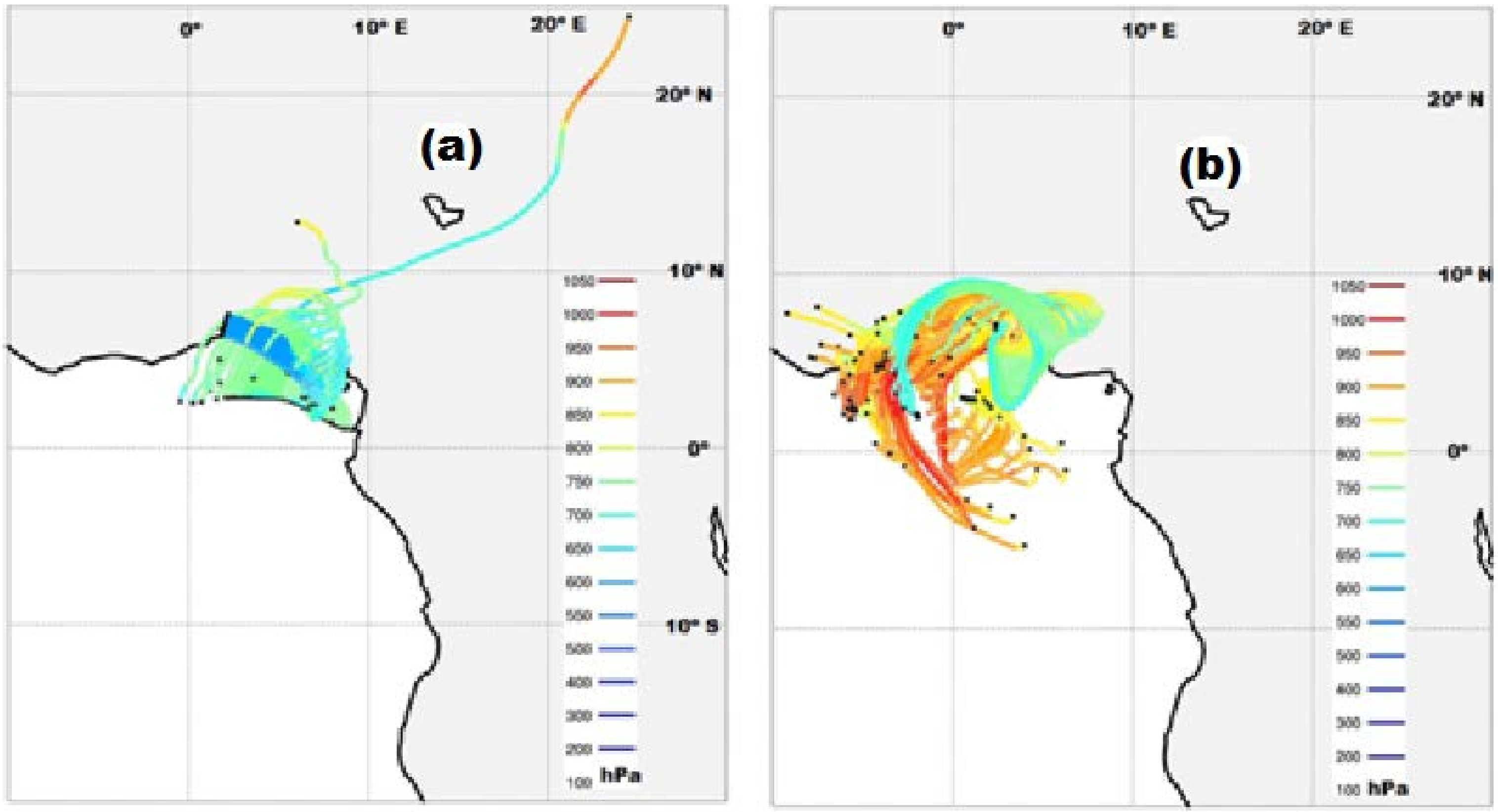

Figure 5.7: For flight B231b: (a) back trajectory plot of flight time 31000 – 32000 in time step of 10 seconds, and (b) back trajectory plot of flight time 34500 – 36000 in time step of 10 seconds

5.4.3 Case study III: Flight B222

AMMA flight B222 flew around Benin on July 30, 2006 carrying out the mapping of biogenic emissions. As shown in the trajectory density plot in Figure 5.2(c) and Figure 5.3(c), < 1 % of the air mass sampled on the flight is suggested to have been impacted by gas flaring emissions while >25 % were impacted by anthropogenic emissions from Lagos. There is no significant enhancement in the mixing ratio of CO which was around 200 ppb throughout the duration of the flight except for very few spikes (see Figure 5.8(a)). Mixing ratios of ozone and NMHCs are also relatively low (see Figure 5.8(b) and Table 5.4) in contrast to the other two flights that sampled air parcels that were suggested to have been impacted by emissions from both the region of intense gas flaring and Lagos, Nigeria. Table 5.4 presents the statistics summary of CO, O_3 and alkane species measured on flight B222.

5.5 Conclusion

During AMMA SOP 2, on 30 July, 8 and 13 August 2006, FAAM BAe-146 carried out three scientific flights that sampled air parcels around Benin and the ocean around the Gulf of Guinea during sections of the flights durations. Portions of the air parcel sampled were suggested to have been significantly impacted by anthropogenic emissions from the gas flaring activities in the Niger Delta region and the city of Lagos. These flights sampled air parcels within the lower and mid-troposphere. On flights B228 and B231, there were portions of the flight with strongly enhanced mixing ratios of carbon monoxide (CO) and ozone. These enhancements were attributed to emissions from the region of intense gas flaring in the Niger Delta and Lagos, Nigeria because of the highly enhanced levels of short-chained alkane species and histories of air parcel sampled which is obtained from the back trajectory analysis. At a height of about 6 km, slight enhanced mixing ratios of CO and ozone observed is attributable to long-range transport of pollutants. Air parcels sampled on flight B222 was suggested to be strongly impacted by emissions from Lagos but almost insignificantly by emissions from the Niger Delta, hence, the relatively low mixing ratios of CO, ozone

Table 5.4: Statistics of alkane species measured on flight B222.

	mean	**min**	**max**	**median**
CO (ppbv)	118.1	0.043*	528.0	125.3
Ozone (ppbv)	27.0	0*	61.4	28.1
ethane (pptv)	123.6	13.9	346.0	86.3
propane (pptv)	27.1	3.1	91.6	22.6
n-butane (pptv)	214.9	55.1	346.3	206.2
i-pentane (pptv)	6.2	0*	21.1	5.0
n-pentane (pptv)	7.7	3.9	19.8	6.4
cyclopentane (pptv)	4.5	0*	7.2	4.5
cyclohexane (pptv)	3.2	0.72	4.32	3.3

* value might be due to equipment failure.

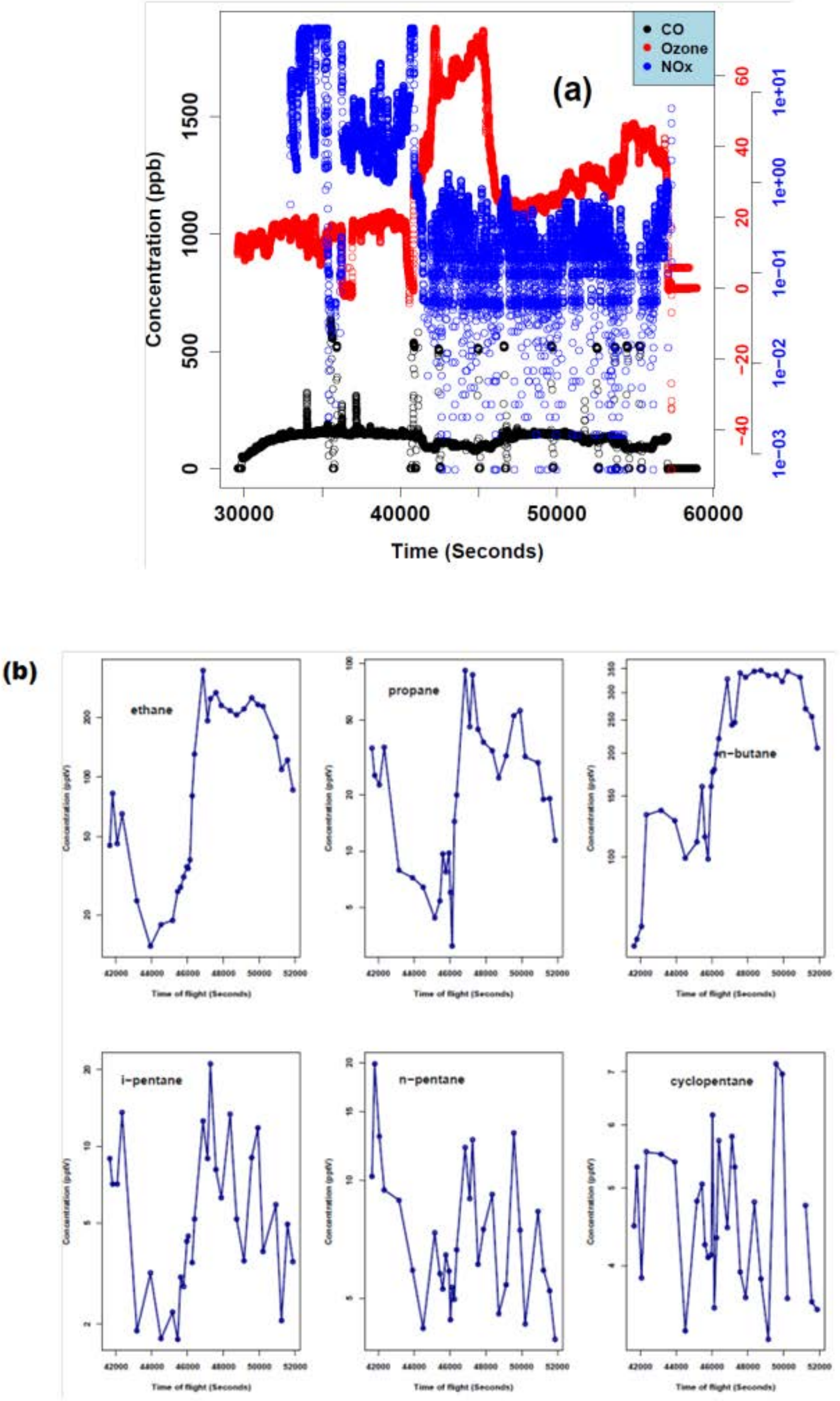

Figure 5.8: (a) For flight B222: (a) plot of concentration of CO, NO_X and O_3 against flight time (b) concentration of alkane species against measurement time

and short-chained alkanes. Analysis of short-chained alkanes species and cycloalkanes are limited by the number and cycles of NMHCs measurements on these flights. With our understanding of the extent of contributions of gas flaring in this region to levels of ambient pollutants coupled with limited and insufficient data to characterise emission from this source (gas flaring), we make a strong case for the need for further in-depth studies to understand the emissions, atmospheric transport and behaviour of emissions from this unique stationary source of aerosol pollutant under the impact of the peculiar climatic conditions of the West Africa region.

Chapter 6

Detection of a gas-flaring signature in the optical and microphysical properties of aerosols at a tropical station over West Africa using AERONET data

6.1 Abstract

The West African region, with its peculiar climate and atmospheric dynamics coupled with enhanced aerosol loading from diverse sources (anthropogenic and biogenic), is suitable to investigate the impact of aerosol types on climatic conditions. Reliable and long-term in-situ measurements of aerosol properties are not readily available across the region. In this study, AERONET Version 2 Level 2 direct sunphotometer products from the Ilorin, Nigeria site were used to determine the multi-year variability of the aerosol optical depth (AOD) and Angstrom Exponent (AE), while the Version 2 Level 1.5 AERONET data were used to study the absorption and size distribution properties of the aerosols from dominant sources identified by trajectory analysis. The trajectory analysis was used to define four sources of aerosols for the periods 2005-2009 and 2011-2015: desert dust (DD); biomass burning (BB); urban (CC); and gas flaring (GF). Sorting the AERONET aerosol retrievals by these putative sources, the hypothesis that there exists an optically distinct gas-flaring signal was tested. The dominance of each source cluster varies with season: desert dust (DD) and biomass burning (BB) aerosols are dominant in the months prior to the West African Monsoon (WAM); urban (CC) and gas flaring (GF) aerosol are dominant during the WAM months. According to their optical and size properties, desert dust (DD) and urban aerosol (CC) can be categorized as coarse-absorbing while biomass burning (BB) and gas-flaring (GF) aerosols can be categorized as fine-absorbing. Biomass burning (BB) aerosol, with single scattering albedo (SSA) at 675 nm value of 0.86±0.03 and gas-flaring aerosol with SSA (675 nm) value of 0.9±0.07, are the most absorbing of the aerosol categories. The range of Absorption Angstrom Exponent (AAE) for DD, BB, CC and GF clusters are 1.99±0.35, 1.45±0.26, 1.21±0.38 and 0.98±0.25, respectively, indicating different aerosol composition for each source. The AAE (440-870 nm) and Extinction Angstrom Exponent (EAE) (440-870 nm) relationships further show the spread and overlap of the variation of the optical and microphysical properties of these clusters, presumably due in part to similarity in the sources of aerosols and in part, due to mixing of air parcels from different sources en-route to the measurement site.

The entire work discussed in this chapter was carried out by me. However, Prof. Rachel T. Pinker (the PI of the Ilorin AERONET site) of the University of Maryland, USA read and gave comments on the manuscript "**Olusegun G. Fawole, Xiaoming Cai, James G. Levine, Rachel T. Pinker, A.R. MacKenzie** (2016), Detection of a gas-flaring signature in the optical and microphysical properties of aerosols at a tropical station over West Africa using AERONET data", which is in the revision stage of publication in ***Journal of Geophysical Research: Atmosphere***. This work has also been presented at the 17th IUAPPA World Clean Air Congress and 9th CAA Better Air Quality conference, Busan, South Korea. and 2016 EGU General Assembly, Vienna, Austria. And, as such, they are documented in the online version of conference proceedings/book of abstracts for the conferences. For example;

- http://adsabs.harvard.edu/abs/2016EGUGA..1811733M).

- http://aerosol-soc.com/files/Poster_Abstracts_AASC_2015/2%20Olusegun%20Fawole%20Poster%20AASC2015.pdf

6.2 Introduction

Tracking atmospheric aerosols from the source requires an understanding of the chemical character of the source and the prevailing meteorological conditions (Eck et al., 2010; Giles et al., 2012; Rozwadowska et al., 2010). With atmospheric residence times of 5-8 days, gas flaring associated aerosol, especially BC, is a good tracer for gas flaring emissions (Shindell et al., 2008). This study aims to assess and quantify the contributions of intense gas flaring activities in the Nigeria oil field to regional aerosol loadings. Gas flaring is a prominent contributor to atmospheric aerosol loading, on both local and regional scales, in leading oil producing nations of the world, including Russia, Nigeria, USA, Iran and Iraq (Doherty et al., 2014; Fawole et al., 2016b).

Aerosol in the atmosphere can be classified in many different ways; here it is useful to consider fine- and coarse-absorbing classes, based on their radiation absorption potential and Mie-scattering particle-size equivalence (Mielonen et al., 2009). The spectral dependence of aerosol optical and microphysical properties derived from remote sensing measurements of aerosol properties have been used to establish dominant aerosol signals (e.g., (Giles et al., 2012; Russell et al., 2010)). Aerosol nature and properties vary with region; so, adequate knowledge of major sources of aerosol in a region should enhance identification of dominant aerosol types at a measurement site in the region. Back trajectory analysis and adequate knowledge of the sources contributing to aerosol loadings in a region can, therefore, give a clearer understanding of the properties of the aerosol from the dominant sources (Milinevsky et al., 2014).

The Aerosol Robotic Network (AERONET) consists of more than 400 sites distributed around the globe. This network of automated sun photometers has provided retrievals of aerosol properties for more than 20 years at some sites (Holben et al., 2001, 1998). Many studies have utilized aerosol retrievals from the AERONET dataset to analyse optical properties and size distribution, and hence, composition of aerosols in different regions of the world e.g. (Giles et al., 2012; Kim et al., 2011; Milinevsky et al., 2014; Russell et al., 2010; Sato et al., 2003).

Previous studies have classified the Ilorin AERONET site in West Africa, and these are described in more detail below, as either a predominant dust (Lee et al., 2010; Pandithurai et al., 2001; Pinker et al., 2010; Smirnov et al., 2002) or mixed aerosol (Eck et al., 2010; Giles et al., 2012) site. The location of Ilorin (Figure 6.1) as the boundary city between the densely populated and industrialised Monsoonal forest region of the South and Savanna region of the North of Nigeria places it at a strategic location for aerosol-climate interactions. The prevailing winds are the dry northeasterly 'Harmattan' (NEH) and moist southwesterly monsoon (SWM) winds. NEH brings dry Harmattan dust from the Sahara and Sahel region, usually between late November and early February, while the SWM brings in moist cool air that gives rain (Sultan and Janicot, 2003) but which may also carry urban and industrial aerosols from the South.

To the south of the Ilorin AERONET site is the gas flaring region in Nigeria with over 300 active flare sites (Anejionu et al., 2015a; Elvidge et al., 2015) and an estimated annual average volume gas flare of 15 bcm (billion cubic metres). In the region, gas flaring is a daily routine at many of the sites, owing to the large amounts of natural gas produced, and inadequate piping to facilitate bringing the product to the market. Nigeria, presently ranked the second leading gas flaring nation of the world, is estimated to flare about 25 % of its annual gas production (Ite and Ibok, 2013). Figure 6.1 shows the spatial distribution of active flare sites in the Niger Delta, Nigeria and location of the Ilorin AERONET site.

In 2012, of the 325 active flare sites identified in the Nigeria oil field, 97 ($\sim$ 30 %) ranked among the top 1000 largest flares identified globally. Anejionu et al. (2015b), in their analysis of the multi-year spatial dispersion of gas flaring gaseous emissions from the Niger Delta region classified the airshed of more than 70 % of the Niger Delta as moderate to high pollution risk areas. Giwa et al. (2014), using emission factors from literature, estimated that gas flaring contributes about 10 Gg of BC to ambient BC concentration in the Niger Delta annually. Findings from Diffuse and Inefficient Combustion Emission in Africa (DICE-Africa) shows that significant fraction of BC in the Sahara desert and Gulf of Guinea could be attributed to gas flaring activities in the Niger Delta area of Nigeria (Marais and Chance, 2016). According to Marais and Chance (2015), in the Niger Delta, hotspot of HCHO (Formaldehyde) observed on the ozone monitoring instrument (OMI) on NASA's EOS Aura platform is from the oxidation of non-methane volatile organic compounds from combustion including gas flaring.

In the present study, using a combination of trajectory analysis and knowledge of dominant aerosol sources in the region, clusters of dominant aerosol types at the site for 2005 – 2009 and 2011 - 2015 were created. The statistics of the optical properties of these measurement clusters were then analysed for: Aerosol Optical Depth (AOD), Absorption Angstrom Exponent (AAE), Extinction Angstrom Exponent (EAE), Single Scattering Albedo (SSA) and Fine Mode Fraction (FMF). See (Dubovik and King, 2000; Dubovik et al., 2000; Holben et al., 2006) for a full description of the derivation of these metrics from radiances measured by ground-based Sun-sky scanning radiometers at AERONET sites globally.

6.3 Methodology

6.3.1 Description of the AERONET site and major sources of aerosol

The AERONET site is located in Ilorin, Nigeria (8.32^o N, 4.34^o E) (Figure 6.1). Based on the Köppen-Geiger climatic classification, Ilorin can be classified as tropical desert (Aw). In Ilorin, the annual mean rainfall and temperature are about 1220 mm and 26.5 ^{o}C, respectively (Olaniran, 1982; Tunde et al., 2013). The site has two big cities - Lagos and Oyo, city regions with populations of 17 and 5 million, respectively - and the gas flaring region (Niger

Delta) to the south, the Sahel and Sahara region to the north and major sources of biomass burning emissions in West Africa to the East and West. The movement of the intertropical convergence zone (ITCZ) and intertropical front (ITF) determine the pre-onset and onset of the West African Monsoon (WAM) in the region. Biomass burning emissions are intense in the region between November and March (Roberts et al., 2009), a period during which there is also significant dust transport from the Sahel and Sudan region. Saharan dust is predominant between late November and January, a period of intense Harmattan conditions. Depending on the season and prevailing meteorological conditions there is an influx of urban and industrial aerosols from the south. It is expected that this influx of urban-industrial air will predominate during the WAM months, between April and October. It is hypothesised that aerosols from each of these sources exhibit statistically significant differences in their optical – and, hence, microphysical - properties.

Figure 6.1 shows the locations of the Ilorin AERONET site and dense concentration of gas flaring sites in the Niger Delta area, Nigeria. The brown area shown in Figure 6.1 is the Sahara and Sahel regions, which is the major sources of dust in the region. Data for the locations of the gas flaring sites were obtained from the supplementary material in Elvidge et al. (2015).

6.3.2 Trajectory calculation and classification

For the months when AERONET data were available for the site over the period considered, 2005 – 2015 (excluding 2010), 7-day back trajectories were calculated using the UK Universities Global Atmosphere Modelling Programme (UGAMP) offline trajectory model. This model is driven by six-hourly ERA-Interim (European Centre for Medium-Range Weather Forecasts Interim Reanalysis) wind analyses data. Three dimensional meteorological data are interpolated to the trajectory locations. For each integration time, values of meteorological fields (temperature, potential temperature and pressure) are assigned as attributes to the particle in the trajectory. Detailed technical descriptions of the UGAMP trajectory model can be found in Methven (1997) and Methven et al. (2001).

Nine (9) backward trajectories spaced 0.05^o x 0.05^o (i.e. about 5 km x 5 km) apart on a 0.1^o x 0.1^o grid were released six hourly, that is, at 0000, 0600, 1200 and 1800 UTC, at 900 hPa (i.e. approximately 1.5 km altitude) on each of the days for which the calculations were done. It must be noted that these trajectories, in general, change altitude as a function of transit time: 900 hPa is the arrival pressure at the AERONET site. The choice of 7-day back trajectory length is due to the atmospheric life-time of between 5 and 9 days estimated for BC and particulate organic matter (POM) (Cooke et al., 1997; Cooke and Wilson, 1996; Koch et al., 2009; Stier et al., 2006), both of which are major constituent of aerosol in the study area.

The clustering of the aerosol signals by their trajectory paths enables a consideration of the major sources of aerosol in the region. As shown in Figure 6.2, the desert dust (DD) source chosen is the Sahara region which is the dominant source of dust in Nigeria. While the biomass burning BB) aerosol sources chosen, according to Roberts et al. (2009), are the predominant source of BB aerosol in the region during the non-WAM months. In this study, the classification was based solely on the trajectory coordinates, considering whether the trajectory had passed through the gridded regions of one or more of the major aerosol sources where they are suggested to have picked up aerosol signatures peculiar to such sources. The classification algorithm developed and used in this study allows the large dataset (10 years of trajectories) to be processed automatically avoiding manual inspection of trajectory maps.

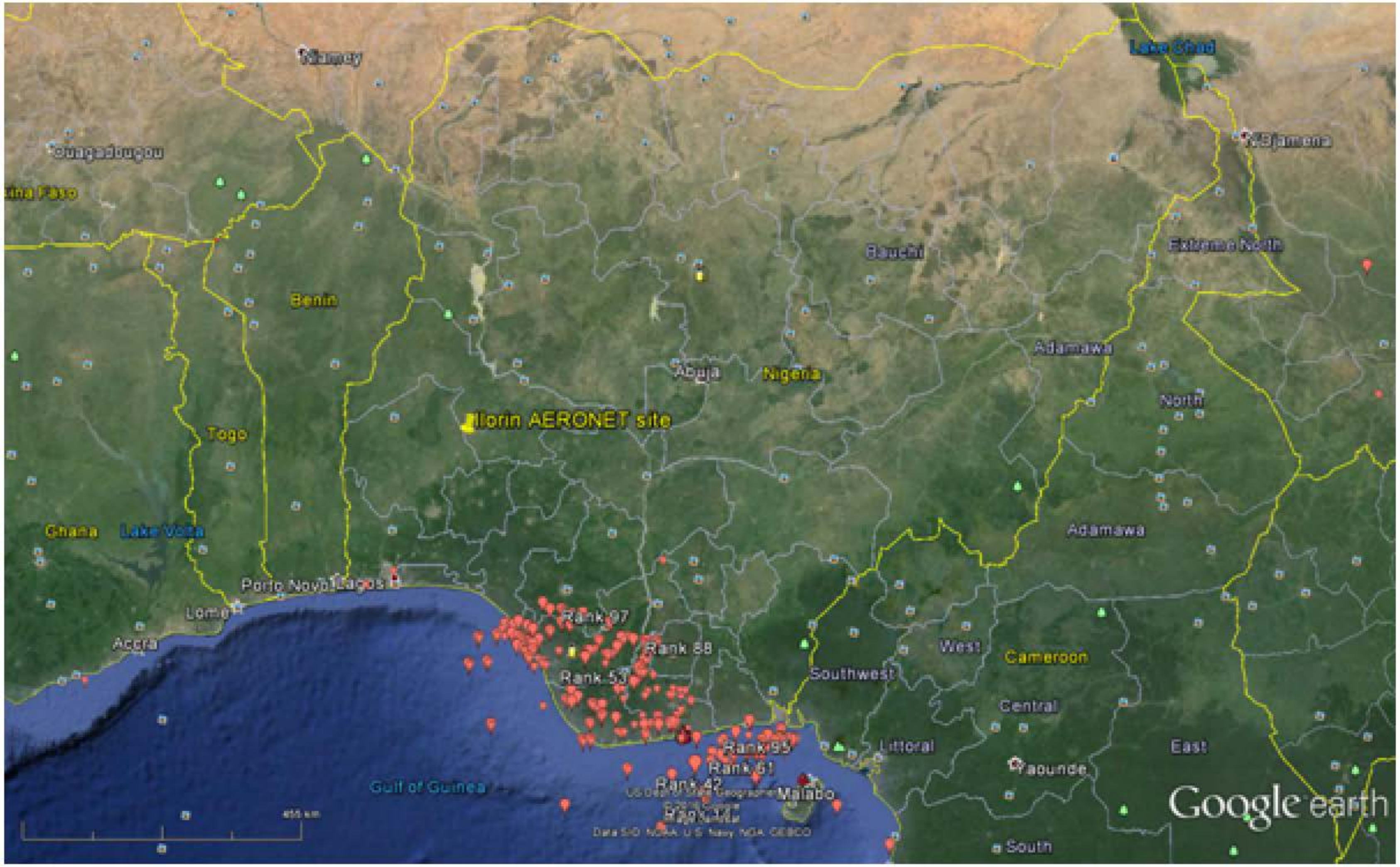

Figure 6.1: Google Earth image showing location of Ilorin AERONET site and the cluster of active gas flaring sites in the Niger Delta, Nigeria (gas flare locations are from the KML file from Elvidge et al. (2015)

When at least six of the nine trajectories released at a point in time pass through one of the source region, that region is considered to be the dominant source of the aerosol signal measured. When there are almost equal numbers of trajectories from two sources in the four sets of 6-hourly trajectories released on a day, the aerosol signal recorded on that day is regarded as a mixture of the two most dominating sources. In this way, eight clusters were created: BB, DD, CC, GF, DD-BB, DD-CC, GF-CC and GF-DD. BB-CC and BB-GF clusters occurred less than 1 % of the time and are therefore, not investigated further.

6.3.3 AERONET Data

AERONET network provides sun photometer measurements of AOD at up to eight wavelengths between 340 and 1020 nm. The network has been in operation since mid-1990s (Holben et al., 1998) and currently with over 400 sites globally (Chubarova et al., 2016). It also measures the angular distribution of sky radiance at four wavelengths (0.44, 0.675, 0.87 and 1.02 μm). An inversion algorithm is used for the retrieval of optical and microphysical properties of atmospheric aerosols, such as volume size distribution, asymmetric parameter (g), complex refractive index (n), and single scattering albedo (SSA) at 0.44, 0.675, 0.87 and 1.02 μm (Dubovik et al., 2002; Dubovik and King, 2000; Eck et al., 2010). For sites like Ilorin where differences in the diurnal variation of aerosol are very pronounced, the use of monthly averages of aerosol parameters will provide only highly generalised estimates of the optical and microphysical properties of aerosol at such a site.

The Angström exponent (AE), a measure of the wavelength (λ) dependence of aerosol optical depth (τ), indicates the dominant aerosol size because the spectral shape of the extinction is inversely related to the particle size (Eck et al., 1999; Schuster et al., 2006). The wavelength dependence of scattering as quantified by AE (α) is given by Equation (6.1):

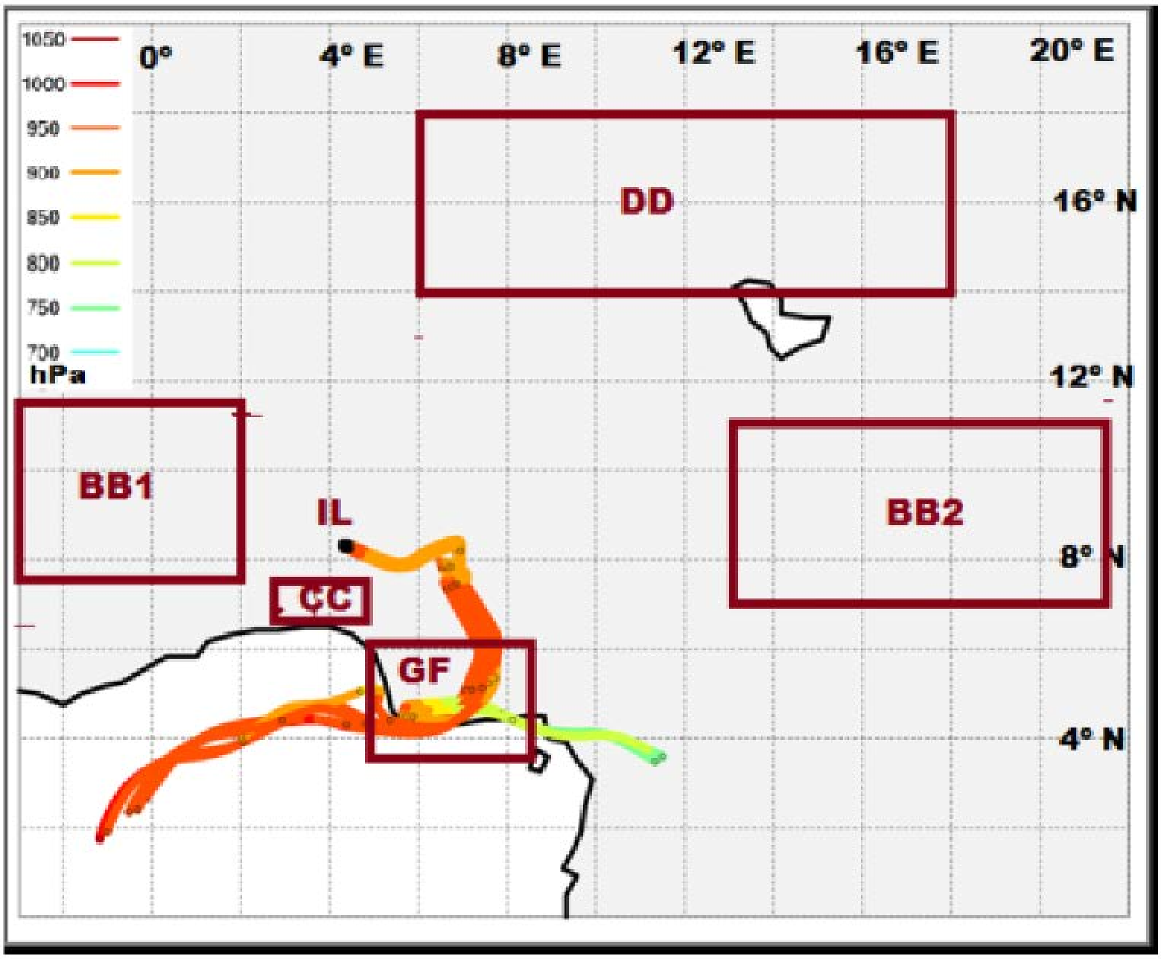

Figure 6.2: An example of trajectory plot together with the areas of major aerosol sources and the AERONET site (BB, DD, CC and, GF represent biomass emissions, desert dust, urban, gas flaring sources while IL indicate the AERONET site at Ilorin, Nigeria)

$$\alpha = -\frac{\ln\left(\frac{\tau_{\lambda_1}}{\tau_{\lambda_2}}\right)}{\ln\left(\frac{\lambda_1}{\lambda_2}\right)} \tag{6.1}$$

Level 1.5 of Version 2 AERONET retrievals were used in the analyses of the optical and microphysical properties of the clusters because Level 2 data, especially inversion products, were not sufficiently available. Level 2 of the direct algorithm retrieval were used to analyse the dynamics of the seasonal variation of fine-mode fraction (FMF), AOD and AE (470-870 nm).

The variation of absorption aerosol optical thickness (τ_{abs}) with wavelength (λ) can be approximated with a power-law wavelength dependence to infer the Absorption Angstrom Exponent, AAE, (α_{abs}), as given in Equation (6.2). Similarly, as given in Equation (6.3), the Extinction Angstrom Exponent, EAE, (α_{ext}) is obtained from the spectral dependence of extinction aerosol optical thickness (τ_{ext}) with wavelength (λ) on a logarithmic scale.

$$\alpha_{abs} = -\frac{d\ln[\tau_{abs}(\lambda)]}{d\ln(\lambda)} \tag{6.2}$$

$$\alpha_{ext} = -\frac{d\ln[\tau_{ext}(\lambda)]}{d\ln(\lambda)} \tag{6.3}$$

The spectral single scattering albedo (SSA) of an aerosol, as given in Equation (6.4), is the ratio of scattering to extinction (the sum of absorption and scattering). SSA (ω) depends on the strength of the aerosol sources and the aging of the aerosol during atmospheric transport.

For atmospheric aerosols, the value of SSA and AOD determines the sign and magnitude of its radiative forcing, respectively.

$$\omega = \frac{\beta_{sca}}{\beta_{ext}} = \frac{\beta_{sca}}{\beta_{sca} + \beta_{abs}} \tag{6.4}$$

6.3.4 Climatic condition at the study site

The predominant seasons at the site are governed by the movement of the Inter-tropical Convergence Zone (ITCZ) and Inter-tropical Front (ITF). The ITF is the northern limit of the southwesterly winds of the monsoon. The pre-onset stage of the West African Monsoon (WAM), usually between May and June, is characterised by the movement of the ITF further north to 15^o N which brings in the first period of rain. A further shift of the ITF to its northernmost position around 20^o N takes place between July and August, a period which signifies the onset of WAM (Sultan and Janicot, 2000, 2003). At the onset of the WAM, there is an abrupt shift in the latitudinal position of the ITCZ from a location of 5^o N in May-June to a location at 10^o N in July-August.

6.4 Statistical Analysis

For statistical analysis of aerosol optical and microphysical properties, the SPSS statistics package 22 (SPSS Inc., Chicago, IL, USA) was used. The mean values and variability of AAE and EAE for all four clusters – DD, BB, CC and GF – were compared pair-wise to establish the statistical significance of the differences between these mean values. For statistical analysis, the clusters were paired as follows for comparison: (a) CC-GF (b) GF-BB

(c) CC-BB (d) BB-DD (e) CC-DD and (f) GF-DD.

6.4.1 Independent sample t-test

In statistics, t-test is used to determine if significant differences exists between two groups of data. T-test can be dependent or independent if the sets of data are related or not, respectively. The t-test compares the mean values of the two sets of data. Since t-test is a parametric statistical test, it works on the basic assumption that the set of data are normally distributed or are very close to being normally distributed. Parametric test are statistically more powerful than equivalent non-parametric test.

6.4.2 Normality Test

Before the application of a parametric test to a set of data and especially a small set of data, there is the need to test the normality of the set of data. Due to the central limit theorem, normal distribution is fundamental to statistics. The probability density function for a normal distribution is the bell-shaped curve and it is given by the relationship in Equation (6.5).

$$f(x) = \frac{1}{\sigma\sqrt{2\pi}}\, exp\left(-\frac{(x-a)^2}{2\sigma^2}\right) \tag{6.5}$$

where μ and σ are the mean and standard deviation of the set of data, respectively.

To test for normality of a set of data, several methods can be applied; commonly used methods including histogram, boxplot, Q-Q (quartile-quartile) plot, Shapiro-Wilks (SW) and Kolmogorov-Smirnov (K-S) test. The K-S test is perhaps the most robust method to test the normality of a set of data. Like most statistical tests, the K-S test involves the formulation of a null hypotheses and testing to see if it can be rejected in favour of an alternative hypothesis (Wilks, 2011).

6.4.3 Kolmogorov-Smirnov (K-S) test

The K-S test belongs to the empirical distribution function (EDF) statistics. This class of statistics is based on the largest vertical difference between the hypothesized and empirical distribution (Conover, 1999). According to Conover (1999), for a data set of length n, the test proposed by Kolmogorov (1992) can be defined by equation (6.6):

$$T = sup_x|F^*(x) - F_n(x))| \tag{6.6}$$

where *'sup'* stands for supremum which means greatest. F^*(x) and F_n(x) are the hypothesized distribution function and empirical distribution function, respectively. The Kolmogorov-Smirnov (K-S) statistics is defined as a maximum absolute difference between the empirical distribution and the theoretical distribution, which in our study is the Gaussian distribution (Huth and Pokorna, 2004).

Software packages such as R, SPSS and Surfer could be used to calculate K-S statistics. After calculating the K-S test statistics, it is compared against the critical value for the K-S statistic at a given level of significance.

6.5 Non-Parametric t-test

If a set of data is skewed or contains too few data points to be tested for normality, non-parametric statistics are applied. This class of statistics, often termed distribution-free statistics, does not consider the distribution of the data in its analysis. Non-parametric test are usually less powerful and have greater uncertainties when compared to parametric test

(Huth and Pokorna, 2004; Townend, 2013). Although, a distribution-free statistics, some non-parametric tests require some assumptions to be fulfilled for them to be applied correctly. For example, the Mann-Whitney U-test requires that the distribution of two sets of data should be similar (Wheater and Cook, 2000).

6.5.1 Mann-Whitney U-test

The Mann-Whitney U-test, just like the t-test, is used for the comparison of two independent samples. And, hence, test if two independent groups of data are significantly different from each other. For a severely skewed set of data, the Mann-Whitney U-test is more powerful. It is based on ranking of data rather than observed values of data. The null hypothesis stipulates that the two groups of data are homogenous and have the same distribution while the alternative hypothesis stipulates that the distribution of the first group of data differs from that of the second group of data.

6.6 Results and Discussions

6.6.1 Dynamics of seasonal variation of AOD and AE

During the pre-onset and onset of the WAM (May – September), there is a sharp decrease in the average monthly AOD (440 nm) by a factor of about 4 from 1.22±0.17 in DJF (December – February) to 0.35±0.06 in JJA (June – August) over the five-year period (2005 -2009) considered in Figure 6.3(a). This is arguably due to the northwards shift of the ITCZ and ITF (as discussed in Section 6.3.4) which cuts off the intense intrusion of Saharan dust but increases the inland flow of SWM wind. The SWM wind brings aerosol from the large cities (urban, CC) and industries (including gas flaring, GF) downwind of the AERONET site. As shown in Figure 6.3(b), the fine-mode aerosol fraction dominates (FMF > 0.7) the period of low AOD (JJAS): combustion – biomass burning, biofuel, vehicular and fossil - emissions are major sources of fine-mode aerosol fraction.

Figure 6.3(a) presents the temporal variation of the average monthly AE for the period 2005-2009. Low AOD periods are associated with high AE values (> 0.7) which is typical of combustion aerosols like fossil fuel and biomass burning. In the region, biomass burning is predominantly between November and March which does not overlap with the low AOD period.

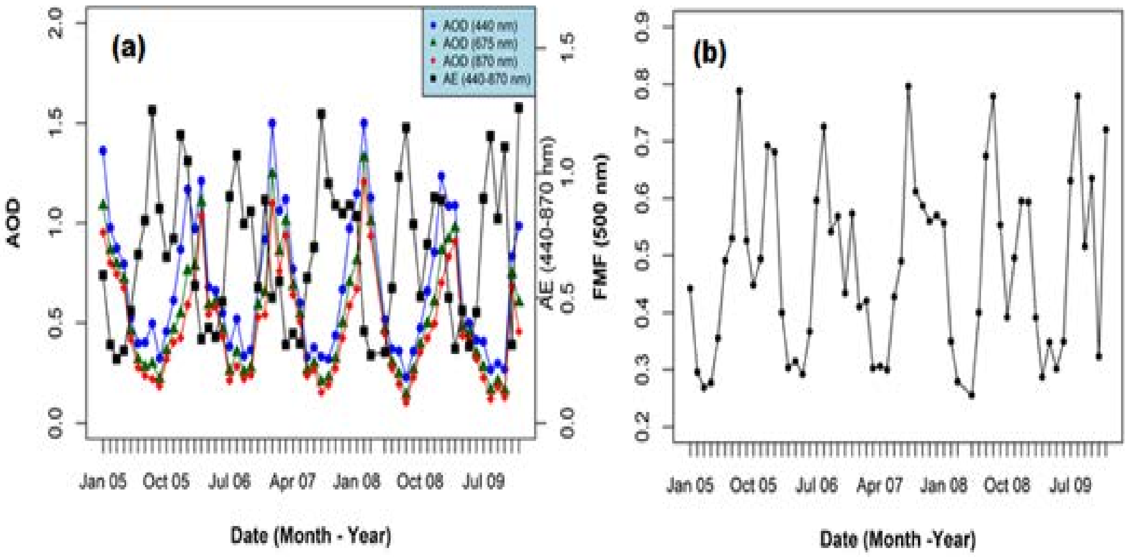

Figure 6.3: Temporal variation of monthly averages of (a) AOD at various wavelengths and AE (440-870 nm) (b) FMF (500 nm)

The monthly average AOD pattern is shown in Figure 6.3(a) for 440, 675 and 870 nm. For the analysis of the daily variation of AOD and AE, this five-year period (2005-2009) was chosen because there were very few missing data during these years. At the Ilorin AERONET site, there are frequent breaks in data availability probably due to adverse meteorological conditions for example, persistent cloud cover, or instrument breakdown. Figure 6.4 shows the overall distribution of AOD observed in the monthly dataset shown in Figure 6.3(a). During the WAM months, the several spikes observed in the daily data are most likely due to local dust rather than dust transport from the Sahara. In contrast to cities in the developed world, there is a dominant coarse-mode aerosol fraction in the aerosol from major Nigerian cities due to frequent resuspension of dust from the large expanse of unpaved roads (Akinlade et al., 2015; Obioh et al., 2013; Owoade et al., 2013).

Figure 6.4 presents the distribution of the daily AOD (40 bins) between 2005 and 2009 at 440 and 657 nm for both the WAM and non-WAM months. In these classifications, the WAM months are April – October while the non-WAM are November - March. All four histograms are positively skewed with few bins as outliers. For the WAM months, the AOD distribution is less skewed at both 440 and 675 nm. The median values of AOD (440 nm) and AOD (870 nm) for the WAM months are 0.48 and 0.31 and, 0.95 and 0.6 for the non-WAM months, respectively.

AERONET's sun-photometers measure aerosol properties throughout the aerosol column. In the West Africa region, according to aerosol vertical profile presented in Haywood et al. (2008), there is the possibility of a warm layer of biomass burning aerosols overlaying a deserts dust layer due to advection of different air masses. A reverse situation is very unlikely as biomass burning aerosol are always warmer. This might result in a 'contamination' of the desert dust (DD) cluster identified in this study by biomass burning (BB) aerosols. This overlay of BB aerosol layer on the DD aerosol layer could possibly explain the relatively high EAE value for the DD cluster (see Table 6.1). Hence, the DD cluster is not pure but rather DD-dominant cluster. During the WAM months, air masses from the south are advected north in the WAM along the surface to the Ilorin AERONET site. Mari et al. (2011); Reeves et al. (2010) shows that for majority of the time during the WAM months, no other aerosols exist in the column aloft the aerosol layer from the south around the Gulf of Guinea.

6.6.2 Seasonal dynamics of aerosol absorption: single scattering albedo (SSA)

Single scattering albedo (SSA) of atmospheric aerosols is an important parameter in estimating the radiative effect of the aerosol. SSA plays a prominent role in determining the sign of the radiative effect, hence its cooling/warming potential; it ranges from 0 (zero) for a purely absorbing aerosol to 1 for a purely scattering aerosol.

During the WAM months (MJJA), the average monthly SSA decreases with increasing wavelength (see the green ellipses in Figure 6.5), and slightly increases with increasing wavelength during the non-WAM months (DJF). This decrease, between 5.2 and 5.7 %, is attributable to the fact that scattering often decreases faster than absorption with wavelength for carbonaceous particles (Bergstrom et al., 2007). SSA is also highest during these months for the five-year period shown in Figure 6.5, due, presumably, to increased concentrations of carbonaceous particles in the aerosol influx from the urban and gas flaring (industrial) regions downwind of Ilorin. SO_2, a precursor gas for atmospheric sulfate, is a major pollutant from gas flaring of ‘sour’ natural gas sources (Fawole et al., 2016b). Mixtures of sulfate and BC (carbonaceous particles) have been associated with high SSA values (Lim et al., 2014).

6.6.3 Optical and Microphysical properties of aerosol clusters

Figure 6.6 presents scatter plots of AAE (440-870 nm) versus EAE (440-870 nm), and AAE (440-870 nm) versus FMF (500 nm), to show the range of unique optical and microphysical properties exhibited by the different clusters created from the trajectory and source analysis. Scatter plots such as these have been used to classify aerosol loadings, measured remotely by sunphotometers, in terms of their compositions, nature and potential origin (Dubovik et al., 2002; Milinevsky et al., 2014; Russell et al., 2010).

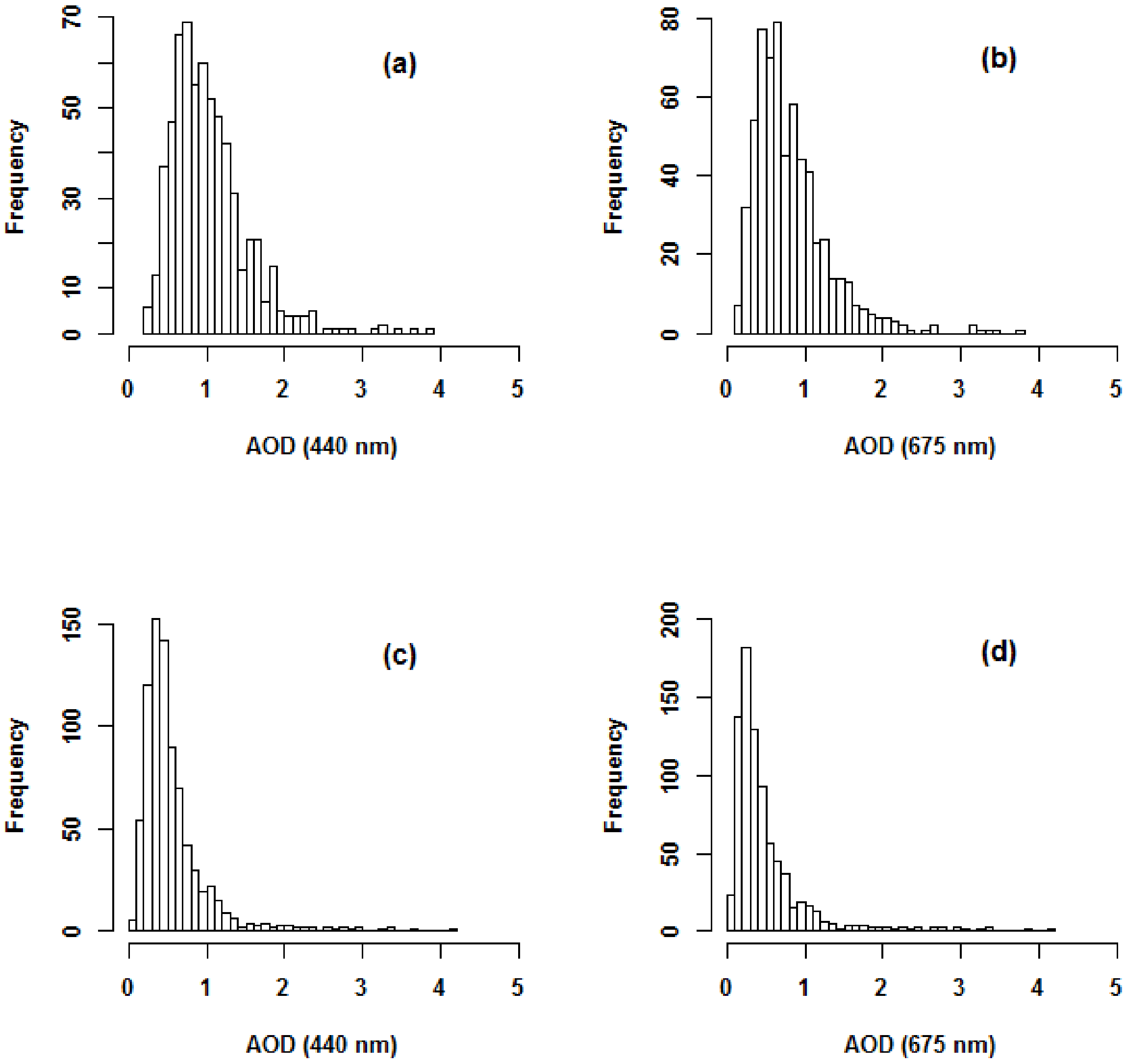

Figure 6.4: Distribution of daily variation of AOD for non-WAM months at (a) 440 nm, and (b) 675 nm; WAM months at (c) 440 nm, and (d) 675 nm over a five-year period (2005-2009). Bin widths are ∼0.1 units of AOD

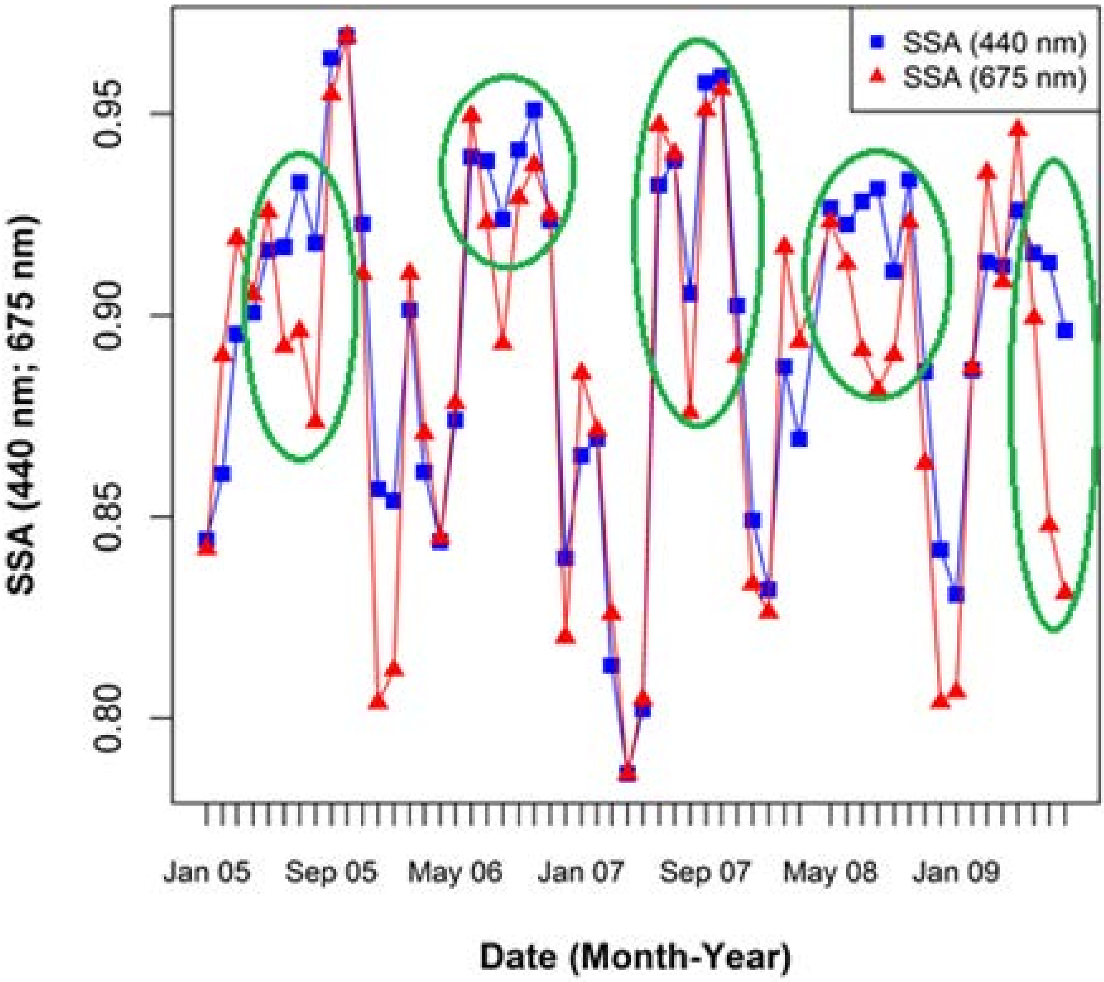

Figure 6.5: Multiyear (2005-2009) seasonal variation of SSA at 440 and 675 nm. Green eclipses denote times, during the WAM months, when SSA decreases with wavelength

Of the total number (N=810) of measurement of aerosol signatures assigned to the 'pure' clusters, BB, CC, GF and DD account for 184 (23 %), 215 (27 %), 173 (21 %) and, 238 (29 %), respectively. This suggests that gas flaring (GF) is a major contributor to the aerosol signature in the region, especially during the WAM months. The number of trajectories classified into each of the 'mixed clusters is: CC-GF (N=145); GF-DD (N=55); DD-CC (N=63); and BB-DD (N=119).

6.6.3.1 Desert Dust (DD) aerosol cluster

Desert dusts are predominant in the region with the coming of the NEH wind usually between late November and February when both the ITCZ and ITF are nearer the equator. this cluster is suggested to be 'contaminated' with BB aerosol as explained in section 6.6.1. The DD cluster is associated with high AOD (median=1.02; Q1 and Q3 are 0.72 and 1.32, respectively): the association of high AOD and low AE is typical of desert dust (Toledano et al., 2007).

As presented in Table 6.1, for the DD cluster, the range of values for the AAE and EAE are $1.64 \leq \alpha_{abs} \leq 2.34$ and $0.19 \leq \alpha_{ext} \leq 0.49$, respectively. These values corroborate findings from similar sites (Giles et al., 2012; Russell et al., 2010). The absorption potential of desert dust as shown in the SSA_{675} values, $\omega = 0.95 \pm 0.02$ in Table 6.1, are determined by the hematite (iron oxides) content of desert dust, which is a strong determinant of the radiative effect of the aerosol. As expected for aerosol in this cluster, the EAE values show a dominance of the coarse-mode fraction. Hence, this cluster can be referred to as coarse-absorbing.

6.6.3.2 Biomass burning (BB) aerosol cluster

Aerosol in this cluster is predominant in the months before the pre-onset of the WAM, i.e. between November and March. In West Africa, March is usually the peak of the dry season and, as such, intense agricultural burning takes place between November and March to

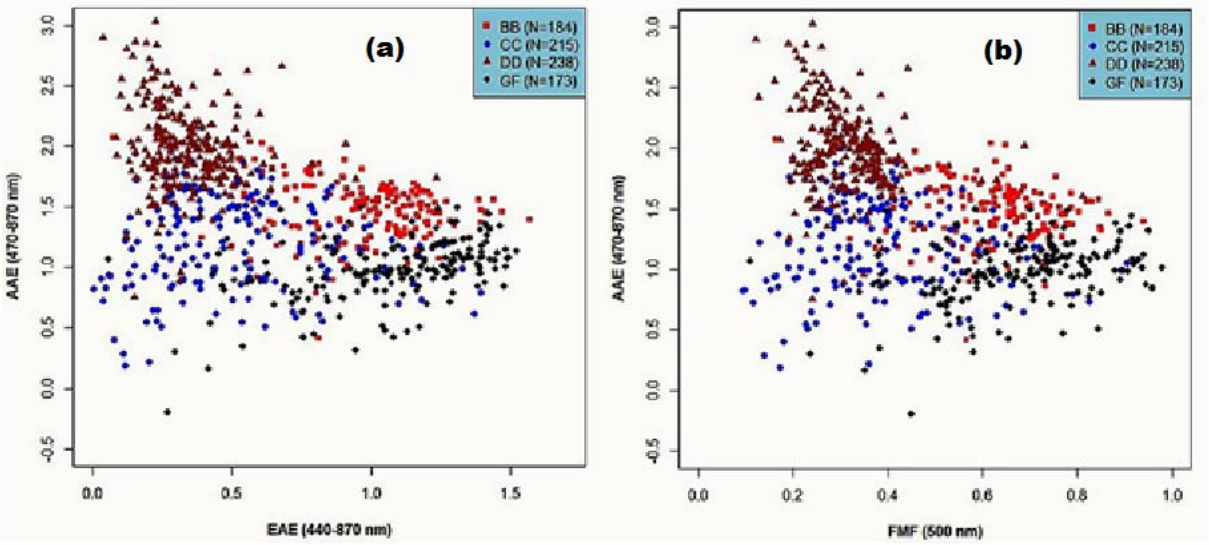

Figure 6.6: Scatter plot of (a) AAE (440-870 nm) versus EAE (440-870 nm) (b) AAE (440-870 nm) versus FMF (500 nm) for the four identified aerosol clusters

prepare the land for planting during the forthcoming rainy season. Intrusion of desert dust is also a regular occurrence within this period. The trajectory clustering enabled us to identify days of dominance of both aerosol signatures with these months (NDJFM). There are days of an almost equal contribution of trajectories from these sources (DD and BB) to the back trajectory analysis. Such days are categorised as a mixture from both sources; that is, DD-BB.

The BB cluster is characterised by high AOD and high AE values; the high AE value is evident in the EAE values shown in Table 6.1. The high carbon (brown carbon, BrC) content of biomass burning aerosols is responsible for its high absorbing nature as expressed by its SSA_{675} values ($\omega = 0.86 \pm 0.04$), the lowest of the four clusters. The ranges of the AAE and EAE values are $1.19 \leq \alpha_{abs} \leq 1.71$ and $0.73 \leq \alpha_{ext} \leq 1.23$, respectively. This cluster, similar to value from other biomass burning sites in the literature, has a relatively high FMF value, while the EAE value for this cluster is slightly lower than expected. This probably relates to the nature of vegetation burned, the aging of aerosol during transport to the measurement site, or a slight contribution from dust.

Table 6.1: Mean optical and microphysical properties of the aerosol clusters. The values in brackets are standard deviations showing the spread of the values

Aerosol properties	BB	CC	GF	DD
AAE (440-870)	1.45 (0.26)	1.21 (0.38)	0.98 (0.25)	1.99 (0.35)
EAE (440-870)	0.98 (0.25)	0.57 (0.35)	1.07 (0.29)	0.34 (0.15)
FMF (500 nm)	0.63 (0.12)	0.42 (0.18)	0.68 (0.16)	0.31 (0.08)
SSA (675 nm)	0.86 (0.04)	0.92 (0.04)	0.9 (0.06)	0.95 (0.02)

Table 6.2: Median values of optical and microphysical properties of the clusters. The values in brackets are the 25 % and 75 % percentiles

Aerosol properties	BB	CC	GF	DD
AAE (440-870)	1.47 (1.27, 1.64)	1.19 (0.93, 1.5)	0.99 (0.87, 1.14)	1.98 (1.79, 2.18)
EAE (440-870)	0.98 (0.78, 1.15)	0.51 (0.3, 0.79)	1.14 (0.95, 1.3)	0.3 (0.23, 0.41)
FMF (500 nm)	0.63 (0.53, 0.7)	0.38 (0.29, 0.53)	0.7 (0.59, 0.79)	0.3 (0.25, 0.35)
SSA (675 nm)	0.85 (0.83, 0.88)	0.93 (0.9, 0.96)	0.9 (0.84, 0.95)	0.95 (0.94, 0.97)

6.6.3.3 Urban aerosol (CC) aerosol cluster

Urban (CC) aerosol signatures are predominant in the trajectory classification between May and October; it is often most frequent between June and September (JJAS). This is due to the northwards shift of the ITCZ and ITF (as discussed in section 2.4) which allows inland influx of moist SWM wind that bring rain. This wind brings pollution laden aerosol from the large cities, Lagos and Oyo.

The CC cluster has an average SSA_{675} value of 0.92($\pm$0.04), that is, it is relatively strongly absorbing due to the presence of carbonaceous particles from combustion processes and vehicular emissions. The range of AAE values, $0.83 \leq \alpha_{abs} \leq 1.59$, is very similar to observations from similar urban sites (Giles et al., 2012). The average EAE value, compared to similar sites in literature, is lower by a factor of 2.5 which suggests the dominance of coarse-mode particles. This lower EAE values are attributable to dust re-suspension from the predominantly unpaved and damaged paved road networks that lie across major cities in Nigeria. Several in-situ PM measurements across various site classifications (residential, marine, heavy-traffic and industrial) in major Nigeria cities have reported the dominance of the coarse-mode ($PM_{2.5-10}$) PM fraction (Akinlade et al., 2015; Ezeh et al., 2012; Obioh et al., 2013; Owoade et al., 2013).

6.6.3.4 Gas flaring (GF) aerosol cluster

The gas flaring region, about 500 km south of the AERONET site, contains no fewer than 300 flaring sites scattered around the Niger Delta, a land mass of about 70, 000 km^2 (Anejionu et al., 2014; Elvidge et al., 2015). Onyeuwaoma et al. (2015), studying aerosol loading patterns in major Nigerian cities from MODIS and OMI data, identified gas flaring from the oil and gas fields in the Niger Delta area as a contributor to elevated concentrations of carbon monoxide (CO) observed in cities near the flaring region. Air mass trajectories from the gas flaring region are captured in the trajectory analysis predominantly during the WAM months.

Of the four dominant clusters identified, aerosols in the GF cluster have the lowest average AAE (0.98). This value, which is very close to the theoretical AAE value of 1 associated with BC (Bergstrom, 1973; Bohren and Huffman, 1983), is attributed to the BC component of gas flaring aerosols. There is some overlap in the AAE values of the BB and GF clusters, probably due to their both having substantial carbonaceous particle content. But their EAE values are distinct (see Figure 6.8). For the GF cluster, the ranges of the AAE and EAE values are $0.73 \leq \alpha_{abs} \leq 1.23$ and $0.78 \leq \alpha_{ext} \leq 1.36$, respectively. See Figure 6.8 for boxplots showing the spread and overlap of the different properties for the four clusters. The average SSA_{675} ($\omega = 0.9 \pm 0.06$) value for the GF cluster shows that it is more absorbing than the CC dominated aerosol cluster. Like BB-dominated aerosol cluster, aerosols in this cluster can be referred to as fine-absorbing.

Figure 6.9 presents the spread of the AAE and EAE of the four aerosol clusters identified. DD dominated aerosols are almost isolated in terms of AAE and EAE while there are varying degrees of overlaps in those of CC, BB and GF dominated aerosols. Section 6.7 presents statistical comparison of these mean values.

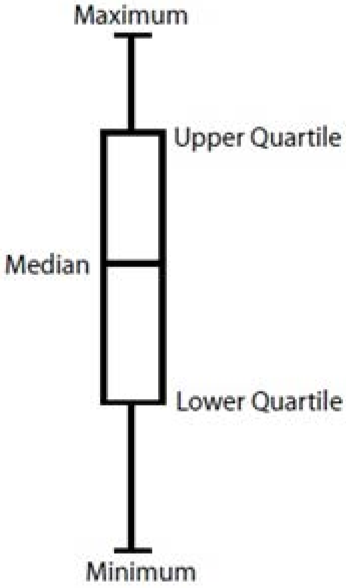

Figure 6.7: Parts of a typical boxplot

A boxplot is a typical plot used to present a quick and comprehensive summary of a dataset. Boxplots as shown in Figure 6.7, consists of boxes extending from the 1st quartile (Q1) to the 3rd quartile (Q3), an indicator of the median (Q2), and whiskers extending from the 1st quartile to the minimum, and from the 3rd quartile to the maximum (Dawson, 2011).

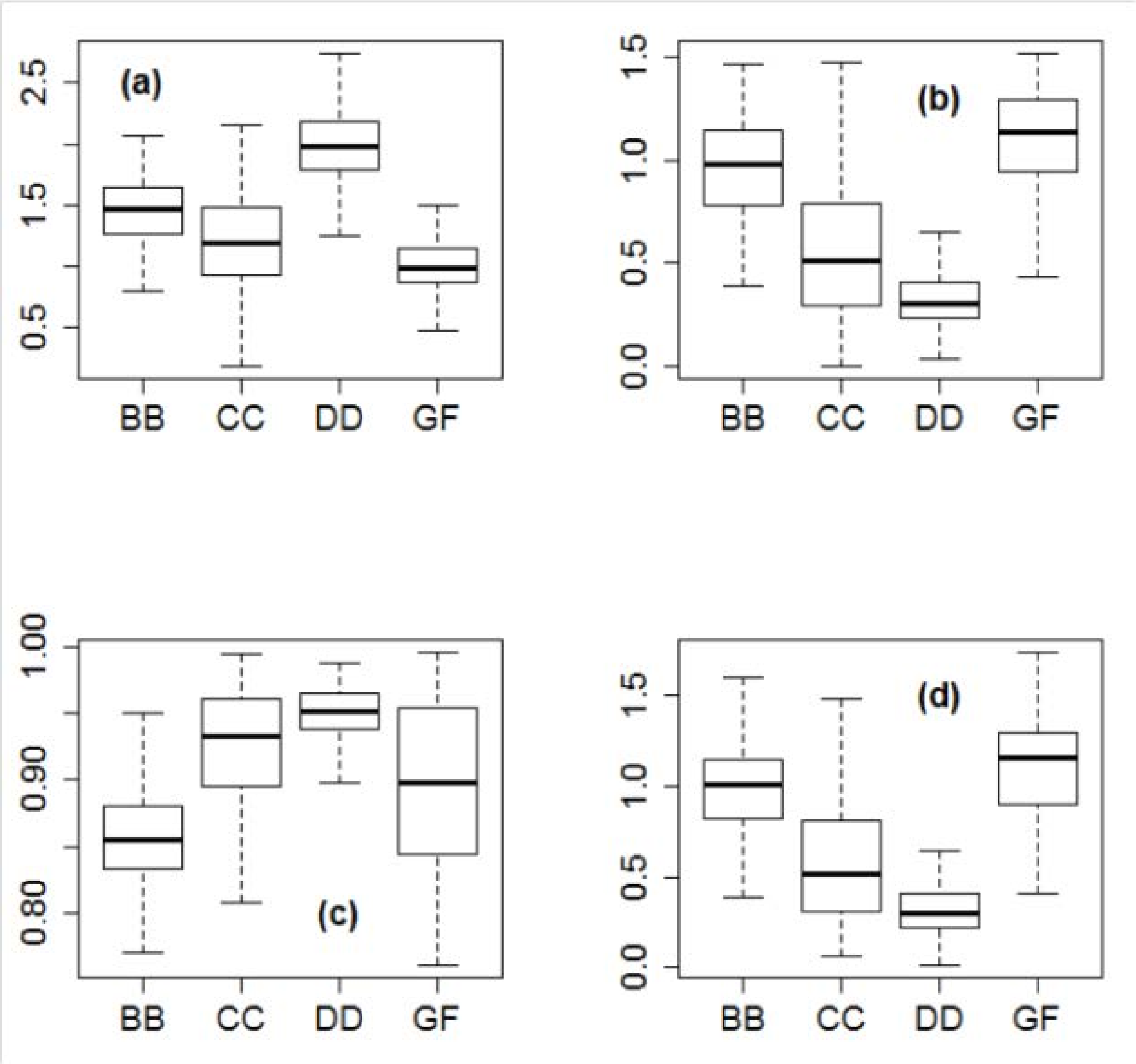

Figure 6.8: Boxplots for the four identified aerosol classes showing the statistical summaries of (a) AAE (440-870 nm); (b) EAE (440-870 nm); (c) SSA (675 nm); and (d) AE (440-870 nm)

To examine the distribution of the aerosol parameters, Table 6.2 presents the median values of the optical and microphysical properties of the four aerosol clusters identified. The skewness

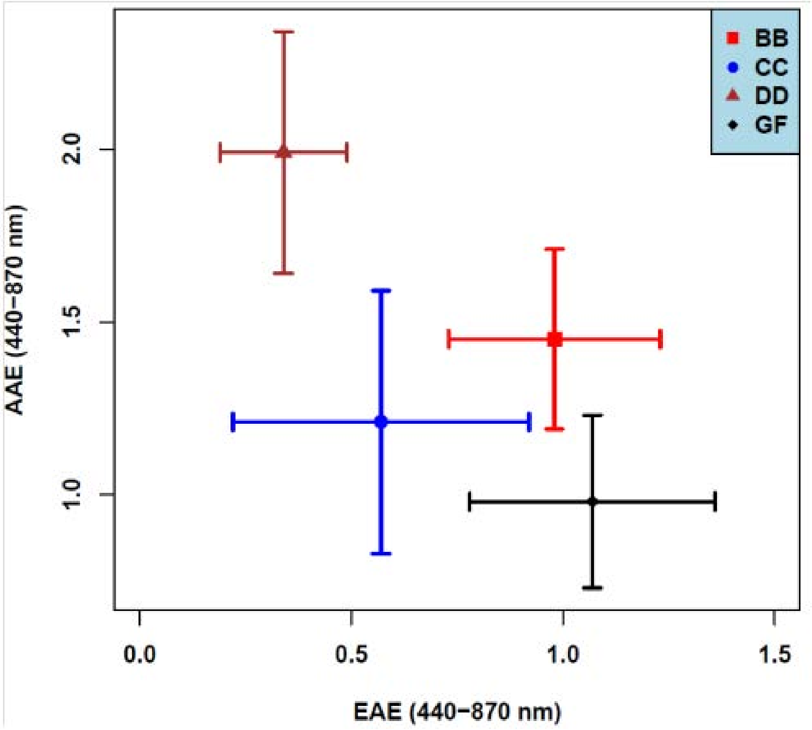

Figure 6.9: Scatterplot with X and Y error bars for the AAE versus EAE mean values for the four aerosol clusters. The error bars represents the standard deviations

of the distribution of these properties in all the clusters is very mild as shown by the closeness of the mean and median values of the aerosol parameters as shown in Tables 6.1 and 6.2.

6.7 Statistical analysis of clusters properties

As a result of overlaps in AAE and EAE values of the aerosol clusters, especially CC, BB and GF, pair-wise statistical significance tests (independent samples t-test) of AAE and EAE were performed. The comparisons carried out were between CC and GF, GF and BB and, CC and BB. We have used a confidence level (CL) of 0.95 for all the t-test analysis.

In the CC – GF pair: For the mean AAE values; t_{387} = 6.682, $p < 0.001$, we can be 99.9 % sure that the AAE mean value of the CC aerosol cluster is between 0.15 and 0.29 higher than that of the GF cluster. And, for mean EAE values; t_{387} = -15.16, $p < 0.001$, we can be 99.9 %

Table 6.3: Statistical comparison (T-test) for clusters' optical and microphysical properties

Test variable	Group	Mean diff.	Std. error diff.	p-value	t-score
AAE	**CC-GF**	0.23	0.03	<0.001	6.68
	GF-BB	-0.47	0.03	<0.001	-17.22
	CC-BB	-0.24	0.03	<0.001	-7.37
	BB-DD	-0.54	0.03	<0.001	-17.42
	CC-DD	-0.79	0.03	<0.001	-22.8
	GF-DD	-1.01	0.03	<0.001	-32.0
EAE	**CC-GF**	-0.51	0.03	<0.001	-15.16
	GF-BB	0.09	0.03	0.001	3.26
	CC-BB	-0.41	0.03	<0.001	-13.39
	BB-DD	0.64	0.02	<0.001	33.27
	CC-DD	0.23	0.02	<0.001	9.31
	GF-DD	0.74	0.02	<0.001	33.25

sure that the mean EAE value of the CC aerosol cluster is between 0.44 and 0.57 lower than that of GF.

In the GF-BB pair: For the mean AAE value; $t_{354.4}$ = -17.223, $p < 0.001$, we can be 99.9 % sure that the AAE mean value of the GF aerosol cluster is between 0.42 and 0.52 lower than that of the BB cluster. And, for mean EAE values; t_{355} = 3.256, $p = 0.001$, we can be 99.9 % sure that the mean EAE value of the GF aerosol cluster is between 0.04 and 0.15 higher than that of BB. The mean EAE values of these two clusters are close because they are both emission from combustion processes.

In the CC-BB pair: For the mean AAE value; t_{398} = -7.368, $p < 0.001$, we can be 99.9 % sure that the AAE mean value of the CC aerosol cluster is between 0.18 and 0.31 lower than that of the BB cluster. And, for mean EAE values; t_{398} = -13.386, $p < 0.001$, we can be 99.9 % sure that the mean EAE value of the CC aerosol cluster is between 0.35 and 0.47 lower than that of BB.

In the DD-BB pair: For the mean AAE value; t_{420} = -17.422, $p < 0.001$, we can be 99.9 % sure that the AAE mean value of the DD aerosol cluster is between 0.48 and 0.60 higher than that of the BB cluster. And, for mean EAE values; t_{420} = 33.265, p = <0.001, we can be 99.9 % sure that the mean EAE value of the DD aerosol cluster is between 0.61 and 0.68 lower than that of BB.

In the CC-DD pair: For the mean AAE value; t_{452} = -22.8, $p < 0.001$, we can be 99.9 % sure that the AAE mean value of the CC aerosol cluster is between 0.72 and 0.85 lower than that of the DD cluster. And, for mean EAE values; t_{452} = 9.305, p = 0.001, we can be 99.9 % sure that the mean EAE value of the CC aerosol cluster is between 0.18 and 0.28 higher than that of DD.

In the GF-DD pair: For the mean AAE value; t_{409} = -32.002, $p < 0.001$, we can be 99.9 % sure that the AAE mean value of the GF aerosol cluster is between 0.95 and 1.07 lower than that of the DD cluster. And, for mean EAE values; t_{409} = 3.256, p = <0.001, we can be 99.9 % sure that the mean EAE value of the GF aerosol cluster is between 0.69 and 0.78 higher than that of DD.

In all four (4) clusters, for both the AAE and EAE, the significance value is much less than 0.05. Hence, we can conclude that in all four clusters, (a) there are statistically significant differences between the mean AAE values; (b) there are statistically significant differences between the mean EAE values.

AAE and EAE values for the four clusters were tested for normality using the Kolmogorov-Smirnov (K-S) and Shapiro-Wilk tests. AAE values for all four clusters and EAE values for BB passed the normality test. The remaining three parameters were only mildly skewed from a normal distribution. As a confirmation of the t-test results, a non-parametric test of the parameters was undertaken using the Mann-Whitney U test (at 0.05 significance level) which does not require a normal (Gaussian) distribution (Fay and Proschan, 2010). Probably due to the number of data involved or the fact that some of the set of data are just slightly skewed, the results of both the t-test and Mann-Whitney U-test are very similar. The results of the Mann-Whitney U test show statistically significant (<0.001 significance value) differences between the compared mean values of AAE and EAE for the six pairs of clusters.

6.8 Conclusion

Earlier studies have classified the Ilorin AERONET site as dominated by dust or a mixture of dust and biomass burning aerosols. Analysis presented here for ten years of aerosol data from this site allows, for the first time, the identification and analysis of contribution of dominant sources to the mixed aerosol loading at the site. The aerosol optical depth (AOD) and Angström exponent (AE) vary significantly during the year due to a significant change in the nature and composition of dominant aerosols at the site. The months before the West African Monsoon (WAM) are characterised by aerosol with high AOD and low AE while the WAM months witness aerosols with low AOD and high AE.

Back trajectories are classified for the study period (2005-2009 and 2011-2015) and known major source contributors to aerosol loading in the region were used to create four 'pure' source-related clusters from AERONET retrievals, which vary significantly in optical and microphysical properties. Biomass burning and desert dust dominant aerosols are prominent in the pre-WAM months while gas-flaring and urban aerosols dominate the WAM months.

The unique properties and contribution of gas flaring aerosol to the overall aerosol loading underpins the need for further studies on this ‘overlooked’ source of aerosol. The optical and size properties identified for these clusters can be used to identify similar aerosol signatures for similar sites.

Chapter 7

Analysis of radiative properties and direct radiative forcing estimates of dominant aerosol clusters over an urban-desert region in West Africa

7.1 Abstract

Ilorin, Nigeria, is situated between a densely populated south and a desert-dust source region to the north, and as such, receives a varying amount and types of aerosols all year round. Ilorin has been an Aerosol Robotic Network (AERONET) observing site since the late 90s with the aim to monitor aerosol properties. Due to the strategic location of the site, it is possible to obtain information on several types of aerosol and their radiative effects. The strong reversal of wind direction occasioned by the movement of the ITCZ during the West Africa Monsoon (WAM) plays a major role in the variability of aerosol nature at this site. Aerosol optical depth (AOD) (675 nm) and Angstrom exponent (AE) (440-870 nm) with 1st and 99th percentile values of 0.08 and 2.16, and 0.11 and 1.47, respectively, confirms a highly varying nature of aerosol at this site.

In this study, direct radiative forcing (DRF) and radiative forcing efficiency (RFE) of aerosol as retrieved from the AERONET sun-photometer measurements are estimated using radiative transfer calculations for the period 2005-2009 and 2011-2015. The DRF and RFE of dominant aerosol classes – desert dust (DD), biomass burning (BB), urban (CC) and gas flaring (GF) have been estimated. Median values of DRF at top-of-atmosphere (TOA) for the DD, BB, CC and GF aerosol classes are -27.5±13.2 $\mathrm{W\,m^{-2}}$, -27.1±8.3 $\mathrm{W\,m^{-2}}$, -11.5±13.2 $\mathrm{W\,m^{-2}}$ and -9.6±8.0 $\mathrm{W\,m^{-2}}$, respectively. The median values of RFE for DD, BB, CC and GF aerosol classes are -26.2±4.1 $\mathrm{W\,m^{-2}}\delta^{-1}$, -35.2±4.6 $\mathrm{W\,m^{-2}}\delta^{-1}$, -31.0±8.4 $\mathrm{W\,m^{-2}}\delta^{-1}$ and -37.0±10.3 $\mathrm{W\,m^{-2}}\delta^{-1}$, respectively. The DD aerosol class showed the largest DRF but the smallest RFE, arguably, due to the high SSA and asymmetry factor values for this aerosol type. While having the smallest AOD, the GF aerosol class is the only class that has both cooling and warming potential of the Earth's atmosphere in the region, possible, due to the presence of black carbon and other co-emitted aerosol, and the ageing of the GF aerosols. This study presents the first estimate of DRF for gas flaring and shows that it can be of similar magnitude to desert dust, biomass burning, and urban aerosol in West Africa.

The work (data analysis and calculations) in this chapter were carried out by me. However, Prof. Rachel T. Pinker of the University of Maryland, USA provided the five-year surface reflectance data used for the DRF and RFE estimation. She also read and gave comments on the manuscript being prepared for publication. Some of her comments are used in the writing up of this chapter. A large chunk of the data and results in this chapter have been presented at 17th IUAPPA World Clean Air Congress and 9th CAA Better Air Quality conference, Busan, South Korea, and the 2015 AGU fall meeting, San Francisco, USA. As such, they are documented in conference proceedings for the conferences.

7.2 Introduction

Atmospheric aerosols perturb the Earth's radiative energy balance both indirectly and directly on regional and global scales (Charlson et al., 1992; Haywood and Shine, 1995). The ability of the aerosols to alter the amount of radiation depends on their concentration, composition, and particle size distribution. All of these determining factors vary significantly with aerosol sources. Increased concentrations of anthropogenic aerosols in the atmosphere since the pre-industrial times has been suggested to be partly responsible for the onset of global warming (IPCC, 2013).

When perturbation of the radiative budget of the Earth-atmosphere system results from the scattering and absorption of incoming solar radiation by atmospheric aerosol, the resulting radiative forcing is termed ***Direct Radiative Forcing*** (DRF). When atmospheric aerosols absorb radiation, they eventually dissipate such radiation, thereby altering the microphysical properties and lifetime of clouds, which invariably affect precipitation. Forcing resulting from such alterations is termed ***Indirect Radiative Forcing*** (IPCC, 2013). The contribution of aerosol to the total forcing due to well-mixed greenhouse gases is still associated with large uncertainties (Myhre, 2013).

The West African climate has a unique weather pattern due to the West African Monsoon (WAM) which is characterised by large-scale seasonal reversals of wind regimes (Barry and Chorley, 2009; Sultan and Janicot, 2000). Winds are south-westerly to the south of the trough and north-easterly to the North. The lack of a large mountain range in the north of West Africa strongly enhances the northward advance of the WAM compared to its South Asian counterpart. The position of the leading edge of the WAM trough may oscillate greatly from day-to-day through several degrees of latitude (Barry and Chorley, 2009). The movement of the Intertropical Convergence Zone (ITCZ) and Intertropical front (ITF) is responsible for the seasonal reversal of the prevailing wind pattern in the region. Deep convection occurs in organised systems referred to as Mesoscale Convective System (MCS) (Mathon and Laurent, 2001). MCS associated with the ITCZ can lead to rapid uplift and large scale redistribution of aerosols (Reeves et al., 2010).

In recent years, in the West Africa region, anthropogenic emissions of aerosols and gaseous pollutants have increased substantially, largely due to increasing population and industrialisation in the region. This trend is expected to continue until 2030 (Liousse et al., 2014). The dominant anthropogenic sources of aerosol at the study site are fossil fuel combustion, vehicular emission, biomass burning, and industrial emission while the dominant natural aerosol source is desert dust. Despite growing evidences in support of the impacts of anthropogenic aerosols on regional radiative budget, strict regulations on emissions are still not available in major African cities and, where they are available, they are very weak (Liousse et al., 2012).

In Nigeria, the various wind patterns and seasons are associated with different dominant aerosol types. While the North-easterly Harmattan (NEH) wind, pre-dominant in the dry season (November- February), brings desert dust and biomass burning aerosols into the region. The South-westerly monsoon (SWM) wind, associated with the onset of the WAM (April-October), brings predominantly urban and industrial aerosol which are believed to contain more carbonaceous aerosols (Knippertz et al., 2015). The properties and concentrations of these aerosol types vary significantly with the wind pattern. Studies of atmospheric aerosol and their radiative effects are very scarce in Nigeria.

In this study, the radiative properties of key aerosol types at this urban-desert station was analysed and their DRF and RFE at the TOA was estimated to provide the first estimate of climate forcing from gas-flaring aerosol in the region.

7.3 Methodology

7.3.1 Description of the AERONET site and prevailing climatic condition

The Ilorin Aerosol Robotic Network (AERONET) site (8.32^o N, 4.34^o E) is located at a site between the densely populated monsoonal forest region of the south and Sahel Savanna region of the north. There is pronounced variation in the climatic conditions of the region governed by the movement of the intertropical convergence zone (ITCZ) and intertropical front (ITF), which are responsible for the seasonal reversal of the wind direction (the West African Monsoon (WAM)).

The WAM is a coupled atmosphere-ocean-land system which is characterised by summer rainfall and winter drought (Lafore et al., 2010). The rainfall in the West African sub-region results essentially from the northward movement of the low-level monsoon airflow from March to August and the southward retreat from September to November. At their northernmost position, the humid monsoonal wind from the south meet driers and warmer air to form the ITF (Cornforth, 2012). During the dry season (November - March), the West Africa sub-region experiences strong emissions of pollutants resulting from extensive biomass burning of vegetation often from land preparation for the incoming planting season. During the wet season (May to October), the region is strongly influenced by mesoscale convective systems (MCS), which affects the compositions of the atmosphere through several ways including rapid vertical transport of aerosols to the upper troposphere (Law et al., 2010; Mari et al., 2011).

Gas flaring is a prominent and persistent source of atmospheric aerosols which includes soot (black carbon), SO_2, CO, NO_X ($NO + NO_2$), PAH and VOCs, especially in the oil-rich regions of the world (Fawole et al., 2016b). There are over 300 active flare sites in the region where an estimated 23.7 (44.4 metric tons of CO_2 equivalent) and 15.1 (28.3 metric ton of CO_2 equivalent) billion cubic meters (bcm) of natural gas is flared in 2006 and 2008, respectively (Elvidge et al., 2011; Fawole et al., 2016b). In 2012, of the 325 active flare sites identified in the Nigeria oil field, 97 ($\sim$ 30 %) ranked among the top 1000 largest flares out of the 7467 identified globally (Elvidge et al., 2015).

7.3.2 Trajectory calculation and classification

Seven-day (168 hours) back trajectories were calculated using the UK's Universities Global Atmospheric Modelling Programme (UGAMP) offline trajectory model. The model is driven by six-hourly ERA-Interim (European Centre for Medium-Range Weather Forecasts Interim Re-Analysis) wind analyses data. The trajectories of particles are calculated backward in time by interpolating these wind analysis to the current particle position. The position (latitude, longitude) and pressure were output every trajectory time step of 0.6 hours. The choice of 7-day back trajectory length is due to the atmospheric lifetime of between 5 and 9 days estimated for black carbon (BC) and particulate organic matter (POM), respectively (Cooke et al., 1997; Cooke and Wilson, 1996; Koch et al., 2009; Stier et al., 2006). Both BC and POM are major constituent of aerosol in the study area.

Prominent aerosol classes were identified for the study site in Fawole et al. (2016a) as: Biomass burning (BB), Desert dust (DD), Urban (CC) and Gas flaring (GF) aerosols. In terms of optical and microphysical properties, these classes vary significantly Fawole et al. (2016a); mixed classes (DD-BB, DD-CC, GF-CC and GF-DD) were also identified. In this study, the properties of the single-source classes was analysed to estimate their direct radiative forcing and forcing efficiency. For details of the trajectory classification and analysis of the variation of the optical and microphysical properties of the identified aerosol classes see Fawole et al. (2016a).

7.3.3 AERONET data and analysis

The absolute magnitude of aerosol radiative forcing is determined, predominantly, by the values of aerosol optical depth (AOD) and single scattering albedo (SSA), while its sign is dependent on the SSA. Both AOD and SSA vary significantly with the source of the aerosol. In this study, Version 2 Level 1.5 of AERONET data of AOD, SSA and asymmetric parameter, g, were used to estimate the DRF and RFE of anthropogenic and natural aerosol classes in the west Africa sub-region. Adequate knowledge of aerosol SSA, hemispheric backscatter fraction (b) and AOD can be used to calculate the mean TOA aerosol radiative forcing for optically thin, partially absorbing aerosol (Haywood and Shine, 1995). For sites like Ilorin, where differences in the diurnal variation of aerosol properties (extensive and intensive) can be highly pronounced, the use of monthly averages of aerosol parameters will provide only highly generalised estimates of the optical and microphysical properties of the aerosol at such a site.

One of the key properties that determine the climate forcing ability of an aerosol is the angular distribution of the light scattered by the aerosol particles (Marshall et al., 1995). The angular distribution of scattered light intensity at a specific wavelength is referred to as the Phase Function (P). The asymmetry parameter, g, an important intensive parameter of the aerosol for estimating its radiative forcing effect can be derived from P. Values of g range between -1 for entirely backscattered light to +1 for entirely forward scattered light (Andrews et al., 2006). Hemispheric backscatter fraction, b, (simply referred to as backscatter fraction below) is the ratio of the integral of the volume scattering function over the backward half solid angle divided by the integral of the volume scattered function over the full solid angle (Horvath et al., 2016).

7.3.3.1 Relationship between the asymmetry parameter and the backscatter fraction

Several studies (e.g., Kokhanovsky and Zege (1997), Marshall et al. (1995), and Wiscombe and Grams (1976)) have attempted to parameterise the backscatter fraction (b) in terms of the asymmetry parameter (g). Studies estimating aerosol DRF have either adopted an approximate relation between b and g or look-up tables of parameterisation of aerosol optical properties such as those of Hess et al. (1998) and D'Almeida et al. (1991).

In this study, assuming spherical particles, approximate relations given in equation (7.1) as cited in Horvath et al. (2016) and equation (7.2) according to Delene and Ogren (2002) have been used to estimate backscatter fraction (b) and average upscatter fraction, β, respectively.

$$b = \left[1.1\left(\frac{1}{1-g}\right)^{1.85} + 1\right]^{-1} \tag{7.1}$$

$$\beta = 0.0817 + 1.8495b + 2.9682b^2 \tag{7.2}$$

7.3.4 Aerosol Radiative Forcing

7.3.4.1 Estimating direct radiative forcing

Aerosol direct radiative forcing (DRF), ΔF, at the top of the atmosphere (TOA) is estimated using the expression derived by Charlson et al. (1992). According to Haywood and Shine (1995) the radiative transfer equation proposed by Charlson et al. (1992) is simplified as given in equation (7.3).

$$\Delta F \cong -DS_oT_{at}{}^2(1-A_c)\omega\bar{\beta}\bar{\delta}\left((1-R_s)^2 - \frac{2R_s}{\bar{\beta}}\left(\frac{1}{\omega}-1\right)\right) \tag{7.3}$$

where D is the fractional day length, ω is the spectrally weighted single scattering albedo, S_o is the Solar constant, T_{at} is the atmospheric transmission, A_c is the fractional cloud amount, R_s is the surface reflectance, $\bar{\beta}$ is the spectrally weighted backscattered fraction and, $\bar{\delta}$ is the spectrally weighted AOD. The critical value of SSA at which the DRF shifts from positive to negative is dependent on the surface albedo and asymmetric parameter, g (Haywood and Boucher, 2000; Kassianov et al., 2007). An advantage of an analytical solution for the radiative transfer equation as stated above (equation 7.3) over a radiative transfer model is an explicit dependence on individual parameters determining the radiative forcing (Chylek and Wong, 1995). As cloud cover (A_c) is a parameter in Equation 7.3, to use the expression, the assumption is that the cloud cover is above the aerosol layer which is a typical atmospheric condition in the region.

Schemes of wavelength-dependent aerosol parameters are time-consuming and quite complex to be incorporated into radiative forcing calculations and radiative transfer codes that can produce representative and accurate estimates of radiative forcing with one or two wavelength regions (Blanchet, 1982). In their study to examine the possibility of replacing aerosol parameters by wavelength-independent parameters, and the accuracy and representativeness of such average parameters, Blanchet (1982) found out that results of calculations with average parameter are in close agreement with corresponding terms at a wavelength of 700 nm. Haywood (1995), using detailed radiative transfer codes, tested the representivity of average aerosol parameter and found that results at 700 nm were quite similar to those of using the entire solar spectrum. Hence, the use of aerosol parameters at λ=675 nm, which is the closest to 700 nm in the range of wavelengths at which aerosol parameters are measured by AERONET sun-photometers, in our estimations..

Fractional day-length, Solar constant and atmospheric transmittance are assumed to be 0.5, 1370 Wm^{-2} and 0.76, respectively (Haywood and Shine, 1995). To estimate DRF and RFE of the different aerosol classes, monthly mean values of cloud amount (A_c) was obtained from the ASOS-AWOS-METAR dataset (NOAA, 1998; Yang et al., 2016) from the nearest airport (Cotonou) to the site. The surface reflectance data used are model output for albedo simulations for Ilorin (2005 – 2009) (R.T Pinker, personal communication, August 2016). Figure 7.3 presents the time series for the mean monthly surface albedo for Ilorin during

2005 – 2009. The yearly pattern of the variation is quite similar for the five-year period.

7.3.4.2 Radiative forcing efficiency

To compare the forcing potential of the various aerosol classes, the forcing efficiency was estimated using equation (7.4). Forcing efficiency, $(\frac{\Delta F}{\delta})$, is the aerosol radiative forcing per unit AOD. AOD is a major extensive property of the aerosol, which determines the magnitude of its radiative forcing. Forcing efficiency depends only on the nature and composition of the aerosol rather than its amount (Sheridan and Ogren, 1999).

$$\frac{\Delta F}{\delta} \cong -DS_oT_{at}{}^2(1-A_c)\omega\bar{\beta}\ \left((1-R_s)^2 - \frac{2R_s}{\bar{\beta}}\left(\frac{1}{\omega}-1\right)\right) \tag{7.4}$$

Virkkula et al. (2014), in their study to assess the effect of aerosol from different phases of biomass burning (flaming and smouldering) on the chemical and physical properties of airborne aerosols in the Boreal forest, used the expression in equation 7.4 to estimate the radiative forcing efficiency of biomass burning aerosols.

7.4 Results and Discussions

7.4.1 Climatology of aerosol properties

Significant variation of aerosol optical and microphysical properties in the multiyear analysis of aerosol properties at the AERONET site is a strong indication of the varying sources of aerosols at the site. The range of values, at λ=675 nm, for aerosol optical depth (AOD), single scattering albedo (SSA) and asymmetry parameter (g) are 0.04 – 3.71, 0.68 – 0.99, and 0.58 – 0.8, respectively. The variation of aerosol properties is more pronounced between the pre-WAM and WAM months due to seasonal reversal of the prevailing wind direction, and hence, a change of dominant sources of aerosols.

7.4.1.1 Temporal variability of aerosol optical depth and Angström exponent at the study site

During the NEH months (NDJF), the values of the aerosol optical depth (AOD) and Angström Exponent (AE) are 1.22±0.17 and 0.35±0.06, respectively. These are months of intense biomass burning in the West African sub-region as well as intrusion of dust from the Sahara and Sahel regions. Aerosol loading in the SWM months (April-October), are characterised by lower AOD and high AE with values of 0.62±0.23 and 1.02±0.19, respectively. Compared to AE values for similar dust sites, the relatively high average AE value of the dust aerosol in the NEH months is probably due to contributions of biomass burning aerosol at that time of the year (Fawole et al., 2016a).

The significant seasonal pattern in the AE at the site, as seen in Figure 7.1(b) and 7.1(c), is due to aerosol sources and/or changes in atmospheric transport. The Angström exponent peaks between July – September and is lowest between February and March. The lower AE values during the peak of the dry season show the strong intrusion of dust in this region at that period of the year. During the WAM months, the peak AE values between July – September coincide with the peak values of backscatter fraction (b) (see Figures 7.1(c) and 7.2(d)). This strongly suggests an increase in fine particle fraction, which is attributable to inflow of urban and industrial emissions from the south of the AERONET site.

7.4.1.2 Temporal variability of single scattering albedo and backscatter fraction (b)

There are significant differences in the relative amount of scattering and absorption of aerosols at different periods of the year. These differences result in the variation of SSA during the year as shown Figures 7.2(a) and 7.2(b). During the SWM months, as shown in the multiyear daily and mean monthly single scattering albedo (SSA) values in Figures 7.2(a) and 7.2(b), respectively, inland flow of south-westerly monsoon winds are rich in partially absorbing

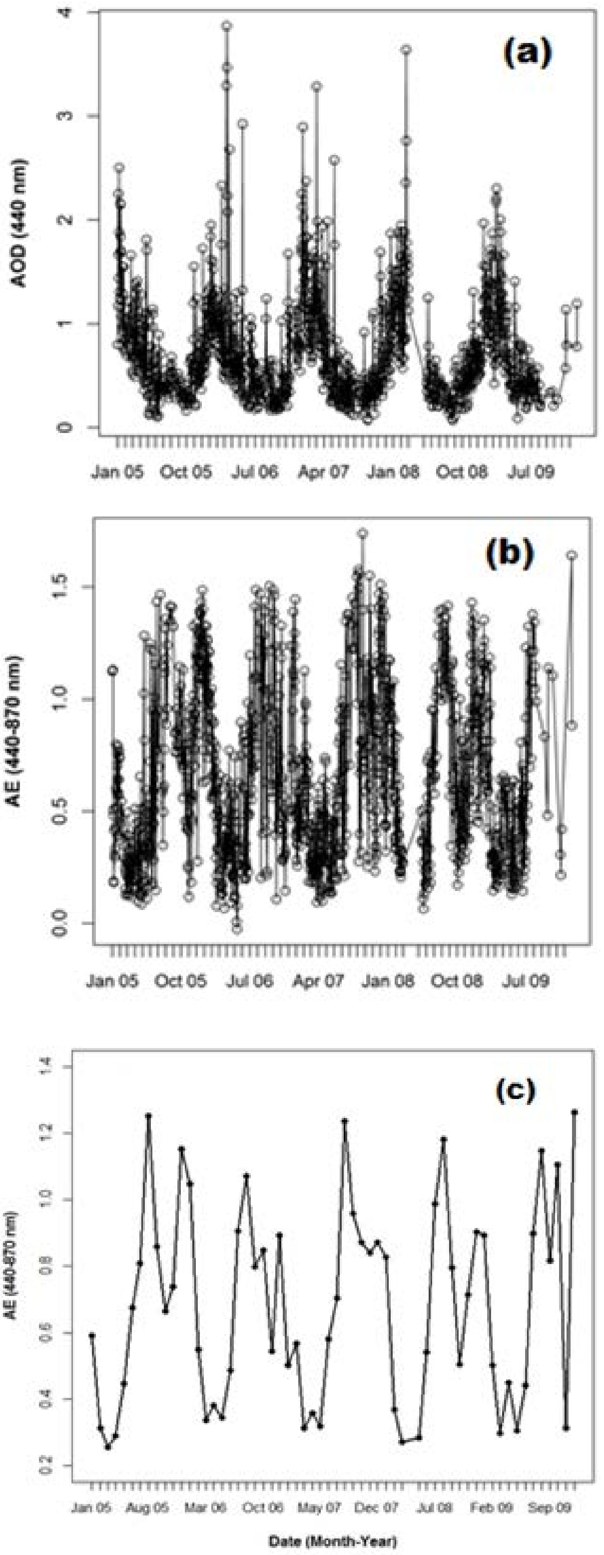

Figure 7.1: Multiyear daily variation of (a) AOD, (b) Angstrom exponent (AE), and (c) multiyear mean monthly variation of AE

aerosols from the urban and industrial site including gas flaring emissions from the intense gas flaring activities in the Niger Delta region. In Figure 7.2(b), the WAM months (April – August) exhibit the widest range of SSA (0.66 - 0.98) which could result in a wider range of DRF. This wide range of SSA could be attributable to the diverse nature of aerosol in the urban and industrial emissions from the south of Ilorin.

The boxplots in Figure 7.2(d) show a steady increase in the backscatter fraction from the lowest average values of 0.07±0.01 during March (peak of the NEH months) to the highest average values of 0.1±0.02 during the peak of the WAM months. The NEH and WAM months median backscatter fraction values correspond to asymmetric parameter *(g)* values of 0.72±0.1 and 0.61±0.1, respectively. This arguably suggests a steady increase in the concentration of fine-mode aerosol fraction during the WAM months which is attributable to increased inflow of combustion aerosols from urban and industrial emissions. Mie theory predicts a higher backscatter fraction for fine-mode spherical aerosol particles (Andrews et al., 2011). The wide range of backscatter fraction during the NEH months (NDJF) is due to mixture of biomass burning and intrusion of desert dust which are intense during the Harmattan haze period in the region. The mean monthly value of backscatter fraction in Figure 7.2(d) shows a bi-modal distribution with peaks during the intense biomass burning season (NDJ) and the peak of the WAM months (July-August) when the ITCZ is northernmost allowing enhanced inland flow of aerosol from south of the AERONET site.

7.4.2 Variability of Angström exponent and aerosol optical depth for the different aerosol classes

The average values of the optical and microphysical properties of the different aerosol classes are presented in Table 7.1. Unless otherwise stated, average values of aerosol parameters are reported at 675 nm. The Angström exponents (AE) discussed for the aerosol classes are estimated using the 440 nm and 870 nm wavelength pair. The highly varying range of AOD_{440} and AE values; 0.07 – 3.87 and 0.01 – 1.74 for AOD and AE, respectively, strongly

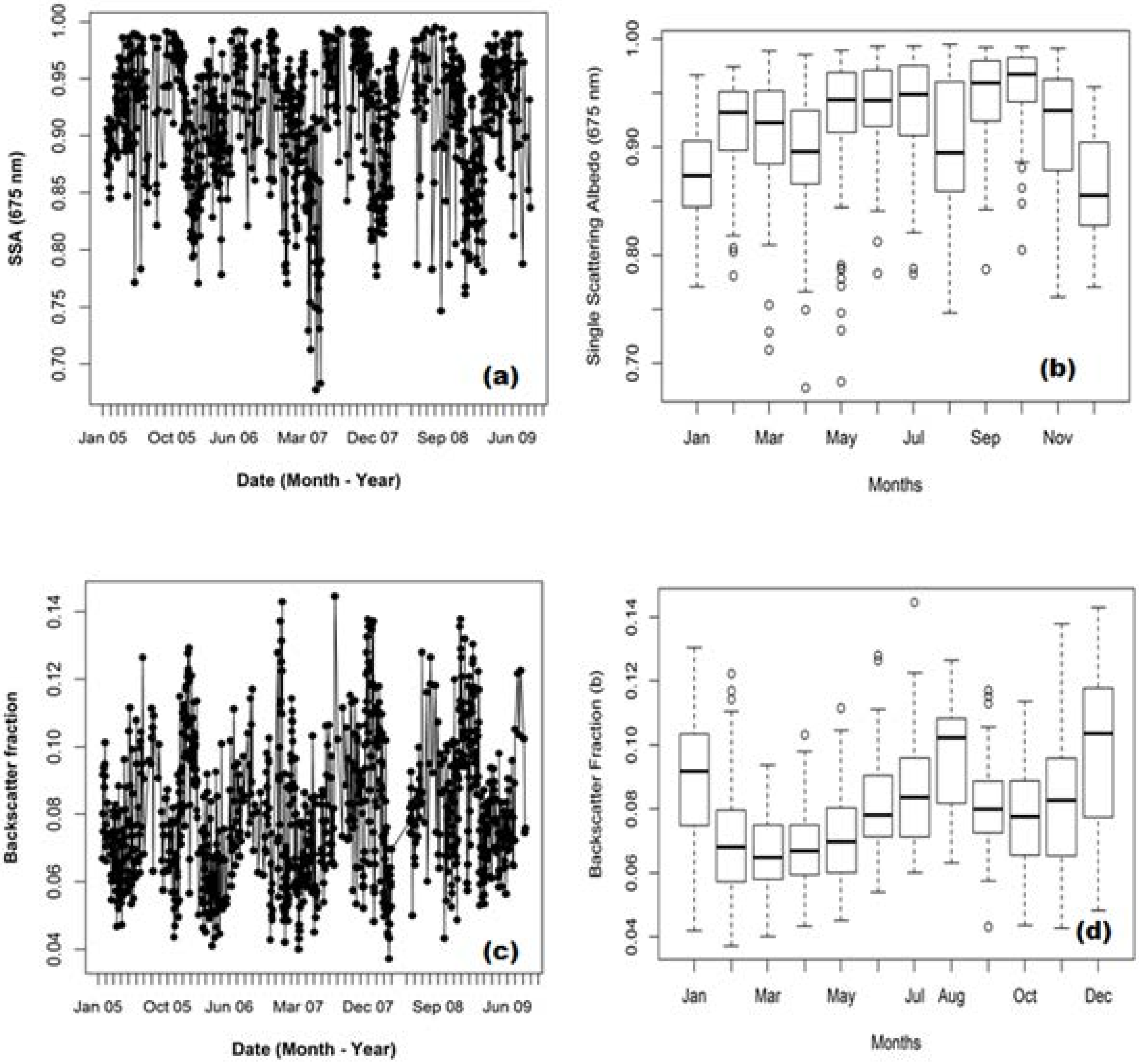

Figure 7.2: (a) diurnal variation of SSA (675 nm), (b) mean monthly variation of SSA (675 nm), (c) diurnal variation of backscatter fraction, and (d) mean monthly variation of backscatter fraction for 2005-2009

suggests a broad range of contributing sources to the aerosol loading at the study site. As the distribution of most of the aerosol parameters for the classes are slightly non-Gaussian, the median values are reported with the standard deviation given in brackets.

7.4.2.1 Desert dust

The DD aerosol class consists of 238 days of aerosol signals, which are predominant in the NEH months and the early days of the onset of WAM months. The major source of desert dust considered in this class classification is the Sahara and Sahel dust regions (13 – 18^o N; 6 – 17^o E). The median values of AOD_{440} and AE for this aerosol class is 1.13(0.54) and 0.3(0.12), respectively. These values agree well with those from studies from similar sites in the Bodélé depression of Northern Chad (Todd et al., 2007) and China (Wang et al., 2004). The average value for AOD is highest for the desert dust class while AE is the least. With a median SSA value of 0.95(0.02), this class is the least absorbing.

7.4.2.2 Urban aerosol

The aerosol signature in the urban aerosol class is prominent in the WAM months when the south-westerly moist monsoon wind is prevalent in the region. For this class, the Median AOD_{440} and AE values are 0.53(0.35) and 0.52(0.34), respectively. Even though this AE value is low, it is still higher than that for the DD aerosol class. The DD aerosol class is expected to contain a higher fraction of coarse aerosol. This class of aerosol (Urban), with a median value of SSA of 0.93(0.04), is partially absorbing arguably due to increased carbonaceous particle content from anthropogenic sources in the urban area.

7.4.2.3 Gas flaring aerosol

This class is similar to the urban class but has a lower median value of AOD_{440} and an average AE value, which is higher than that of the urban aerosol by a factor of $\sim$2. For this class, the median values of AOD_{440} and AE values are 0.41(0.26) and 1.16(0.29), respectively. A median value of SSA of 0.9(0.06) makes it more absorbing than the urban aerosol class, which is attributable to it having a relatively higher carbonaceous particulate content. This class is estimated to have an average Absorption Angstrom Exponent (AAE) of 0.98±0.25 in contrast to urban aerosols, which has an AAE value of 1.2±0.38 (Fawole et al., 2016a). The gas-flaring region, south of the AERONET site, contains more than 300 active flares (Elvidge et al., 2015), where it is estimated that more than 25 % of the annual natural gas production is flared (Anejionu et al., 2015a; Elvidge et al., 2009; Ite and Ibok, 2013).

Gas flaring, a prominent source of soot (BC), also emit other pollutants including volatile organic compounds (VOCs), SO_2, NO_X, some of which exert a cooling effect on the climate (USEPA, 2012).

7.4.2.4 Biomass burning

The BB aerosol class is characterised by high AOD and high AE, which is typical of biomass burning sites. It is prevalent almost at the same time as the desert dust season during the NEH months. For this class, the median values of AOD_{440} and AE are 0.93(0.3) and 1.0(0.25), respectively. The range of values for AOD_{440} and AE are in agreement with values reported by (Ogunjobi et al., 2008) and (Pace et al., 2006) for similar biomass burning sites in West Africa and around Central Mediterranean, respectively. The region of biomass burning considered in the classification of this class are (i) 6.5 – 11.5^{o}N; 3^o W – 3^o E and (ii) 6.5 – 11.5^o N; 13.6 – 22.5^o E. The choice of these BB regions are made based on data obtained from MODIS active fire detection over Africa (Roberts et al., 2009). In agreement with reports from previous studies from similar sites, this class, with median SSA value of 0.85(0.04), the most absorbing class, presumably due to its enhanced organic carbon (OC) content.

Table 7.2 presents the mean monthly surface reflectance, Rs, and cloud amount used in the DRF estimation; sources of these parameters are stated in section 7.3.4.1

Table 7.1: Summary of parameter for aerosol classes used to estimate their DRF

	Backscatter fraction (b)	**AOD (675 nm)**	**Asymmetric parameter (675 nm)**	**SSA (675 nm)**	**DRF** $\mathrm{W\,m^{-2}}$	**RFE** $\mathrm{W\,m^{-2}}\delta^{-1}$
DD	0.06±0.01	1.07±0.51	0.73±0.02	0.95±0.02	-28.3±13.2	-29.5±4.1
BB	0.1±0.02	0.66±0.26	0.65±0.03	0.86±0.04	-23.2±8.3	-35.4±4.6
CC	0.08±0.02	0.5±0.35	0.7±0.03	0.93±0.04	-16.2±13.2	-30.8±8.4
GF	0.1±0.02	0.31±0.22	0.66±0.04	0.9±0.06	-11.2±8.0	-37.3±10.3

Table 7.2: Mean monthly surface reflectance and cloud amount used

	Jan	**Feb**	**Mar**	**Apr**	**May**	**Jun**	**Jul**	**Aug**	**Sep**	**Oct**	**Nov**	**Dec**
$\mathbf{R_s}$	0.13	0.14	0.15	0.15	0.15	0.14	0.14	0.14	0.13	0.13	0.12	0.12
Cloud amount	0.22	0.35	0.34	0.33	0.33	0.37	0.36	0.39	0.37	0.36	0.32	0.15

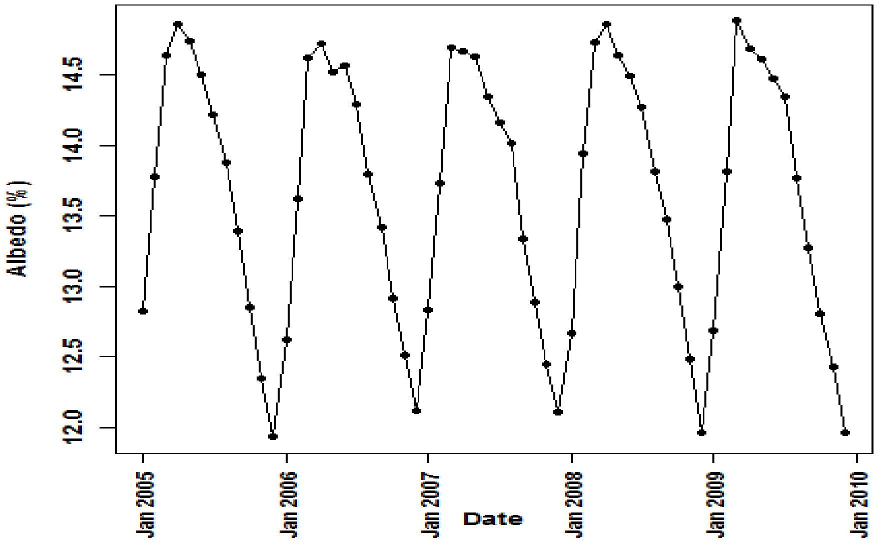

Figure 7.3: Time series for monthly mean surface albedo at Ilorin for the period (01/2005 – 01/2009)

7.4.3 Aerosol radiative forcing

Using the relationship in equation (7.3), the direct radiative forcing (DRF) for each class at the top-of-the-atmosphere (TOA) was estimated. The values of surface reflectance, R_S, and cloud amount used in the estimations range between 0.12 – 0.15 and 0.15 – 0.39, respectively. Table 7.1 presents, for each cluster, the range of values of τ, ω, b used in the estimation of DRF. The daily average values of these aerosol parameters were used for the DRF estimations of the four classes.

Figure 7.4 presents the variation of the DRF estimates at TOA for each aerosol cluster. The DD aerosol class with median AOD_{675} value of 1.07(0.51) has the highest DRF of -28.3±13.2 Wm^{-2} at TOA. Of the four classes identified, this class has the highest mean AOD. The median DRF value for this class, as shown in Figure 7.4 is highest. The high DRF value is believed to be due to the high AOD (1.07±0.51) of this aerosol cluster, and the largest asymmetry factor, g, of 0.73±0.02, which causes more forward scattering of incoming radiation, compared to the other aerosol classes. Thus, consistent with the findings of (Garcıa et al., 2012), this class has the most effective cooling effect on the earth-atmosphere system at the TOA in the region.

The biomass burning (BB) aerosols class has an estimated DRF of -23.2±8.2 Wm^{-2} at TOA with average AOD_{675} value of 0.66(0.26). Compared to the DD class, this class has a relatively shorter range of DRF. This value of DRF is comparable to the mean DRF obtained by García et al. (2011) and Yoon et al. (2005) for similar biomass burning site in South America and South Africa, respectively. Compared to the DD and BB aerosol classes, the urban (CC) class exerts a smaller cooling effect. This class (urban) with average AOD_{675} of 0.5(0.35), believed to be rich in anthropogenic urban aerosol is estimated to have a DRF value of -16.2±13.2 Wm^{-2}. In a similar study by Yoon et al. (2005), similar values of DRF was obtained for US East Coast (Goddard Space Flight Center (GSFC)), a heavily populated urban area. The GF class is the only DRF distribution that contains any positive DRF values. With DRF value of -11.2±8.0 Wm^{-2} (AOD_{675} = 0.31±0.22), the GF class has the least cooling effect at TOA. The GF class is believe to be rich in fossil fuel combustion emissions including sulfate and black carbon (Fawole et al., 2016b).

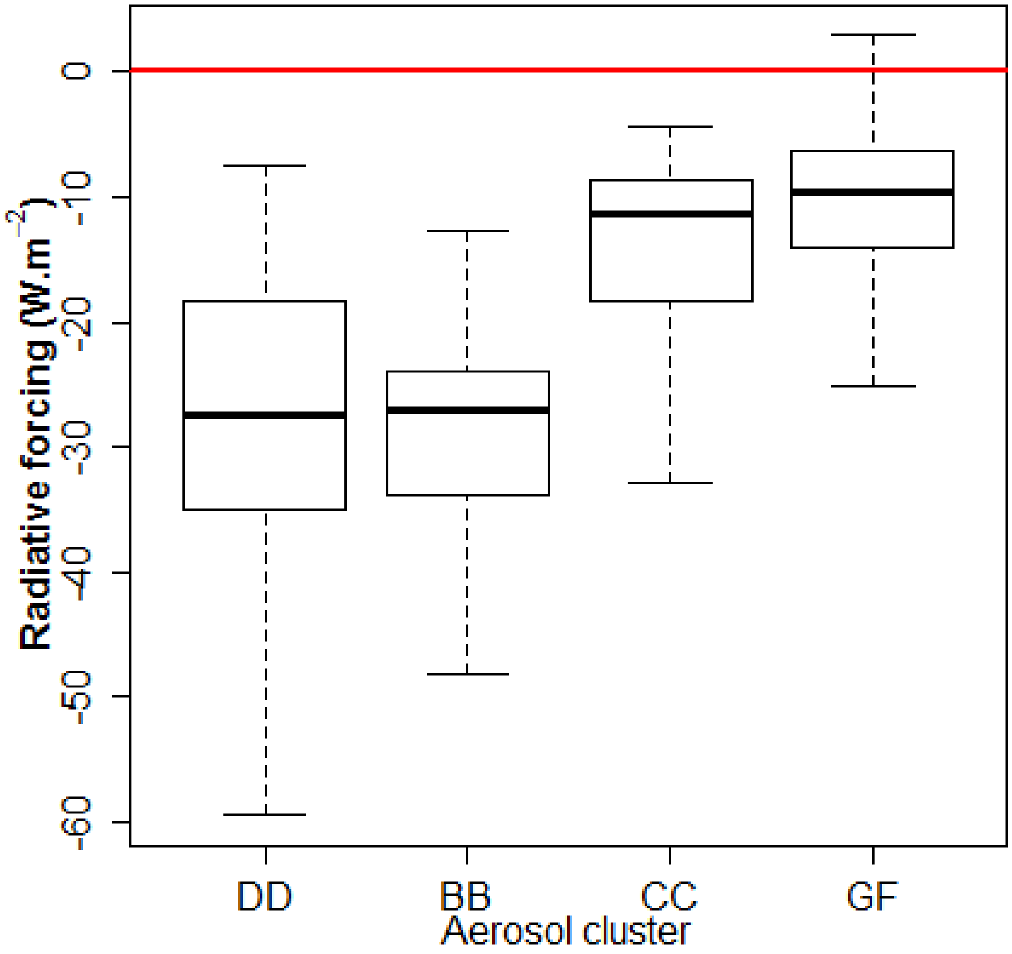

Figure 7.4: Direct radiative forcing (DRF) at the TOA for the different aerosol classes

7.4.4 Radiative forcing efficiency (RFE)

The absolute magnitude of the DRF is dependent not only on the amount of radiation entering the atmosphere but also on the quantity of aerosol perturbing the atmosphere (Bush and

Valero, 2003). For a better understanding of the impact of aerosol optical depth (AOD) on the estimation of aerosol DRF, the radiative forcing efficiency (RFE) of the different classes was estimated using equation (7.4). Since RFE is independent of AOD, it is a useful tool to compare the forcing efficiencies of different aerosol types. As such, the influences of other variables, such as SSA, absorption and scattering properties and, surface albedo may become more evident (Garcıa et al., 2012).

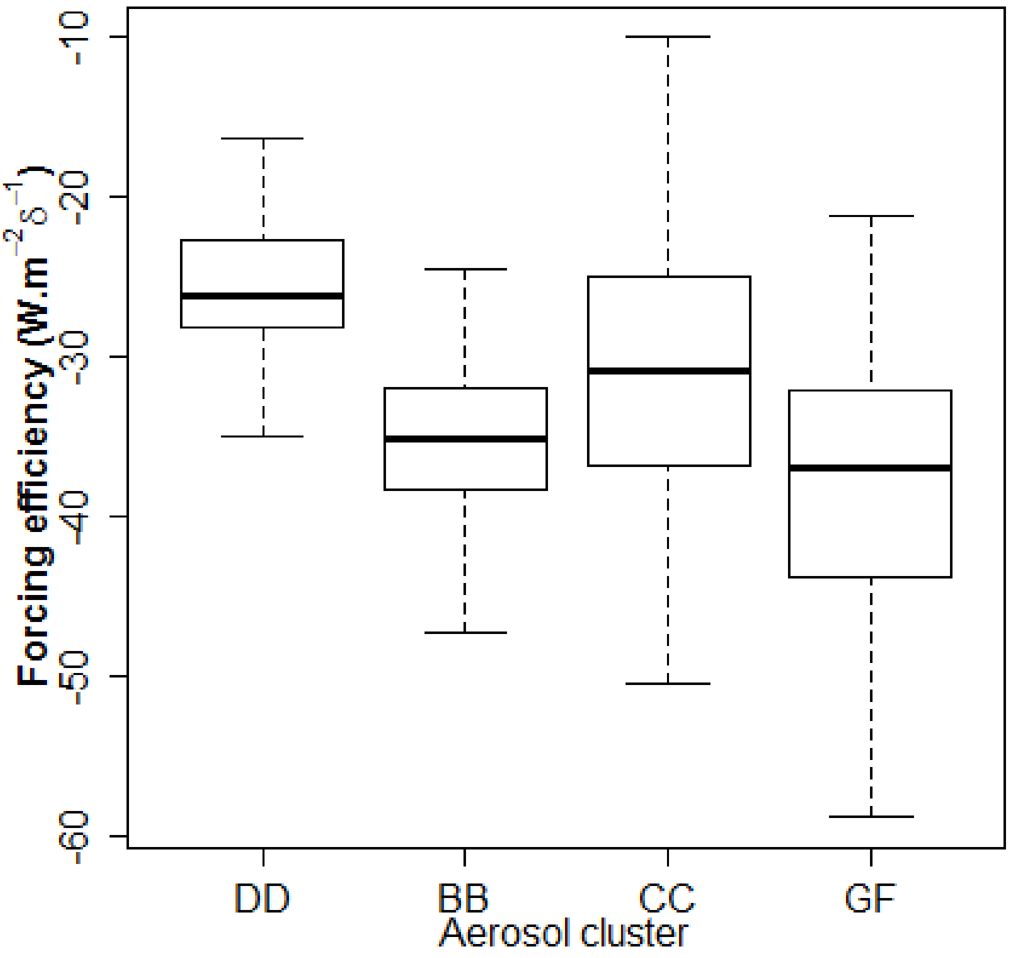

Figure 7.5: Radiative forcing efficiency (RFE) for the different classes

Figure 7.5 shows the variation of the RFE for the different aerosol classes. The natural aerosol; desert dust (DD), has the least average RFE of -29.5±5.0 $Wm^{-2}\delta^{-1}$. The BB aerosol class, like the DD class, has a short range of RFE, but a higher mean RFE value of -35.4±4.6 $Wm^{-2}\delta^{-1}$. The CC and GF aerosol classes have average RFE of -30.8±8.4 and -37.3±10.3, respectively. The GF aerosol class has the highest RFE. These two classes (CC and GF), compared to the DD and BB aerosol classes, have relatively wider ranges of RFE. Hence, aerosols in these two classes have the ability to perturb the Earth-atmosphere system more in this region.

Figure 7.6 presents the relationship between DRF and aerosol optical depth AOD_{675} for the different aerosol types. The slope of best-fit line, shown in red in Figure 7.6, gives the average forcing efficiency, equivalent to the estimations in equation. (7.4).

7.5 Conclusion

The variations of the aerosol optical and microphysical parameters – AOD, SSA, asymmetric parameter, Angstrom exponent and backscatter fraction – were studied for the West African sub-region using AERONET retrievals from Ilorin, Nigeria. The DD aerosol class is characterised by high AOD and low AE. The BB aerosol class is characterised by high AOD and high AE while the GF class is characterised by low AOD and high AE. The direct radiative forcing of various dominant aerosol types has been estimated using aerosol parameters from AERONET retrievals as inputs in a simplified radiative transfer equation proposed by Haywood and Shine (1995). Due to differences in methodologies and varying aerosol sources/nature, it is difficult to directly compare results (average DRF values) from literature. Desert dust (DD) and biomass burning aerosols were found to be the most effective cooling aerosol at the TOA in the region. CC and GF aerosol classes, suggested to be rich in emissions from the combustion of fossil fuel, that is, black carbon and sulfate, have less cooling effects. The more absorbing aerosols (GF and BB) show the higher forcing efficiency;

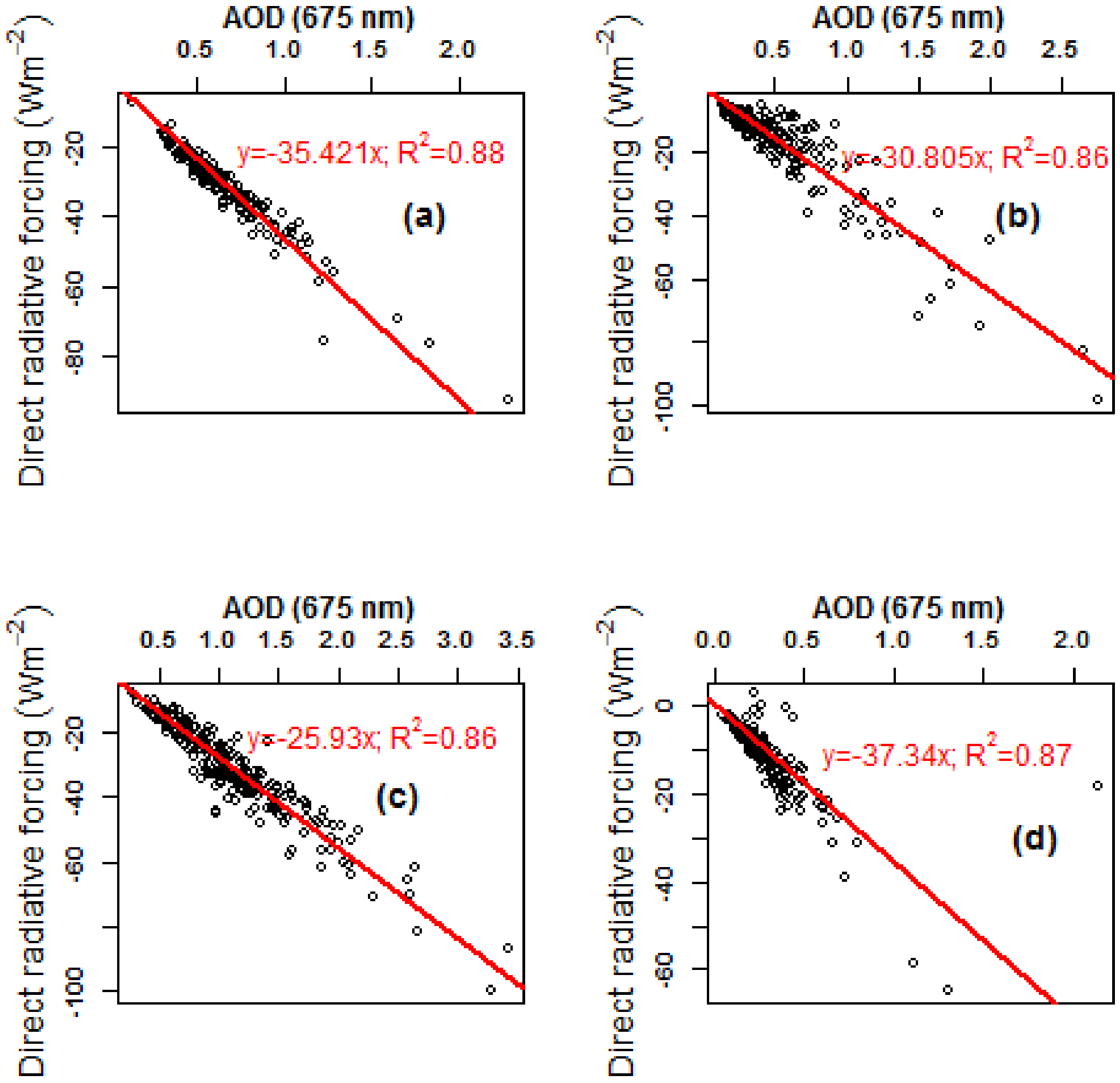

Figure 7.6: The relationship between DRF and AOD (675 nm) for (a) Biomass burning (n=184) (b) Urban (n=215) (c) Desert dust (n=238) (d) Gas flaring (n=180) aerosol classes

and, GF aerosol class, the largest variability in RFE. These results suggest the need for concerted efforts to adequately characterise and quantify emissions from real-world gas flares as they make significant contributions to the radiative transfer in the Earth-atmosphere system, particularly in oil-rich regions, where gas flaring is persistent, continuous and substantial. To the best of our knowledge, this is the first estimate of DRF for gas-flaring dominant aerosol class.

Chapter 8

Summary and future works

This chapter will present a summary of the different aspects of the work carried out and reported in this thesis. A general overview of the important findings and inferences drawn from the various sections of the work is collated here. Recommendations are also made to policy-makers, researchers and scientist based on findings from this study. Finally, areas of the study to be further explored in the nearest future are identified and discussed.

8.1 Summary

8.1.1 Development of a model to estimate emission factors and combustion parameters

As a result of the gaps and shortcomings identified in the literature, this study carried out the development of a model to estimate the emissions of carbon-containing pollutants from typical gas flares. Emissions estimation outputs from the model are fuel composition and combustion process dependent, a major improvement it has over earlier estimations. The model also provides estimates of combustion parameters such as quantity of heat given off, flame length, buoyancy flux, momentum flux, effective stack height, et cetera. The model requires the composition (as percentage of the total volume flared) of each chemical component of the natural gas flared (which is made up of alkanes with trace amounts of other organic compounds, and sulphur compounds), the amount of oxygen available for the combustion (defined using the equivalence ratio), stack geometry and environmental variables (ambient temperature and pressure).

Using two fuel gas of highly different compositions, and hence, significantly varying thermodynamic properties, this study found out that a difference of 0.04 in the mass weighted carbon-to-hydrogen (C:H) ratio results in increases of factors of about 3, 1.4 and 1.7 in the emission factors of soot, carbon monoxide and carbon dioxide. There is also a very significant dependence of soot, carbon monoxide and carbon dioxide on the equivalence ratio. Overall, findings from the model output show the great dependence of emission yields on the composition of the fuel and extent of completeness of the combustion which is determined by the amount of oxygen (equivalence ratio, ϕ) available for the combustion.

8.1.2 Atmospheric dispersion of gas flaring emissions

During the non-WAM months, the dispersion of pollutants from gas flares in the Niger Delta are towards both the inland and coastal communities; though at a lower level of concentration compared to the WAM months. Dispersion of pollutants (BC and GHGs) towards the coastal communities increases level of aerosol optical depth over the Ocean, where surface reflectance is highly variant and dependent on the level of AOD. This will alter the Earth radiative budget over the ocean in a different way to that on land. The ground-level concentrations of pollutants are greater during the WAM months and are dispersed predominantly in the north-eastern direction from the flares. During the WAM months, it is suggested that people in the communities should spend lesser times out-doors and reduce inflow of outdoor air into their indoor environments.

Denser fuel composition and higher fuel flow flux enhances the buoyancy flux and momentum flux of the plume exiting the stack. Buoyant plumes are dispersed further down from the flare and gives rise to lower ground-level concentrations. Rather than flare gas from "small" flares, linking two or more of such flares together to enhance the volume flow flux with will increase the buoyancy flux and momentum flux, and hence, reduce ground-level concentration level.

8.1.3 Evidence of contribution of a gas flaring sources to alkane and enhancement of ozone levels in West Africa

Of the several scientific flights conducted during the AMMA campaign between July and August 2006, flights B222, B228 and B231 passed over or very near to Nigeria and are suggested to have sampled air parcels impacted by urban emission from Lagos and gas flaring emissions from the Niger Delta. Of these three AMMA flights (B222, B228 and B231), back-trajectory analysis strongly suggest that flights B228 and B231 sampled air parcels that have been impacted by gas flaring emission from the Niger Delta; while air parcels sampled on flight B222 are impacted more by urban emission from Lagos. Strongly enhanced levels of alkane species and accompanying carbon monoxide levels sampled on flight B228 and B231 are attributable to gas flaring emission. These enhanced levels of alkane species and accompanying elevated carbon monoxide levels are thought to be responsible for the enhanced level of ozone which is in excess of 100 ppb. Levels of CO and alkane species sampled on flight B222 are less than those sampled on flight B228 and B231.

Results from this analysis suggests that gas flaring is a significant contributor to aerosol loadings in the region. As such, there is the need for further studies to characterise and quantify emissions from gas flares in the region, so as to quantify the extent of contributions from gas flaring to atmospheric aerosol loadings in the region.

8.1.4 Classification and properties of aerosol parameters from AERONET retrievals

Aerosol parameters retrieved from the Ilorin AERONET site indicate that sources of aerosol at the site are diverse. Using adequate knowledge of major sources of atmospheric aerosol in the region and back trajectory analysis over a 10-year period (2005-2009 and 2011-2015), aerosol at the site were clustered into four classes; biomass burning (BB), urban (CC), desert dust (DD) and gas flaring (GF). There are also mixed clusters - DD-BB, DD-CC, GF-CC and GF-DD- which were not investigated further in this study.

These aerosol clusters are significantly different from one another in term of their optical and microphysical properties. The GF aerosol class has a mean Absorption Angstrom Exponent (AAE) of 0.98, a value very close to 1; the typical AAE value of black carbon. Using statistical analysis tools, the differences between the mean values of the Absorption Angstrom Exponent (AAE) and Extinction Angstrom Exponent (EAE) of the four aerosol classes are found to be statistically significant. The BB and DD aerosols are predominant in the non-WAM months while the GF and CC aerosol are predominant in the WAM months.

Results of the direct radiative forcing (DRF) and radiative forcing efficiency (RFE) calculations for the four classes of aerosol identified at the site shows that aerosol from gas flaring (GF) might be a significant contributor to local DRF around Ilorin considering the proximity of the flares to the Ilorin AERONET site. BB aerosol could possibly contribute more to the DRF on a regional scale considering the widespread of BB aerosol sources across West Africa. The RFE estimates suggest that GF aerosols have the potential to perturb the Earth-atmosphere system more than the other classes of aerosol in this region.

8.2 Recommendations

It is highly recommended that further studies be undertaken to adequately characterise and quantify emissions from flares in the region to be able to quantify their contributions to atmospheric loadings of aerosol and gaseous pollutants. A short-term mitigation option for acute pollution from flaring may be to encourage operators of "small" flares to link up two or more of such flares to enhance the volume flow rate as well as build taller stacks so as reduce ground-level concentration of pollutant.

Appropriate agencies should enlighten the populace of the need to spend less time outdoors during the WAM months when the ground-level concentrations are higher and mostly dispersed towards the inland communities.

Appropriate government agencies should also encourage and probably mandate oil companies in the region to make available data needed to assess and quantify emissions from their gas flares.

8.3 Future works

The initial conception of this study was to carry out an assessment of the contribution of gas flaring emissions to ambient air pollution on local and regional scales. But after a thorough review of literature, a gap was discovered in the estimates of emissions, especially black carbon, from gas flaring processes. This prompted the idea of developing a model whose estimates of emissions from the combustion of hydrocarbons, typical of gas flares, will be dependent on the fuel composition and some combustion parameter. The model that was developed, though not yet comprehensive, provide estimates of carbon-containing emissions which vary with fuel composition and combustion parameter. These estimates compare favourably well with the few estimates available in the literature, especially for carbon monoxide and carbon dioxide.

In the very near future, further validation and update of the model will be carried out in collaboration with academics, that have done some work of estimating emissions from gas flares, from the department of Chemical Engineering in my home university (Obafemi Awolowo University, Nigeria). Probably set up a flare pilot study, whose output will find direct and easy application in updating the model, if the necessary funds are obtained.

A further comparison of the properties (optical and microphysical) of the four aerosol classes identified in this study to aerosol properties from AERONET stations where each of the four classes is dominant. Tomsk (Russia), Mongu (South Africa), Dakhla (Mauritania) and GSFC (Maryland, US) have been identified as GF, BB, DD and CC dominant site, respectively will be investigated. The method developed here for aerosol classification could also be applied to similar AERONET sites with composite sources of aerosol.

Calculation of the direct radiative forcing (DRF) at the surface due to the four aerosol classes identified will be carried out using a robust radiative transfer model with the sole aim of estimating the atmospheric heating due to these aerosol classes. Collaborative effort of Prof. R.T. Pinker's group at the University of Maryland, USA will be sought in this regard.

References

Abdulkareem, A. (2005). Evaluation of ground level concentration of pollutant due to gas flaring by computer simulation: A case study of Niger-Delta area of Nigeria. *Leonardo Electronic Journal of Practices and Technologies*, 6(1):29–42.

Abdulkareem, A. and Odigure, J. (2006). Deterministic model for noise dispersion from gas flaring: A case study of Niger–Delta area of Nigeria. *Chemical and biochemical engineering quarterly*, 20(2):157–164.

Akeredolu, F. and Sonibare, J. (2004). A review of the usefulness of gas flares in air pollution control. *Management of Environmental Quality: An International Journal*, 15(6):574–583.

Akinlade, G. O., Olaniyi, H. B., Olise, F. S., Owoade, O. K., Almeida, S. M., Almeida-Silva, M., and Hopke, P. K. (2015). Spatial and temporal variations of the particulate size distribution and chemical composition over Ibadan, Nigeria. *Environmental monitoring and assessment*, 187(8):1–14.

Alberta Environment (2003). Emergency/process upset flaring management: Modelling guidance. Technical report, Science and Standards Branch, Alberta Environment, Edmonton, Alberta.

Almanza, V., Molina, L., and Sosa, G. (2012). Soot and SO_2 contribution to the supersites in the MILAGRO campaign from elevated flares in the Tula refinery. *Atmospheric Chemistry and Physics*, 12(21):10583–10599.

Ana, G., Sridhar, M., and Emerole, G. (2012). Polycyclic aromatic hydrocarbon burden in ambient air in selected Niger Delta communities in Nigeria. *Journal of the Air & Waste Management Association*, 62(1):18–25.

Andreae, M. O. (1995). Climatic effects of changing atmospheric aerosol levels. *World survey of climatology*, 16:347–398.

Andrews, E., Ogren, J., Bonasoni, P., Marinoni, A., Cuevas, E., Rodríguez, S., Sun, J., Jaffe, D., Fischer, E., Baltensperger, U., et al. (2011). Climatology of aerosol radiative properties in the free troposphere. *Atmospheric Research*, 102(4):365–393.

Andrews, E., Sheridan, P. J., Fiebig, M., McComiskey, A., Ogren, J. A., Arnott, P., Covert, D., Elleman, R., Gasparini, R., Collins, D., et al. (2006). Comparison of methods for deriving aerosol asymmetry parameter. *Journal of Geophysical Research: Atmospheres*, 111(D5).

Anejionu, O. C., Blackburn, G. A., and Whyatt, J. D. (2015a). Detecting gas flares and estimating flaring volumes at individual flow stations using MODIS data. *Remote Sensing of Environment*, 158:81–94.

Anejionu, O. C., Whyatt, J. D., Blackburn, G. A., and Price, C. S. (2015b). Contributions of gas flaring to a global air pollution hotspot: Spatial and temporal variations, impacts and alleviation. *Atmospheric Environment*, 118:184–193.

Anejionu, O. C. D., Blackburn, G. A., and Whyatt, J. D. (2014). Satellite survey of gas flares: development and application of a Landsat-based technique in the Niger Delta. *International Journal of Remote Sensing*, 35(5):1900–1925.

Anomohanran, O. (2012). Determination of greenhouse gas emission resulting from gas flaring activities in Nigeria. *Energy Policy*, 45:666–670.

Arctic Council (2013). Recommendations to reduce black carbon and methane emissions to slow arctic climate change. Technical report, Arctic Council Task Force on Short-Lived Climate Forcers (https://oaarchive.arctic-council.org/handle/11374/1205).

Arya, S. P. (1999). *Air pollution meteorology and dispersion*. Oxford University Press New York.

Avwiri, G. and Nte, F. (2003). Environmental sound quality of some selected flow stations in the Niger Delta of Nigeria. *Journal of Applied Sciences and Environmental Management*, 7(2):75–77.

Barry, R. G. and Chorley, R. J. (2009). *Atmosphere, weather and climate*. Routledge.

Becker, H. and Liang, D. (1982). Total emission of soot and thermal radiation by free turbulent diffusion flames. *Combustion and Flame*, 44(1-3):305–318.

Becker, H. and Yamazaki, S. (1978). Entrainment, momentum flux and temperature in vertical free turbulent diffusion flames. *Combustion and Flame*, 33:123–149.

Bergstrom, R. (1973). Extinction and absorption coefficients of the atmospheric aerosol as a function of particle size. *Contr. Atmos. Phys*, 46:223–234.

Bergstrom, R. W., Pilewskie, P., Russell, P., Redemann, J., Bond, T., Quinn, P., and Sierau, B. (2007). Spectral absorption properties of atmospheric aerosols. *Atmospheric Chemistry and Physics*, 7(23):5937–5943.

Beychok, M. R. (2005). *Fundamentals of stack gas dispersion*. MR Beychok.

Bishop, G. and Stedman, D. (1996). Measuring the emissions of passing cars. *Accounts of Chemical Research*, 29(10):489–495.

Blanchet, J.-P. (1982). Application of the Chandrasekhar mean to aerosol optical parameters. *Atmosphere-Ocean*, 20(3):189–206.

Bohren, C. and Huffman, D. (1983). *Light Scattering and Absorption by Small Particles*. Wiley, New York.

Bond, T. C., Doherty, S. J., Fahey, D., Forster, P., Berntsen, T., DeAngelo, B., Flanner, M., Ghan, S., Kärcher, B., Koch, D., et al. (2013). Bounding the role of black carbon in the climate system: A scientific assessment. *Journal of Geophysical Research: Atmospheres*, 118(11):5380–5552.

Bond, T. C., Streets, D. G., Yarber, K. F., Nelson, S. M., Woo, J.-H., and Klimont, Z. (2004). A technology-based global inventory of black and organic carbon emissions from combustion. *Journal of Geophysical Research: Atmospheres*, 109(D14).

Bourguignon, E., Johnson, M., and Kostiuk, L. (1999). The use of a closed-loop wind tunnel for measuring the combustion efficiency of flames in a cross flow. *Combustion and flame*, 119(3):319–334.

BP (2013). 2013 statistical review of world energy. Technical report, British Petroleum, Great Britian.

BP (2015). 2015 statistical review of world energy. Technical report, British Petroleum, Great Britian.

Briggs, G. A. (1965). A plume rise model compared with observations. *Journal of the Air Pollution Control Association*, 15(9):433–438.

Burney, J. and Ramanathan, V. (2014). Recent climate and air pollution impacts on Indian agriculture. *Proceedings of the National Academy of Sciences*, 111(46):16319–16324.

Bush, B. C. and Valero, F. P. (2003). Surface aerosol radiative forcing at Gosan during the ACE-Asia campaign. *Journal of Geophysical Research: Atmospheres*, 108(D23).

Canteenwalla, P., Thomson, K., Smallwood, G., and Johnson, M. (2007). Soot emissions from turblent diffusion flames burning simple alkane fuels. National Research Council, Canada.

Carruthers, D., Edmunds, H., Bennett, M., Woods, P., Milton, M., Robinson, R., Underwood, B., Franklin, C., and Timmis, R. (1997). Validation of the adms dispersion model and assessment of its performance relative to R–91 and ISC using archived LIDAR data. *International Journal of Environment and Pollution*, 8(3-6):264–278.

Carslaw, D. (2015). The openair manual - open-source tools for analysing air pollution data. manual for version 1.1-4. Technical report, King's College, London.

Carslaw, D. C. and Ropkins, K. (2012). Openair - an R package for air quality data analysis. *Environmental Modelling & Software*, 27:52–61.

Casadio, S., Arino, O., and Serpe, D. (2012). Gas flaring monitoring from space using the ATSR instrument series. *Remote Sensing of Environment*, 116:239–249.

Castineira, D. and Edgar, T. F. (2006). CFD for simulation of steam-assisted and air-assisted flare combustion systems. *Energy & fuels*, 20(3):1044–1056.

CERC (2012). ADMS 5 Atmospheric Dispersion Modelling System. Technical report, Cambridge Environmental Research Consultants Ltd., Cambridge, UK.

Charlson, R., Langer, J., Rodhe, H., Leovy, C., and Warren, S. (1991). Perturbation of the northern hemispheric radiative balance by backscattering from anthropogenic sulfate aerosol. *Tellus*, 43:152–163.

Charlson, R. J., Schwartz, S., et al. (1992). Climate forcing by anthropogenic aerosols. *Science*, 255(5043):423.

Chow, J. C., Watson, J. G., Lu, Z., Lowenthal, D. H., Frazier, C. A., Solomon, P. A., Thuillier, R. H., and Magliano, K. (1996). Descriptive analysis of PM2.5 and PM10 at regionally representative locations during SJVAQS/AUSPEX. *Atmospheric Environment*, 30(12):2079–2112.

Chubarova, N., Poliukhov, A., and Gorlova, I. (2016). Long-term variability of aerosol optical thickness in eastern europe over 2001–2014 according to the measurements at the Moscow MSU MO AERONET site with additional cloud and NO_2 correction. *Atmospheric Measurement Techniques*, 9(2):313–334.

Chung, S. H. and Seinfeld, J. H. (2005). Climate response of direct radiative forcing of anthropogenic black carbon. *Journal of Geophysical Research: Atmospheres*, 110(D11).

Chylek, P. and Wong, J. (1995). Effect of absorbing aerosols on global radiation budget. *Geophysical research letters*, 22(8):929–931.

Connan, O., Leroy, C., Derkx, F., Maro, D., Hébert, D., Roupsard, P., and Rozet, M. (2011). Atmospheric dispersion of an elevated release in a rural environment: Comparison between field SF 6 tracer measurements and computations of Briggs and ADMS models. *Atmospheric environment*, 45(39):7174–7183.

Conover, W. (1999). Statistics of the Kolmogorov-Smirnov type. *Practical nonparametric statistics*, pages 428–473.

Cooke, W. F., Jennings, S., and Spain, T. (1997). Black carbon measurements at Mace Head, 1989–1996. *Journal of Geophysical Research: Atmospheres*, 102(D21):25339–25346.

Cooke, W. F. and Wilson, J. J. (1996). A global black carbon aerosol model. *Journal of Geophysical Research: Atmospheres*, 101(D14):19395–19409.

Cornforth, R. (2012). Overview of the West African Monsoon 2011. *Weather*, 67(3):59–65.

D'Almeida, G. A., Koepke, P., and Shettle, E. P. (1991). *Atmospheric aerosols: global climatology and radiative characteristics*. A Deepak Pub.

Davoudi, M., Rahimpour, M., Jokar, S., Nikbakht, F., and Abbasfard, H. (2013). The major sources of gas flaring and air contamination in the natural gas processing plants: A case study. *Journal of Natural Gas Science and Engineering*, 13:7–19.

Dawson, R. (2011). How significant is a boxplot outlier. *Journal of Statistics Education*, 19(2):1–12.

De Gouw, J., Cooper, O., Warneke, C., Hudson, P., Fehsenfeld, F., Holloway, J., Hübler, G., Nicks Jr, D., Nowak, J., Parrish, D., et al. (2004). Chemical composition of air masses transported from Asia to the US West Coast during ITCT 2K2: Fossil fuel combustion versus biomass-burning signatures. *Journal of Geophysical Research: Atmospheres*, 109(D23).

Delene, D. J. and Ogren, J. A. (2002). Variability of aerosol optical properties at four North American surface monitoring sites. *Journal of the Atmospheric Sciences*, 59(6):1135–1150.

Delichatsios, M. (1993a). Smoke yields from turbulent buoyant jet flames. *Fire safety journal*, 20(4):299–311.

Delichatsios, M. (1993b). Transition from momentum to buoyancy-controlled turbulent jet diffusion flames and flame height relationships. *Combustion and Flame*, 92(4):349–364.

Delichatsios, M. A. (1987). Air entrainment into buoyant jet flames and pool fires. *Combustion and Flame*, 70(1):33–46.

Djuricin, S., Pataki, D. E., and Xu, X. (2010). A comparison of tracer methods for quantifying CO_2 sources in an urban region. *Journal of Geophysical Research: Atmospheres*, 115(D11).

Doherty, S. J., Dang, C., Hegg, D. A., Zhang, R., and Warren, S. G. (2014). Black carbon and other light-absorbing particles in snow of central North America. *Journal of Geophysical Research: Atmospheres*, 119(22).

Dubovik, O., Holben, B., Eck, T. F., Smirnov, A., Kaufman, Y. J., King, M. D., Tanré, D., and Slutsker, I. (2002). Variability of absorption and optical properties of key aerosol types observed in worldwide locations. *Journal of the atmospheric sciences*, 59(3):590–608.

Dubovik, O. and King, M. D. (2000). A flexible inversion algorithm for retrieval of aerosol optical properties from Sun and sky radiance measurements. *Journal of Geophysical Research*, 105(D16):20673–20696.

Dubovik, O., Smirnov, A., Holben, B., King, M., Kaufman, Y., Eck, T., and Slutsker, I. (2000). Accuracy assessments of aerosol optical properties retrieved from aerosol robotic network (AERONET) Sun and sky radiance measurements. *Journal of Geophysical Research: Atmospheres*, 105(D8):9791–9806.

Dung, E. J., Bombom, L. S., and Agusomu, T. D. (2008). The effects of gas flaring on crops in the Niger Delta, Nigeria. *GeoJournal*, 73(4):297–305.

E & F Forum (1994). Methods of estimating atmospheric emission from E&P operations; OGP Report No. 2.59/197. Technical report, The Oil Industry International Exploration and Production forum, 25-28 Old Burlington street, London (http://www.ogp.org.uk/pubs/197.pdf).

Eck, T., Holben, B., Reid, J., Dubovik, O., Smirnov, A., O'Neill, N., Slutsker, I., and Kinne, S. (1999). Wavelength dependence of the optical depth of biomass burning, urban, and desert dust aerosols. *Journal of Geophysical Research*, 104:31333.

Eck, T. F., Holben, B., Sinyuk, A., Pinker, R., Goloub, P., Chen, H., Chatenet, B., Li, Z., Singh, R. P., Tripathi, S. N., et al. (2010). Climatological aspects of the optical properties of fine/coarse mode aerosol mixtures. *Journal of Geophysical Research: Atmospheres*, 115(D19).

Edwards, P., Brown, S., Roberts, J., Ahmadov, R., Banta, R., Dube, W., Field, R., Flynn, J., Gilman, J., Graus, M., et al. (2014). High winter ozone pollution from carbonyl photolysis in an oil and gas basin. *Nature*, 514(7522):351–351.

Edwards, P. M., Young, C. J., Aikin, K., deGouw, J., Dubé, W. P., Geiger, F., Gilman, J., Helmig, D., Holloway, J. S., Kercher, J., Lerner, B., Martin, R., McLaren, R., Parrish, D. D., Peischl, J., Roberts, J. M., Ryerson, T. B., Thornton, J., Warneke, C., Williams, E. J., and Brown, S. S. (2013). Ozone photochemistry in an oil and natural gas extraction region during winter: simulations of a snow-free season in the Uintah Basin, Utah. *Atmospheric Chemistry and Physics*, 13(17):8955–8971.

EEA (2006). Waste incineration: Flaring in gas and oil extraction, emission inventory guidebook. Technical report, European Environment Agency, Copenhagen, Denmark.

EEMS (2008). Atmospheric emissions calculations. Technical report, Environmental Emissions Monitoring System, United Kingdom.

Elvidge, C. D., Baugh, K., Tuttle, B., Howard, A., Pack, D., Milesi, C., and Erwin, E. (2007). A twelve year record of national and global gas flaring volumes estimated using satellite data. Technical report, NOAA National Geophysical Data Center, Boulder, Colorado, USA.

Elvidge, C. D., Baugh, K. E., Ziskin, D., Anderson, S., and Ghosh, T. (2011). Estimation of gas flaring volumes using NASA MODIS fire detection products. Technical report, NOAA National Geophysical Data Center (NGDC), Boulder, Colorado, USA.

Elvidge, C. D., Zhizhin, M., Baugh, K., Hsu, F.-C., and Ghosh, T. (2015). Methods for global survey of natural gas flaring from visible infrared imaging radiometer suite data. *Energies*, 9(1):14.

Elvidge, C. D., Ziskin, D., Baugh, K. E., Tuttle, B. T., Ghosh, T., Pack, D. W., Erwin, E. H., and Zhizhin, M. (2009). A fifteen year record of global natural gas flaring derived from satellite data. *Energies*, 2(3):595–622.

Emde, C., Buras-Schnell, R., Kylling, A., Mayer, B., Gasteiger, J., Hamann, U., Kylling, J., Richter, B., Pause, C., Dowling, T., et al. (2015). The libRadtran software package for radiative transfer calculations (Version 2.0). *Geoscientific Model Development Discussions*, 8(10):237–10.

Enviroware (2012). *Modelling industrial flares impacts*. Enviroware Air Quality Consulting, Concorezzo (MB), Italy.

Ermak, D. L. (1977). An analytical model for air pollutant transport and deposition from a point source. *Atmospheric Environment (1967)*, 11(3):231–237.

European Commission (2009). Emission database for global atmospheric research (EDGAR), release version 4.0. Technical report, Joint Research Centre (JRC)/Netherlands Environmental Assessment Agency (PBL), Netherlands (http://edgar.jrc.ec.europa.eu).

Ezeh, G. C., Obioh, I. B., Asubiojo, O. I., and Abiye, O. E. (2012). PIXE characterization of PM10 and PM2. 5 particulates sizes collected in Ikoyi Lagos, Nigeria. *Toxicological & Environmental Chemistry*, 94(5):884–894.

Fassi-Fihri, A., Suhre, K., and Rosset, R. (1997). Internal and external mixing in atmospheric aerosols by coagulation: Impact on the optical and hygroscopic properties of the sulphate-soot system. *Atmospheric Environment*, 31(10):1393–1402.

Fawole, O., Cai, X.-M., Levine, J., Pinker, R., and MacKenzie, A. (2016a). Detection of a gas-flaring signature in the optical and microphysical properties of aerosols at a tropical station over West Africa using AERONET data. *Journal of Geophysical Research: Atmospheres*, (under revision).

Fawole, O. G., Cai, X.-M., and MacKenzie, A. (2016b). Gas flaring and resultant air pollution: A review focusing on black carbon. *Environmental Pollution*, 216:182–197.

Fay, M. P. and Proschan, M. A. (2010). Wilcoxon-Mann-Whitney or t-test? On assumptions for hypothesis tests and multiple interpretations of decision rules. *Statistics surveys*, 4:1.

Feichter, J. and Stier, P. (2012). Assessment of black carbon radiative effects in climate models. *Wiley Interdisciplinary Reviews: Climate Change*, 3(4):359–370.

Flagan, R. C. and Seinfeld, J. H. (2013). *Fundamentals of air pollution engineering*. Courier Corporation.

Fortner, E., Brooks, W., Onasch, T., Canagaratna, M., Massoli, P., Jayne, J., Franklin, J., Knighton, W., Wormhoudt, J., Worsnop, D., et al. (2012). Particulate emissions measured during the TCEQ comprehensive flare emission study. *Industrial & Engineering Chemistry Research*, 51(39):12586–12592.

Garcıa, O., Dıaz, J., Expósito, F., Dıaz, A., Dubovik, O., Derimian, Y., Dubuisson, P., and Roger, J. (2012). Shortwave radiative forcing and efficiency of key aerosol types using AERONET data. *Atmos. Chem. Phys*, 12:5129–5145.

Gertler, A. W., Sagebiel, J. C., Dippel, W. A., and Farina, R. J. (1998). Measurements of dioxin and furan emission factors from heavy-duty diesel vehicles. *Journal of the Air & Waste Management Association*, 48(3):276–278.

GGFR (2012). Estimated flared volumes from satellite data, 2007-2011. Technical report, Global Gas Flaring Reduction, The World Bank, http://go.worldbank.org/G2OAW2DKZ0.

GGFR (2013). The news flare (issue 14). Technical report, Global Gas Flaring Reduction, The World Bank, Washington DC (http://documents.worldbank.org/curated/en/2013/06/18082251/news-flare-issue-14).

Giles, D. M., Holben, B. N., Eck, T. F., Sinyuk, A., Smirnov, A., Slutsker, I., Dickerson, R., Thompson, A., and Schafer, J. (2012). An analysis of AERONET aerosol absorption properties and classifications representative of aerosol source regions. *Journal of Geophysical Research: Atmospheres*, 117(D17).

Gilman, J. B., Lerner, B., Kuster, W., and De Gouw, J. (2013). Source signature of volatile organic compounds from oil and natural gas operations in northeastern Colorado. *Environmental science & technology*, 47(3):1297–1305.

Giwa, S. O., Adama, O. O., and Akinyemi, O. O. (2014). Baseline black carbon emissions for gas flaring in the Niger Delta region of Nigeria. *Journal of Natural Gas Science and Engineering*, 20:373–379.

Glassman, I. (1996). *Combustion 3rd edition*. Academic Press, San Diego, California.

Golber, E. D. (1985). *Black Carbon in the Environment: Properties and Distribution*. New York, John Wiley.

Hansen, J., Sato, M., Ruedy, R., Nazarenko, L., Lacis, A., Schmidt, G., Russell, G., Aleinov, I., Bauer, M., Bauer, S., et al. (2005). Efficacy of climate forcings. *Journal of Geophysical Research: Atmospheres*, 110(D18).

Harris, M. M., King, G. B., and Laurendeau, N. M. (1986). Influence of temperature and hydroxyl concentration on incipient soot formation in premixed flames. *Combustion and flame*, 64(1):99–112.

Haynes, B. S. and Wagner, H. G. (1981). Soot formation. *Progress in Energy and Combustion Science*, 7(4):229–273.

Haywood, J. and Boucher, O. (2000). Estimates of the direct and indirect radiative forcing due to tropospheric aerosols: A review. *Reviews of geophysics*, 38(4):513–543.

Haywood, J., Pelon, J., Formenti, P., Bharmal, N., Brooks, M., Capes, G., Chazette, P., Chou, C., Christopher, S., Coe, H., et al. (2008). Overview of the dust and biomass-burning experiment and african monsoon multidisciplinary analysis special observing period-0. *Journal of Geophysical Research: Atmospheres*, 113(D23).

Haywood, J. and Shine, K. (1995). The effect of anthropogenic sulfate and soot aerosol on the clear sky planetary radiation budget. *Geophysical Research Letters*, 22(5):603–606.

Haywood, J. M. (1995). *Model investigations into the radiative forcing of climate by anthropogenic emissions of sulphate and soot aerosol*. PhD thesis, University of Reading.

Heist, D., Isakov, V., Perry, S., Snyder, M., Venkatram, A., Hood, C., Stocker, J., Carruthers, D., Arunachalam, S., and Owen, R. C. (2013). Estimating near-road pollutant dispersion:

A model inter-comparison. *Transportation Research Part D: Transport and Environment*, 25:93–105.

Hess, M., Koepke, P., and Schult, I. (1998). Optical properties of aerosols and clouds: The software package OPAC. *Bulletin of the American meteorological society*, 79(5):831–844.

Hitchins, J., Morawska, L., Wolff, R., and Gilbert, D. (2000). Concentrations of submicrometre particles from vehicle emissions near a major road. *Atmospheric environment*, 34(1):51–59.

Hodgson, S., Nieuwenhuijsen, M. J., Colvile, R., and Jarup, L. (2007). Assessment of exposure to mercury from industrial emissions: "comparing distance as a proxy" and dispersion modelling approaches. *Occupational and environmental medicine*, 64(6):380–388.

Holben, B., Eck, T., Slutsker, I., Smirnov, A., Sinyuk, A., Schafer, J., Giles, D., and Dubovik, O. (2006). AERONET's version 2.0 quality assurance criteria. In *Asia-Pacific Remote Sensing Symposium*, pages 64080Q–64080Q. International Society for Optics and Photonics.

Holben, B., Tanre, D., Smirnov, A., Eck, T., Slutsker, I., Abuhassan, N., Newcomb, W., Schafer, J., Chatenet, B., Lavenu, F., et al. (2001). An emerging ground-based aerosol climatology: Aerosol optical depth from AERONET. *Journal of Geophysical Research: Atmospheres*, 106(D11):12067–12097.

Holben, B. N., Eck, T., Slutsker, I., Tanre, D., Buis, J., Setzer, A., Vermote, E., Reagan, J. A., Kaufman, Y., Nakajima, T., et al. (1998). AERONET - A federated instrument network and data archive for aerosol characterization. *Remote sensing of environment*, 66(1):1–16.

Holden, J. (2005). *An introduction to physical geography and the environment*. Pearson Education.

Hopkins, J. R., Evans, M. J., Lee, J. D., Lewis, A. C., H Marsham, J., McQuaid, J., Parker, D. J., Stewart, D. J., Reeves, C. E., and Purvis, R. M. (2009). Direct estimates of emissions from the megacity of Lagos. *Atmospheric Chemistry and Physics*, 9(21):8471–8477.

Horvath, H., Kasahara, M., Tohno, S., Olmo, F., Lyamani, H., Alados-Arboledas, L., Quirantes, A., and Cachorro, V. (2016). Relationship between fraction of backscattered light and asymmetry parameter. *Journal of Aerosol Science*, 91:43–53.

Huang, K., Fu, J. S., Prikhodko, V. Y., Storey, J. M., Romanov, A., Hodson, E. L., Cresko, J., Morozova, I., Ignatieva, Y., and Cabaniss, J. (2015). Russian anthropogenic black carbon: Emission reconstruction and Arctic black carbon simulation. *Journal of Geophysical Research: Atmospheres*, 120(21).

Huang, R. F. and Wang, S. M. (1999). Characteristic flow modes of wake-stabilized jet flames in a transverse air stream. *Combustion and Flame*, 117(1):59–77.

Huth, R. and Pokorna, L. (2004). Parametric versus non-parametric estimates of climatic trends. *Theoretical and Applied Climatology*, 77(1-2):107–112.

IEA (2012). IEA statistics: Natural gas information. Technical report, International Energy Agency, Paris, France.

IEA (2013). Key World Energy Statistics. Technical report, International Energy Agency, Paris, France.

IMP (2006). Estudio de las emisiones de la zona industrial de tula y su impacto en la calidad del aire regional. Technical report, Instituto Mexicano del Petróleo, Mexico PS-MA-IF-F21393-1.

IPCC (2007). Climate change 2007: The physical science basis. Contribution of Working Group I to the fourth assessment report of the intergovernmental panel on climate change. Cambridge University, Press Cambridge, United Kingdom and New York, USA.

IPCC (2013). Climate change 2013: The physical science basis. Contribution of Working Group I to the fourth assessment report of the intergovernmental panel on climate change. Cambridge University.

Ismail, O. S. and Umukoro, G. E. (2014). Modelling combustion reactions for gas flaring and its resulting emissions. *Journal of King Saud University-Engineering Sciences*, 28:130–140.

Ite, A. E. and Ibok, U. J. (2013). Gas flaring and venting associated with petroleum exploration and production in the Nigeria's Niger Delta. *American Journal of Environmental Protection*, 1(4):70–77.

Jacobson, M. Z. (2002). Control of fossil-fuel particulate black carbon and organic matter, possibly the most effective method of slowing global warming. *Journal of Geophysical Research: Atmospheres*, 107(D19).

Janicot, S., Thorncroft, C. D., Ali, A., Asencio, N., Berry, G. J., Bock, O., Bourles, B., Caniaux, G., Chauvin, F., Deme, A., et al. (2008). Large-scale overview of the summer monsoon over West Africa during the AMMA field experiment in 2006. *Annales Geophysicae*, 26:2569–2595.

Jin, Z., Charlock, T. P., Smith, W. L., and Rutledge, K. (2004). A parameterization of ocean surface albedo. *Geophysical research letters*, 31(22).

Johansson, J. K., Mellqvist, J., Samuelsson, J., Offerle, B., Lefer, B., Rappenglück, B., Flynn, J., and Yarwood, G. (2014). Emission measurements of alkenes, alkanes, SO_2, and NO_2 from stationary sources in Southeast Texas over a 5 year period using SOF and mobile DOAS. *Journal of Geophysical Research: Atmospheres*, 119(4):1973–1991.

Johnson, M., Devillers, R., and Thomson, K. (2013). A generalized Sky-LOSA method to quantify soot/black carbon emission rates in atmospheric plumes of gas flares. *Aerosol Science and Technology*, 47(9):1017–1029.

Johnson, M. R. and Coderre, A. R. (2011). An analysis of flaring and venting activity in the Alberta upstream oil and gas industry. *Journal of the air & Waste management association*, 61(2):190–200.

Kassianov, E. I., Flynn, C. J., Ackerman, T. P., and Barnard, J. C. (2007). Aerosol single-scattering albedo and asymmetry parameter from MFRSR observations during the ARM Aerosol IOP 2003. *Atmospheric Chemistry and Physics*, 7(12):3341–3351.

Kaufman, Y., Tanré, D., Dubovik, O., Karnieli, A., and Remer, L. (2001). Absorption of sunlight by dust as inferred from satellite and ground-based remote sensing. *Geophysical Research Letters*, 28(8):1479–1482.

Kennedy, I. M. (1997). Models of soot formation and oxidation. *Progress in Energy and Combustion Science*, 23(2):95–132.

Kim, D., Chin, M., Yu, H., Eck, T., Sinyuk, A., Smirnov, A., and Holben, B. (2011). Dust optical properties over North Africa and Arabian Peninsula derived from the AERONET dataset. *Atmospheric Chemistry and Physics*, 11(20):10733–10741.

Kirchstetter, T. W., Harley, R. A., Kreisberg, N. M., Stolzenburg, M. R., and Hering, S. V. (1999). On-road measurement of fine particle and nitrogen oxide emissions from light-and heavy-duty motor vehicles. *Atmospheric Environment*, 33(18):2955–2968.

Klimont, Z., Smith, S. J., and Cofala, J. (2013). The last decade of global anthropogenic sulfur dioxide: 2000-2011 emissions. *Environmental Research Letters*, 8(1):014003.

Knippertz, P., Evans, M. J., Field, P. R., Fink, A. H., Liousse, C., and Marsham, J. H. (2015). The possible role of local air pollution in climate change in West Africa. *Nature Climate Change*, 5(9):815–822.

Koch, D., Schulz, M., Kinne, S., McNaughton, C., Spackman, J., Balkanski, Y., Bauer, S., Berntsen, T., Bond, T. C., Boucher, O., et al. (2009). Evaluation of black carbon estimations in global aerosol models. *Atmospheric Chemistry and Physics*, 9(22):9001–9026.

Kokhanovsky, A. and Zege, E. (1997). Optical properties of aerosol particles: A review of approximate analytical solutions. *Journal of aerosol science*, 28(1):1–21.

Kolmogorov, A. (1992). Sulla determinazione empirica di una leggi di distribuzione," g. inst. ital. attuari, vol. 4, 1933, translated in english in breakthroughs in statistics, by kotz and johnson. *Breakthroughs in Statistics*.

Kostiuk, L., Johnson, M., and Thomas, G. (2004). University of Alberta Flare Research Project: final report. Technical report, University of Alberta, Alberta, Canada.

Lafore, J.-P., Flamant, C., Giraud, V., Guichard, F., Knippertz, P., Mahfouf, J.-F., Mascart, P., and Williams, E. (2010). Introduction to the amma special issue on 'Advances in understanding atmospheric processes over West Africa through the AMMA field campaign'. *Quarterly Journal of the Royal Meteorological Society*, 136(S1):2–7.

Lautenberger, C. W., de Ris, J. L., Dembsey, N. A., Barnett, J. R., and Baum, H. R. (2005). A simplified model for soot formation and oxidation in CFD simulation of non-premixed hydrocarbon flames. *Fire Safety Journal*, 40(2):141–176.

Law, K. S., Fierli, F., Cairo, F., Schlager, H., Borrmann, S., Streibel, M., Real, E., Kunkel, D., Schiller, C., Ravegnani, F., et al. (2010). Air mass origins influencing TTL chemical composition over West Africa during 2006 summer monsoon. *Atmospheric Chemistry and Physics*, 10(22):10753–10770.

Leahey, D. and Davies, M. (1984). Observations of plume rise from sour gas flares. *Atmospheric Environment (1967)*, 18(5):917–922.

Leahey, D. M., Preston, K., and Strosher, M. (2001). Theoretical and observational assessments of flare efficiencies. *Journal of the Air & Waste Management Association*, 51(12):1610–1616.

Lebel, T., Parker, D. J., Flamant, C., Bourlès, B., Marticoréna, B., Mougin, E., Peugeot, C., Diedhiou, A., Haywood, J., Ngamini, J.-B., et al. (2010). The AMMA field campaigns: multiscale and multidisciplinary observations in the West African region. *Quarterly Journal of the Royal Meteorological Society*, 136(S1):8–33.

Lee, J., Kim, J., Song, C., Kim, S., Chun, Y., Sohn, B., and Holben, B. (2010). Characteristics of aerosol types from AERONET sunphotometer measurements. *Atmospheric Environment*, 44(26):3110–3117.

Lenoble, J., Mishchenko, M. I., and Herman, M. (2013). Absorption and scattering by molecules and particles. In *Aerosol Remote Sensing*, pages 13–51. Springer.

Li, C., Hsu, N. C., Sayer, A. M., Krotkov, N. A., Fu, J. S., Lamsal, L. N., Lee, J., and Tsay, S.-C. (2016). Satellite observation of pollutant emissions from gas flaring activities near the Arctic. *Atmospheric Environment*, 133:1–11.

Liberman, M. A. (2010). *Introduction to physics and chemistry of combustion: explosion, flame, detonation*. Springer Science & Business Media.

Lim, S., Lee, M., Kim, S.-W., Yoon, S.-C., Lee, G., and Lee, Y. (2014). Absorption and scattering properties of organic carbon versus sulfate dominant aerosols at Gosan climate observatory in Northeast Asia. *Atmospheric Chemistry and Physics*, 14(15):7781–7793.

Liousse, C., Assamoi, E., Criqui, P., Granier, C., and Rosset, R. (2014). Explosive growth in African combustion emissions from 2005 to 2030. *Environmental Research Letters*, 9(3):035003.

Liousse, C., Galy-Lacaux, C., Ndiaye, S. A., Diop, B., Ouafo, M., Assamoi, E. M., Gardrat, E., Castera, P., Rosset, R., Akpo, A., et al. (2012). Real time black carbon measurements in West and Central Africa urban sites. *Atmospheric environment*, 54:529–537.

Liu, Y., Shao, M., Fu, L., Lu, S., Zeng, L., and Tang, D. (2008). Source profiles of volatile organic compounds (VOCs) measured in China: Part I. *Atmospheric Environment*, 42(25):6247–6260.

MacKay, D. (2008). *Sustainable energy-without the hot air*. UIT Cambridge.

Magnussen, B. F. and Hjertager, B. H. (1977). On mathematical modeling of turbulent combustion with special emphasis on soot formation and combustion. In *Symposium (International) on Combustion*, volume 16, pages 719–729. Elsevier.

Marais, E. A. and Chance, K. (2015). A geostationary air quality monitoring platform for Africa. *Clean Air Journal*, 25(1):40.

Marais, E. A. and Chance, K. (2016). Air quality impact of Diffuse and Inefficient Combustion Emissions in Africa (DICE-Africa). *Environmental Science & Technology*, In press.

Marais, E. A., Jacob, D., Wecht, K., Lerot, C., Zhang, L., Yu, K., Kurosu, T., Chance, K., and Sauvage, B. (2014). Anthropogenic emissions in Nigeria and implications for atmospheric ozone pollution: A view from space. *Atmospheric Environment*, 99:32–40.

Mari, C. H., Reeves, C. E., Law, K. S., Ancellet, G., Andrés-Hernández, M. D., Barret, B., Bechara, J., Borbon, A., Bouarar, I., Cairo, F., et al. (2011). Atmospheric composition of West Africa: highlights from the AMMA international program. *Atmospheric Science Letters*, 12(1):13–18.

Maricq, M. M. (2009). An examination of soot composition in premixed hydrocarbon flames via laser ablation particle mass spectrometry. *Journal of Aerosol Science*, 40(10):844–857.

Marr, L. C., Kirchstetter, T. W., Harley, R. A., Miguel, A. H., Hering, S. V., and Hammond, S. K. (1999). Characterization of polycyclic aromatic hydrocarbons in motor vehicle fuels and exhaust emissions. *Environmental science & technology*, 33(18):3091–3099.

Marshall, S. F., Covert, D. S., and Charlson, R. J. (1995). Relationship between asymmetry parameter and hemispheric backscatter ratio: Implications for climate forcing by aerosols. *Applied optics*, 34(27):6306–6311.

Mathon, V. and Laurent, H. (2001). Life cycle of Sahelian mesoscale convective cloud systems. *Quarterly Journal of the Royal Meteorological Society*, 127(572):377–406.

McAllister, S., Chen, J.-Y., and Fernandez-Pello, A. C. (2011). *Fundamentals of combustion processes*. Springer.

McDaniel, M. and Tichenor, B. (1983). Flare efficiency study. Technical report, US Environmental Protection Agency, Industrial Environmental Research Laboratory, http://www.tceq.state.tx.us/assets/public/implementation/air/rules/Flare/Resource-1.pdf.

McEwen, J. D. and Johnson, M. R. (2012). Black carbon particulate matter emission factors for buoyancy-driven associated gas flares. *Journal of the Air & Waste Management Association*, 62(3):307–321.

McQuaid, J. B., Lewis, A. C., Bartle, K. D., and Walton, S. J. (1998). Sub-ppt atmospheric measurements using PTV-GC-FID and real-time digital signal processing. *Journal of High Resolution Chromatography*, 21(3):181–184.

Methven, J. (1997). Offline trajectories: calculation and accuracy. UK Universities Global Atmospheric Modelling Programme. Technical report, Tech. Rep.

Methven, J., Evans, M., Simmonds, P., and Spain, G. (2001). Estimating relationships between air mass origin and chemical composition. *Journal of Geophysical Research: Atmospheres*, 106(D5):5005–5019.

Mielonen, T., Arola, A., Komppula, M., Kukkonen, J., Koskinen, J., de Leeuw, G., and Lehtinen, K. (2009). Comparison of CALIOP level 2 aerosol subtypes to aerosol types derived from AERONET inversion data. *Geophysical Research Letters*, 36(18).

Milinevsky, G., Danylevsky, V., Bovchaliuk, V., Bovchaliuk, A., Goloub, P., Dubovik, O., Kabashnikov, V., Chaikovsky, A., Miatselskaya, N., Mishchenko, M., et al. (2014). Aerosol seasonal variations over urban-industrial regions in Ukraine according to AERONET and POLDER measurements. *Atmospheric Measurement Techniques*, pages 1459–1474.

Minga, A., Thouret, V., Saunois, M., Delon, C., Serça, D., Mari, C., Sauvage, B., Mariscal, A., Leriche, M., and Cros, B. (2010). What caused extreme ozone concentrations over Cotonou in December 2005? *Atmospheric Chemistry and Physics*, 10(3):895–907.

Miyauchi, T., Mori, Y., and Yamaguchi, T. (1981). Effect of steam addition on NO formation. *Symposium (International) on combustion*, 18(1):43–51.

MoE Ontario (2009). Air dispersion modelling guideline for ontario (version 2.0). Technical report, Ontario Minstry of Environment, Ontario, Canada.

Monaci, F., Moni, F., Lanciotti, E., Grechi, D., and Bargagli, R. (2000). Biomonitoring of airborne metals in urban environments: new tracers of vehicle emission, in place of lead. *Environmental Pollution*, 107(3):321–327.

Moss, J., Stewart, C., and Syed, K. (1989). Flowfield modelling of soot formation at elevated pressure. In *Symposium (International) on Combustion*, volume 22, pages 413–423. Elsevier.

Müller-Dethlefs, K. and Schlader, A. (1976). The effect of steam on flame temperature, burning velocity and carbon formation in hydrocarbon flames. *Combustion and flame*, 27:205–215.

Myhre, G., Shindell, D., Bréon, F., Collins, W., Fuglestvedt, J., Huang, J., Koch, D., Lamarque, J., Lee, D., Mendoza, B., Nakajima, T., Robock, A., Stephens, G., Takemura, T., and Zhan, H. (2013). Anthropogenic and natural radiative forcing. In Stocker, T., Qin, D., Plattner, G., Tignor, M., Allen, S., Boschung, J., Nauels, A., Xia, Y., Bex, V., and Midgley, P., editors, *Climate Change 2013: The Physical Science Basis. Contribution of Working Group I to the Fifth Assessment Report of the Intergovernmental Panel on Climate Change*, chapter 8. Cambridge University Press, Cambridge, United Kingdom and New York, NY, USA.

NOAA (1998). Automated Surface Observing System (ASOS) Users' guide. Technical report, National Oceanic and Atmospheric Administration, US.

Noone, D. and Simmonds, I. (1999). A three-dimensional spherical trajectory algorithm. In Ritchie, H., editor, *Research Activities in Atmospheric and Oceanic Modelling, Report No. 28, WMO/TD-No. 942*, volume 3, pages 26–27. World Meteorological Organization, Geneva, Switzerland.

Nwaichi, E. and Uzazobona, M. (2011). Estimation of the co_2 level due to gas flaring in the Niger Delta. *Research Journal of Environmental Sciences*, 5(6):565.

Obanijesu, E., Adebiyi, F., Sonibare, J., and Okelana, O. (2009). Air-borne SO_2 pollution monitoring in the upstream petroleum operation areas of Niger-Delta, Nigeria. *Energy Sources, Part A*, 31(3):223–231.

Obioh, I., Ezeh, G., Abiye, O., Alpha, A., Ojo, E., and Ganiyu, A. (2013). Atmospheric particulate matter in Nigerian megacities. *Toxicological & Environmental Chemistry*, 95(3):379–385.

OGP (2000). Flaring and venting in the oil and gas exploration and production industry: An overview of purpose, quantities, issues, practices and trends. Technical report, International association of oil and gas producers UK (Report No. 2.79/288) http://www.ogp.org.uk/pubs/288.pdf.

Ogunjobi, K., He, Z., and Simmer, C. (2008). Spectral aerosol optical properties from AERONET sun-photometric measurements over West Africa. *Atmospheric Research*, 88(2):89–107.

Olaniran, O. (1982). The physiological climate of Ilorin, Nigeria. *Archives for meteorology, geophysics, and bioclimatology, Series B*, 31(3):287–299.

Onyeuwaoma, N. D., Nwofor, O. K., Chineke, T. C., Eguaroje, E. O., and Dike, V. N. (2015). Implications of MODIS impression of aerosol loading over urban and rural settlements in Nigeria: Possible links to energy consumption patterns in the country. *Atmospheric Pollution Research*, 6(3):484–494.

OPEC (2015). OPEC annual statistical bulletin. Technical report, Organisation of Petroleum Exporting Countries, Austria.

Osuji, L. C. and Adesiyan, S. O. (2005). The Isiokpo oil-pipeline leakage: Total organic carbon/organic matter contents of affected soils. *Chemistry & biodiversity*, 2(8):1079–1085.

Osuji, L. C. and Onojake, C. M. (2004). Trace heavy metals associated with crude oil: A case study of Ebocha-8 oil-spill-polluted site in Niger Delta, Nigeria. *Chemistry & biodiversity*, 1(11):1708–1715.

Ouf, F.-X., Vendel, J., Coppalle, A., Weill, M., and Yon, J. (2008). Characterization of soot particles in the plumes of over-ventilated diffusion flames. *Combustion Science and Technology*, 180(4):674–698.

Owoade, K. O., Hopke, P. K., Olise, F. S., Adewole, O. O., Ogundele, L. T., and Fawole, O. G. (2016). Source apportionment analyses for fine (PM 2.5) and coarse (PM 2.5–10) mode particulate matter (PM) measured in an urban area in southwestern Nigeria. *Atmospheric Pollution Research*, 7(5):843–857.

Owoade, O. K., Fawole, O. G., Olise, F. S., Ogundele, L. T., Olaniyi, H. B., Almeida, M. S., Ho, M.-D., and Hopke, P. K. (2013). Characterization and source identification of airborne particulate loadings at receptor site-classes of Lagos Mega-City, Nigeria. *Journal of the Air & Waste Management Association*, 63(9):1026–1035.

Pace, G., Sarra, A. d., Meloni, D., Piacentino, S., and Chamard, P. (2006). Aerosol optical properties at lampedusa (Central Mediterranean). 1. Influence of transport and identification of different aerosol types. *Atmospheric Chemistry and Physics*, 6(3):697–713.

Pandithurai, G., Pinker, R., Dubovik, O., Holben, B., and Aro, T. (2001). Remote sensing of aerosol optical characteristics in sub-Sahel, West Africa. *Journal of Geophysical Research: Atmospheres*, 106(D22):28347–28356.

Pasquill, F. (1961). The estimation of the dispersion of windborne material. *Meteorol. Mag*, 90(1063):33–49.

Pinker, R., Liu, H., Osborne, S., and Akoshile, C. (2010). Radiative effects of aerosols in sub-Sahel Africa: Dust and biomass burning. *Journal of Geophysical Research: Atmospheres*, 115(D15).

Pohl, J. and Soelberg, N. (1985). Evaluation of the efficiency of industrial flares: flare head design and gas composition. Final report, October 1983-December 1984. Technical report, Energy and Environmental Research Corp., Irvine, CA (USA).

Pope III, C. A., Burnett, R. T., Thun, M. J., Calle, E. E., Krewski, D., Ito, K., and Thurston, G. D. (2002). Lung cancer, cardiopulmonary mortality, and long-term exposure to fine particulate air pollution. *Jama*, 287(9):1132–1141.

Ramana, M., Ramanathan, V., Feng, Y., Yoon, S., Kim, S., Carmichael, G., and Schauer, J. (2010). Warming influenced by the ratio of black carbon to sulphate and the black-carbon source. *Nature Geoscience*, 3(8):542–545.

Ramanathan, V. and Carmichael, G. (2008). Global and regional climate changes due to black carbon. *Nature geoscience*, 1(4):221–227.

Ramanathan, V., Chung, C., Kim, D., Bettge, T., Buja, L., Kiehl, J., Washington, W., Fu, Q., Sikka, D., and Wild, M. (2005). Atmospheric brown clouds: Impacts on South Asian climate and hydrological cycle. *Proceedings of the National Academy of Sciences of the United States of America*, 102(15):5326–5333.

Redelsperger, J.-L., Thorncroft, C. D., Diedhiou, A., Lebel, T., et al. (2006). African Monsoon Multidisciplinary Analysis: An international research project and field campaign. *Bulletin of the American Meteorological Society*, 87(12):1739.

Reeves, C., Formenti, P., Afif, C., Ancellet, G., Attié, J.-L., Bechara, J., Borbon, A., Cairo, F., Coe, H., Crumeyrolle, S., et al. (2010). Chemical and aerosol characterisation of the troposphere over West Africa during the monsoon period as part of AMMA. *Atmospheric Chemistry and Physics*, 10(16):7575–7601.

Ricchiazzi, P., Yang, S., Gautier, C., and Sowle, D. (1998). SBDART: A research and teaching software tool for plane-parallel radiative transfer in the Earth's atmosphere. *Bulletin of the American Meteorological Society*, 79(10):2101.

Roberts, G., Wooster, M., and Lagoudakis, E. (2009). Annual and diurnal african biomass burning temporal dynamics. *Biogeosciences*, 6(5).

Roiger, A., Thomas, J.-L., Schlager, H., Law, K. S., Kim, J., Schäfler, A., Weinzierl, B., Dahlkötter, F., Krisch, I., Marelle, L., et al. (2015). Quantifying emerging local anthropogenic emissions in the Arctic region: The ACCESS aircraft campaign experiment. *Bulletin of the American Meteorological Society*, 96(3):441–460.

Rosenfeld, D. (2000). Suppression of rain and snow by urban and industrial air pollution. *Science*, 287(5459):1793–1796.

Rozwadowska, A., Zieliński, T., Petelski, T., and Sobolewski, P. (2010). Cluster analysis of the impact of air back-trajectories on aerosol optical properties at Hornsund, Spitsbergen. *Atmospheric Chemistry and Physics*, 10(3):877–893.

RTI (2011). Emission protocol for petroleum refineries v 2.1.1. Technical report, RTI International, USA, Research Triangle Park, NC 27709-2194.

Russell, P., Bergstrom, R., Shinozuka, Y., Clarke, A., DeCarlo, P., Jimenez, J., Livingston, J., Redemann, J., Dubovik, O., and Strawa, A. (2010). Absorption Angstrom Exponent in AERONET and related data as an indicator of aerosol composition. *Atmospheric Chemistry and Physics*, 10(3):1155–1169.

Sanchez, M., Karnae, S., and John, K. (2008). Source characterization of volatile organic compounds affecting the air quality in a coastal urban area of South Texas. *International journal of environmental research and public health*, 5(3):130–138.

Santos, F., Fraser, M., and Bird, J. (2014). Atmospheric black carbon deposition and characterization of biomass burning tracers in a northern temperate forest. *Atmospheric Environment*, 95:383–390.

Sato, M., Hansen, J., Koch, D., Lacis, A., Ruedy, R., Dubovik, O., Holben, B., Chin, M., and Novakov, T. (2003). Global atmospheric black carbon inferred from AERONET. *Proceedings of the National Academy of Sciences*, 100(11):6319–6324.

Sauvage, B., Thouret, V., Cammas, J.-P., Gheusi, F., Athier, G., and Nédélec, P. (2005). Tropospheric ozone over Equatorial Africa: regional aspects from the MOZAIC data. *Atmospheric Chemistry and Physics*, 5(2):335.

Schug, K., Manheimer-Timnat, Y., Yaccarino, P., and Glassman, I. (1980). Sooting behavior of gaseous hydrocarbon diffusion flames and the influence of additives. *Combustion Science and Technology*, 22(5-6):235–250.

Schultz, C. (2014). Texas refinery air pollution emissions are being severely underestimated. *Eos, Transactions American Geophysical Union*, 95(24):208–208.

Schuster, G. L., Dubovik, O., and Holben, B. N. (2006). Angstrom exponent and bimodal aerosol size distributions. *Journal of Geophysical Research: Atmospheres*, 111(D7).

Schwarz, J. P., Holloway, J. S., Katich, J. M., McKeen, S., Kort, E. A., Smith, M. L., Ryerson, T. B., Sweeney, C., and Peischl, J. (2015). Black carbon emissions from the Bakken Oil and Gas Development region. *Environmental Science & Technology Letters*, 2(10):281–285.

Seila, R. L., Lonneman, W. A., and Meeks, S. A. (1989). Determination of C2 to C12 ambient air hydrocarbons in 39 US cities from 1984 through 1986. Technical report, Computer Sciences Corp., Research Triangle Park, NC (USA).

Seinfeld, J. (2008). Atmospheric science: Black carbon and brown clouds. *Nature geoscience*, 1(1):15–16.

Seinfeld, J. H. and Pandis, S. N. (2016). *Atmospheric chemistry and physics: from air pollution to climate change*. John Wiley & Sons.

Sheridan, P. J. and Ogren, J. A. (1999). Observations of the vertical and regional variability of aerosol optical properties over central and eastern North America. *Journal of Geophysical Research: Atmospheres*, 104(D14):16793–16805.

Shindell, D., Chin, M., Dentener, F., Doherty, R., Faluvegi, G., Fiore, A. M., Hess, P., Koch, D., MacKenzie, I., Sanderson, M., et al. (2008). A multi-model assessment of pollution transport to the Arctic. *Atmospheric Chemistry and Physics*, 8(17):5353–5372.

Siegel, K. (1980). *Degree of conversion of flare gas in refinery high flares*. PhD thesis, Ph. D. dissertation, Fridericiana University, Karlsruhe, Germany.

Sivathanu, Y. and Faeth, G. (1990). Soot volume fractions in the overfire region of turbulent diffusion flames. *Combustion and Flame*, 81(2):133–149.

Smirnov, A., Holben, B., Eck, T., Slutsker, I., Chatenet, B., and Pinker, R. (2002). Diurnal variability of aerosol optical depth observed at AERONET (Aerosol Robotic Network) sites. *Geophysical Research Letters*, 29(23).

Smith, D. and Chughtai, A. (1995). The surface structure and reactivity of black carbon. *Colloids and Surfaces A: Physicochemical and Engineering Aspects*, 105(1):47–77.

Sonibare, J., Adebiyi, F., Obanijesu, E., and Okelana, O. (2010). Air quality index pattern around petroleum production facilities. *Management of Environmental Quality: An International Journal*, 21(3):379–392.

Sonibare, J. and Akeredolu, F. (2004). A theoretical prediction of non-methane gaseous emissions from natural gas combustion. *Energy Policy*, 32(14):1653–1665.

Stier, P., Feichter, J., Roeckner, E., Kloster, S., and Esch, M. (2006). The evolution of the global aerosol system in a transient climate simulation from 1860 to 2100. *Atmospheric Chemistry and Physics*, 6(10):3059–3076.

Stockie, J. M. (2011). The mathematics of atmospheric dispersion modeling. *Siam Review*, 53(2):349–372.

Stohl, A., Klimont, Z., Eckhardt, S., Kupiainen, K., Shevchenko, V., Kopeikin, V., and Novigatsky, A. (2013). Black carbon in the Arctic: the underestimated role of gas flaring and residential combustion emissions. *Atmospheric Chemistry and Physics*, 13(17):8833–8855.

Stone, D. K., Lynch, S. K., Pandullo, R. F., Evans, L. B., and Vatavuk, W. M. (1992). Flares. part i: flaring technologies for controlling VOC-containing waste streams. *Journal of the Air & Waste Management Association*, 42(3):333–340.

Strosher, M. T. (2000). Characterization of emissions from diffusion flare systems. *Journal of the Air & Waste Management Association*, 50(10):1723–1733.

Sultan, B. and Janicot, S. (2000). Abrupt shift of the ITCZ over West Africa and intra-seasonal variability. *Geophysical Research Letters*, 27(20):3353–3356.

Sultan, B. and Janicot, S. (2003). The West African monsoon dynamics. Part II: The "preonset" and "onset" of the summer monsoon. *Journal of climate*, 16(21):3407–3427.

Talebi, A., Fatehifar, E., Alizadeh, R., and Kahforoushan, D. (2014). The estimation and evaluation of new co, CO_2, and NO_X emission factors for gas flares using pilot scale flare. *Energy Sources, Part A: Recovery, Utilization, and Environmental Effects*, 36(7):719–726.

Tegen, I., Hollrig, P., Chin, M., Fung, I., Jacob, D., and Penner, J. (1997). Contribution of different aerosol species to the global aerosol extinction optical thickness: Estimates from model results. *Journal of Geophysical Research: Atmospheres*, 102(D20):23895–23915.

Tesner, P., Smegiriova, T., and Knorre, V. (1971a). Kinetics of dispersed carbon formation. *Combustion and Flame*, 17(2):253–260.

Tesner, P., Tsygankova, E., Guilazetdinov, L., Zuyev, V., and Loshakova, G. (1971b). The formation of soot from aromatic hydrocarbons in diffusion flames of hydrocarbon-hydrogen mixtures. *Combustion and Flame*, 17(3):279–285.

Todd, M. C., Washington, R., Martins, J. V., Dubovik, O., Lizcano, G., M'bainayel, S., and Engelstaedter, S. (2007). Mineral dust emission from the Bodélé depression, northern Chad, during BoDEx 2005. *Journal of Geophysical Research: Atmospheres*, 112(D6).

Toledano, C., Cachorro, V., Berjon, A., De Frutos, A., Sorribas, M., De la Morena, B., and Goloub, P. (2007). Aerosol optical depth and Ångström exponent climatology at El Arenosillo AERONET site (Huelva, Spain). *Quarterly Journal of the Royal Meteorological Society*, 133(624):795–807.

Torres, V. M., Herndon, S., and Allen, D. T. (2012a). Industrial flare performance at low flow conditions. 2. Steam-and air-assisted flares. *Industrial & Engineering Chemistry Research*, 51(39):12569–12576.

Torres, V. M., Herndon, S., Kodesh, Z., and Allen, D. T. (2012b). Industrial flare performance at low flow conditions. 1. Study overview. *Industrial & Engineering Chemistry Research*, 51(39):12559–12568.

Townend, J. (2013). *Practical statistics for environmental and biological scientists*. John Wiley & Sons.

Tripathi, S., Dey, S., Tare, V., and Satheesh, S. (2005). Aerosol black carbon radiative forcing at an industrial city in northern India. *Geophysical Research Letters*, 32(8).

Tumolva, L., Park, J.-Y., Kim, J.-s., Miller, A. L., Chow, J. C., Watson, J. G., and Park, K. (2010). Morphological and elemental classification of freshly emitted soot particles and atmospheric ultrafine particles using the TEM/EDS. *Aerosol Science and Technology*, 44(3):202–215.

Tunde, A., Adeleke, E., and Adeniyi, E. (2013). Impact of climate variability on human health in Ilorin, Nigeria. *Environment and Natural Resources Research*, 3(1):127.

Turner, D. B. (1994). *Workbook of atmospheric dispersion estimates: an introduction to dispersion modeling*. CRC press.

Twomey, S. A., Piepgrass, M., and Wolfe, T. (1984). An assessment of the impact of pollution on global cloud albedo. *Tellus B*, 36(5):356–366.

USEPA (1995a). AP 42-Compilation of air pollutant emission factors. Section 13.5: Industrial flares. Technical report, U.S Environmental Protection Agenecy, Office of Air quality planning and standards, Research Triangle Park, NC (http://www.epa.gov/ttn/chief/ap42/ch13/final/c13s05.pdf).

USEPA (1995b). SCREEN3 Model User's Guide EPA-454/B-95-004. Technical report, U.S. Environmental Protection Agency, Research Triangle Park, NC, USA.

USEPA (2000). Test Method 5-Determination of particulate matter emissions from stationary sources. Technical report, U.S Environmental Protection Agenecy, Research Triangle Park, NC.

USEPA (2008). Test Direct emissions from stationary combustion sources. Technical report, U.S Environmental Protection Agenecy, Research Triangle Park, NC.

USEPA (2010). Integrated science assessment for particulate matter. Technical report, US Environmental Protection Agency, Research Triangle Park, NC.

USEPA (2011). Emission estimation protocol for petroleum refineries. Technical report, U.S Environmental Protection Agenecy, Research Triangle Park, NC.

USEPA (2012). Report to congress on Black Carbon. EPA-450/R-12-001. Technical report, U.S Environmental Protection Agenecy, Research Triangle Park, NC.

USEPA (2014). AP 42-Compilation of air pollutant emission factors. Section 13.5: Industrial flares. Technical report, U.S Environmental Protection Agenecy, Research Triangle Park, NC.

Vignati, E., Karl, M., Krol, M., Wilson, J., Stier, P., and Cavalli, F. (2010). Sources of uncertainties in modelling black carbon at the global scale. *Atmospheric chemistry and physics*, 10(6):2595–2611.

Villasenor, R., Magdaleno, M., Quintanar, A., Gallardo, J., López, M., Jurado, R., Miranda, A., Aguilar, M., Melgarejo, L., Palmerın, E., et al. (2003). An air quality emission inventory of offshore operations for the exploration and production of petroleum by the Mexican oil industry. *Atmospheric Environment*, 37(26):3713–3729.

Virkkula, A., Levula, J., Pohja, T., Aalto, P., Keronen, P., Schobesberger, S., Clements, C. B., Pirjola, L., Kieloaho, A.-J., Kulmala, L., et al. (2014). Prescribed burning of logging slash in the boreal forest of Finland: emissions and effects on meteorological quantities and soil properties. *Atmospheric Chemistry and Physics*, 14(9):4473–4502.

Wang, J., Xia, X., Wang, P., and Christopher, S. A. (2004). Diurnal variability of dust aerosol optical thickness and Angström exponent over dust source regions in China. *Geophysical Research Letters*, 31(8).

Wang, X., Heald, C., Ridley, D., Schwarz, J., Spackman, J., Perring, A., Coe, H., Liu, D., and Clarke, A. (2014). Exploiting simultaneous observational constraints on mass and absorption to estimate the global direct radiative forcing of black carbon and brown carbon. *Atmospheric Chemistry and Physics*, 14(20):10989–11010.

Weyant, C. L., Shepson, P. B., Subramanian, R., Cambaliza, M. O., Heimburger, A., McCabe, D., Baum, E., Stirm, B. H., and Bond, T. C. (2016). Black carbon emissions from associated natural gas flaring. *Environmental science & technology*, 50(4):2075–2081.

Wheater, C. P. and Cook, P. A. (2000). *Using statistics to understand the environment*. Psychology Press.

Wilks, D. S. (2011). *Statistical methods in the atmospheric sciences*. Academic press.

Williams, F. (1964). *The Fundamental Theory of Chemically Reacting Flow Systems*, volume 4. New York: Perseus.

Wiscombe, W. and Grams, G. (1976). The backscattered fraction in two-stream approximations. *Journal of the Atmospheric Sciences*, 33(12):2440–2451.

WMO (2015). The climate in Africa: 2013. Technical report, World Meteorological Organisation, Switzerland (WMO-No. 1147).

Yang, X., You, Z., Hiller, J., and Watkins, D. (2016). Updating and augmenting weather data for pavement mechanistic-empirical design using ASOS/AWOS database in Michigan. *International Journal of Pavement Engineering*, pages 1–9.

Yoon, S.-C., Won, J.-G., Omar, A. H., Kim, S.-W., and Sohn, B.-J. (2005). Estimation of the radiative forcing by key aerosol types in worldwide locations using a column model and AERONET data. *Atmospheric Environment*, 39(35):6620–6630.

Young, E. M. (2013). *Food and development*. Routledge, Oxon, United Kingdom.

Yu, H., Kaufman, Y., Chin, M., Feingold, G., Remer, L., Anderson, T., Balkanski, Y., Bellouin, N., Boucher, O., Christopher, S., et al. (2006). A review of measurement-based assessments of the aerosol direct radiative effect and forcing. *Atmospheric Chemistry and Physics*, 6(3):613–666.

Zannetti, P. (2013). *Air pollution modeling: theories, computational methods and available software*. Springer Science & Business Media.

Zhang, J. J. and Morawska, L. (2002). Combustion sources of particles: 2. Emission factors and measurement methods. *Chemosphere*, 49(9):1059–1074.

Appendix A

Emission factors estimation code

```
%Begin user defined
    prompt1 = ’CH4’, ’C2H6’, ’C3H8’, ’nC4H10’, ’iC4H10’, ’nC5H12’, ’iC5H12’, ’C6H14’,
’C7H16’, ’C8H18’, ’H2S’, ’N2’, ’CO2’;
name = ’% molar composition by volume’;
num_lines = 1;
%def = ’88.72’, ’5.93’, ’1.28’, ’0.26’, ’0.26’, ’0.06’, ’0.09’, ’0.06’, ’0.1’, ’0.0’, ’0.03’, ’0.66’,
’2.55’;%mine_light
def = ’69.58’, ’0.25’, ’12.54’, ’2.35’, ’5.12’, ’5.20’, ’2.54’, ’1.97’, ’0.0’, ’0.0’, ’0.0’, ’0.24’,
’0.21’;%mine_heavy
%def = ’85.24’, ’7.06’, ’3.11’, ’1.44’, ’0.0’, ’0.0’, ’0.0’, ’0.0’, ’0.0’, ’0.0’, ’0.0’, ’1.24’,
’1.91’;%McEwen

    mol_percent = inputdlg(prompt1, name, num_lines, def);

    prompt2 = ’pressure (Pa)’, ’temperature (degC)’;
name = ’Input ambient conditions’;
num_lines = 1;
def = ’1.0133E5’, ’25.0’;
```

```
ambient_cond = inputdlg(prompt2, name, num_lines, def);

     prompt3 = ’equivalence ratio, phi’, ’stack diameter (m)’,’stack height (m)’, ’volume flux (m3/s)’;
name = ’Flow characteristics’;
num_lines = 1;
def = ’1.1’, ’0.75’,’50.0’ ’1.174’;
ER = inputdlg(prompt3, name, num_lines, def);

     %ambient conditions and constants
pressure = str2double(ambient_cond1,1) ; %Pa
ambient_temp = str2double(ambient_cond2,1)+273.15 ; %temp in K

     %Stack characteristics
volume_flux =str2double(ER4,1) ;% 1.174 ;%m3/s
stack_diam = str2double(ER2,1); %meters
phi = str2double(ER1,1);
stack_height = str2double(ER(3,1)); %meters

     %Constants
mol_weight_O2 = 32; %g/mol
mol_weight_C = 12.01 ; %g/mol
mol_weight_H = 1.008 ; %g/mol
mol_weight_CO2 = 44.01 ; %g/mol
mol_weight_H2S = 34.08188 ; %g/mol
mol_weight_SO2 = 64.066 ;%g/mol
mol_weight_CO = 28; %g/mol
mol_weight_N2 = 28.013; %g/mol
mol_weight_CH4 = 16.043; %g/mol
```

```
mol_weight_C2H6 = 30.07; %g/mol
mol_weight_C3H8 = 44.097; %g/mol
mol_weight_nC4H10 = 58.123; %g/mol
mol_weight_iC4H10 = 58.123; %g/mol
mol_weight_nC5H12 = 72.15; %g/mol
mol_weight_iC5H12 = 72.15; %g/mol
mol_weight_C6H14 = 86.18; %g/mol
mol_weight_C7H16 = 100.204; %g/mol
mol_weight_C8H18 = 114.23; %g/mol
Rgas = 8.3145 ; %m3Pa/K.mol
grav_accn = 9.80665; %m/s2
spec_heat_air_js = 1021; %J/kgK
spec_heat_air_cs = 0.24 ; %Cal/sec

mol_weight = [mol_weight_CH4;mol_weight_C2H6;mol_weight_C3H8;mol_weight_nC4H10
;mol_weight_iC4H10;...
mol_weight_nC5H12;mol_weight_iC5H12;mol_weight_C6H14;mol_weight_C7H16
;mol_weight_C8H18;mol_weight_H2S;...
mol_weight_N2;mol_weight_CO2];
%hydrogen:carbon ratio for hydrocabon species
y_CH4 = 4;
y_C2H6 = 3 ;
y_C3H8 = 8/3;
y_nC4H10 = 10/4;
y_iC4H10 = 10/4;
y_nC5H12 = 12/5;
y_iC5H12 = 12/5;
y_C6H14 = 14/6;
y_C7H16 = 16/7;
```

```
y_C8H18 = 18/8;

    aCO2 = 44.3191; %J/mol.K
bCO2 = 0.00730; %J/mol.K
aH2O = 32.4766; %J/mol.K
bH2O = 0.00862; %J/mol.K
aCO = 29.6127; %J/mol.K
bCO = 0.00301; %J/mol.K
aN2 = 29.2313; %J/mol.K
bN2 = 0.00307; %J/mol.K

    % Reaction coefficients (at T = 298.15 K)
deltahCO2 = -394.088 ;
deltahH2O = -242.174 ;
deltahCH4 = -74.73 ;
deltahC2H6 = -83.68 ;
deltahC3H8 = -104.89 ;
deltahnC4H10 = -133.14 ;
deltahiC4H10 = -133.14 ;
deltahnC5H12 = -165.52 ;
deltahiC5H12 = -165.52 ;
deltahC6H14 = -180.13 ;
deltahC7H16 = -199.88 ;
deltahC8H18 = -220.26 ;
deltahH2S = -20.447 ;
deltahCO = -110.7 ;
deltahSO2 = -297.269 ;
```

```
    % Fuel gas composition in molar percentage
CH4 = str2double(mol_percent1,1) ;
C2H6 = str2double(mol_percent2,1) ;
C3H8 = str2double(mol_percent3,1) ;
nC4H10 = str2double(mol_percent4,1) ;
iC4H10 = str2double(mol_percent5,1) ;
nC5H12 = str2double(mol_percent6,1) ;
iC5H12 =str2double (mol_percent7,1) ;
C6H14 =str2double (mol_percent8,1) ;
C7H16 =str2double( mol_percent9,1) ;
C8H18 =str2double( mol_percent10,1) ;
H2S =str2double(mol_percent11,1) ;
N2 =str2double(mol_percent12,1);
CO2 =str2double(mol_percent13,1) ;

total_mol_percent=CH4+C2H6+C3H8+nC4H10+iC4H10+nC5H12+iC5H12+C6H14+C7H16
+C8H18+H2S+N2+CO2;

    if total_mol_percent == 100.0000
disp(’TOTAL MOLE PERCENT is equal to 100.0’);
else
disp(’TOTAL MOLE PERCENT is not equal to 100.0’);
end

    %%
%Model Calculations
% b,c,z are used to estimate the adiabatic temperature
OCOM = [2;3.5;5;6.5;6.5;8;8;9.5;11;12.5];
OCOM_phi = OCOM./phi;
```

```
NCAR = [1;2;3;4;4;5;5;6;7;8];
NWAT = [2;3;4;5;5;6;6;7;8;9];
N2COM = [7.56; 13.23; 18.9; 24.57; 24.57; 30.24; 30.24; 35.91; 41.58; 47.25];
N2COM_phi = N2COM./phi;
if phi > 1.0
b = 2.*OCOM.*(1-1/phi);
c = NCAR - b;
z = N2COM_phi;
else
wT = OCOM_phi-OCOM; %excess oxygen
b = 2.*NCAR -2.*OCOM_phi + NWAT+(0.0018*OCOM_phi+2*wT);
c = NCAR - b;
z = N2COM_phi;
end

    %% Fuel and stack characteristics

input_c=[CH4/100;C2H6/100;C3H8/100;nC4H10/100;iC4H10/100;nC5H12/100;iC5H12/100;
C6H14/100;C7H16/100;...
C8H18/100;H2S/100;N2/100;CO2/100];
input_c_1=[CH4/100;C2H6/100;C3H8/100;nC4H10/100;iC4H10/100;nC5H12/100;iC5H12/100;
C6H14/100;C7H16/100;...
C8H18/100];

    molar_mass_fuel_gas=0;
for q=1:length(input_c)
molar_mass_fuel_gas=molar_mass_fuel_gas+(input_c(q)*mol_weight(q));%g/mol
end
```

```
    molar_mass_fuel_gas_without=0;
for o=1:length(input_c)-2
molar_mass_fuel_gas_without=molar_mass_fuel_gas_without+(input_c(o)*mol_weight(o));%g/mol
end

    molar_volume=Rgas.*ambient_temp./pressure ; %m3/mol

    density_fuel_gas=molar_mass_fuel_gas.*1.0E-3/molar_volume; % kg/m3

    molar_density = density_fuel_gas/(molar_mass_fuel_gas*1.0E-3);%mol/m3

    rmmair = 0.78*0.028 + 0.22*0.032 ; % kg/mol 0.0288...

    density_ambient_air = pressure*rmmair/(Rgas*ambient_temp) ; % kg/m3
density_ambient_air_gm = density_ambient_air*1000 ; %g/m3

    Vs=4*volume_flux/(pi*stack_diam^2); % m/s

    %% HEAT RELEASE AND ADIABATIC TEMPERATURE

    deltah_comb_CH4 = c(1,1)*deltahCO2+b(1,1)*deltahCO+2*deltahH2O-deltahCH4 ; % kJ/mol
heat_value_CH4 = abs(deltah_comb_CH4)*CH4/100 ;

    deltah_comb_C2H6 = c(2,1)*deltahCO2+b(2,1)*deltahCO+3*deltahH2O-deltahC2H6 ;
heat_value_C2H6 = abs(deltah_comb_C2H6)*C2H6/100 ;
```

```
    deltah_comb_C3H8 = c(3,1)*deltahCO2+b(3,1)*deltahCO+4*deltahH2O-deltahC3H8 ;
heat_value_C3H8 = abs(deltah_comb_C3H8)*C3H8/100 ;

    deltah_comb_nC4H10 = c(4,1)*deltahCO2+b(4,1)*deltahCO+5*deltahH2O-2*deltahnC4H10
;
heat_value_nC4H10 = abs(deltah_comb_nC4H10)*nC4H10/100 ;

    deltah_comb_iC4H10 = c(5,1)*deltahCO2+b(5,1)*deltahCO+5*deltahH2O-deltahiC4H10
;
heat_value_iC4H10 = abs(deltah_comb_iC4H10)*iC4H10/100 ;

    deltah_comb_nC5H12 = c(6,1)*deltahCO2+b(6,1)*deltahCO+6*deltahH2O-deltahnC5H12
;
heat_value_nC5H12 = abs(deltah_comb_nC5H12)*nC5H12/100 ;

    deltah_comb_iC5H12 = c(7,1)*deltahCO2+b(7,1)*deltahCO+6*deltahH2O-deltahiC5H12
;
heat_value_iC5H12 = abs(deltah_comb_iC5H12)*iC5H12/100 ;

    deltah_comb_C6H14 = c(8,1)*deltahCO2+b(8,1)*deltahCO+7*deltahH2O-deltahC6H14
;
heat_value_C6H14 = abs(deltah_comb_C6H14)*C6H14/100 ;

    deltah_comb_C7H16 = c(9,1)*deltahCO2+b(9,1)*deltahCO+8*deltahH2O-deltahC7H16
;
heat_value_C7H16 = abs(deltah_comb_C7H16)*C7H16/100 ;

    deltah_comb_C8H18 = c(10,1)*deltahCO2+b(10,1)*deltahCO+9*deltahH2O-deltahC8H18
;
```

```
heat_value_C8H18 = abs(deltah_comb_C8H18)*C8H18/100 ;

    deltah_comb_H2S = 2*deltahSO2+2*deltahH2O-2*deltahH2S ;
heat_value_H2S = abs(deltah_comb_H2S)*H2S/100 ;

    % J/mol total_heat_value = (heat_value_CH4+heat_value_C2H6+heat_value_C3H8...
+heat_value_nC4H10+heat_value_iC4H10+heat_value_nC5H12+heat_value_iC5H12...
+heat_value_C6H14+heat_value_C7H16+heat_value_C8H18+heat_value_H2S)*1e3 ;

    total_heat_valueMJkg =
(total_heat_value*1e-6)/(molar_mass_fuel_gas*1e-3) ;%MJ/Kg
LHV = total_heat_valueMJkg*density_fuel_gas ;%MJ/m3
HHV = LHV*1.1 ;%MJ/m3

    deltah = [deltah_comb_CH4;deltah_comb_C2H6;deltah_comb_C3H8;deltah_comb_nC4H10;...
deltah_comb_iC4H10;deltah_comb_nC5H12;deltah_comb_iC5H12;deltah_comb_C6H14;
deltah_comb_C7H16; deltah_comb_C8H18];

    A=0;
for k=1:length(input_c)-3
A = A + (c(k).*aCO2 + b(k).*aCO + NWAT(k).*aH2O + z(k).*aN2)*(input_c(k));
end

    B=0;
for l=1:length(input_c)-3
B = B + (c(l).*bCO2./2 + b(l).*bCO./2 + NWAT(l).*bH2O./2 + z(l).*bN2./2)*(input_c(l));
end
```

```
C=0;
for p=1:length(input_c)-3
C = C+(deltah(p)./phi).*input_c(p)*1000;
end

D = [B A C];
T = roots(D);

T_ad = T(2,:)+ambient_temp;

%%
% NOx emission as a function of net heat released
net_heat_release = volume_flux*density_fuel_gas*total_heat_valueMJkg*(10^6)*0.75; %J/s
%0.75=1-Fr
net_heat_release_cs = net_heat_release*0.24; %heat released in cal/sec
net_heat_GJ_kg = net_heat_release/volume_flux/density_fuel_gas/1E9;
% net_heat_release_MW = net_heat_release*1.0E-6;
%heat_released_MW
net_heat_releaseMMBtu_hr = net_heat_release*3.412E-6; %1J/s = 3.412E-6 MMBtu/hr
EFnox = net_heat_releaseMMBtu_hr*(0.001); % lb/MMBtu
EFnox_g_MJ = EFnox*(453.59/1055.9); %g/MJ
EFnox_gm3 = EFnox_g_MJ*total_heat_valueMJkg*density_fuel_gas; %g/m3 %(g/MJ*MJ/kg*kg/m3)
EFnox_kg_kg = EFnox_gm3*1E-3./density_fuel_gas; %kg/kg
EFnox_gs = EFnox_gm3 * volume_flux; %g/s

% net_heat_release USED IN BEYCHOK (1979)
flame_length = 4.56E-3*(net_heat_release/4.1868)^0.478; %metres %Beychok(1979)
```

density_flue = density_fuel_gas/(T_ad/ambient_temp); %kg/m3
scaling_parameter = (0.5955+0.61*(density_fuel_gas))/(0.45); % scaling parameter interms of Richarson ratio
% scaling_parameter = (0.5272+0.6092*(density_fuel_gas))/(0.42);
%% SO2 YIELD
% 1 moles of H2S gives 1 mole of SO2
SO2_yield_mole = H2S/100;
EFSO2_gm3 = (SO2_yield_mole.*pressure.*mol_weight_SO2)./(Rgas.*ambient_temp);
EFSO2_gs = EFSO2_gm3.*volume_flux;
EFSO2_kg_kg = EFSO2_gm3*1E-3./density_fuel_gas;
%% Momentum flux of emission, Fm
equi_stack_diameter_ds = ((4.0*net_heat_release_cs*T_ad)/(pi*spec_heat_air_cs density_ambient_air_gm*ambient_temp *Vs*(T_ad-ambient_temp)))$^{0.5}$; %North_Dakota_DoH
momentum_flux_Fm1 = (Vs^{2}*equi_stack_diameter_ds^{2}*ambient_temp)/(4*T_ad); %m4/s2
momentum_flux_Fm2 = (Vs*net_heat_release)/(3.142*1.012*1225*(T_ad-ambient_temp)); %m4/s2

%% Buoyancy flux, Fb
buoyancy_flux_Fb = (grav_accn*net_heat_release)/(3.142*1012*1.225*ambient_temp); %m4/s3(Ontario)

%% Effective stack height
eff_stack_height = stack_height+(4.56E-3*((net_heat_release_cs)$^{0.478}$)); %meters
deltaHeight = eff_stack_height - stack_height; %meters

%% Air/fuel mass ratio estimation
H_C_ratio=[y_CH4;y_C2H6;y_C3H8;y_nC4H10;y_iC4H10;y_nC5H12;y_iC5H12;y_C6H14; y_C7H16;y_C8H18];

```
Air_fuel_mass_ratio = 0;

for t=1:length(input_c)-3
Air_fuel_mass_ratio = Air_fuel_mass_ratio+(4.76/phi).*(1+0.25.*H_C_ratio(t)).*(rmmair.*1e3./
(12.01+1.008.*H_C_ratio(t))).*(input_c(t));
end
%fs = 1/(1+Air_fuel_mass_ratio);
fs = phi/((Air_fuel_mass_ratio*phi)+phi);% same as fs above (both are right)

%% Reynolds number, Richardson ratio and Froude numbers
fuel_gas_Froude_number =Vs*(fs)^1.5/((grav_accn*stack_diam)^0.5)*(density_fuel_gas/
density_ambient_air)^0.25;
% fuel_gas_Froude_number = 0.12;
if (0.1 < fuel_gas_Froude_number)
disp ('Fuel Gas Froude Number is not within model limit')
break
end

if (fuel_gas_Froude_number < 0.001)
disp ('Fuel Gas Froude Number is not within model limit')
break
end

Source_Reynolds_number_Re = Vs*stack_diam/(1.04E-5/density_fuel_gas);
fprintf('Reynolds number = %f \n', Source_Reynolds_number_Re);
if (Source_Reynolds_number_Re < 4000)
disp ('Reynolds number is not within the model limit')
break
```

```
end

    fire_Froude_number =Vs*(fs)^1.5/((((T_ad - ambient_temp)/ambient_temp)*
grav_accn*stack_diam)^0.5)* (density_fuel_gas/density_ambient_air)^0.25;

    if (fire_Froude_number < 0.0012 )
disp('Fire Froude number is too low')

    elseif (0.003 > fire_Froude_number) &&
(fire_Froude_number >= 0.0012)
soot_yield = ((0.0389*fire_Froude_number) +
5E-05)*((2.4872+1.3701*(density_fuel_gas))/(1.5));
disp('Fire Froude number is btw 0.0012 and 0.003')

    elseif (0.007 > fire_Froude_number) &&
(fire_Froude_number >= 0.003)
soot_yield = ((0.0975*fire_Froude_number) -
0.0001)*((2.4872+1.3701*(density_fuel_gas))/(1.5));
disp('Fire Froude number is btw 0.003 and 0.007')

    elseif (0.01 > fire_Froude_number) &&
(fire_Froude_number >= 0.007)
soot_yield = ((-0.0529*fire_Froude_number) +
0.00095)*((2.4872+1.3701*(density_fuel_gas))/(1.5));
disp('Fire Froude number is btw 0.007 and 0.01')

    elseif (0.02 > fire_Froude_number) &&
(fire_Froude_number >= 0.01) soot_yield = ((-0.023*fire_Froude_number) +
0.000635)*((2.4872+1.3701*(density_fuel_gas))/(1.5));
```

```
disp('Fire Froude number is btw 0.01 and 0.02')

    elseif (0.03 >= fire_Froude_number) &&
(fire_Froude_number >= 0.02)
soot_yield = ((-0.007*fire_Froude_number) +
0.00032)*((2.4872+1.3701*(density_fuel_gas))/(1.5));
disp('Fire Froude number is btw 0.02 and 0.03')

    elseif fire_Froude_number > 0.03
disp ('Fire Froude number too high')
else
end

    %% Richardson Ratio;

    RiL = pi*grav_accn*density_ambient_air*((flame_length)^3)/(4*density_flue*pi*
((stack_diam/2)^2)*(Vs^2));

    %% CO2, CO and Soot estimations

    carbon_soot_num = ((soot_yield*(molar_mass_fuel_gas*1E-3)*CH4/100)*1000)/12; %
scalar number
matrix_carbon_soot_num = carbon_soot_num.*NCAR;

    % total_carbon = NCAR.*input_c_1;
% carbon_soot_num = ((soot_yield*(molar_mass_fuel_gas*1E-3)./carbon_number)*1000)/12;
% scalar number
% matrix_carbon_soot_num = carbon_soot_num.*NCAR;
```

```
    %oxy_factor =2E-6*molar_mass_fuel_gas+0.0018; %g/mol %oxy_factor
=2E-5*molar_mass_fuel_gas+0.0006; %g/mol % oxy_factor = 0.002; % 0.24% of O2.
CO/CO2 of the order of 2E-3 which is the yield of least CO possible

    w = (0.005.*NCAR-2.01.*OCOM.*(1-1/phi)+2.005.*matrix_carbon_soot_num)/2.01;
%oxygen_leftover
if (phi <= 0)
disp ('invalid phi')

    elseif (phi < 1)

    v = NCAR-matrix_carbon_soot_num; %CO2
%using the ratio CO/CO2 =0.0024 (EEMS)
% w = oxy_factor.*OCOM+(OCOM_phi-OCOM) ; %oxygen_leftover

    % w = (0.0024.*NCAR-2.0048.*OCOM.*(1-1/phi)+2.0024.*matrix_carbon_soot_num)/2.0048;
%oxygen_leftover
y = 2.*OCOM*(1-1/phi)+2.*w-2.*matrix_carbon_soot_num;
x = NCAR-matrix_carbon_soot_num-y;

    % x = matrix_carbon_soot_num - 2.*w;
% y = 2.*(NCAR - matrix_carbon_soot_num)-(2*OCOM_phi - NWAT-2*w);
% x = NCAR-matrix_carbon_soot_num-y;
z = N2COM_phi;

    nleftoverO2_nfuelgas = 0;
for a = 1:length(input_c)-3
nleftoverO2_nfuelgas = nleftoverO2_nfuelgas + (w(a).*input_c(a)) ;
```

```
end

    leftoverO2_gm3 = (nleftoverO2_nfuelgas.*pressure.*mol_weight_O2)./(Rgas.*ambient_temp);
%oxygen_leftover

    nCO2_nfuelgas = 0;
for j=1:length(input_c)-3
nCO2_nfuelgas=nCO2_nfuelgas + (x(j).*input_c(j)) ;
end
nCO2_nfuelgas=nCO2_nfuelgas+input_c(end);

    EFCO2_gm3 = (nCO2_nfuelgas.*pressure.*mol_weight_CO2)./(Rgas.*ambient_temp);
%g/m3

    EFCO2_gs = EFCO2_gm3.*volume_flux;
EFCO2_kg_kg = EFCO2_gm3*1E-3./density_fuel_gas;

    nCO_nfuelgas=0 ;
for i=1:length(input_c)-3
nCO_nfuelgas =nCO_nfuelgas+ y(i).*input_c(i) ;
end
EFCO_gm3 = (nCO_nfuelgas.*pressure.*mol_weight_CO)./(Rgas.*ambient_temp); %g/m3

    EFCO_gs = EFCO_gm3.*volume_flux;
EFCO_kg_kg = EFCO_gm3*1E-3./density_fuel_gas;
elseif (phi =1)

    % v = NCAR-matrix_carbon_soot_num; %CO2
```

```
    % w = oxy_factor.*OCOM; %oxygen_leftover %using the ratio CO/CO2 =0.0024
(EEMS)
% w = (0.0024.*NCAR+2.0024.*matrix_carbon_soot_num)/2.0048; %leftover O2 i.e VO2
y = 2.*(w-matrix_carbon_soot_num);
%y = 2.*(NCAR - matrix_carbon_soot_num)-(2*OCOM_phi - NWAT-2*w);
x = NCAR+matrix_carbon_soot_num - 2.*w;
z = N2COM_phi;

    nleftoverO2_nfuelgas = 0;
for a = 1:length(input_c)-3 nleftoverO2_nfuelgas = nleftoverO2_nfuelgas + (w(a).*input_c(a))
;
end

    leftoverO2_gm3 = (nleftoverO2_nfuelgas.*pressure.*mol_weight_O2)./(Rgas.*ambient_temp);
%oxygen_leftover

    nCO2_nfuelgas = 0;
for j=1:length(input_c)-3 nCO2_nfuelgas=nCO2_nfuelgas + (x(j).*input_c(j)) ;
end
nCO2_nfuelgas=nCO2_nfuelgas+input_c(end);

    EFCO2_gm3 = (nCO2_nfuelgas.*pressure.*mol_weight_CO2)./(Rgas.*ambient_temp)+CO2/100;
%g/L

    EFCO2_gs = EFCO2_gm3.*volume_flux;
EFCO2_kg_kg = EFCO2_gm3*1E-3./density_fuel_gas;
EFCO2_kg_GJ = EFCO2_kg_kg/net_heat_GJ_kg;
```

```
    nCO_nfuelgas=0 ;
for i=1:length(input_c)-3
nCO_nfuelgas =nCO_nfuelgas+ y(i).*input_c(i) ;
end
EFCO_gm3 = (nCO_nfuelgas.*pressure.*mol_weight_CO)./(Rgas.*ambient_temp); %g/L

    EFCO_gs = EFCO_gm3.*volume_flux;
EFCO_kg_kg = EFCO_gm3*1E-3./density_fuel_gas;
EFCO_kg_GJ = EFCO_kg_kg/net_heat_GJ_kg;

    elseif (phi > 1)

    % y = 2.*(NCAR - matrix_carbon_soot_num)-(2*OCOM_phi - NWAT);
y = 2.*OCOM*(1-1/phi)-2.*matrix_carbon_soot_num;
x = NCAR-matrix_carbon_soot_num - y;
z = N2COM_phi;

    nCO_nfuelgas=0 ;
for i=1:length(input_c)-3
nCO_nfuelgas =nCO_nfuelgas+ y(i).*input_c(i) ;
end

    EFCO_gm3 = (nCO_nfuelgas.*pressure.*mol_weight_CO)./(Rgas.*ambient_temp); %g/L

    EFCO_gs = EFCO_gm3.*volume_flux;
EFCO_kg_kg = EFCO_gm3*1E-3./density_fuel_gas;

    nCO2_nfuelgas=0;
for j=1:length(input_c)-3 nCO2_nfuelgas=nCO2_nfuelgas + (x(j).*input_c(j)) ;
```

```
end

    nCO2_nfuelgas=nCO2_nfuelgas+input_c(end);
EFCO2_gm3 = (nCO2_nfuelgas.*pressure.*mol_weight_CO2)./(Rgas.*ambient_temp)+CO2/100;
%g/L

    EFCO2_gs = EFCO2_gm3.*volume_flux;
EFCO2_kg_kg = EFCO2_gm3*1E-3./density_fuel_gas;
else
end

    mass_soot = 0;
for f=1:length(input_c)-3
mass_soot = mass_soot + 12.*(matrix_carbon_soot_num(f)).*(input_c(f)); %g/mol
end

    EF_soot_gm3 = molar_density * mass_soot; %g/m3
EF_soot_kg_kg = EF_soot_gm3*1E-3/density_fuel_gas; %kg/kg
EF_soot_gs = EF_soot_gm3 * volume_flux; %g/s

    soot_CO_ratio = EF_soot_gm3/EFCO_gm3 ;
CO_CO2_ratio = EFCO_gm3/EFCO2_gm3;
```

Appendix B

Trajectory classification algorithm

```
Program clustering _trajs
implicit none
!include ’netcdf.inc’
! DECLARATIONS
!character*4,parameter :: flightn=’B735’ ! Flight number; used to define trajectory and
flight-track files read in, ’traj _ file’ and ’flight _ track _ file’
integer,parameter :: npar=10 ! Max number of parameters in command line
integer,parameter :: ntraj=9 ! Number of back-trajectories bound for flight track, ’flightn’;
CHECK ’traj _ file’
integer,parameter :: ntime=281 ! Number of time points on each trajectory; number of 36
min timesteps in 7 days.. +1
integer,parameter :: ltimestep=2160 ! Length of timestep, or separation of time points, in
secs; 36 mins x 60 secs
integer,parameter :: ninfo=4 ! Number of pieces of information (besides time) read in from
’traj _ file’; lon, lat, p, and travel _ time
integer,parameter :: nsource=7 ! Number of source to detect:
! 1: gas flaring
! 2: biomass burning-1
! 3: desert
```

```
! 4: city-1
! 5: city-2
! 6: biomass burning-2
! 7: biomass burning-3
!integer,parameter :: start _ year=2012
!integer,parameter :: start _ month=06
!integer,parameter :: start _ day=1
!integer,parameter :: start _ hour=0
integer,parameter :: nfile=1
!integer,parameter,dimension(12) :: month _ days=(/31,29,31,30,31,30,31,31,30,31,30,31/)
!integer :: year,month,day,hour
integer :: i,iarg,idxb,idxc,ip
integer :: ifile,itime,itraj,isr,iline ! Counter for looping
integer :: dumint ! Dummy integer
integer :: npart ! Number of particles read in from ’traj_file’; should equal ntraj - used as an
internal check
integer :: nattr ! Number of attributes included in ’traj_file’; affects size of traj_line_data
array - used for internal check
character*5 :: dumstr ! Dummy string
character*78 :: traj_file ! Trajectory file
character*65,parameter :: flare_metrics_file=’C:\ Users\user\Dropbox\My_trajectories\traj_outputs’
! flare metrics output file
character*70 :: ldumstr ! Long dummy string
character*40,dimension(npar) :: ch ! Long dummy string
character*20 fmt,fmat,date
character*80 outfn,filename
real,dimension(ntraj,ntime,ninfo) :: traj_data ! Array to hold trajectory information
real,dimension(6) :: traj_data_line ! Array to hold line of trajectory data
integer,dimension(ntraj,nsource) :: traj_number ! Array to hold trajectory number
```

```
integer,dimension(ntraj,nsource) :: source_hit ! Array to hold trajectory flare-hit information
real,dimension(ntraj,nsource) :: travel_time ! Array to hold the travel time of the trajectory from source to receptor
real,dimension(ntraj,nsource) :: pressure ! Array to hold trajectory flare pressure-level information of source
! Array to hold the geographical information of each source box
real,dimension(4,nsource) :: geog_source = (/ &
5.10, 3.9, 8.10, 6.0,&
21.55, -17.67, 33.50, -12.00, &
6.2, 13.9, 17.0, 18.8 , &
3.32, 6.43, 3.52, 6.60, &
3.85, 7.27, 4.0, 7.45, &
357.0, 6.5, 3.0, 11.5, &
13.6, 6.5, 22.5, 11.5 /)
! geog_source(1,:) - longitude of the lower-left corner of the source box
! geog_source(2,:) - latitude of the lower-left corner of the source box
! geog_source(3,:) - longitude of the upper-right corner of the source box
! geog_source(4,:) - latitude of the upper-right corner of the source box
! geog_source info for gas-flaring box
! geog_source(1,1) = 5.1 ! longitude of ll-corner of the box
! geog_source(2,1) = 3.9 ! latitude of ll-corner of the box
! geog_source(3,1) = 8.1 ! width in longitude
! geog_source(4,1) = 6.0 ! depth in latitude
! !geog_source info for biomass burning-1 box
! geog_source(1,2) = 21.55 ! longitude of ll-corner of the box
! geog_source(2,2) = -17.67 ! latitude of ll-corner of the box
! geog_source(3,2) = 33.50 ! width in longitude
! geog_source(4,2) = -12.00 ! depth in latitude
! geog_source info for desert box
```

```
! geog_source(1,3) = 6.2 ! longitude of ll-corner of the box
! geog_source(2,3) = 13.9 ! latitude of ll-corner of the box
! geog_source(3,3) = 17.0 ! width in longitude
! geog_source(4,3) = 18.8 ! depth in latitude
!geog_source info for city-1 box
! geog_source(1,4) = 3.32 ! longitude of ll-corner of the box
! geog_source(2,4) = 6.43 ! latitude of ll-corner of the box
! geog_source(3,4) = 3.52 ! width in longitude
! geog_source(4,4) = 6.60 ! depth in latitude
! geog_source info for city-2 box
! geog_source(1,5) = 3.85 ! longitude of ll-corner of the box
! geog_source(2,5) = 7.27 ! latitude of ll-corner of the box
! geog_source(3,5) = 4.0 ! width in longitude
! geog_source(4,5) = 7.45 ! depth in latitude
! geog_source info for biomass burning-2 box
! geog_source(1,2) = 357.0 ! longitude of ll-corner of the box
! geog_source(2,2) = 6.5 ! latitude of ll-corner of the box
! geog_source(3,2) = 3.0 ! width in longitude
! geog_source(4,2) = 11.5 ! depth in latitude
! !geog_source info for biomass burning-3 box
! geog_source(1,2) = 13.6 ! longitude of ll-corner of the box
! geog_source(2,2) = 6.5 ! latitude of ll-corner of the box
! geog_source(3,2) = 22.5 ! width in longitude
! geog_source(4,2) = 11.5 ! depth in latitude

!=====================================================================
! Beginning of the programme
!=====================================================================
iarg = iargc()
```

```
if(iarg .ne. 1) then
print*,’Usage 1: backtraj filename’
print*,’ filename: Ilorin_back_2006110100, Ilorin_back_2006110112,...’
print*,"Example 1: backtraj utraj-df_B235_2006081718"
print*,’ ’
stop
endif
do i=1,iarg
call getarg(i,ch(i))
enddo
ip=1
filename = ch(ip)
! ip=ip+1
! date = ch(ip)
! ip=ip+1
! fmat=ch(ip)

    ! ZERO ARRAYS
traj_data_line(:)=0.0
!ft_data_line(:)=0.0
traj_data(:,:,:)=0.0

    !traj_file=’C:\Users\user\Dropbox\My_trajectories\trajs\traj_201206\gf_ftrajs_’ ! sdate
! traj_file=’C:\Users\ogf327\Dropbox\My_trajectories\backtrajs\utraj-df_B235_2006081718’
! traj_file=’./gf_ftrajs_2006010100’
!————————————————————————
! open input file and read
!————————————————————————
idxb = index(filename,’ ’) - 1
```

```
traj_file = filename(1:idxb)
write(6,*)’traj_file=’,filename(1:idxb)
open(unit=10,file=traj_file,form=’formatted’,status=’old’)
do iline=1,3
read(10,’(A)’) ldumstr
enddo

    read(10,’(A33,I8)’) ldumstr,npart
! write(6,*)’npart=’,npart
if (npart.ne.ntraj) then ! Check that npart = ntraj
write(6,*)’Stopping: npart /= ntraj’
write(6,*)’ntraj=’,ntraj
stop
endif

    read(10,’(A25,I4)’) ldumstr,nattr
! write(6,*)’nattr=’,nattr
if (nattr.ne.1) then ! Check that nattr = 1 (value dictated by choice in John Methven’s trajectory code)
write(6,*)’Stopping: nattr /= 1 hence size of traj_line_data is wrong’
stop
endif

    do iline=1,8
read(10,’(A)’) ldumstr
enddo

    do itraj=1,ntraj
do iline=1,4
```

```
read(10,’(A)’)ldumstr
enddo !200
do itime=1,ntime
read(10,*)traj_data_line(:)
traj_data(itraj,itime,4)=traj_data_line(2) ! Hour
traj_data(itraj,itime,2)=traj_data_line(3) ! Lat
traj_data(itraj,itime,1)=traj_data_line(4) ! Lon
traj_data(itraj,itime,3)=traj_data_line(5) ! Pres
enddo
enddo
close(10)
! enddo

    ! CALCULATE trajectories METRICS
!do ifile=1,nfile
do isr=1,nsource
do itraj=1,ntraj
do itime=2,ntime
! Does air parcel lie in the box of interest AND in the ABL (>=900hPa)?
! if (traj_data(itraj,itime,1).ge.5.1.and.traj_data(itraj,itime,1).le.7.6) then !longitude
! if (traj_data(itraj,itime,2).ge.4.1.and.traj_data(itraj,itime,2).le.6.1) then !latitude
if (traj_data(itraj,itime,1) .ge. geog_source(1,isr) .and. &
traj_data(itraj,itime,1) .le. geog_source(3,isr)) then !longitude
if (traj_data(itraj,itime,2) .ge. geog_source(2,isr) .and. &
traj_data(itraj,itime,2) .le. geog_source(4,isr)) then !latitude
!if (traj_data(itraj,itime,3).le.900.0) then !pressure
source_hit(itraj,isr)=1
pressure(itraj,isr)= traj_data(itraj,itime,3) ! pressure data
travel_time(itraj,isr)= traj_data(itraj,itime,4) ! travel time
```

```
traj_number(itraj,isr)= itraj ! trajectory number
exit ! skip through rest of itime and jump to next itraj
endif
endif
enddo
enddo
enddo
! enddo

    !——————————————————————————
! open output file and write
!——————————————————————————
!open(unit=12,file=flare_metrics_file,form='formatted')
idxc = index(filename,' ') - 1
outfn = filename(1:idxc)//'.out'
open(12,file=outfn) ! it is ascii format

    ! idxc=index(fmat,' ')-1
! fmt='('//fmat(1:idxc)//')'
! print*,'Output format:',fmt

    ! WRITE OUT FLARE METRICS
write(12,*)'Source# Traj# Pressure(mb) Travel_time(hr)'
do isr=1,nsource
! write (12, *)'=== Source No.', isr, ' has a total hits of ',sum(source_hit(:,isr))
do itraj=1,ntraj
if(source_hit(itraj,isr).ne.0)then
write (12, '(i5,i8,f14.3,f14.1)')
isr,traj_number(itraj,isr),pressure(itraj,isr),travel_time(itraj,isr)
```

```
! write (12, fmt) isr,traj_number(itraj,isr),pressure(itraj,isr),travel_time(itraj,isr)


   ! write (12, *)’Pressure:’
! write (12, fmt) pressure(itraj,isr)
! write (12, *)’Travel time:’
! write (12, fmt) travel_time(itraj,isr)
! write (12, *)’Traj number:’
! write (12, ’(10i6)’) traj_number(itraj,isr)
endif
enddo
enddo
close(12)
end
```

Appendix C

Plots of spatial distribution of pollutants

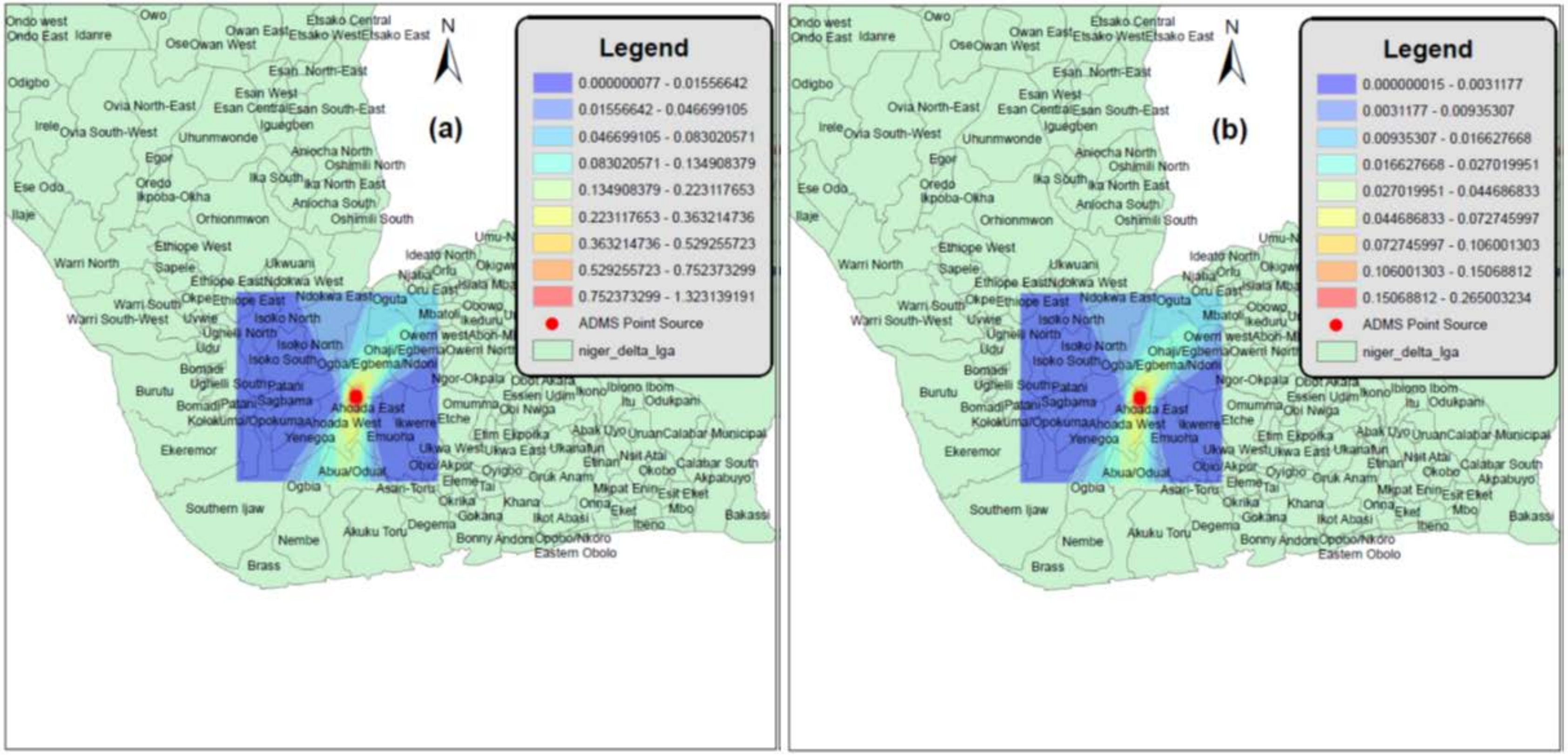

Figure C.1: Modelled dispersion and monthly mean ground-level concentrations of (a) CO and (b) BC using fuel with lower heat content (fuel I) during a non-WAM months (Jan. 2015).

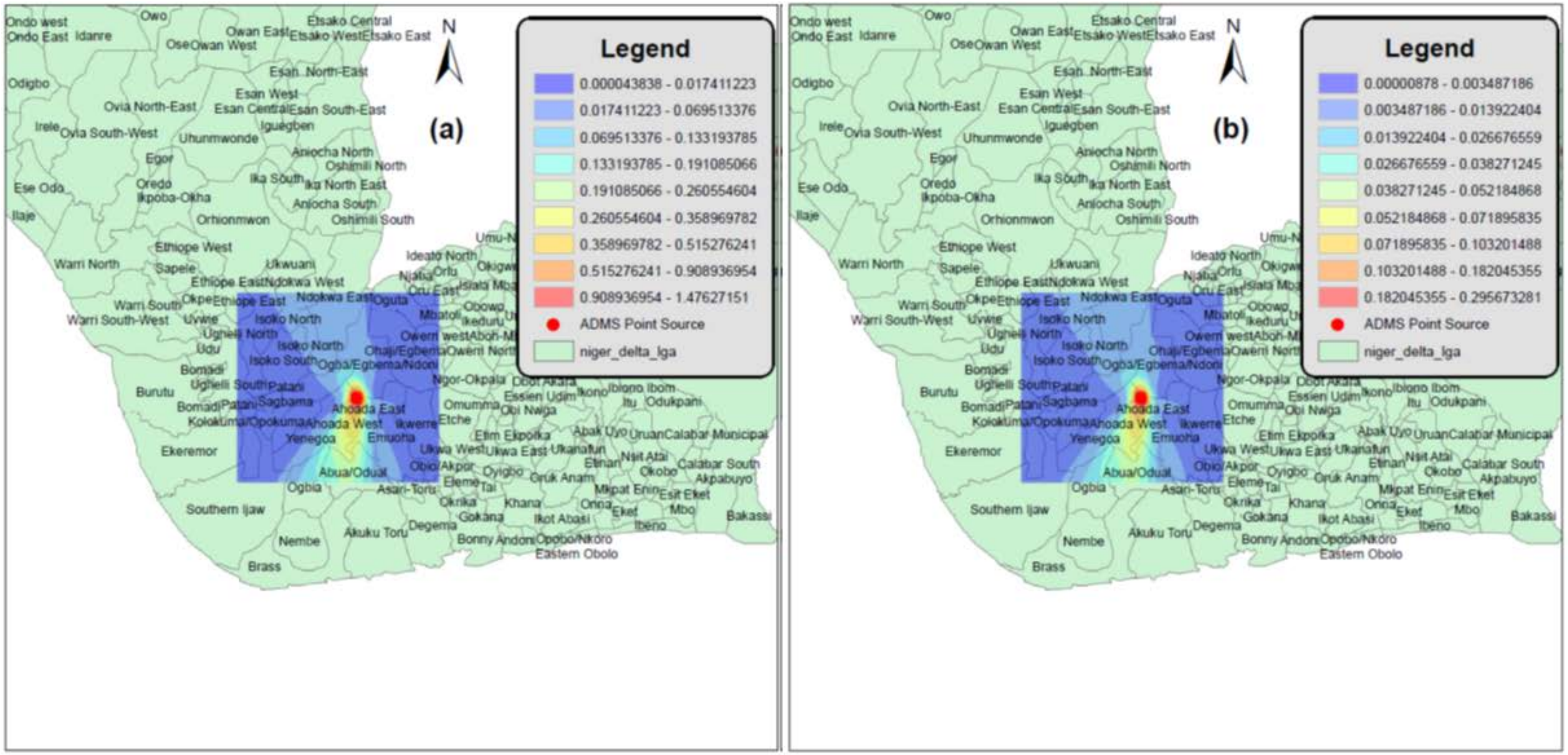

Figure C.2: Modelled dispersion and monthly mean ground-level concentrations of (a) CO and (b) BC using fuel with lower heat content (fuel I) during a non-WAM months (Dec. 2015).

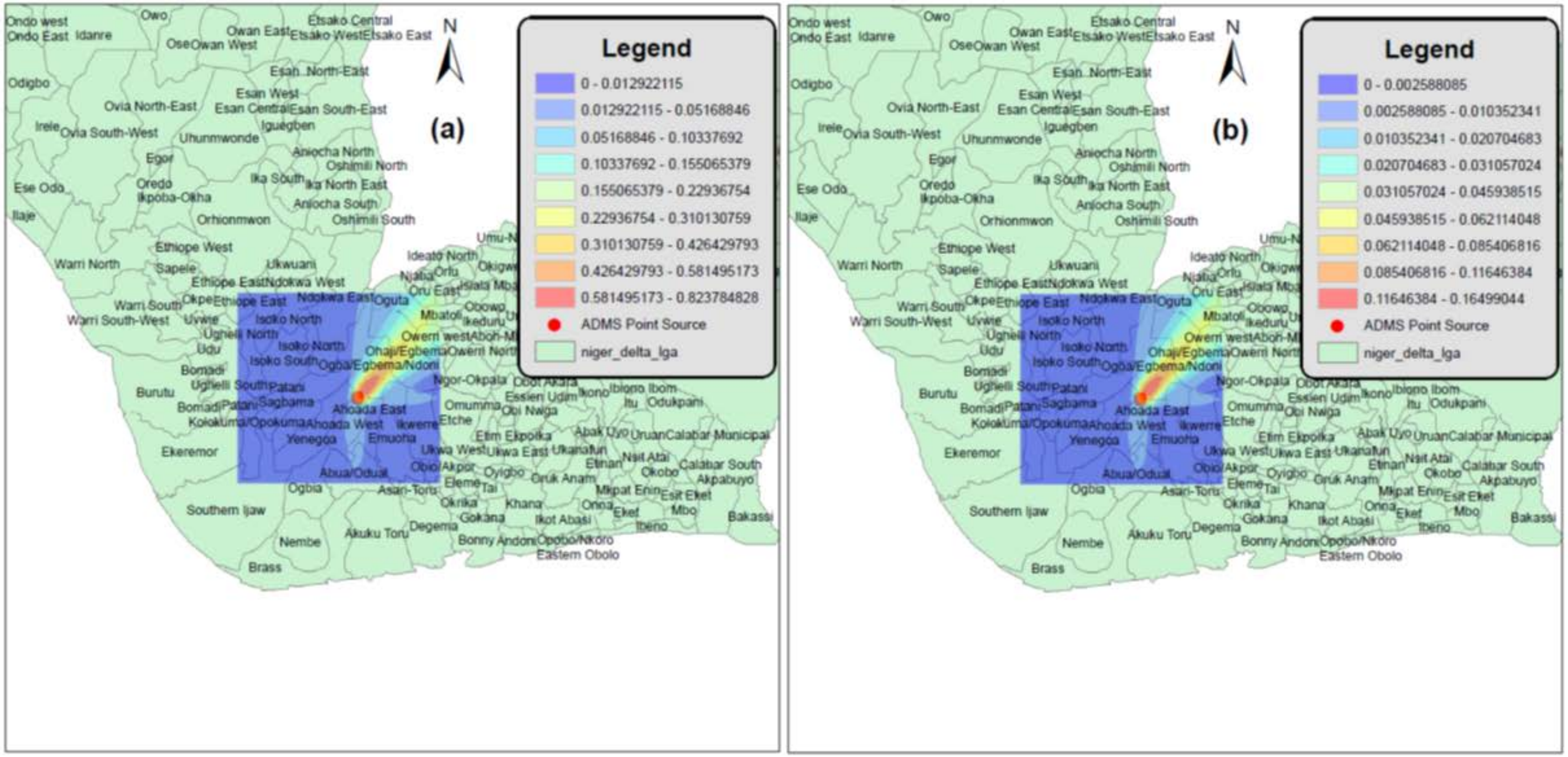

Figure C.3: Modelled dispersion and monthly mean ground-level concentrations of (a) CO and (b) BC using fuel with lower heat content (fuel I) during a WAM months (Aug. 2014).

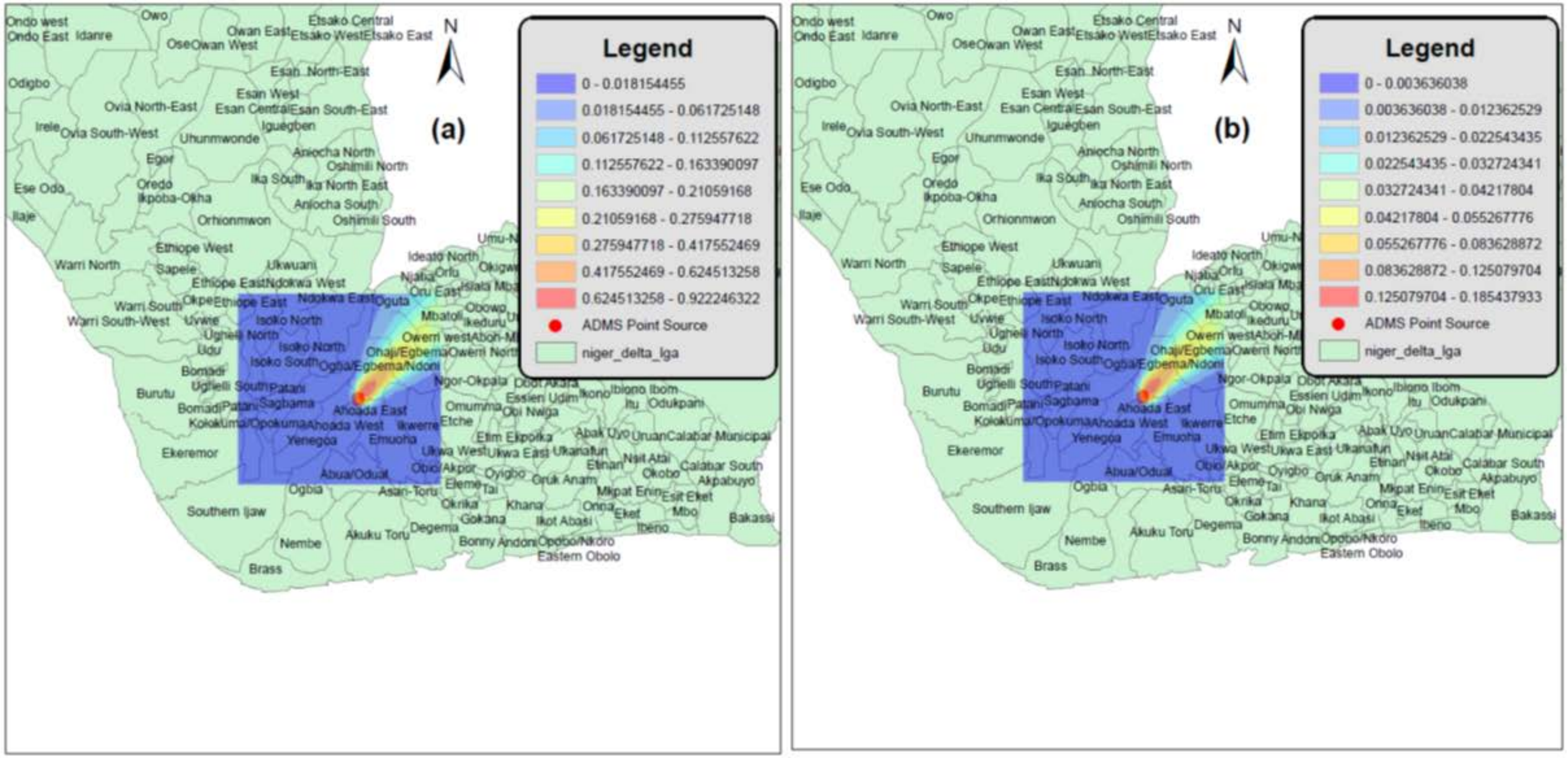

Figure C.4: Modelled dispersion and monthly mean ground-level concentrations of (a) CO and (b) BC using fuel with lower heat content (fuel I) during a WAM months (Aug. 2015).

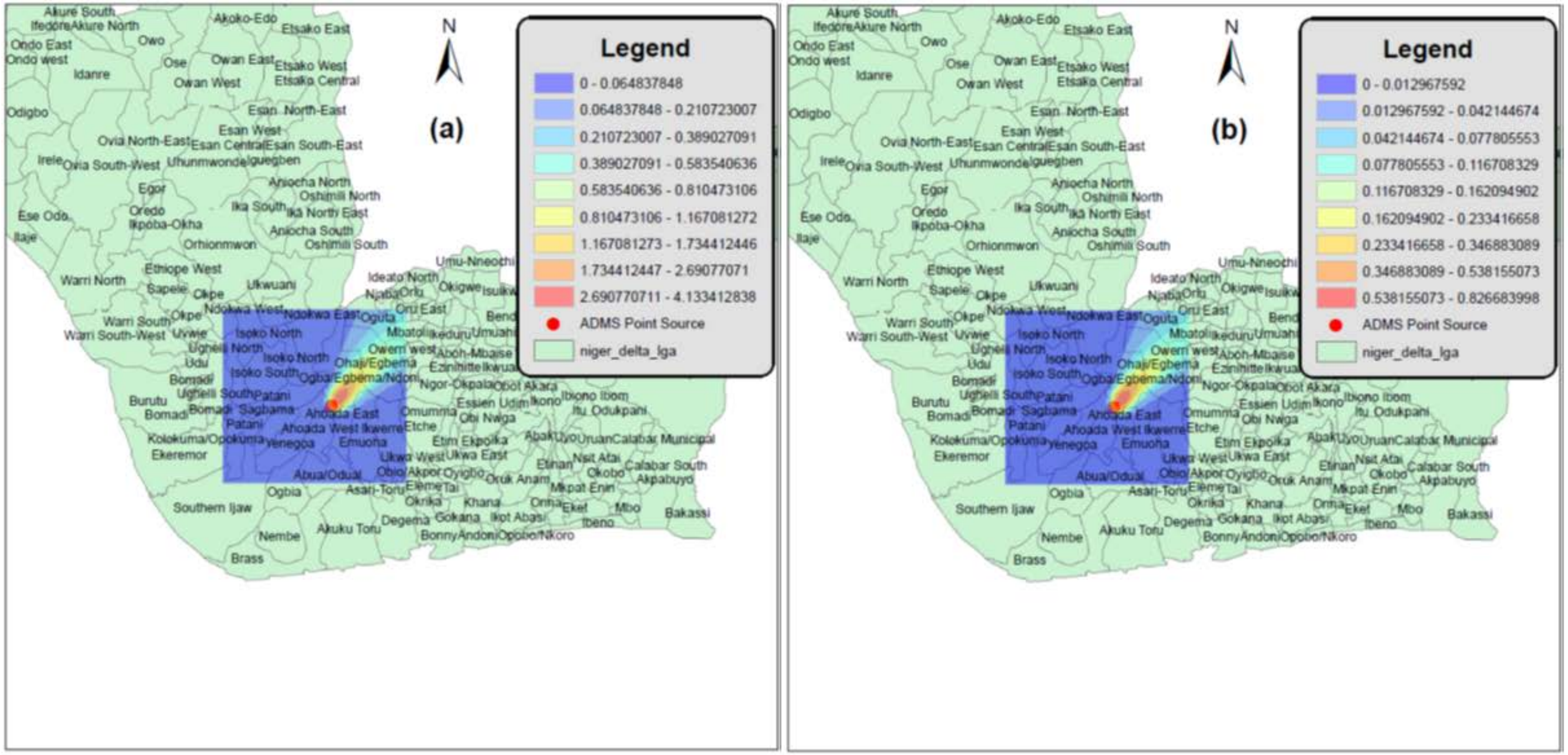

Figure C.5: Modelled dispersion pattern and monthly mean ground-level concentration for (a) CO, and (b) BC for flare modelled as non-buoyant source (Aug 2015).

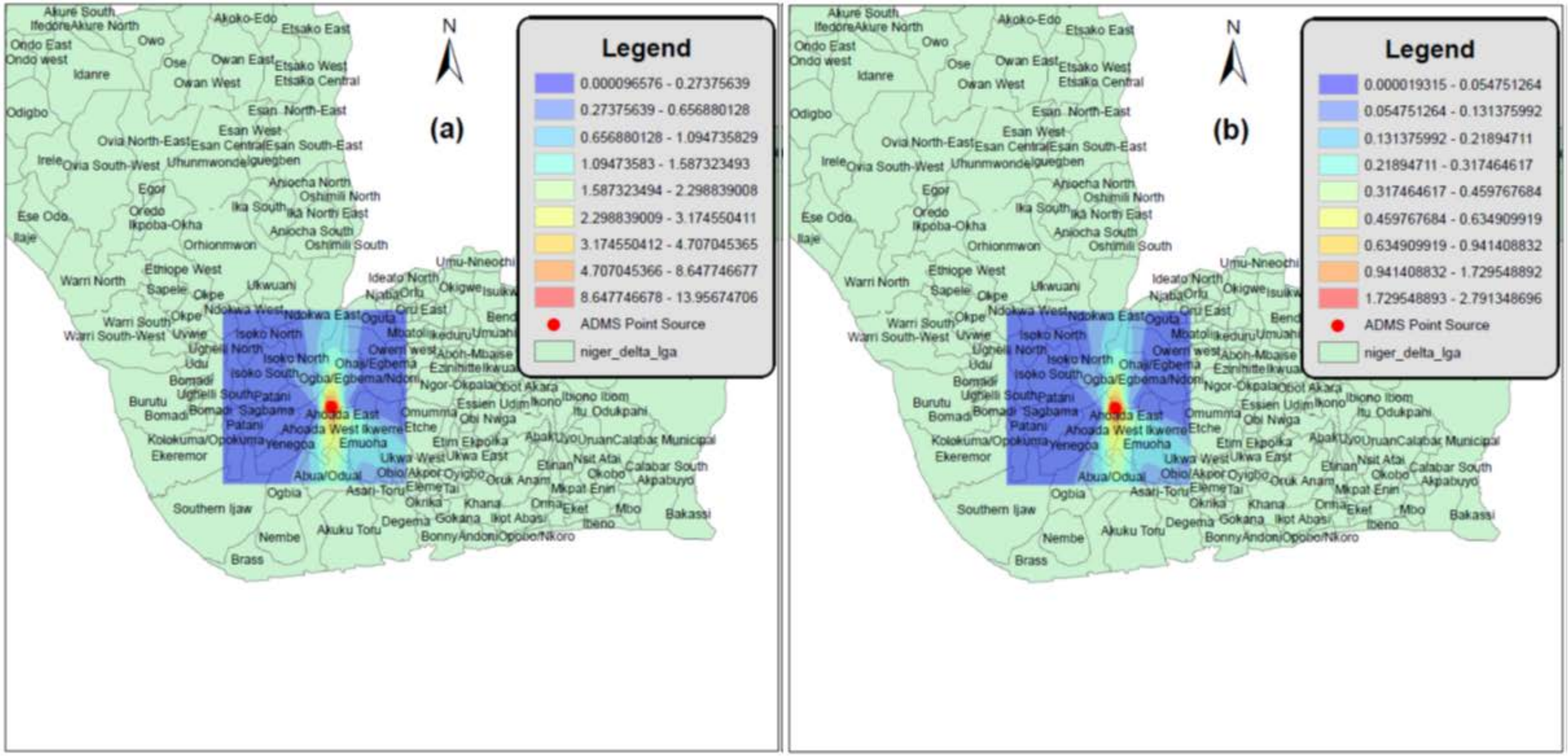

Figure C.6: Modelled dispersion pattern and monthly mean ground-level concentration for (a) CO, and (b) BC for flare modelled as non-buoyant source (Jan 2015).